8-10-2021

Chemistry of a Dehydrogenase and Di-heme Enzyme Related to Tryptophan Oxidation

Christopher Ian Davis

Georgia State University

Recommended Citation

Davis, Christopher Ian, "Chemistry of a Dehydrogenase and Di-heme Enzyme Related to Tryptophan Oxidation." Dissertation, Georgia State University, 2021.
https://scholarworks.gsu.edu/chemistry_diss/201

CHEMISTRY OF A DEHYDROGENASE AND DI-HEME ENZYME RELATED TO TRYPTOPHAN OXIDATION

by

CHRISTOPHER IAN DAVIS

Under the Direction of Aimin Liu PhD

ABSTRACT

Tryptophan is an essential amino acid that is used as a building block to construct proteins, the biosynthetic precursor for several essential molecules, and is modified to serve as a cofactor in some enzymes. This dissertation focuses on two enzymes involved in tryptophan oxidation, AMSDH and MauG.

AMSDH is a dehydrogenase in the kynurenine pathway, which is the main metabolic route for tryptophan catabolism. In addition to breaking down tryptophan, the kynurenine pathway is also involved in regulating the innate immune response, NAD biosynthesis, and some neurodegenerative. As such, enzymes of the kynurenine pathway are of fundamental interest for study. This work leveraged a bacterial homologue of human AMSDH to solve its crystal structure in various forms, including several catalytic intermediates. The knowledge gained from the bacterial enzyme was then used to identify and verify human ALDH8A1 as the human AMSDH.

MauG is the enzyme responsible for catalyzing the formation of the tryptophan-derived cofactor of methylamine dehydrogenase. It is a diheme enzyme that utilizes hydrogen peroxide perform long-range oxidations on its protein substrate. MauG possesses the remarkable ability to store two oxidizing equivalents as a *bis*-Fe(IV) species that is stabilized through a type III charge resonance phenomenon. The nature of the charge resonance phenomenon was investigated with exogenous small molecules, radical traps, and temperature dependent studies. Finally, a cryogenic method for generating radicals was developed to study the electronic structure of model compounds similar to the substrate of MauG.

INDEX WORDS: Aldehyde dehydrogenase, Kynurenine pathway, Enzyme mechanism, Reaction intermediates, Radical enzymology, Electron paramagnetic resonance

CHEMISTRY OF A DEHYDROGENASE AND DI-HEME ENZYME RELATED TO TRYPTOPHAN OXIDATION

by

CHRISTOPHER IAN DAVIS

A Dissertation Submitted in Partial Fulfillment of the Requirements for the Degree of

Doctor of Philosophy

in the College of Arts and Sciences

Georgia State University

2021

CHEMISTRY OF A DEHYDROGENASE AND DI-HEME ENZYME RELATED TO TRYPTOPHAN OXIDATION

by

CHRISTOPHER IAN DAVIS

Committee Chair: Aimin Liu

Committee: Donald Hamelberg
Markus Germann

Electronic Version Approved:

Office of Graduate Services
College of Arts and Sciences
Georgia State University
August 2021

DEDICATION

This work is dedicated to my mother and grandmother. Without their unwavering love and support, this would not have been possible.

ACKNOWLEDGEMENTS

This has been a long journey, and there are too many people to recognize them all properly. First, I thank all members, past and present, of the Liu Lab for their comradery, support, and willingness to help each other. I will always cherish the highly collaborative nature of the group. I appreciate Fange (Kathy) Liu for taking me in as an undergrad and teaching me how to purify protein, the first step in any enzymologists research. I thank Dr. Shahab Shamsi and his post-doc Dr. Xiaochun Wang for their collaborative efforts that lead to my first peer-reviewed work.

I am deeply indebted to Lu (Cindy) Huo and Jifeng (Jeff) Geng. Without their training, mentorship, and collaboration this dissertation would not exist. The work on ACMSD lead by Lu Huo, though not part of this dissertation, was instrumental in my learning the basics of enzymology and applying biophysics concepts to an enzyme. She then worked hand-in-hand with me to get the AMSDH project off the ground. Jiafeng Geng was the lead on the MauG project, and I thank him for teaching me the tricky business of purifying a protein without an overexpression system and for many valuable discussions about EPR. I also thank Dr. Victor Davidson for providing the MauG expression system.

I am extremely grateful to Dr. Jurek Krzystek and all of the staff at the National High Magnetic Field Lab in Tallahassee, FL (funded by the NSF through a Cooperative Agreement DMR 1157490, the State of Florida, and the U.S. Department of Energy). I think Dr. Andrzej Ozarowski for the software package, DOUBLET, which was used to analyze all high-field/high-frequency EPR spectra. I also thank Ross Terrell, our resident organic chemist and my collaborator on the tryptophan radical project. Our time spent at the high field lab was the most hard-working and rewarding time of my graduate program.

I thank Dr. Yu Yang, Dr. Daniel Wherritt, and Dr. Wendell Griffith for their guidance and contributions. Dr. Yang was an ideal collaborator who carried on Lu's work while also providing indispensable assistance to the AMSDH project. I thank Dr. Wherritt for teaching me almost everything I know about practical NMR and many fruitful discussions (The NMR spectrometer is a shared instrument sponsored by the National Science Foundation under Award 1625963). I thank Dr. Griffith for teaching me all about mass spectrometers and how they can be applied to biochemical research (The mass spectrometry facility was sponsored by National Institutes of Health Grant G12MD007591).

I am grateful to the Departments of Chemistry at GSU (from where I will graduate) and UTSA (where I am currently) for having me as a student/researcher and providing great environments for academic research. I would also like to thank my dissertation committee for taking spending the time necessary to ensure a successful start to what will hopefully be a long career in science. I especially thank Dr. Donald Hamelberg for providing a final push to make sure things get finished.

Finally, I am most grateful to my PhD advisor, Dr. Aimin Liu. He took a chance accepting a completely inexperienced undergrad into his lab and has been extremely patient and encouraging. In addition to training in experimental techniques and scientific writing, I am extremely appreciative of him sharing so much of what goes on 'behind the scenes' to keep an academic research lab running. It has been a truly unique experience that I carry with me for the rest of my life. I also feel privileged to work under a PI who heavily emphasizes training workshops, traveling for academic conferences, and the art of making an impactful presentation.

I would like to acknowledge NSF award MCB-0843537 for "Mechanistic studies of tryptophan-oxidizing enzymes," and R01 GM108988 for "Heme and protein radical-mediated

remote enzyme catalysis” for supporting this dissertation work during different time periods on various enzymes. I would also like to thank the Molecular Basis of Disease Area of Focus graduate fellowship for supporting me and providing a forum to interact with other young scientists at GSU. X-ray data were collected at the Southeast Regional Collaborative Access Team (SER-CAT) 22-ID and 22-BM beamlines at the Advanced Photon Source, Argonne National Laboratory. Use of the Advanced Photon Source was supported by the U.S. Department of Energy, Office of Science, Office of Basic Energy Sciences, under Contract No. W-31-109-Eng-38. Single-crystal spectroscopy data were obtained at beamline X26-C of the National Synchrotron Light Source (NSLS), Brookhaven National Laboratory with the support of the U.S. Department of Energy under Contract No. DE-AC02-98CH10886. I thank The Texas Advanced Computing Center (TACC) for accessing computational resources.

TABLE OF CONTENTS

LIST OF TABLES

LIST OF FIGURES

LIST OF ABBREVIATIONS

KP	kynurenine pathway
NAD	nicotinamide adenine dinucleotide
QUIN or QA	quinolinic acid
TDO	tryptophan 2,3-dioxygenase
IDO	indolamine 2,3-dioxygenase
HAO	3-hydroxyanthranilic acid dioxygenase
NMDA	N-methyl-D-aspartate
ACMSD	α-amino-β-carboxymuconate-ϵ-semialdehyde decarboxylase
PIC or PA	picolinic acid
AMSDH	α-aminomuconate-ϵ-semialdehyde dehydrogenase
2-AMS	2-aminomuconate-6-semialdehyde
2-AM	2-aminomuconate
HMSDH	hydroxymuconate semialdehyde dehydrogenase
ALDH	aldehyde dehydrogenase
ACMS	2-amino-3-carboxymuconate-6-semialdehyde
2-HMS	2-hydroxymuconate-6-semialdehyde
MW	molecular weight
3-HAA	3-hydroxyanthranilic acid
RMSD	root mean square deviation
CR	charge resonance
NIR	near-infrared
MO	molecular orbital

ET	electron transfer
TTQ	tryptophan tryptophylquinone
MADH	methylamine dehydrogenase
preMADH	immature precursor to MADH
CN	cyanide
IM	imidazole
F	fluoride
DMPO	5,5-dimethyl-1-pyrroline *N*-oxide
DMPOX	5,5-dimethyl-2-oxopyrroline-1-oxyl
DMPOXH	1-hydroxy-5,5-dimethylpyrrolidin-2-one
EPR	electron paramagnetic resonance
HPLC	high-performance liquid chromatography
NB	nitrosobenzene
HFEPR	high-frequency/high-field EPR
COSMO	conductor-like screening model
L-Trp	L-tryptophan
D-Trp	D-tryptophan
5-F-Trp	5-fluorotryptophan
5-MeOx-Trp	5-methoxytryptophan
5-OH-Trp	5-hydroxytryptophan
7-OH-Trp	7-hydroxytryptophan

1 THE KYNURENINE PATHWAY OF TRYPTOPHAN CATABOLISM

This chapter is adapted from the published work authored by ID: Davis I and Liu A (2015) What is the tryptophan kynurenine pathway and why is it important to neurotherapeutics? *Expert Review in Neurotherapeutics*, 15(7), 719-721. DOI: 10.1586/14737175.2015.1049999

1.1 Abstract

The kynurenine pathway has received increasing attention as its connection to inflammation, the immune system and neurological conditions has become more apparent. It is the primary route for tryptophan catabolism in the liver and the starting point for the synthesis of nicotinamide adenine dinucleotide in mammals. Dysregulation or overactivation of this pathway can lead to immune system activation and accumulation of potentially neurotoxic compounds. These aspects make the kynurenine pathway a promising target for therapeutic development to treat inflammation and disease with neurological aspects, especially in cancer patients undergoing chemotherapy.

1.2 The kynurenine pathway

Tryptophan is an essential amino acid that is used to build protein and is a biosynthetic precursor to numerous neurologically active compounds. It is probably most well known as the starting point for the biosynthesis of serotonin and melatonin. While the generation of these two compounds may have garnered the most attention in the past, a less well-known pathway for tryptophan metabolism, the kynurenine pathway, has recently seen steadily increasing research activity. The importance of the kynurenine pathway, which accounts for the catabolism of approximately 99% of ingested tryptophan not used for protein synthesis [1], was originally ascribed to its role in the biogenesis of nicotinamide adenine dinucleotide (NAD); however, apparent links with neurodegenerative diseases, tumor proliferation, inflammation and depression are currently driving the study of the kynurenine pathway.

The kynurenine pathway was first discovered in 1853 through the detection of excreted products from animals fed tryptophan. In the ensuing century, much work was performed to establish the chemical transformations, enzymes involved, and possible disease relations of the kynurenine pathway. In the 1960s, the component enzymes of the kynurenine pathway were fully elucidated through the laborious work of extracting each component enzyme from mammalian tissue and determining their corresponding activities [2].

As the link between the kynurenine pathway and major depressive disorder became more apparent, the serotonin hypothesis was proposed, stating that upon activation, the kynurenine pathway would divert available tryptophan away from serotonin production towards further catabolism [3]. Although the correlation between kynurenine pathway activity and inflammation has been confirmed in many instances, the serotonin hypothesis has not survived in its original form. It was shown that kynurenine pathway activation by IFN-α did not significantly lower the tryptophan concentration in cerebrospinal fluid, although it did lead to inflammation by increasing the amounts of kynurenine pathway metabolites, namely kynurenine, kynurenic acid and quinolinic acid (abbreviated as QA or QUIN), concentrations in cerebrospinal fluid [4]. Inflammation caused by kynurenine pathway activation has also been implicated in the treatment resistance of some patients suffering from depression as well as with patients undergoing chemotherapy [5].

Thanks to modern molecular biological methods, as well as the discovery of analogous kynurenine pathways in bacterial species [6], it recently became possible to study the individual enzymes of the kynurenine pathway at the molecular level. The first and rate-limiting step of the kynurenine pathway is catalyzed by tryptophan 2,3-dioxygenase (TDO) or indoleamine 2,3-dioxygenase (IDO). These heme-dependent enzymes insert molecular oxygen across the 2–3 bond of the indole moiety of tryptophan [7] and were formerly known as tryptophan pyrrolase. TDO is a homotetramer with rigid substrate selectivity which is found mostly in hepatic tissue, whereas IDO is a monomer with much more relaxed specificity that is found in most tissues. Notably, IDO is increasingly recognized as a link between the immune system and the kynurenine pathway, as it is activated by cytokines and appears to have some anti-inflammatory effects. It is also implicated in the tumor-suppressive abilities of IFN-γ [8]. From a mechanistic enzymology viewpoint, these enzymes are unique, as they are the only known dioxygenases that employ a heme prosthetic group as a cofactor. Furthermore, IDO is the only enzyme, other than superoxide dismutase that can utilize superoxide as a substrate, implicating it in oxidative stress response.

The product of the TDO/IDO-catalyzed reaction, N-formylkynurenine, is then hydrolyzed to kynurenine. Depending on the tissue type, kynurenine either continues down its pathway toward the tricarboxylic acid cycle or is transformed to kynurenic acid in microglial cells or astrocytes, respectively [9]. Kynurenine and its immediate metabolites do not appear to have any direct effects on neurons; however, they do possess various pro- and antioxidant activities. Alternatively, kynurenic acid competitively antagonizes glutamate receptors and non-competitively inhibits the α7 nicotinic acetylcholine receptor [9].

Further down the kynurenine pathway, a second dioxygenase, 3-hydroxyanthranilic acid dioxygenase (HAO), is utilized to open the remaining aromatic ring that once belonged to tryptophan. HAO is a type III, non-heme, iron-dependent extradiol dioxygenase [10]. Although not as unique as TDO/IDO, HAO still has interesting features. Notably, HAOs from bacterial sources often contain an extra, rubredoxin-like metal binding domain that is not necessary for catalysis. This domain is not found in HAOs from animal sources, raising the question as to the function and significance of such an extra metal binding domain. HAO cleaves the ring of 3-hydroxyanthranilic acid, a known free radical generator, to create α-amino-β-carboxymuconate-ϵ-semialdehyde, a compound that decays non-enzymatically to the NAD precursor, QUIN. The renewed interest in the kynurenine pathway is due in large part to the discovery that QUIN can selectively activate N-methyl-D-aspartate (NMDA) receptors [11-12]. Although the basal levels of QUIN are not such that they can significantly excite NMDA receptors, activation of the kynurenine pathway can lead to dangerous QUIN levels, which are associated with numerous neurological diseases: Alzheimer's disease, anxiety, depression, epilepsy, human immunodeficiency virus-associated neurocognitive disorders and Huntington's disease [11, 13-17]. The generation of QUIN is thought to be the major link between the kynurenine pathway and inflammatory response [18].

The next enzyme in the kynurenine pathway not only exhibits unique chemistry but is also the major branching point between a non-enzymatic formation of the excitotoxic NAD precursor, QUIN and further metabolism. This enzyme is α-amino-β-carboxymuconate-ϵ-semialdehyde decarboxylase (ACMSD), the only known metal-dependent, oxygen-independent decarboxylase. The x-ray crystal structure of this enzyme was recently solved, and biochemical work has shown a potential mechanism for regulating the activity of this enzyme. It was shown that only the homo-dimer form of ACMSD is able to catalyze the decarboxylation of the substrate, opening the door to the possibility that modulation of the quaternary structure of ACMSD may be the dominant regulatory mechanism for this enzyme [19-20]. Another interesting feature of ACMSD is that both its substrate and product are unstable and will undergo electrocyclizations to QUIN and picolinic acid, respectively. Although there are a wealth of studies showing the deleterious effects of QUIN, the literature on the effects of picolinic acid is sparse, and no consensus has yet been reached as to its physiological roles and effects [21]. It seems to represent a metabolic dead-end for the kynurenine pathway, as it is excreted.

At least in the in vitro studies, the substrate of ACMSD is an order of magnitude more stable than its product [22], which brings up the natural question of how the rates of these two non-enzymatic decay reactions are controlled in the cell. Answering this question will require detailed knowledge of the enzymatic mechanism of HAO, ACMSD, and the next enzyme in the pathway, α-aminomuconate-ϵ-semialdehyde dehydrogenase (AMSDH). The structure and mechanism of ACMSD are relatively well studied [19-20], and the structure of HAO is defined [23]. However, little was known about this third enzyme, which presumably controls the partitioning between further metabolism and picolinic acid formation, until very recently, when the crystal structure was solved, and catalytic mechanism proposed [22]. α-Aminomuconate-ϵ-semialdehyde dehydrogenase (AMSDH) is a member of the aldehyde dehydrogenase superfamily and the first energy harvesting step of the kynurenine pathway, oxidizing its semialdehyde substrate while reducing NAD.

To summarize, the primary metabolic route for tryptophan catabolism in mammals produces neuroactive compounds, one of which, QUIN, is both the biosynthetic precursor to NAD production and an agonist of NMDA receptors. Elevation of QUIN concentrations in cerebrospinal fluids has been seen in several neurodegenerative diseases, and injection of exogenous QUIN can cause neurodegeneration in mice. The kynurenine pathway can be stimulated in the brain by treatment with IFN-α. These findings point to the production of QUIN by the kynurenine pathway as a contributing factor to neurodegenerative diseases that are associated with inflammation.

1.3 Conclusion

The kynurenine pathway is the major route for tryptophan catabolism in mammalian cells, and many of the intermediates and products of this pathway are implicated in numerous neurological diseases. As such, the kynurenine pathway is a ripe target for drug discovery, especially because so little is known regarding its regulation. The kynurenine pathway also has some connection to tumor growth and proliferation through one of its initiating enzymes, IDO, and there are IDO inhibitors currently in Phase II clinical trials [24]. In recent years, the kynurenine pathway has received increased attention from clinicians, biologists, and biochemists as its medical relevance became more apparent. Even with the renewed effort, there is still a lack of understanding of how the production of arguably the most detrimental metabolite, QUIN, is controlled and work must be done to target its production therapeutically. There is a current need for investigations into the mechanisms by which the kynurenine pathway is regulated, especially the enzymes involved in QUIN formation.

2 CRYSTALLOGRAPHIC AND SPECTROSCOPIC SNAPSHOTS REVEAL A DEHYDROGENASE IN ACTION

This chapter is adapted from the published work co-first authored by ID: Huo L, Davis I, Liu F, Andi B, Esaki S, Iwaki H, Hasegawa Y, Orville AM, and Liu A (2015) Crystallographic and spectroscopic snapshots reveal a dehydrogenase in action. *Nature Communications*, 6:5935.
DOI: 10.1038/ncomms6935

2.1 Abstract

Aldehydes are ubiquitous intermediates in metabolic pathways and their innate reactivity can often make them quite unstable. There are several aldehydic intermediates in the metabolic pathway for tryptophan degradation that can decay into neuroactive compounds that have been associated with numerous neurological diseases. An enzyme of this pathway, 2-aminomuconate-6-semialdehyde dehydrogenase, is responsible for 'disarming' the final aldehydic intermediate. Here we show the crystal structures of a bacterial analogue enzyme in five catalytically relevant forms: resting state, one binary and two ternary complexes, and a covalent, thioacyl intermediate. We also report the crystal structures of a tetrahedral, thiohemiacetal intermediate, a thioacyl intermediate and an NAD^+-bound complex from an active site variant. These covalent intermediates are characterized by single-crystal and solution-state electronic absorption spectroscopy. The crystal structures reveal that the substrate undergoes an *E*/*Z* isomerization at the enzyme active site before an sp^3-to-sp^2 transition during enzyme-mediated oxidation.

2.2 Introduction

The dominant route of tryptophan catabolism, the kynurenine pathway, has recently garnered increased attention given its apparent association with numerous inflammatory and neurological conditions, for example, gastrointestinal disorders, depression, Parkinson's disease, Alzheimer’s disease, Huntington’s disease and AIDS dementia complex [25-30]. Though the precise mechanism by which the kynurenine pathway influences these diseases has not yet been fully elucidated, it has been determined that several metabolites of this pathway are neuroactive. Notably, the concentration of quinolinic acid, a non-enzymatically derived decay product of an intermediate of the kynurenine pathway used for NAD^+ biosynthesis, is elevated over 20-fold in patients’ cerebrospinal fluid with AIDS dementia complex, aseptic meningitis, opportunistic infections or neoplasms [31], and more than 300-fold in the brain of human immunodeficiency virus-infected patients [32]. This NAD^+ precursor has also been shown to be an agonist of NMDA receptors, and an increase of its concentration may lead to over-excitation and death of neuronal cells [11, 14].

The apparent medical potential of the kynurenine pathway warrants detailed study and characterization of its component enzymes and their regulation. One enzyme in particular, 2-aminomuconate-6-semialdehyde dehydrogenase (AMSDH), is responsible for oxidizing the unstable metabolic intermediate 2-aminomuconate-6-semialdehyde (2-AMS) to 2-aminomuconate (2-AM) (Figure 2.1a). On the basis of sequence alignment, AMSDH is a member of the hydroxymuconic-semialdehyde dehydrogenase (HMSDH) family under the aldehyde dehydrogenase (ALDH) superfamily [33]. ALDHs are prevalent in both prokaryotic and eukaryotic organisms and are responsible for oxidizing aldehydes to their corresponding carboxylic acids. They use $NAD(P)^+$ as a hydride acceptor to harvest energy from their primary substrate and generate NAD(P)H, which provides the major reducing power to maintain cellular redox balance [34-35]. In addition to being commonly occurring metabolic intermediates, aldehydes are reactive electrophiles, making many of them toxic. Enzymes of the ALDH superfamily are typically promiscuous with regards to their substrates; however, in recent years, this superfamily has had several new members identified with greater substrate fidelity, especially when the substrate is identified as a semialdehyde [36].

The putative native substrate of AMSDH, 2-AMS, is a proposed metabolic intermediate in both the 2-nitrobenzoic acid degradation pathway of *Pseudomonas fluorescens* KU-7 [37] and the kynurenine pathway for L-tryptophan catabolism in mammals [11, 14, 38]. In the presence of NAD^+ and AMSDH, 2-AMS is oxidized to 2-AM (Figure 2.1a); however, it can also spontaneously decay to picolinic acid and water with a half-life of 35 s at neutral pH. [39]. Due to its instability, 2-AMS has not yet been isolated, leaving its identity as the substrate of AMSDH an inference based on decay products and further metabolic reactions. There are several reasons for the poor understanding of this pathway: it is complex with many branches, some of the intermediates are unstable and difficult to characterize, and several enzymes of the pathway, including AMSDH, are not well understood. Hence, the structure of AMSDH will help to address questions such as what contributes to substrate specificity for the semialdehyde dehydrogenase and how 2-AMS is bound and activated during catalysis.

In the present study, we have cloned AMSDH from *Pseudomonas fluorescens*, generated an *E. coli* overexpression system and purified the target protein for molecular study. We also constructed several mutant expression systems to characterize the role of specific active site residues. Enzymatic assays were performed for all forms of the enzyme, and crystal structures were solved for the wild type and one mutant. We were able to capture several catalytic intermediates *in crystallo* by soaking protein crystals in mother liquor containing either the primary organic substrate or a substrate analogue and discovered that in addition to dehydrogenation, the substrate undergoes isomerization in the active site.

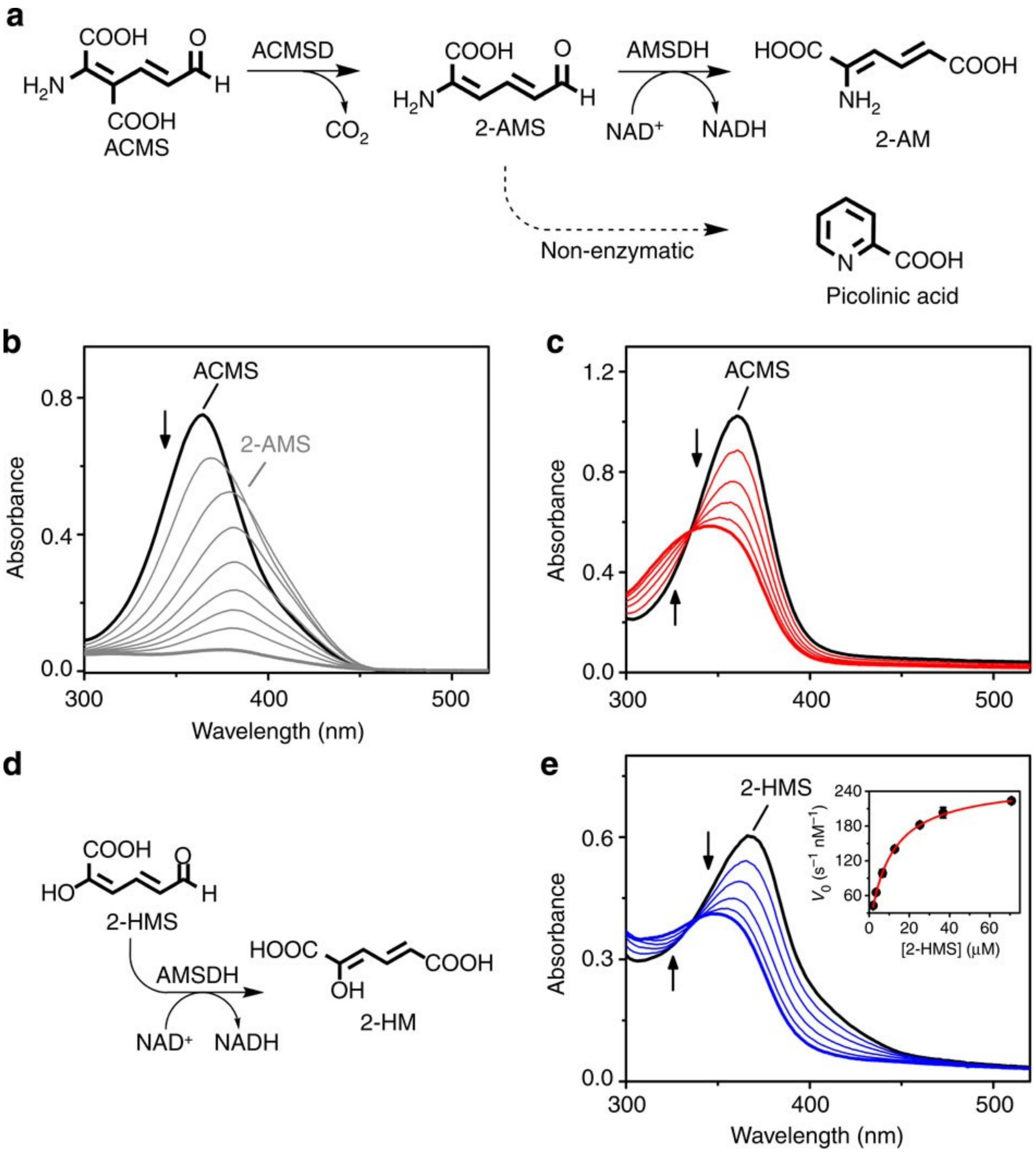

Figure 2.1 Activity of AMSDH. (a) Reaction scheme showing the enzymatic generation of 2-AMS, the reaction catalyzed by AMSDH, and the competing non-enzymatic decay of 2-AMS to picolinic acid. (b) Representative assay showing the ACMSD (1 μM)-catalyzed conversion of ACMS (λ_{max} 360 nm) to 2-AMS (λ_{max} 380 nm), which decays to picolinic acid (transparent). (c) Coupled-enzyme assay in which AMSDH (200 nM) oxidizes 2-AMS, produced in situ as shown in b in 50 s, to 2-AM (λ_{max} 325 nm). (d) Reaction scheme showing 2-HMS oxidation by AMSDH. (e) Representative assay showing the activity of AMSDH (200 nM) on 2-HMS (λ_{max} 375 nm) in 50 s. The inset is a Michaelis-Menten plot.

2.3 Results

2.3.1 Catalytic activity of wild-type AMSDH

Due to the unstable nature of its substrate, 2-AMS, the activity of AMSDH was detected using a coupled-enzyme assay that employed its upstream partner, α-amino β-carboxymuconate ε-semialdehyde decarboxylase (ACMSD), to generate 2-AMS in situ. ACMSD transforms α-amino β-carboxymuconate ε-semialdehyde (ACMS) (λ_{max} at 360 nm) to 2-AMS (λ_{max} at 380 nm) [38-39]. As seen in Figure 2.1b, in an assay that uses only ACMSD, the absorbance peak of its substrate, ACMS, red-shifts to 380 nm as 2-AMS is formed. The absorbance at 380 nm then quickly decreases as 2-AMS decays to picolinic acid, a compound with no absorbance features above 200 nm. In a coupled-enzyme assay, ACMSD, AMSDH and NAD^+ are included in the reaction system. As shown in Figure 2.1c, ACMS is still consumed; however, there is no red shift observed because 2-AMS is enzymatically converted to 2-AM (λ_{max} at 325 nm) rather than accumulating and decaying to picolinic acid. The production of 2-AM requires that an equimolar amount of NAD^+ be reduced to NADH (λ_{max} at 339 nm). A stable alternative substrate, 2-hydroxymuconate-6-semialdehyde (2-HMS), was used to pursue kinetic parameters (Figure 2.1d), when using saturating NAD^+ concentrations (≥1 mM), the k_{cat} and K_M of AMSDH for 2-HMS were 1.30 ± 0.01 s^{-1} and 10.4 ± 0.2 μM, respectively (Figure 2.1e).

2.3.2 Structural snapshots of the dehydrogenase catalytic cycle

We solved five crystal structures of wild-type AMSDH, including the ligand-free (2.20 Å resolution), NAD^+-bound binary complex (2.00 Å), ternary complex with NAD^+ and substrate 2-AMS (2.00 Å) or 2-HMS (2.20 Å), and a thioacyl intermediate (1.95 Å). All five structures belong to space group $P2_12_12_1$. Data collection and refinement statistics are listed in Table 2.1. The complete AMSDH model includes four polypeptides per asymmetric unit describing one homotetramer (Figure 2.2). Each monomer of AMSDH contains three domains: a subunit interaction domain, a catalytic domain and an NAD$^+$ binding domain (Figure 2.2b). For details of the secondary structure, see Supplementary Discussion in 2.4.1.

Table 2.1. X-ray crystallography data collection and refinement statistics.

Data collection	**Apo-AMSDH**	**NAD-AMSDH**	**NAD-2-AMS-AMSDH**	**NAD-2-HMS-AMSDH**	**Thioacyl Intermediate**	**E268A-AMSDH**	**E268A-Thiohemiacetal Intermediate**	**E268A-Thioacyl Intermediate**
detector type	MAR300 CCD	MAR225 CCD	MAR300 CCD	MAR300 CCD	MAR225 CCD	MAR225 CCD	MAR225 CCD	MAR225 CCD
source	APS, Sector 22-ID	APS, Sector 22-BM	APS, Sector 22-ID	APS, Sector 22-ID	APS, Sector 22-BM	APS, Sector 22-BM	APS, Sector 22-BM	APS, Sector 22-BM
space group	$P2_22_12_1$	$P2_22_12_1$	$P2_22_12_1$	$P2_22_12_1$	$P2_22_12_1$	$P2_22_12_1$	$P2_22_12_1$	$P2_22_12_1$
unit cell lengths (Å)	a=88.27, b=141.89, c=172.92	a=88.58, b=142.00, c=174.38	a=88.40, b=142.12, c=174.41	a=88.57, b=142.72, c=175.01	a=88.36, b=141.75, c=174.37	a=88.53, b=141.98, c=173.80	a=88.57, b=141.56, c=174.63	a=88.33, b=141.35, c=173.53
unit cell angles (˚)	α=β=γ=90°	α=β=γ=90°	α=β=γ=90°	α=β=γ=90°	α=β=γ=90°	α=β=γ=90°	α=β=γ=90°	α=β=γ=90°
wavelength (Å)	0.8	1.0	0.8	0.8	1.0	1.0	1.0	1.0
temperature (K)	100	100	100	100	100	100	100	100
resolution (Å) [a]	45.00-2.20 (2.24-2.20)	35.00-2.00 (2.07-2.00)	35.00-1.98 (2.03-1.98)	45.00-2.15 (2.19-2.15)	45.00-1.95 (1.98-1.95)	50.00-2.00 (2.03-2.00)	50.00-2.15 (2.15-2.19)	50.00-2.20 (2.24-2.20)
completeness (%)[a]	99.8 (99.4)	99.8 (98.9)	95.2 (99.7)	99.9 (100.0)	94.9 (88.8)	97.2 (97.4)	99.9 (100)	99.6 (99.2)
R_{merge} (%)[a, b]	8.0 (53.5)	11.2 (89.1)	10.7 (78.3)	12.2 (84.1)	10.4 (84.3)	10.8 (74.5)	14.8 (58.7)	9.9 (71.7)
$I/\sigma I$ [a]	45.2 (4.4)	27.3 (2.3)	22.7 (2.2)	27.1 (2.7)	28.4 (2.2)	13.3 (3.2)	17.7 (3.9)	36.9 (3.7)
multiplicity [a]	14.0 (11.6)	13.7 (9.1)	9.8(7.8)	12.5 (10.3)	10.5 (6.4)	11.9 (10.5)	8.8 (7.6)	11.4 (10.3)
no. of observed reflections	109724	149605	149047	120432	152910	146528	119893	110554
Refinement								
resolution (Å)	2.20	2.00	2.00	2.15	1.95	2.00	2.15	2.20
no. reflections; working/test	109619/5469	149298/7485	147418/7401	114123/6029	145080/7649	144988/7303	119216/5973	110312/5518
R_{work} (%)[c]	18.6	17.2	16.2	18.0	17.6	19.5	19.2	18.4
R_{free} (%)[d]	23.9	21.8	20.8	23.7	21.6	23.7	23.5	22.7
no. of protein atoms	14651	14684	14684	14684	14684	14668	14668	14668
no. of ligand atoms	23	188	220	220	220	204	220	220
no. of solvent sites	702	1682	1397	802	1702	1188	1136	882
Average B-factor (Å^2)								
protein	41.1	28.5	28.5	39.7	27.9	31.7	29.2	36.2
NAD$^+$	N/A	28.8	40.1	56.7	37.5	37.0	41.4	56.4
NA$^+$	35.3	N/A	32.3	41.6	30.7	34.0	43.6	43.9

[a] Values in parentheses are for the highest resolution shell.

[b] $R\text{merge} = \Sigma_i\, |I_{hkl,i} - \langle I_{hkl}\rangle| / \Sigma_{hkl}\, \Sigma_i\, I_{hkl,i}$, where $I_{hkl,i}$ is the observed intensity and $\langle I_{hkl}\rangle$ is the average intensity of multiple measurements.

[c] $R\text{work} = \Sigma||F_o|-|F_c||/\Sigma|F_o|$, where $|F_o|$ is the observed structure factor amplitude, and $|F_c|$ is the calculated structure factor amplitude.

[d] Rfree is the R factor based on 5% of the data excluded from refinement.

[e] Based on values attained from refinement validation options in COOT

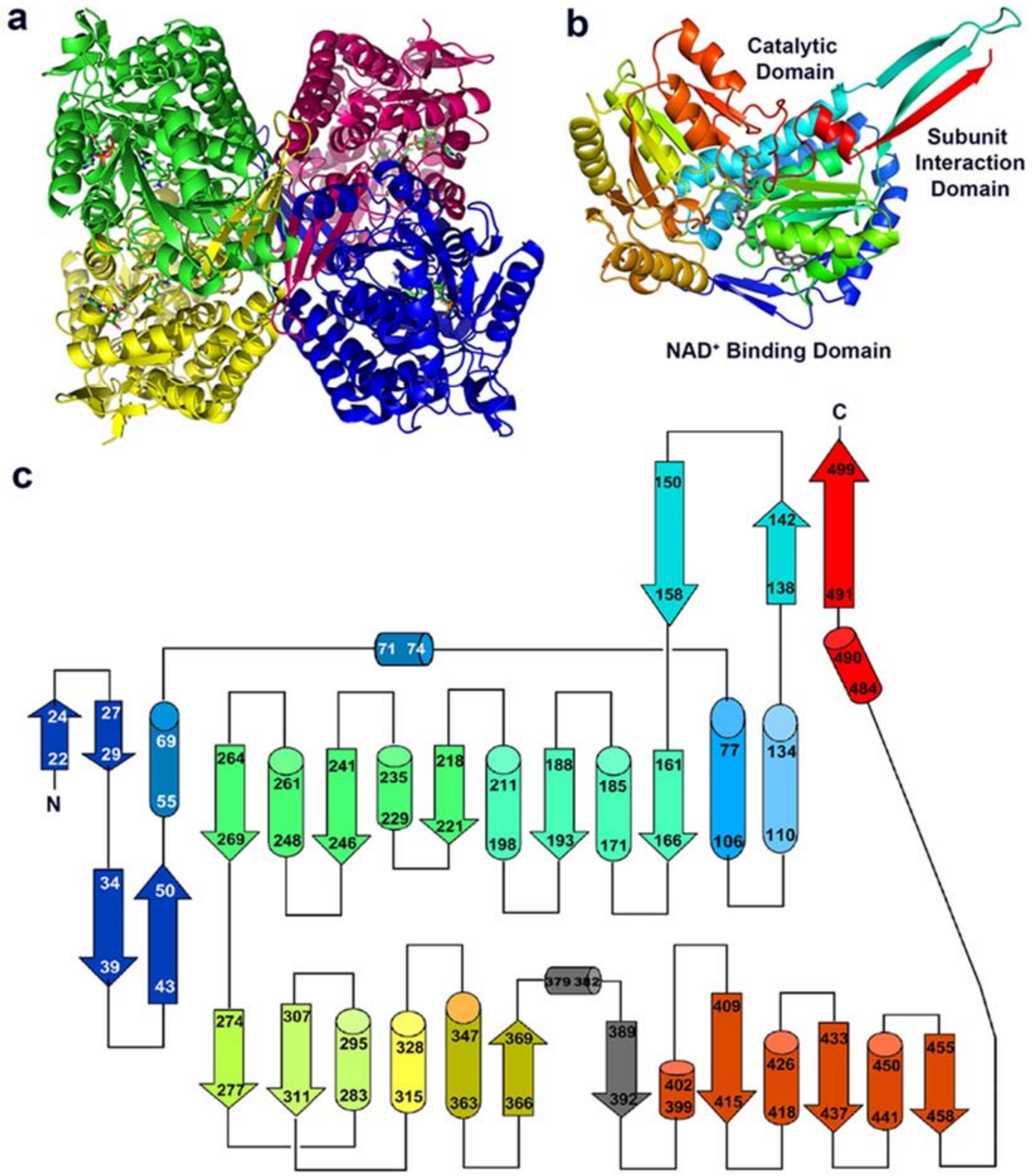

Figure 2.2. Overall crystal structure of AMSDH. (a) View of the tetramer with the subunit A in pink, subunit B in blue, subunit C in yellow, and subunit D in green. Each subunit contains an NAD$^+$ molecule, which is shown in stick representation and colored by elements. (b) Structure of one AMSDH subunit with NAD$^+$ and substrate 2-AMS. The ribbon trace is rainbow-colored with the *N*-terminus in blue and the *C*-terminus in red. Top right is the subunit interaction domain, bottom right shows the cofactor binding domain, and top middle and left is the catalytic domain. NAD$^+$ and 2-AMS are shown as stick models with gray color. (c) Topology diagram showing the AMSDH secondary structure, which is also rainbow-colored according to cartoon in (b).

In the structure of the co-crystallized binary complex, an NAD$^+$ molecule is present in an extended, anti-conformation in the amino-terminal, co-substrate-binding domain of each monomer (Figure 2.3a). The electron density map of NAD$^+$ is well defined, and the interactions between the protein and NAD$^+$ are equivalent in all four subunits as shown in Figure 2.3e. The NAD$^+$-bound AMSDH structure is similar to the ligand-free structure with an aligned r.m.s.d. of 0.239 Å. Residues that belong to the NAD$^+$-binding pocket are also well aligned with the exception of Cys302, Arg108 and Leu116 (Figure 2.4). On binding NAD$^+$, the thiol moiety of Cys302 rotates so that the sulfur is 2.3 Å closer to the substrate-binding pocket and away from the nicotinamide head of NAD$^+$.

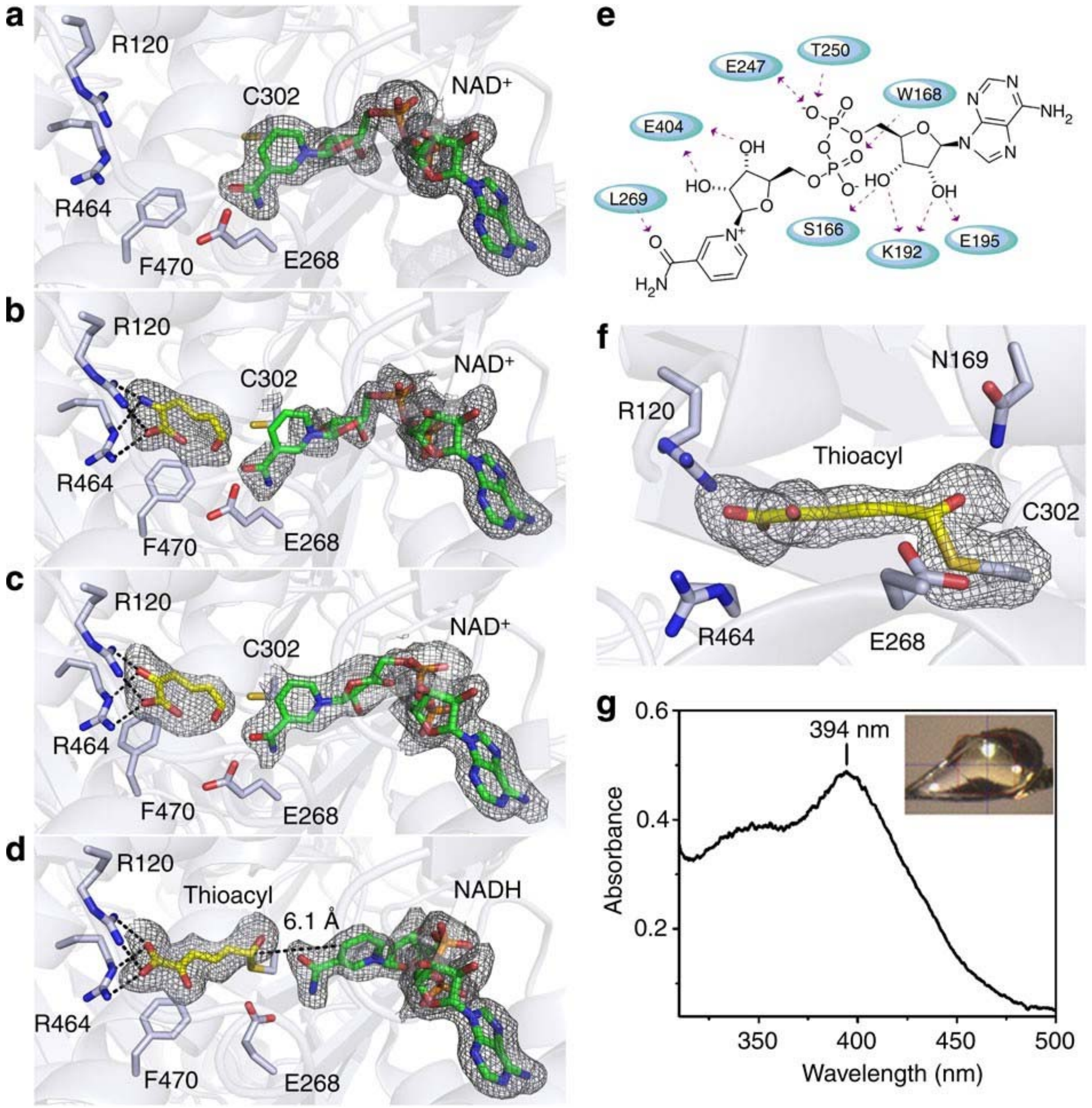

Figure 2.3. Crystal structures of wild-type AMSDH and single-crystal electronic absorption spectrum of a catalytic intermediate. AMSDH was co-crystallized with NAD$^+$ to give AMSDH-NAD$^+$ binary complex crystals which were used for soaking experiments. (a) Active site structure of the binary AMSDH-NAD$^+$ complex, (b) the ternary complex of AMSDH-NAD$^+$ crystals soaked with 2-AMS for 5 minutes before flash-cooling, (c) the ternary complex of AMSDH-NAD$^+$ soaked with 2-HMS for 10 minutes before flash-cooling, (d) the trapped thioacyl, NADH-bound intermediate obtained by soaking AMSDH-NAD$^+$ crystals with 2-HMS for 40 minutes before flash-cooling. (e) 2D-interaction diagram for NAD$^+$ binding. (f) Close-up of the thioacyl intermediate in d. (g) Single-crystal electronic absorption spectrum of d. Protein backbone and residues are shown as light blue cartoons and sticks, respectively. The substrates and intermediate are shown as yellow sticks, and NAD$^+$ and NADH are shown as green sticks. The omit map for ligands is contoured to 2.0 σ and shown as a grey mesh.

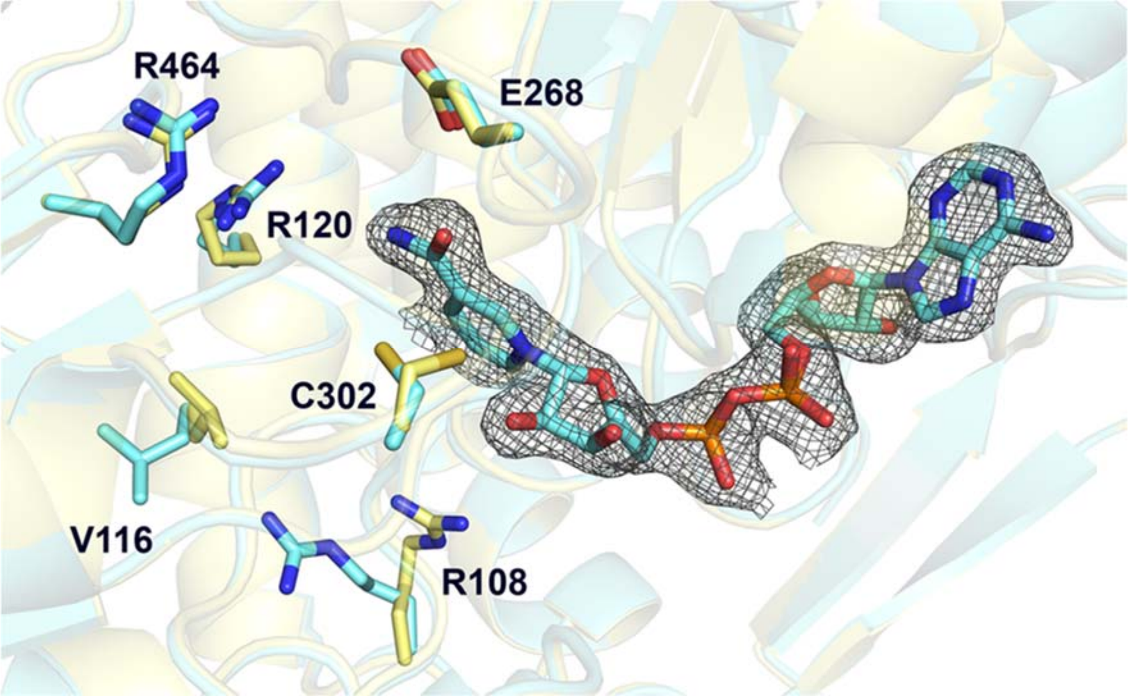

Figure 2.4. Local changes at the active site of AMSDH induced by NAD$^+$ binding. Superimposition of the active sites of apo-AMSDH (yellow) and NAD$^+$-bound-AMSDH (blue). The $2F_o$ - F_c electron density map is contoured to 1.0 σ and shown as a grey mesh. Residues and NAD$^+$ are shown as sticks. The overall structure aligned very well with a RMSD of 0.239 Å. Arg108, Val116, and Cys302 are the only residues to have notable conformational changes caused by NAD$^+$ binding.

2.3.3 Crystal structures of enzyme–substrate ternary complexes

Structures of AMSDH in ternary complex with co-substrate NAD$^+$ and its primary substrates were obtained by soaking co-crystallized AMSDH-NAD$^+$ crystals with 2-AMS and 2-HMS, respectively. Extra density that fits with the corresponding substrate molecule was observed in the active site of each subunit. The co-substrate NAD$^+$ in the ternary complex structures is bound in the same manner as in the binary complex. Binding of the primary substrates introduced minimal change to the protein structure; the r.m.s.d. for the superimposed structures of substrate-free with 2-AMS- and 2-HMS-bound ternary complex structures are 0.170 and 0.276 Å, respectively. These two primary substrates bind to AMSDH in an identical fashion, with two arginine residues, Arg120 and Arg464, playing an important role in stabilizing the substrate by forming two sets of bifurcated hydrogen bonds with one of the carboxyl oxygens and the 2-amino or hydroxyl group of 2-AMS (Figure 2.3b) or 2-HMS (Figure 2.3c), respectively. The observation of two hydrogen bonds being donated by the active site arginines to the 2-amino group of 2-AMS indicates that in the substrate-bound form, 2-AMS may be in its 2-imine rather than 2-enamine tautomer, as an amino group unlikely to accept two hydrogen bonds. Mutation of Arg120 to alanine causes a moderate decrease of the k_{cat} to 0.7 ± 0.2 s^{-1} from 1.30 ± 0.01 s^{-1} and a dramatic increase of the K_{M} with a lower bound of 446.3 ± 195.9 µM (an accurate determination of the K_{M} is hindered by insufficient 2-HMS concentrations) compared with 10.4 ± 0.2 µM in the wild type (Figure 2.5a). Mutation of Arg464 to alanine decreased the k_{cat} to ~0.3 s^{-1}, and not only increased the K_{M} to ~170 µM, but also leads to a significant substrate inhibition effect with a K_{i} of ~6 µM (Figure 2.5b). This substrate inhibition is likely caused by the unproductive binding of a second substrate molecule in the space created by the deletion of

Arg464 or by a failure of the enzyme to properly bind and stabilize the imine form of the substrate.

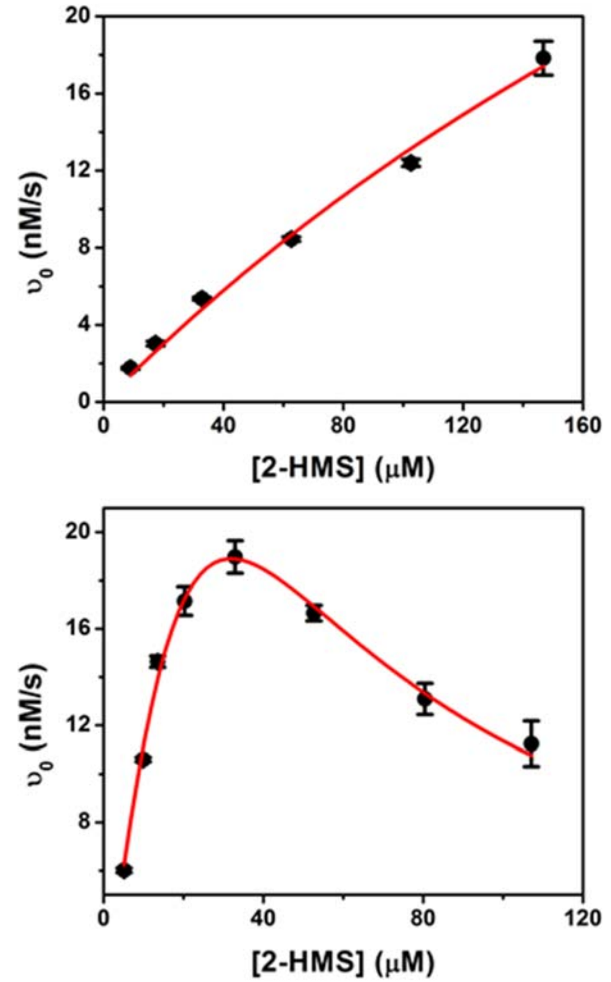

Figure 2.5. Kinetic assays of R120A and R464A with 2-HMS. (a) Activity of R120A fit with the Michaelis-Menten equation. (b) Activity of R464A fit with the Michaelis-Menten equation with substrate inhibition. Assay details can be found in the materials and methods.

2.3.4 Catalytic intermediates trapped after ternary complex formation

Enzyme–NAD$^+$ binary complex crystals were soaked in mother liquor containing 2-HMS for a range of time points from 5 min to more than 3 h before flash cooling in liquid nitrogen. In a crystal that was soaked for 40 min, an intermediate was trapped and refined to a resolution of 1.95 Å (Figure 2.3d). Crystals soaked for longer time points gave a similar intermediate with poorer resolution. In this structure, 2-HMS is observed in the 2*Z*, 4*E* isomer rather than the 2*E*, 4*E* isomer as seen in the substrate-bound ternary structure. Also, the substrate interacts with Arg120 and Arg464 with both of its carboxyl oxygens rather than one carboxyl oxygen and the 2-hydroxy oxygen as shown in the 2-HMS ternary complex structure. Fitting this density with the 2*E*, 4*E* conformation resulted in unsatisfactory $2F_o$–F_c and F_o–F_c density maps as shown in Figure 2.6a. Likewise, attempting to fit the 2*Z*, 4*E* isomer to the ternary complex structure did not produce satisfactory results (Figure 2.6b). On *E* to *Z* isomerization, the carbon chain of the substrate extends, and the distance between its sixth carbon and Cys302's sulfur is now at 1.8 Å, which is within covalent bond distance for a carbon–sulfur bond. Also, the continuous electron density between Cys302-SG and 2-HMS-C6 indicates the presence of a covalent bond (Figure 2.3f). Another feature of this intermediate is that the nicotinamide ring of NAD$^+$ has moved 4.6 Å away from the active site and adopted a bent conformation (Figure 2.3d) compared with the position in the binary or ternary complex structures (Figure 2.3a–c). The structural changes of NAD$^+$ associated with reduction has been observed and well documented [40-41]. In the oxidized state, NAD(P)$^+$ lies in the Rossmann fold in an extended conformation, allowing for hydride transfer from the substrate to its nicotinamide carbon during the first half of the reaction. Reduced NAD(P)H then adopts a bent conformation in which the nicotinamide head moves back towards the protein surface. This movement provides more space in the active site for the second half of the reaction, acyl-enzyme adduct hydrolysis, to take place. Thus, the coenzyme in this intermediate structure is likely to have been reduced to NADH and, as such, the structure is assigned as a thioacyl-enzyme–substrate adduct. The single-crystal electronic absorption spectrum of the sample has an absorbance maximum at 394 nm (Figure 2.3g). The same

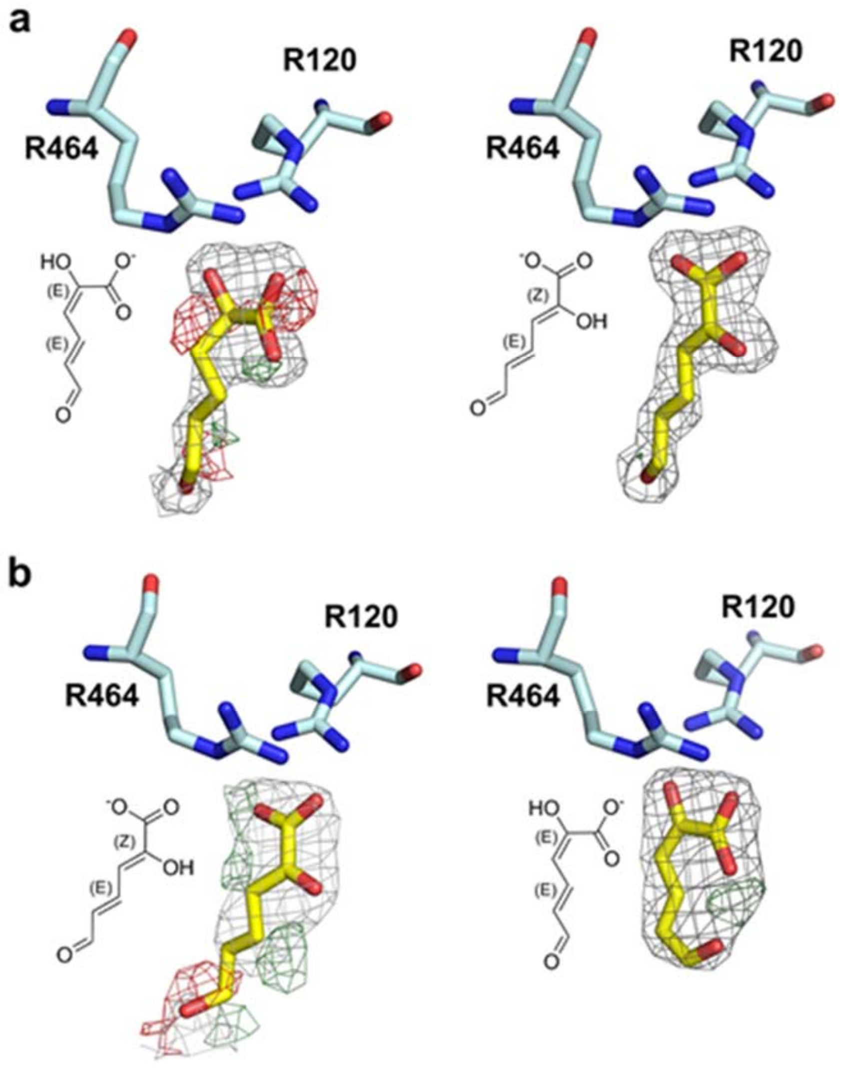

Figure 2.6 Alternate fitting of substrate-bound ternary complex and thioacyl intermediate. (a) Electron density map of the thioacyl intermediate fit with incorrect model of (2*E*, 4*E*)-2-hydroxy-6-oxohex-2,4-enoic acid (left) and the correct model (right), respectively. (b) Electron density map of the substrate-bound ternary complex fit with incorrect model of (2*Z*, 4*E*)-2-hydroxy-6-oxohex-2,4-enoic acid (left) and the correct model (right), respectively. The $2F_o$ - F_c map is shown in gray mesh contoured at 1.0 σ. The F_o - F_c electron density maps are shown in green mesh contoured at 3.0 σ and red mesh contoured at -3.0 σ. The chemical structure of each ligand is shown on the left of the fitting.

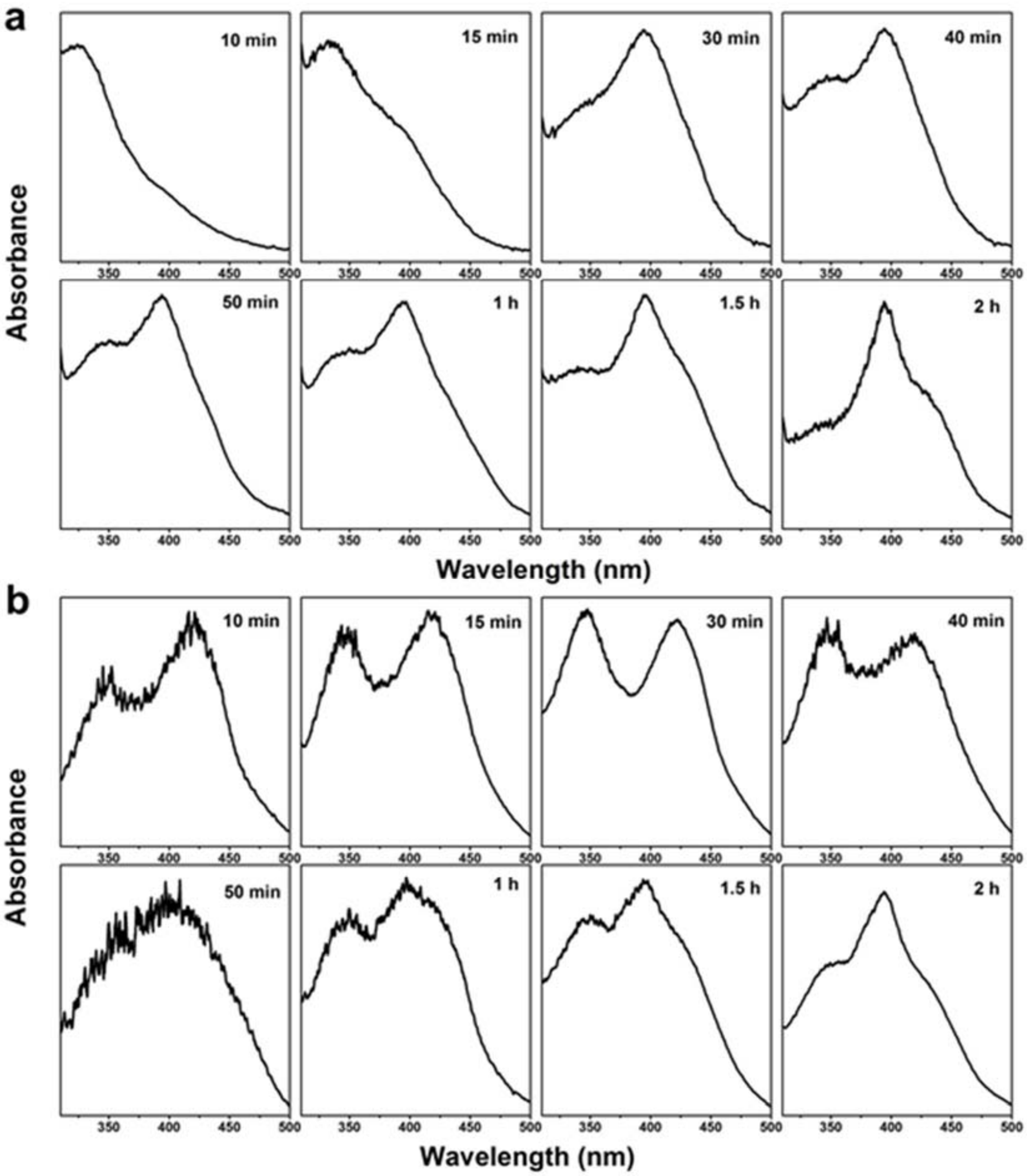

Figure 2.7 Single-crystal electronic absorption spectra of wtAMSDH and E268A AMSDH co-crystallized with NAD$^+$ and soaked with 2-HMS.(a) wtAMSDH co-crystallized with NAD$^+$ and soaked with 2-HMS for increasing time. before flash-cooling in liquid nitrogen. (b) Same experiment as a using E268A AMSDH. The soaking solution contains 0.2 M sodium phosphate dibasic, pH 9.1, 20% polyethylene glycol 3350, and 1 mM 2-HMS.

absorbance band was observed in crystals soaked with 2-HMS from 30 min to 2 h (Figure 2.7). However, this long-lived intermediate in the crystal was not observed in solution with millisecond-to-second time resolution in stopped-flow experiments (Figure 2.8a). Thus, it is either present in an earlier time domain (sub-milliseconds), or alternatively, it may not accumulate in solution because NADH can readily dissociate in solution, whereas it may be trapped in the active site when in the crystalline state.

Another notable change in the intermediate structure is the movement of the side chain of Glu268, which rotates 73° towards the active site (Figure 2.3c,d). To probe the function of Glu268, we constructed an alanine variant and found that it exhibited no detectable activity in steady-state kinetic assays. Interestingly, E268A exhibits completely different pre-steady state activity than the wild-type enzyme. As shown in Figure 2.8b, an absorbance band at 422 nm was formed concomitant with the decay of the 2-HMS peak within 1 s of the reaction. This new species is generated stoichiometrically on titration of 2-HMS with E268A (Figure 2.9d). The moiety that gives rise to this new absorbance band is stable for minutes at room temperature and

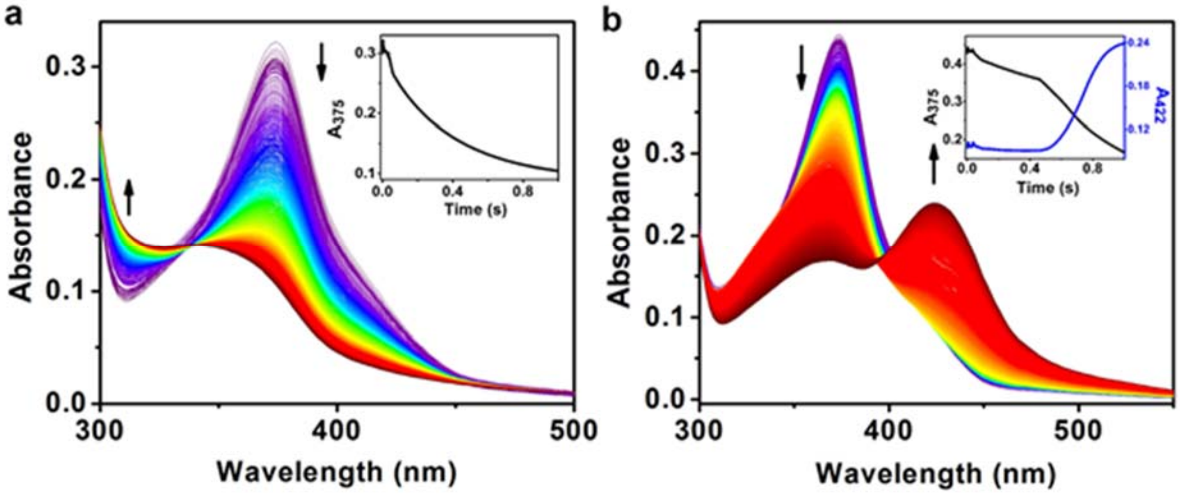

Figure 2.8 Time-resolved, stopped-flow UV-Vis spectra of the reactions of wtAMSDH and E268A with 2-HMS. (a) wtAMSDH (23 μM) is mixed with 2-HMS (25 μM) and observed for 1.0 s. Decay of 2-HMS (λ_{max} 375 nm) is inset. (b) E268A AMSDH (23 μM) is mixed with 2-HMS (25 μM) and observed for 1.0 s. Decay of 2-HMS (λ_{max} 375 nm) and the formation of an intermediate (λ_{max} 422 nm) are inset. The reaction is performed in buffer containing 25 mM HEPES, pH 7.5, and 1 mM NAD$^+$ at 10 °C. The arrows indicate the trends of changes in the spectra.

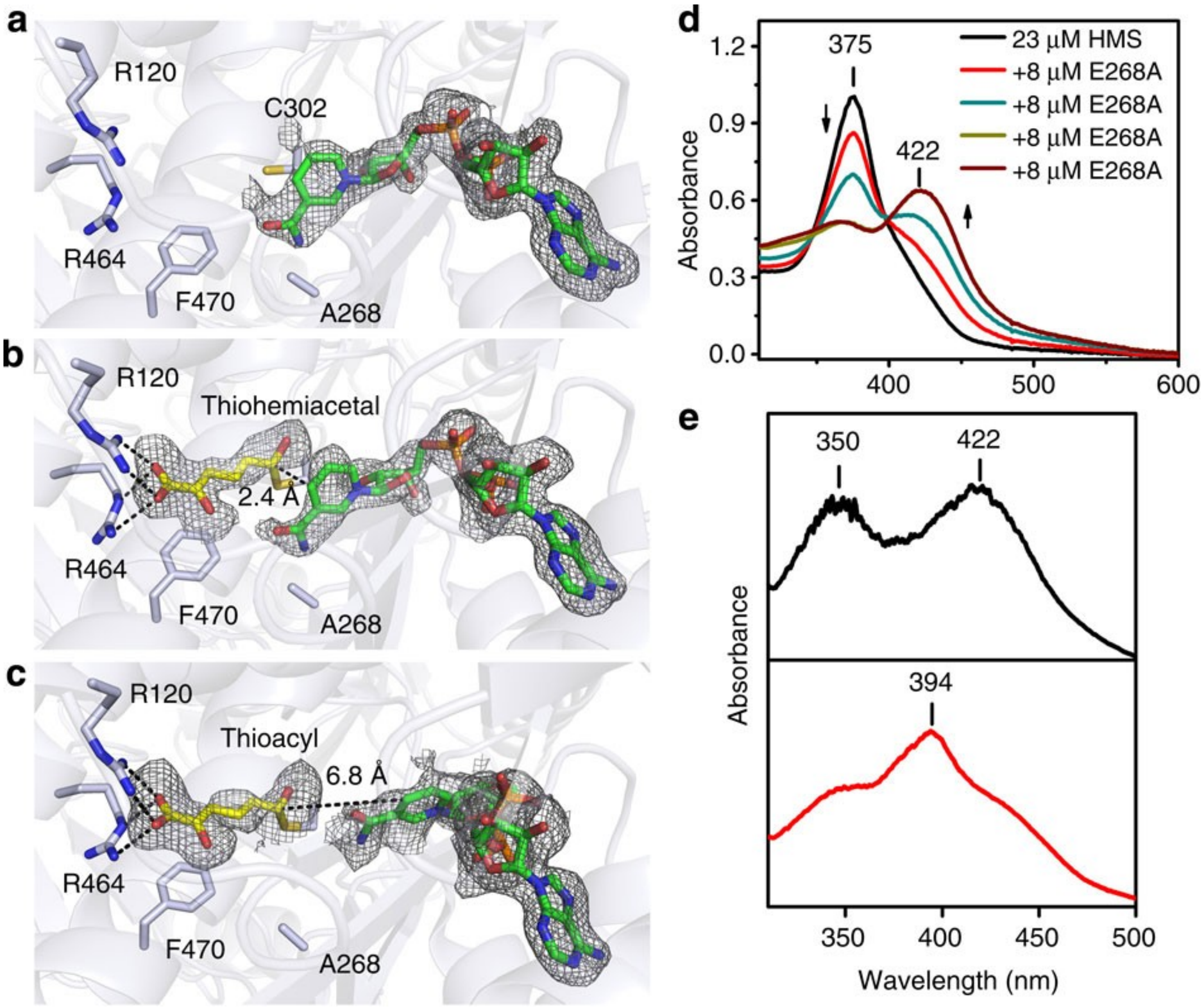

Figure 2.9 Crystal structures of the E268A mutant and its solution and single-crystal electronic absorption spectra. (a) Structure of the active site of the co-crystallized E268A-NAD$^+$ binary complex, (b) a thiohemiacetal intermediate obtained by soaking the E268A-NAD$^+$ crystals with 2-HMS for 30 min before flash-cooling, (c) a thioacyl intermediate obtained by soaking the E268A-NAD$^+$ crystals with 2-HMS for 180 min before flash-cooling. (d) Solution electronic absorption spectra of a titration of 2-HMS with E268A. (e) Single-crystal electronic absorption spectrum of the intermediate in b (top panel), and single-crystal electronic absorption spectrum of the intermediate in c (bottom panel). Protein backbone and residues are shown as light blue cartoons and sticks, respectively. The substrate and intermediate are shown as yellow sticks, and NAD$^+$ and NADH are shown as green sticks. The omit map for ligands is contoured to 2.0 σ and shown as a grey mesh.

cannot be separated from the protein by membrane filtration-based methods [19], suggesting that it is covalently bound to the protein. The formation of an enzyme–substrate adduct in the E268A mutant was investigated by mass spectrometry. For the as-isolated E268A, the resultant multiply

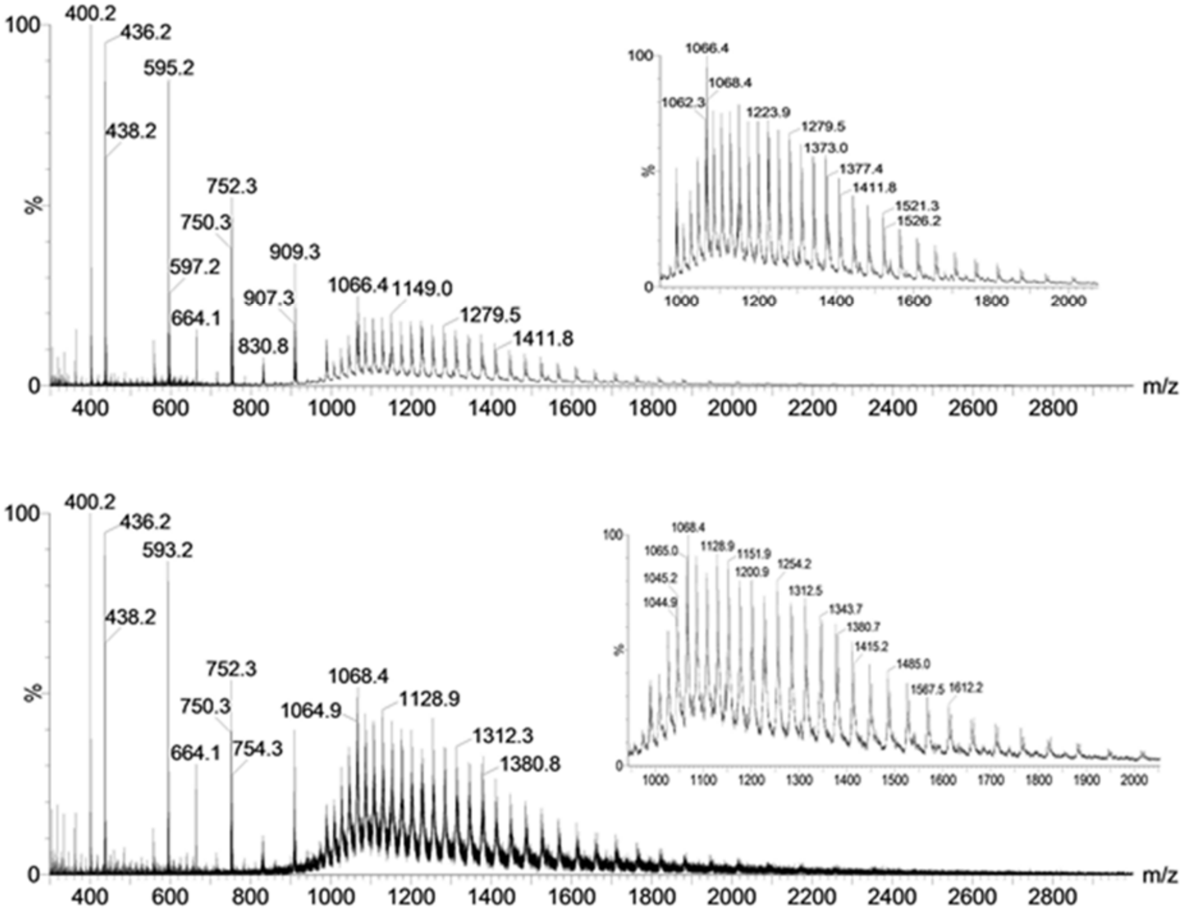

Figure 2.10 Raw ESI mass spectra of E268A AMSDH. As-isolated protein (top) and E268A treated with 2-HMS (bottom). Narrow range scans corresponding to the proteins are shown in the insets.

charged states (Figure 2.10) were deconvoluted to obtain a molecular weight (MW) of 56,252 Da (Figure 2.11, top). This value is in good agreement with the predicted MW of E268A AMSDH plus an amino-terminal His-tag and linking residues, 56,251 Da. The second largest peak in the deconvoluted spectrum has a MW 177 Da greater than that of the most abundant signal. This is likely due to post-translational modification of the His-tag; α-*N*-Gluconoylation of His-tags has been observed in *E. coli*-expressed proteins, which cause 178 Da extra mass [42]. The mutant protein was then treated with the alternate substrate, 2-HMS, and the mass spectrum shows a new major peak at 56,390 Da (Figure 2.11, bottom), 138 Da heavier than the as-isolated mutant.

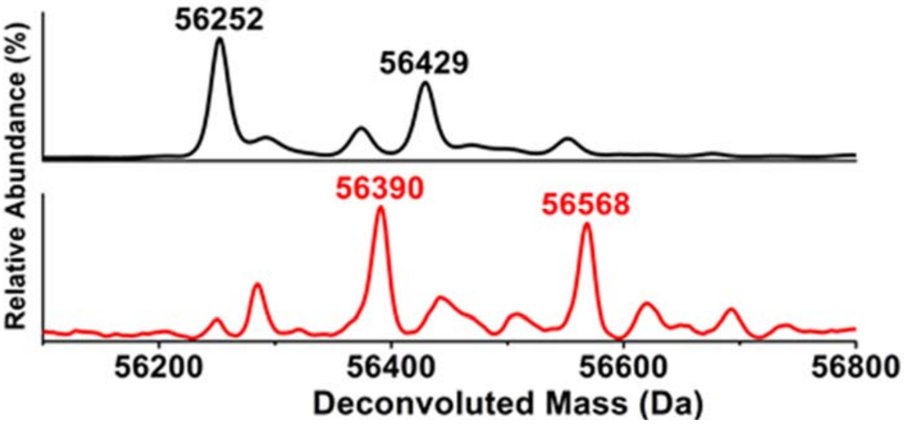

Figure 2.11 Deconvoluted mass spectra E268A AMSDH. As-isolated E268A (top) and 2-HMS treated E268A (bottom). The two major components are labeled with their respective molecular weights

Similarly, the second most abundant peak corresponds to a His-tag modified mutant plus 139 Da. In this spectrum, the peaks arising from the as-isolated mutant are substantially reduced, indicating that 2-HMS, 141 Da, is bound to the E268A mutant enzyme.

We determined the crystal structure of E268A co-crystallized with NAD$^+$ and refined it to 2.00 Å resolution (Figure 2.9a). The overall structure aligns very well with the wild-type

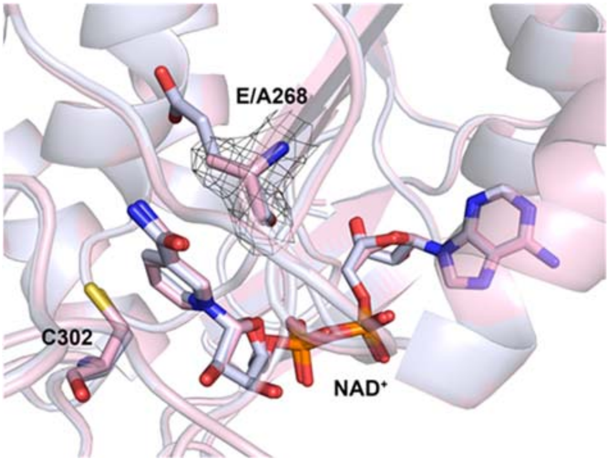

Figure 2.12 Superimposition of E268A active site with wtAMSDH. E268A and wild-type are shown in pink and grey, respectively, Cys302, Glu/Ala 268 and NAD$^+$ are present as sticks. The $2F_o$-F_c electron density map of Ala268 is shown as gray mesh contoured at 1.0 σ.

binary complex structure with an r.m.s.d. of 0.139 Å. The active site of E268A also resembles the native AMSDH structure (Figure 2.12). The nature of the absorbing species at 422 nm was further investigated by soaking co-crystallized E268A-NAD$^+$ crystals in mother liquor containing 2-HMS. By doing so, two temporally, structurally and spectroscopically distinct intermediates were identified.

When E268A-NAD$^+$ crystals are soaked with 2-HMS for 40 min or less, their single-crystal electronic absorption spectra show an absorbance maximum at 422 nm (Figure 2.7b), as was observed in the solution-state titration and the stopped-flow assays. An individual electronic absorption spectrum for an E268A-NAD$^+$ crystal soaked with 2-HMS for 15 min can be found in Figure 2.9e (top). The structure of E268A-NAD$^+$ soaked with 2-HMS for 30 min before flash cooling was solved and refined to 2.15 Å resolution (Figure 2.9b). In this structure, a continuous electron density between Cys302-SG and 2-HMS-C6 is observed, similar to the thioacyl intermediate observed in the wild-type enzyme. However, in contrast to the thioacyl

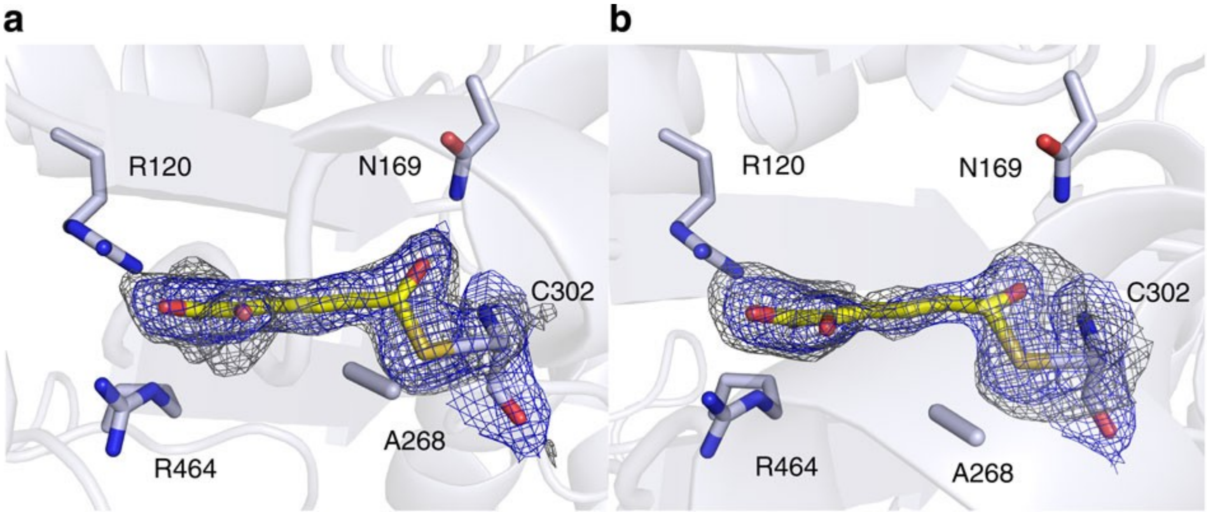

Figure 2.13 Crystal structures of two distinct catalytic intermediates. (a) Electron density map of the thiohemiacetal intermediate obtained from E268A-NAD$^+$ crystal soaked with 2-HMS for 30 min, (b) Electron density map of the thioacyl intermediate obtained from E268A-NAD$^+$ crystal soaked with 2-HMS for 180 minutes. The $2F_o$ - F_c electron density map for ligands and Cys302 is contoured to 1.0 σ and shown as a blue mesh. The omit map for ligands and Cys302 is contoured to 2.0 σ and shown as a gray mesh.

intermediate, the density around C6 is less flat, indicating an sp^3- rather than sp^2-hybridized carbon (Figure 2.13). The angle between the plane of the carbon backbone of the substrate and the formerly aldehydic oxygen is 55 ± 9°, compared with the angle of the wild-type thioacyl intermediate at 26 ± 4° (Table 2.2). More importantly, the C6 of 2-HMS and the C4N of NAD^+ are very close (2.4–2.8 Å), making it unlikely that the hydride has been transferred from the substrate. Taken together, these data allow us to assign this intermediate to a thiohemiacetal enzyme adduct (Figure 2.9b). A similar intermediate has only been trapped once previously in a crystal that contains no co-substrate [43]. Hence, this is the first time for this intermediate to be trapped in the presence of NAD^+.

Table 2.2 Out of plane bending of the C6 oxygen in intermediate structures

PDB entry	wt-thioacyl 4NPI	E268A-thioacyl 4OUB	E268A-thiohemiacetal 4OU2
Subunit A	23.5	18.1	44.4
Subunit B	28.7	22.3	51.9
Subunit C	22.0	26.5	63.5
Subunit D	30.5	14.9	60.3
Average ± SD	26.2 ± 4.1	20.5 ± 5.1	55.0 ± 8.6

If the E268A-NAD^+ crystals are soaked with 2-HMS for longer than 1 h, their single-crystal electronic absorption spectra begin to resemble that of the wild-type, thioacyl intermediate with a corresponding absorbance maximum at 394 nm (Figure 2.7b), as seen in wild-type, thioacyl intermediate crystals. An individual electronic absorption spectrum for an E268A-NAD^+ crystal soaked with 2-HMS for 120 min can be found in Figure 2.9e (bottom). The structure of an E268A-NAD^+ crystal soaked with 2-HMS for 180 min was solved and refined to 2.20 Å (Figure 2.9c). The structure of this intermediate is also similar to the wild-type, thioacyl-enzyme adduct with NADH, rather than NAD^+ found at the active site. The distance between the C4N of NADH and C6 of 2-HMS is longer than 6.1 Å (Figure 2.9c). The electron density around

C6 is flatter (Figure 2.13b) compared with the thiohemiacetal intermediate and similar to the thioacyl intermediate trapped in the wild-type AMSDH structure (Figure 2.3f), and the angle between the plane of the carbon backbone of the substrate and the carbonyl oxygen is 20 ± 5°, which is statistically indistinguishable from that of the wild-type, thioacyl intermediate, 26 ± 4° (Table 2.2). On the basis of the similarities in their absorbance and structures, we conclude that this latter intermediate is equivalent to the wild-type, thioacyl intermediate. It is also worth noting that the strictly conserved asparagine 169 (Figure 2.13) is seen to stabilize both the thiohemiacetal and thioacyl intermediates through hydrogen-bonding interactions.

2.3.5 Investigation of isomerization by computational modelling

The isomerization of 2-AMS from the 2*E* to 2*Z* isomer implied by the solved crystal structures was probed with density functional theory calculations. The free energy profiles obtained were used to help illuminate the nature of 2-AMS and gain insight into how the active site of AMSDH may facilitate the isomerization. The total energies of different isomers and rotamers of 2-AMS in its enamine/aldehyde and imine/eneol tautomers and the rotational barriers about their respective 2–3 bond were compared. For the imine/eneol tautomer, additional computations were performed with the side groups from Arg120 and Arg464 to investigate what effect, if any, they will have on the free energy profile for rotation about the 2–3 bond of 2-AMS.

First, 2-AMS was constructed and optimized in its 2-enamine, 6-aldehyde, 2*E* isomer with a negatively charged 2-carboxylate group (Figure 2.14a). To estimate the energy barrier for an uncatalyzed isomerization from the 2*E* to the 2*Z* isomer, the 2–3 double bond was then restrained at 10° intervals from 180 to 0°, and the structure was optimized at each point. On the basis of the free energy profile (Figure 2.14a), the uncatalyzed isomerization barrier is 31.9 kcal mol^{-1}. The profile also shows that the 2*Z* isomer, as might be expected, is lower in

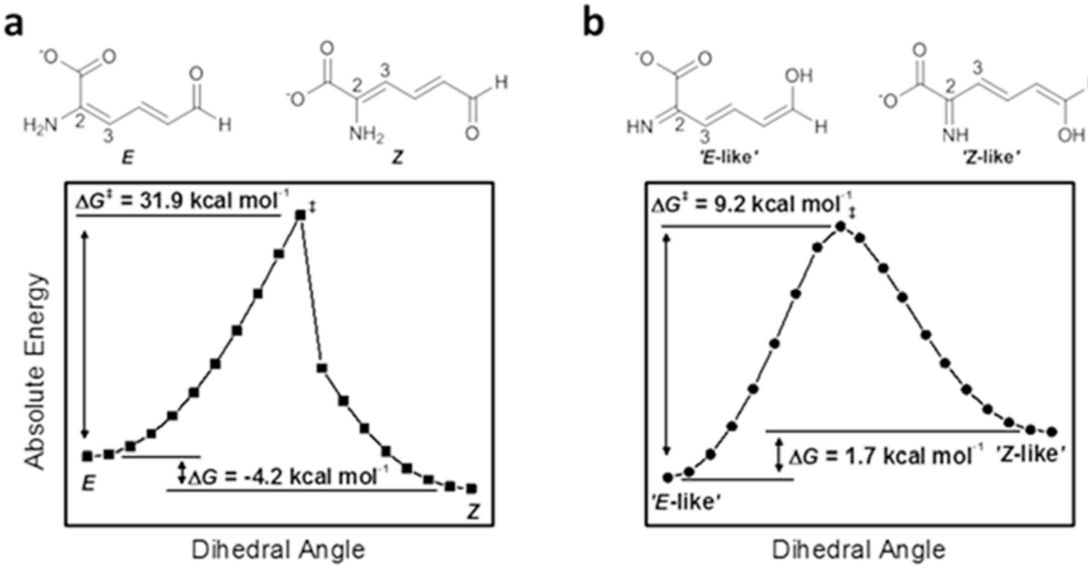

Figure 2.14 Free energy profiles for the rotation about the 2-3 bond of 2-AMS. DFT calculations were performed at the B3LYP/6-31G*+ level of theory for the (a) enamine and (b) imine form, respectively. The dihedral angle about the 2-3 bond was restrained in ten-degree increments, and the structures were optimized at each point.

energy than the 2*E* isomer by 4.2 kcal mol^{-1}. Next, the rotational barrier about the 2–3 bond of 2-AMS when in its 2-imine, 6-enol tautomer, as is suggested by the ternary complex structure, was calculated in the same manner. The barrier was found to be 9.2 kcal mol^{-1}, and opposite to the enamine tautomer, the '2*Z*-like' rotamer is higher in energy than the '2*E*-like' rotamer by 1.7 kcal mol^{-1} (Figure 2.14b). Unsurprisingly, the rotational barrier about the 2–3 bond is much lower in the imine tautomer; however, the '2*Z*-like' rotamer of the imine tautomer is 21.8 kcal mol^{-1} higher in energy than the 2*Z* isomer of the enamine tautomer.

Possible influences of the two active site arginines on the free energy profile for rotation were also considered. To mimic the conditions of the enzyme active site, similar calculations as those above were performed, which included the guanidinium heads of Arg120 and Arg464. The starting model was built using the active site geometry of the ternary complex crystal structure (PDB entry: 4I25), and on inspection, it is immediately apparent that with two arginines in such close proximity to the substrate, there is insufficient space for two hydrogen atoms on the nitrogen at the 2-position of 2-AMS, and attempts to optimize an enamine tautomer with the hydrogen-bonding pattern of the ternary complex produced structures within which the entire 2-AMS molecule rotates so that only the carboxylate group interacts with the guanidinium moieties. The absolute positions of the guanidinium groups were fixed and the structure of 2-AMS in the imine tautomer was optimized. The dihedral angle of the 2–3 bond of 2-AMS was then increased in 45° increments and the structure optimized while restraining the position of the guanidinium groups and the 2–3 bond to build a rough free energy profile to estimate the rotational barrier. In the presence of the active site arginines, the barrier about the 2–3 bond of 2-AMS is further reduced to 8.5 kcal mol^{-1} (Table 2.3). Another interesting finding is that in the presence of the guanidinium groups, the '2*E*-like' and '2*Z*-like' rotamers of 2-AMS are nearly isoenergetic, with a free energy difference of 0.2 kcal mol^{-1} (Table 2.3).

Table 2.3 Relative energy of 2-AMS with the Arg120 and Arg464 guanidinium groups.

	Dihedral Angle[a] (degrees)	Relative Energy[b] (kcal mol^{-1})
'***Z***-like'	0	0.18
	45	2.23
	90	8.47
	135	4.06
'***E***-like'	180	0.00

[a] The angle about the 2-3 bond of 2-AMS was constrained.

[b] The lowest energy structure ('*E*-like') was set as zero.

2.4 Discussion

The substrate of AMSDH, 2-AMS, contains an unstable aldehyde in conjugation with an enamine and can decay to picolinic acid and water, presumably through an electrocyclization reaction similar to its metabolic precursor, ACMS [44]. To assay the enzymatic activity, the upstream enzyme was utilized in the reaction mixture to generate substrate, and it was shown that AMSDH is catalytically active. Unfortunately, no kinetic parameters can be reliably determined because the concentration of 2-AMS is not well defined in the coupled-enzyme assay. To circumvent this issue, a previously-identified, stable alternative substrate, 2-HMS [45-46], in which a hydroxyl group replaces the amino group in 2-AMS to prevent cyclization, was used to characterize the activity of AMSDH and to examine the activity of the mutants.

Substrate-bound, ternary complex structures were obtained by soaking co-crystallized protein and NAD^+ with 2-AMS or 2-HMS. 2-AMS is an unstable compound which decays with a $t_{1/2}$ of about 9 s at pH 7.5 and 37 °C or 35 s at pH 7.0 and 20 °C. Notably, this is its first reported structure. It appears to be stabilized in the enzyme active site in its imine tautomer by forming two sets of bifurcated hydrogen bonds with Arg120 and Arg464 so that the electrocyclization reaction cannot occur. Both arginine residues are close to the protein surface and in good positions to serve as gatekeepers, bringing the substrate into the active site. As a residue residing on a loop, Arg464 should be relatively flexible. The electron density for the side chain of Arg120 is partially missing in the binary complex structure but very well resolved in both ternary complex structures. This observation indicates that the presence of substrate can stabilize what may be a flexible residue. It becomes evident from the coordinates that Arg120 and Arg464 play an important role in substrate recognition, stabilization and possibly product release. Two arginine residues are rarely observed in such close proximity, stabilizing one end of the same molecule with multiple hydrogen bonds. With the exception of the hydrogen bonds provided by Arg120 and 464, the substrate-binding pocket is mostly composed of hydrophobic residues. On the basis of sequence alignment (Figure 2.15), these two arginine residues are strictly conserved throughout the HMSDH family but are not found in other members of the ALDH superfamily. We propose that these dual arginines combined with the size restrictions provided by the hydrophobic pocket endow this enzyme with its specificity towards small α-substituted carboxylic acids with an aldehyde moiety, such as 2-AMS and 2-HMS. Furthermore, our computational work suggests that these arginines are crucial for stabilizing the imine tautomer of 2-AMS to allow for rotation about its 2–3 bond.

Two strictly conserved catalytic residues, Cys302 and Glu268, are present at the interior of the substrate-binding pocket. General features regarding these residues in the ALDH

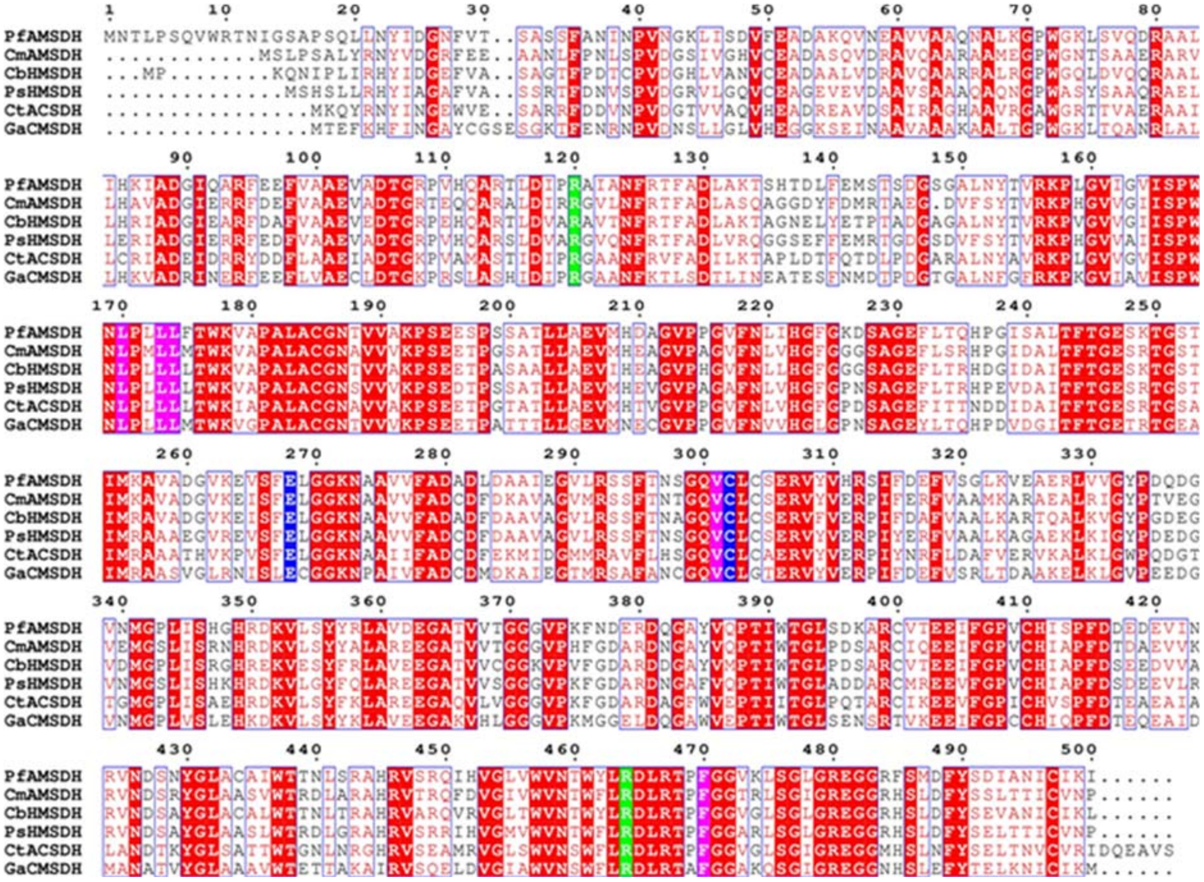

Figure 2.15 Identification of substrate binding residues for the hydroxymuconic semialdehyde dehydrogenase (HMSDH) family.Sequence alignment of several enzymes from the HMSDH family of aldehyde dehydrogenase superfamily: AMSDH from *Psuedomonas fluorescens* (gene ID: 28971621), AMSDH from *Cupriavidus metallidurans* (gene ID: 94314125), HMSDH from *Cupriavidus basilensis* (gene ID: 493151182), HMSDH from *Pseudomonas sp.* M1 (gene ID: 575528385), ACSDH from *Comamonas testosterone* (gene ID: 190571970), CHSDH from *Glaciecola arctica* (gene ID: 494892710). Highly conserved residues are shown with red text and boxed in blue, strictly conserved residues are shown with a red background, conserved arginines for substrate binding are shown with a green background, the catalytic cysteine and glutamate are shown with a blue background, and hydrophobic residues in the active-site pocket are shown with pink background. This figure was prepared using ESPript.

superfamily are (1) that the cysteine serves as a catalytic nucleophile, which is anticipated to form a covalent-adduct intermediate with the substrate by a nucleophilic addition during catalysis [47-49] and (2) that the glutamate serves as a base to activate water for hydrolysis of the thioacyl-enzyme adduct [50-53]. Previous studies indicate that the catalytic cysteine can adopt two conformations, resting and attacking [41]. In the ligand-free structure, Cys302 is far from where the carbonyl carbon of the substrate should be and is in the resting state. In the ternary complex structures, Cys302 is located at an ideal position to initiate catalysis, which is the attacking state. It is proposed to attack the aldehydic carbon (C6) of the substrate. In the two ternary complex structures, the distance between the sulfur of Cys302 and the C6 of the substrate is ~3.3 Å. Cys302 and the aldehydic carbon form a covalent bond in both thioacyl and thiohemiacetal intermediates. Mutation of Cys302 to serine led to enzyme with no detectable dehydrogenase activity, further confirming its catalytic significance.

Examining the wild-type AMSDH structures shows that in the NAD^+-bound binary complex, Glu268 adopts a ‘passive’ conformation, pointing away from the substrate-binding pocket, and forms hydrogen bonds with both NE of Trp177 (3.2 Å distance) and the backbone oxygen of Phe470 (3.6 Å) to leave space for the reduction of NAD^+. Its electron density is very well-resolved and the side chain B-factor is close to average: 28.2 $Å^2$/28.5 $Å^2$. The thiol moiety of Cys302 is 7.14 Å from Glu268 and is unlikely to form interactions. Interestingly, in both substrate-bound structures, Glu268 becomes more flexible and exhibits much weaker electron density and increased side chain B-factors compared with average protein B-factors: 37.8 $Å^2$/28.5 $Å^2$ and 66.37 Å2/39.7 $Å^2$. In the thioacyl intermediate structure, the electron density of Glu268 becomes very well defined again, but its side chain rotates 73° towards the bound substrate and seems to be in an ‘active’ position to abstract a proton from a deacylating water

(Figure 2.3d). At this point in the reaction cycle, the NADH molecule needs to leave the active site to make room for the catalytic water molecule. Movement of the nicotinamide ring of NAD^+ coupled with the rotation of an active site glutamate has previously been observed in other ALDHs during catalysis [51-52, 54].

Mutation of Glu268 to alanine led to the accumulation of the thiohemiacetal intermediate in both solution and crystalline states. The strictly conserved glutamate residue in the active site of ALDH enzymes has been proposed to play up to three possible roles during catalysis. It is strictly required to activate the deacylating water that allows for product release, it is in a 'passive' conformation during $NAD(P)^+$ reduction, and in some cases, it may serve to activate cysteine for nucleophilic attack [55]. On the basis of these roles, mutation to alanine would be expected to decrease the rate of hydrolysis of the thioacyl adduct, have no effect on the rate of reduction of NADH and possibly decrease the rate of nucleophilic attack by cysteine. With this understanding, deletion of the active site glutamate should cause an accumulation of the thioacyl intermediate. However, in this work, the E268A mutant is shown to accumulate the preceding thiohemiacetal intermediate both in crystal and in solution. This finding suggests an additional catalytic role for this residue: rotation of Glu268 towards the active site facilitates the hydride transfer from the tetrahedral thiohemiacetal adduct to NAD^+. The rapid formation of the intermediate in solution indicates that Glu268 of AMSDH does not play a role in activating cysteine. However, it does appear necessary to complete hydride transfer from the substrate to NAD^+, and its removal turns the native, primary substrate into a suicide inhibitor.

On the basis of previous studies of the ALDH mechanism, the eight high-resolution crystal structures solved (Table 2.1) as well as our biochemical and computational studies, we propose a catalytic mechanism for AMSDH. As shown in Figure 2.16, NAD^+ binds to the

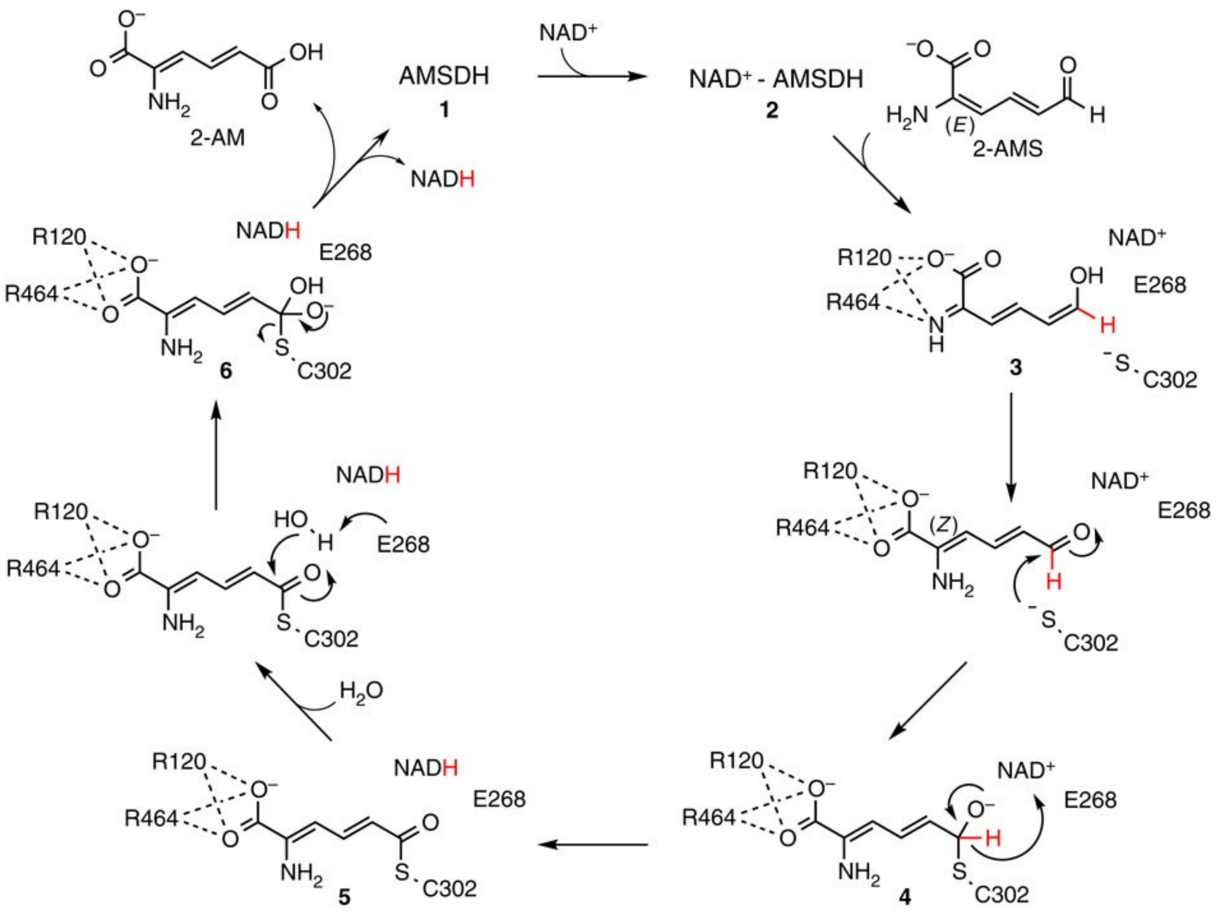

Figure 2.16 Proposed catalytic mechanism for the oxidation of 2-AMS by AMSDH. The primary substrate (2*E*, 4*E*)-2-aminomuconate-semialdehyde binds to the enzyme in its imine tautomer to form the ternary complex (**3**). An isomerization and attack by cysteine on the aldehydic carbon form the (2*Z*, 4*E*)-2-aminomuconate-thiohemiacetyl adduct (**4**). AMSDH-mediated oxidation of 4 concomitant with reduction of NAD^+ to NADH follows, generating a thioacyl enzyme intermediate (**5**). Hydrolysis of **5** then allows the release of the products 2-AM and NADH, restoring the ligand-free enzyme for the next catalytic cycle.

enzyme, **1**, to form an NAD^+-bound AMSDH complex, **2**. The substrate, 2-AMS, is then recognized by Arg120 and Arg464 through multiple hydrogen-bonding interactions, and its imine tautomer is stabilized in the active site, **3**. At this point, the order of the rotation, tautomerization and nucleophilic attack by C302 on the aldehydic carbon to produce the tetrahedral, thiohemiacetal intermediate, **4**, is not yet clear. The isomerization and nucleophilic attack drive a translation of the substrate away from Arg120 and Arg464 so that they are only able to interact with the carboxylate group of the substrate. Next, NAD^+ is reduced to NADH by abstraction of a hydride from **4**, forming a thioacyl intermediate, **5**, a process which involves an sp^3-to-sp^2 transition during oxidation of the organic substrate by NAD^+. On reduction, the nicotinamide portion of NADH moves away from the substrate as Glu268 rotates into position to activate a water molecule to perform a nucleophilic attack on the same carbon that was previously attacked by Cys302, forming a second tetrahedral intermediate, **6**. Finally, the second tetrahedral intermediate collapses, breaking the C–S bond and releasing the final products, 2-AM and NADH. Species **1**–**5** are spectroscopically and structurally characterized, while intermediate **6** was not seen to accumulate.

2.4.1 Supplementary Discussion

2.4.1.1 Secondary Structure Features.

Each polypeptide contains 500 amino acids, but the first 16 – 17 amino acids are not included in our model due to missing electron density even though full-length AMSDH was used for crystallization. It is most likely that these *N*-terminal residues belong to a random coil as in most other ALDH structures. The first 135 residues comprise a cap which surrounds the cofactor binding domain. This cap region starts with two β-hairpin motifs (residues 22 - 50) and is followed by four α-helixes (residues 51 - 134). The sequence then extends to the subunit interaction domain with two beta strands (residues 138 -158). The central strand of the cofactor binding domain starts at residue 161 and stops at residue 266 and resembles a distorted Rossmann fold. The catalytic domain (residues 267 - 476) is based on a topologically related βαβ polypeptide fold and contains a thiol, Cys302, in the catalytic center (Figure 2.2). The sequence ends with a *C*-terminal helix and a beta strand (residue 477 - 500), which is part of the oligomerization domain. The active site is located in the region between the NAD^+ binding domain and the catalytic domain with entrances for NAD^+ and primary substrate on two separate sides.

2.4.1.2 Binary and Ternary Complex Features.

The adenine ribose ring and the two phosphate groups are the main components that stabilize the NAD^+ position by interacting with protein residues which all belong to the surrounding loops, except Thr250, which belongs to the 8th α-helix. The nicotinamide half of NAD^+ has fewer interactions with local residues. Two oxygen atoms (O2 and O3) of the ribose ring form hydrogen bonds with OE2 and OE3 of Glu404, respectively. On the other ribose ring, the O3 atom forms an H-bond with the Nz of Lys192 while its O2 atom forms a hydrogen bonds with both Lys192 (Nz) and Glu195 (OE1). The O1 belonging to the phosphate group nearer the nicotinamide is hydrogen-bonded to NE1 of Trp168. The anionic O2 of the other phosphate group forms hydrogen bonds with both Thr250 (OG1) and Glu247 (N) (Figure 2.3e). For the 2-AMS and 2-HMS binding pocket, except for the hydrogen bonds provided by Arg120 and 464, the substrate binding pocket is mostly composed of hydrophobic residues including four leucine residues (170, 173, 174, and 303), one valine (Val301), and one phenylalanine residue (Phe470) which rotates upon substrate binding, and they are all conserved residues (Figure 2.15). This hydrophobic residue cluster may also help stabilize the loop on which Arg464 is located through hydrophobic interactions with Tyr462 and Trp461.

2.5 Conclusion

In this work, five catalytically relevant structures of the wild-type AMSDH and three mutant structures yield a comprehensive understanding of the protein’s overall structure, co-substrate-binding mode and elucidate the primary residues responsible for substrate specificity among the HMSDH family of the ALDH superfamily. The structural and spectroscopic snapshots capture the crystal structure of an unstable kynurenine metabolite, 2-AMS, and two catalytic intermediates, including stabilizing a tetrahedral intermediate in a mutant protein, which was further verified by mass spectrometry. Capture of a thiohemiacetal intermediate upon deletion of E268 also points to a new role for this well-established active site base in hydride transfer from the substrate to NAD^+. Another interesting finding revealed through solving the ternary complex and intermediate crystal structures and supported by computational studies is that an *E* to *Z* isomerization of the substrate occurs in this dehydrogenase before hydride transfer. To the best of our knowledge, this is the first piece of structural evidence illustrating an ALDH that proceeds via an *E*/*Z* isomerization of its substrate during catalysis.

2.6 Methods

2.6.1 Expression and purification of pfAMSDH and pfACMSD

To construct a His_{10}-tagged AMSDH expression plasmid, *nbaE* gene from *P. fluorescens* (accession: AB088043.2) encoding AMSDH was amplified by the polymerase chain reaction (PCR) using genomic DNA of *P. fluorescens* strain KU-7 as a template and primers 5'-GGAATTC<u>CATATG</u>AATACCTTACCAAGTCAAG-3' and 5'-CC<u>CTCGAG</u>TTAAATTTTTATGCAGATGTTGG-3' (built-in NdeI and XhoI sites are underlined). The PCR product was purified from a 0.8% agarose gel, digested with NdeI and XhoI, and ligated in the equivalent sites of pET-16b (Novagen). Ligation product was transformed to *Escherichia coli* BL21(DE3) for protein expression. A single colony was introduced to 10 mL of autoclaved LB medium containing 100 μg/mL ampicillin and cultured at 37 °C. When cells reached ca. 0.6 OD at 600 nm, 1.5 mL of cells were diluted into 500 mL autoclaved LB medium containing ampicillin. The cells were cultured in 37 °C until the optical density reached ca. 0.8 at 600 nm. Isopropyl β-D-1-thiogalactopyranoside was then added to a final concentration of 0.6 mM, and the temperature was lowered to 28 °C for 12 hours to induce AMSDH expression before the cells were harvested by centrifugation at 8,000 × g. The harvested cells were then resuspended in 50 mM potassium phosphate buffer, pH 8.0, containing 300 mM NaCl and 5% glycerol. The cell slurry was passed through an M-110P Microfluidics cell disruptor and the debris was removed by centrifugation at 27,000 × g for 30 min at 4 °C. The supernatant containing AMSDH was purified using a Ni-NTA affinity column on an ÄKTA FPLC system (GE Healthcare). The major fraction with AMSDH activity was eluted by increased imidazole concentration. Purified protein was concentrated and desalted on a prepacked HiTrap desalting column (GE Healthcare) using buffer containing 50 mM HEPES (pH 7.5), 150 mM NaCl, and 1 mM DTT. Expression, purification and protein re-constitution of ACMSD were performed as described previously1.

2.6.2 Site-directed mutagenesis

C302S, E268A, R120A, and R464A single mutation variants were constructed by the PCR overlap extension mutagenesis technique2. Plasmid containing AMSDH from *P. fluorescens* was used as a template. The forward primers used in the site-directed mutagenesis are 5'-CAACTCGGGGCAGGTCagcCTGTGTTCCGAACG-3' for C302S, 5'-GAAAGAAGTGTCTTTCgcgTTGGGGGCAAGAACG-3' for E268A, 5'-GGACCCTCGATATTCCTgcgGCCATTGCCAACTTTC-3' for R120A, and 5'-GAACACCTGGTACTTGgcgGATCTGCGTACGCC-3' for R464A. The insert of each mutant was verified by DNA sequencing and the positive clone was transformed to *E. coli* BL21(DE3). The expression and purification of the mutants are the same as wtAMSDH.

2.6.3 Preparation of ACMS and 2-HMS

ACMS was generated by catalyzing the insertion of molecular oxygen to 3-hydroxyanthranilic acid by purified, Fe^{2+} reconstituted 3-hydroxyanthranilate 3,4-dioxygenase as described previously [19, 38]. 2-HMS is generated non-enzymatically from ACMS following a previously established method [45]. The pH of solutions containing ACMS was adjusted to ~2 by the addition of hydrochloric acid. 2-HMS formation was monitored on an Agilent 8453 diode-array spectrophotometer at 315 nm. The solutions were then neutralized with sodium hydroxide once the absorbance at 315 nm stopped increasing. 2-HMS at neutral pH has a maximum absorbance at 375 nm [45].

2.6.4 Enzyme activity assay using 2-HMS as substrate

Steady-state kinetics analyses were carried out at room temperature on an Agilent 8453 diode-array spectrophotometer. Reaction buffer contains 25 mM HEPES and 1 mM NAD^+, pH 7.5. Consumption of 2-HMS by 200 nM AMSDH was detected by monitoring the decrease of its absorbance at 375 nm with a molar extinction coefficient of 43,000 $M^{-1}cm^{-1}$ (ref. 24) for 15 s with a 0.5 s integration time. For mutants, 700 nM protein and a wavelength of 420 nm, ε_{420} 11,180 $M^{-1}cm^{-1}$, was used. Absorbance at 375 nm decreased and blue shifted to 295 nm, the maximum ultraviolet absorbance for the product, 2-hydroxymuconic acid. This is consistent with previous reports in which the ending compound was purified and verified as the correct product [45]. Data were either fitted with either the Michaelis-Menten equation:

$$\frac{v_0}{[E_T]} = \frac{[S] \times k_{cat}}{[S] + K_\mathrm{M}}$$

or the Michaelis-Menten equation with substrate inhibition, as appropriate:

$$\frac{v_0}{[E_T]} = \frac{[S] \times k_{cat}}{[S] + K_\mathrm{M} + {}^{[S]^2}\!/_{K_i}}$$

The pre-steady state spectra were obtained with an Applied Photophysics Stopped-Flow Spectrometer SX20 (UK) with the mixing unit hosted inside an anaerobic chamber made by Coy Laboratory Products (MI, USA). Pre-steady state activity used the same reaction buffer but with 23 μM AMSDH or E268A and 25 μM 2-HMS and were carried out at 10 °C. The change in absorbance was monitored for 1.0 s.

2.6.5 X-ray crystallographic data collection and refinement

Purified AMSDH samples at a final concentration of 10 mg ml^{-1} containing no NAD^+ or 10 equiv. of NAD^+ were used to set up sitting-drop vapor diffusion crystal screening trays in Art Robbins 96-well Intelli-Plates using an ARI Gryphon crystallization robot. The initial crystallization conditions were obtained from PEG-Ion 1/2 (Hampton Research) screening kits at room temperature. The screened conditions were optimized by increasing protein concentration to 40 mg ml^{-1} and lowering crystallization temperature to 18 °C. NAD^+-bound AMSDH crystals were obtained from drops assembled with 1.5 μl of protein (preincubated for 10 min with 10 equiv. of NAD^+) mixed with 1.5 μl of a reservoir solution containing 20% polyethylene glycol 3350 and 0.2 M sodium phosphate dibasic monohydrate, pH 9.1, by hanging drop diffusion in VDX plates (Hampton Research). Pyramid shaped crystals that diffract up to ~1.9 Å appeared overnight. The reservoir solution for crystallizing the cofactor-free AMSDH crystals contains 12% polyethylene glycol 3350, 0.1 M sodium formate, pH 7.0. Crystals belonging to the same space group formed within 2–3 days with an irregular plate shape and diffracted up to ~2.2 Å. NAD^+-AMSDH crystals were used for substrate-soaking experiments. Crystals were transferred to mother liquor solution containing ~1 mM 2-HMS and incubated for 10–180 min before flash cooling in liquid nitrogen. Soaking 2-AMS as a substrate is more complicated because of its instability. Crystallization solution containing ~1.5 mM ACMS were used for soaking. After transferring several crystals to the soaking solution (8 μL), 2 μL of 1 mM purified ACMSD was included to catalyze the conversion of ACMS to 2-AMS. Crystals were flash frozen after a 5 min-incubation. Crystallization solution containing 20% glycerol or ethylene glycol was used as cryoprotectant. X-ray diffraction data were collected on SER-CAT beamline 22-ID or 22-BM of the Advanced Photon Source, Argonne National Laboratory.

2.6.6 Ligand refinement and molecular modelling

The first AMSDH structure, the cofactor NAD^+ bound structure, was solved by the molecular replacement method with the Advanced Molecular Replacement coupled with Auto Model Building programs from the PHENIX software using 5-carboxymethyl-2-hydroxymuconate semialdehyde dehydrogenase (PDB: 2D4E) as a search model, which shares 39% of amino-acid sequence identity with *P. fluorescens* AMSDH. The ligand-free, mutant and ternary complex structures were solved by molecular replacement using the refined NAD^+-AMSDH as the search model. Refinement was conducted using PHENIX software [56]. The program Coot was used for electron density map analysis and model building [57]. NAD^+/NADH, substrates 2-AMS and 2-HMS and Cys-substrate covalent-adduct intermediate were well defined and added to the model based on the $2F_o{-}F_c$ and $F_o{-}F_c$ electron density maps. Refinement was assessed as complete when the $F_o{-}F_c$ electron density contained only noise. The structural figures were generated using PyMOL software [58].

2.6.7 Single-crystal spectroscopy

Electronic absorption spectra from single crystals held at 100 K were collected at beamline X26-C of the National Synchrotron Light Source (NSLS) [59]. The electronic absorption data were typically obtained between 200 and 1,000 nm with a Hamamatsu (Bridgewater, N.J.) L10290 high-power ultraviolet–visible light source. The lamp was connected to one of several 3-m long solarization-resistant optical fibers with an internal diameter of 115, 230, 400 or 600 μm (Ocean Optics, Dunedin, FL). The other end was connected to a 40-mm diameter, 35 mm working distance 4 ×, Schwardchild design reflective microscope objective (Optique Peter, Lentilly France). The spectroscopy spot size is a convolution of the optical fiber diameter and the magnification of the objective, which in this case produced 28, 50, 100 or 150 μm diameter spots, respectively. Photons that passed through the crystal were collected with a second, aligned objective that was connected to a similar optical fiber or one with a slightly larger internal diameter. The spectrum was then recorded with either an Ocean Optics USB4000 or QE65000 spectrometer. Anisotropic spectra and an image of the crystal/loop were collected as a function of rotation angle in 5° increments. These were analyzed by XREC37 to determine the flat face and optimum orientation.

2.6.8 Mass spectrometry

To prepare samples for ESI mass spectrometry, as-isolated E268A AMSDH was buffer-exchanged to 10 mM Tris (pH 8.0) by running through a desalting column (GE Healthcare). Intermediate bound E268A was obtained by mixing E268A with 3 equiv. of 2-HMS. Excess 2-HMS was removed by desalting chromatography using the same buffer. Desalted proteins were concentrated to a final concentration of 20 μM. Freshly prepared samples were rinsed by acetonitrile and 0.1% formic acid (1:1 ratio) before injection. Mass spectrometry experiments were conducted using a Waters (Milford, MA) Micromass Q-TOF micro (ESI-Q-TOF) instrument operating in positive mode. The capillary voltage was set to 3,500 V, the sample cone voltage to 35 V and the extraction cone voltage to 2 V. The source block temperature and the desolvation temperature were set to 100 and 120 °C, respectively. The samples were introduced into the ion source by direct injection at a flow rate of 5 µl min^{-1}. The raw data containing multiple positively charged protein peaks were deconvoluted and smoothed using MassLynx 4.1.

2.6.9 Computational studies

All ground-state density functional theory calculations were performed with Gaussian 03 Revision-E.01 at the B3LYP/6-31G*+ level of theory [60]. The chemical structures were optimized using the ternary complex crystal structure (PDB entry: 4I25) as a starting model. To calculate the isomerization barrier, the dihedral angle about the 2–3 bond was restrained and the rest of the molecule was optimized. For the calculations that included the guanidinium heads of Arg120 and Arg464, the geometry was obtained from the crystal structure, and their positions were fixed while the substrate was optimized.

3 A PITCHER-AND-CATCHER MECHANISM DRIVES ENDOGENOUS SUBSTRATE ISOMERIZATION BY A DEHYDROGENASE IN KYNURENINE METABOLISM

This chapter is adapted from the published work co-first authored by ID: Yang Y, Davis I, Ha U, Wang Y, Shin I, and Liu A (2016) A Pitcher-and-Catcher Mechanism Drives Endogenous Substrate Isomerization by a Dehydrogenase in Kynurenine Metabolism. *Journal of Biolological Chemistry*, 291(51), 26252 – 26261. DOI: 10.1074/jbc.M116.759712

3.1 Abstract

Aldehyde dehydrogenases typically perform oxidation of aldehydes to their corresponding carboxylic acid while reducing NAD(P)$^+$ to NAD(P)H via covalent catalysis mediated by an active-site cysteine residue. One member of this superfamily, the enzyme 2-aminomuconate-6-semialdehyde dehydrogenase (AMSDH), is a component of the kynurenine pathway, which catabolizes tryptophan in mammals and certain bacteria. AMSDH catalyzes the NAD$^+$-dependent oxidation of 2-aminomuconate semialdehyde to 2-aminomuconate. We recently determined the first crystal structure of AMSDH and several catalytic cycle intermediates. A conserved asparagine in the oxyanion hole, Asn169, is found to be H-bonded to substrate-derived intermediates in the active site of AMSDH during catalysis, including both covalently bound thiohemiacetal and thioacyl intermediates. To better interrogate the significance of the hydrogen bond provided by Asn169 to the reaction mechanism of AMSDH, we created Ala, Ser, Asp, and Gln variants and studied them using biochemical, kinetic, crystallographic, and computational studies. The *in crystallo* chemical reaction of the primary substrate with the co-crystalized complex of the N169D variant and NAD$^+$ led to the successful trapping of a new catalytic intermediate that was not previously seen. The structural and

computational data are consistent with a substrate imine/enol tautomer intermediate being formed prior to the formation of the covalent bond between the substrate and the active-site cysteine. Thus, AMSDH surprisingly includes an isomerization process within its known catalytic mechanism. These data establish a hidden intrinsic isomerization activity of the dehydrogenase and allow us to propose a pitcher-catcher type of catalytic mechanism for the isomerization.

3.2 Introduction

The kynurenine pathway is the catabolic route for tryptophan degradation in mammals and certain bacteria. In mammals, the pathway has been found to produce neuroactive compounds that correlate with depression and neurodegenerative disease states such as Alzheimer's, Parkinson's, and Huntington's diseases [9, 11, 14]. Moreover, the kynurenine pathway is a de novo biosynthetic route to produce the coenzyme NAD^+/NADH, which is involved in many fundamental biological processes as an energy carrier and redox mediator. In the kynurenine pathway, tryptophan metabolites are partitioned by both enzymatic and non-enzymatic reactions [61]. Three consecutive enzymes of the pathway, 3-hydroxyanthranilate dioxygenase (HAO), 2-amino-3-carboxymuconate-6-semialdehyde decarboxylase (ACMSD), and 2-aminomuconate-6-semialdehyde dehydrogenase (AMSDH), compete with the non-enzymatic auto-cyclization of their substrates and products for further metabolism (Figure 3.1). The trio of enzymes is also present in the 2-nitrobenzoic acid biodegradation pathway.

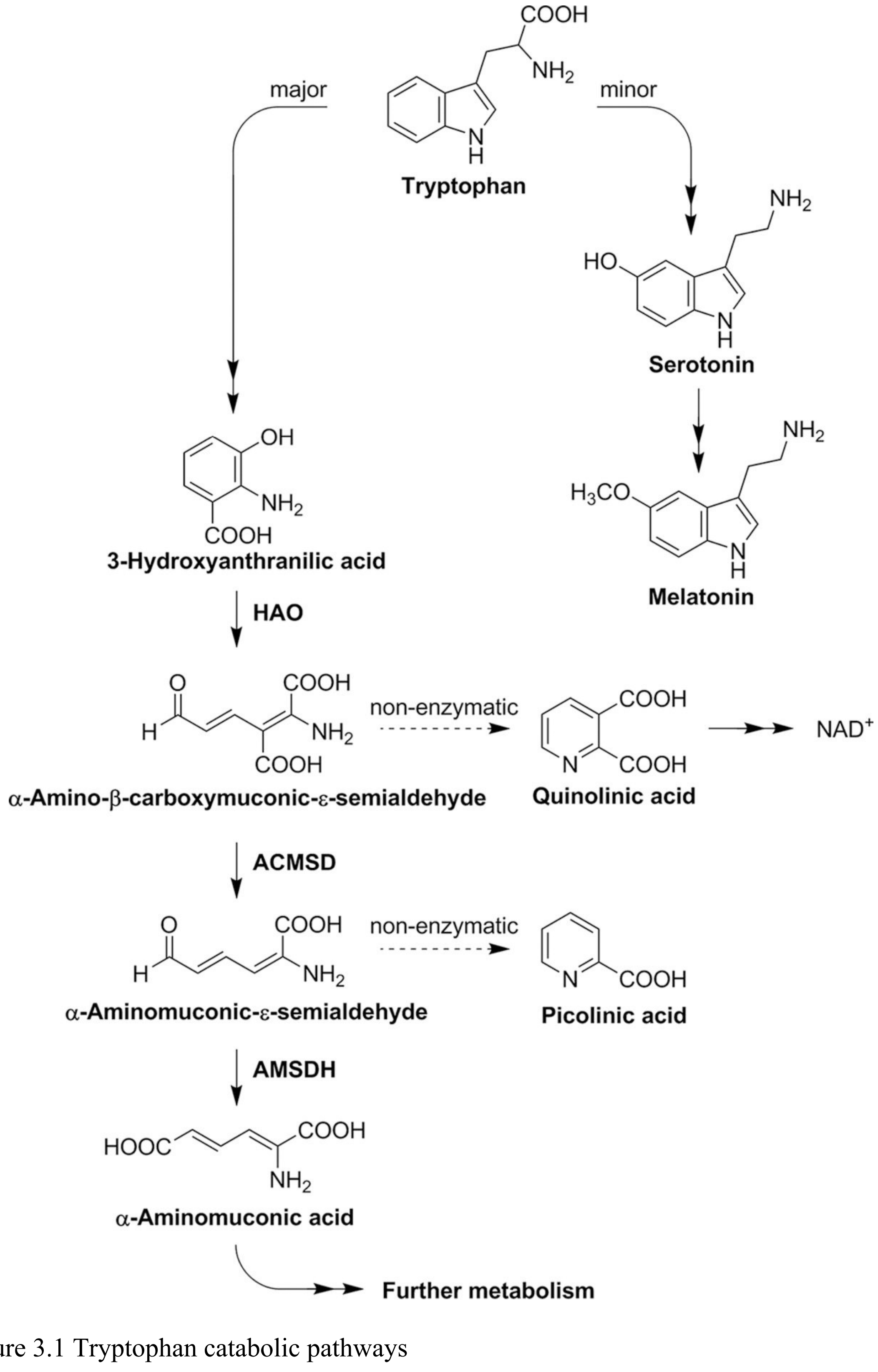

Figure 3.1 Tryptophan catabolic pathways

Investigations at the molecular level of the kynurenine pathway were extended to AMSDH in our recent work [22]. AMSDH is a 216-kDa homotetrameric protein (500 amino acid residues in each subunit) that belongs to the aldehyde dehydrogenase superfamily. It competes with a spontaneous, non-enzymatic cyclization of 2-aminomuconate semialdehyde (2-AMS) to prevent overproduction of picolinic acid. The off-pathway product, picolinic acid, is a metal chelator in human milk that is barely detectable in blood serum and below the detection limit in other tissues [62]. AMSDH oxidizes 2-AMS to 2-aminomuconate and directs the metabolic flux to enzyme-controlled reactions. We have shown the anticipated enzymatic activity of AMSDH using isolated protein and determined its first crystal structure [22]. Furthermore, the binary and ternary complexes as well as two catalytic intermediates, thiohemiacetal and thioacyl, were characterized by soaking single crystals of the binary enzyme-NAD^+ complex under varied time periods with substrates, widening our knowledge of the catalytic mechanism of this semialdehyde dehydrogenase.

In the active site of AMSDH, as in ACMSD [19], two arginine residues appear to stabilize the carboxyl group of their respective substrates [22]. In AMSDH, Cys302 and Glu268 are reported to have critical roles in the reaction catalyzed by AMSDH [22]. Cys302 serves as a catalytic nucleophile and Glu268 acts as a general base based on our recent findings and literature reports of enzymes in the same family [22, 49, 55]. In addition to their catalytic nucleophile and general base, members of the aldehyde dehydrogenase superfamily also possess a strictly conserved asparagine in their active site (Figure 3.2), i.e., residue 169 in AMSDH. Such an active-site asparagine residue is hypothesized to provide catalytic contribution as an oxyanion hole residue in other aldehyde dehydrogenases [50, 52]. Substitution of the asparagine by alanine eliminated the dehydrogenase activity [54, 63]. However, the precise role of the asparagine residue remains unexplored in any member of the aldehyde dehydrogenase superfamily, including AMSDH. Asn169 is within H-bonding distance of the substrate-derived intermediates of the catalytic cycle [22]. As shown in the thioacyl intermediate structure of AMSDH (Protein Data Bank (PDB) entry: 4NPI), the amide moiety of Asn169 forms a hydrogen bond with the oxo moiety of the thioacyl, substrate-enzyme adduct. Thus, Asn169 is expected to stabilize the bound substrate, 2-AMS, as well as to stabilize the thiohemiacetal and thioacyl intermediates through hydrogen-bonding interactions during the oxidation of 2-AMS by AMSDH.

In this work, we constructed and expressed several variants to illuminate the precise role of Asn169 in the reaction catalyzed by AMSDH. Kinetic analysis and crystallography were employed to study those mutants. Unexpectedly, we captured an isomerization reaction intermediate in addition to the previously trapped intermediates in the native protein.

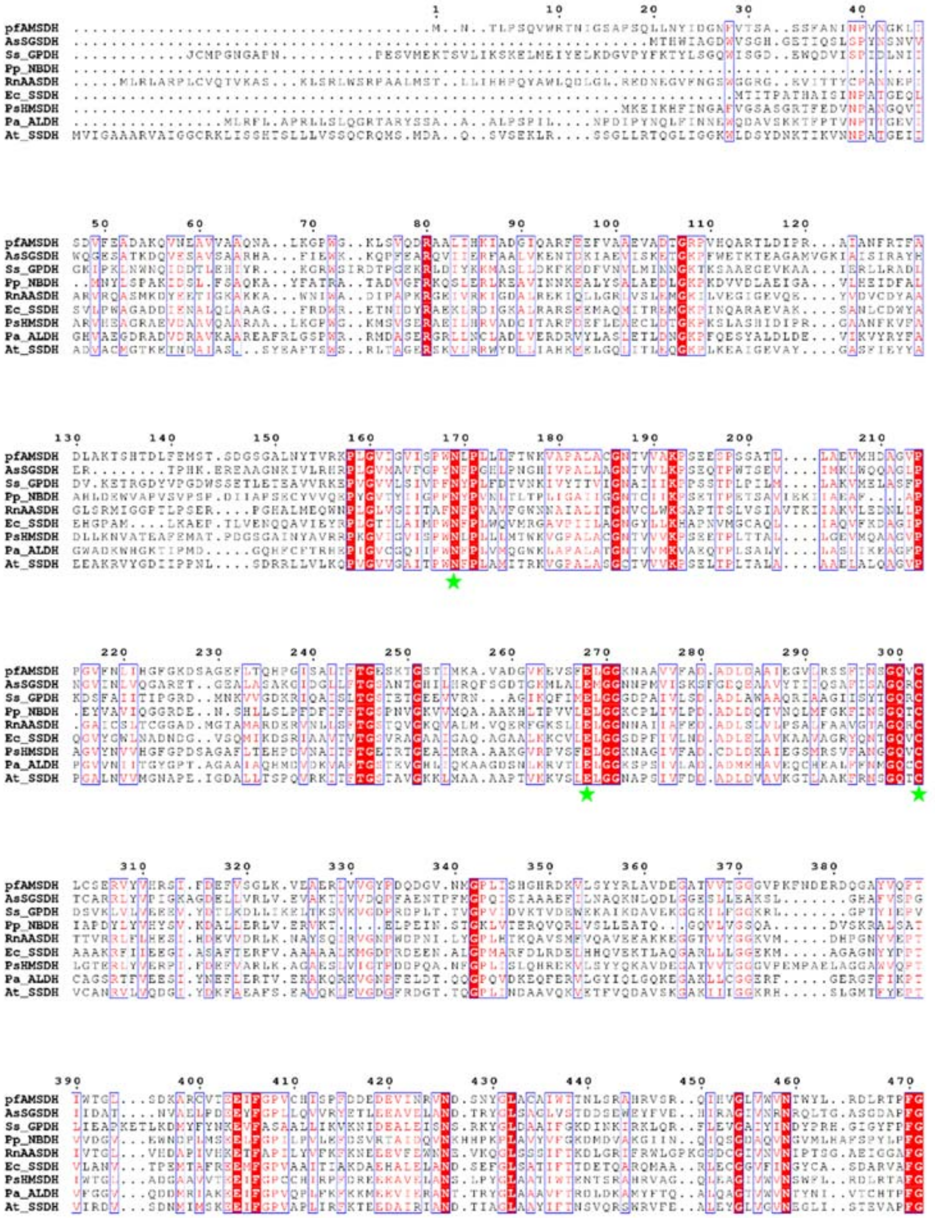

Figure 3.2 Aldehyde dehydrogenase (ALDH) sequence alignment. The conserved catalytic residues are marked by green stars. AMSDH from *Psuedomonas flurenscens* (accession number: Q83V33); *N*-succinylglutamate 5-semialdehyde dehydrogenase from *Aliivibrio salmonicida* (accession number: B6EML5); NAD(P)-dependent glyceraldehyde-3-phosphate dehydrogenase from *Sulfolobus solfataricus* (accession number: Q97U30); NAD(P)-dependent benzaldehyde dehydrogenase from *Pseudomonas putida* (accession number: Q84DC3); α-aminoadipic semialdehyde dehydrogenase from *Rattus norvegicus* (accession number: Q64057); Succinate semialdehyde dehydrogenase from *Escherichia coli* (strain K12) (accession number: P76149); HMSDH from *Pseudomonas* sp. (strain CF600) (accession number: P19059); ALDH from *Pongo abelii* (accession number: Q5R6B5); SSDH from *Arabidopsis thaliana* (accession number: Q9SAK4).

3.3 Results

3.3.1 Steady-state Kinetics

Asn169 was mutated to alanine, glutamine, aspartate, and serine, respectively, to explore the function of the active-site asparagine residue. The steady-state kinetic parameters were determined for each of the active mutants. As compared with the kinetic parameters of the wild-type enzyme (wtAMSDH), N169S, N169Q, and N169D variants have similar K_M but a much lower k_{cat}. The observation of a greater than 100-fold reduction in reaction rate with a less than 2-fold change in the K_M indicates that before the first irreversible step of the reaction, Asn169 is not heavily involved in catalysis. Therefore, the hydrogen-bonding interaction between Asn169 and the C6 oxygen of the alternate substrate, 2-hydroxymuconate-6-semialdehyde (2-HMS) (5), appears to be essential to the rate-limiting steps of the reaction. Substitution of Asn169 with alanine creates an enzyme variant that does not contain any side-chain functional group capable of forming H-bonds, eliminating a possible stabilizing interaction at this position. As indicated in Table 3.1, there is no detectable steady-state activity with the N169A variant.

Table 3.1 Kinetic parameters of N169 mutants with 2-HMS at pH 7.5

	K_M (μM)	k_{cat} (s^{-1})	k_{cat}/K_M ($M^{-1}s^{-1}$)
Native	10.4 ± 0.2	1.30 ± 0.01	1.25×10^5
N169Q	5.7 ± 0.7	0.0034 ± 0.0001	5.9×10^2
N169S	8.7 ± 0.8	0.0077 ± 0.0003	8.8×10^2
N169D	7.7 ± 0.6	0.0110 ± 0.0004	1.4×10^3
N169A	ND	ND	ND

In the thioacyl intermediate of wtAMSDH, the amide side chain of Asp169 forms an H-bond with the C6 oxo of the 2-HMS-enzyme adduct (2.8 Å distance). In this arrangement, the NH group of Asn169 is expected to be the H-bond donor, and the adduct oxo group is expected to be the H-bond acceptor. With this understanding, the N169D variant should only be able to donate a hydrogen for the formation of an intermediate-stabilizing H-bond at lower pH values. To test this hypothesis, pH profiles were obtained for N169D using wtAMSDH as the control. As shown in Figure 3.3, the k_{cat} value of N169D increases with decreasing pH such that at pH 4.5, the k_{cat} value is an order of magnitude larger than at pH 8.0. Meanwhile, the K_M values present less change with no consistent trend. By comparison, the k_{cat} value of wtAMSDH

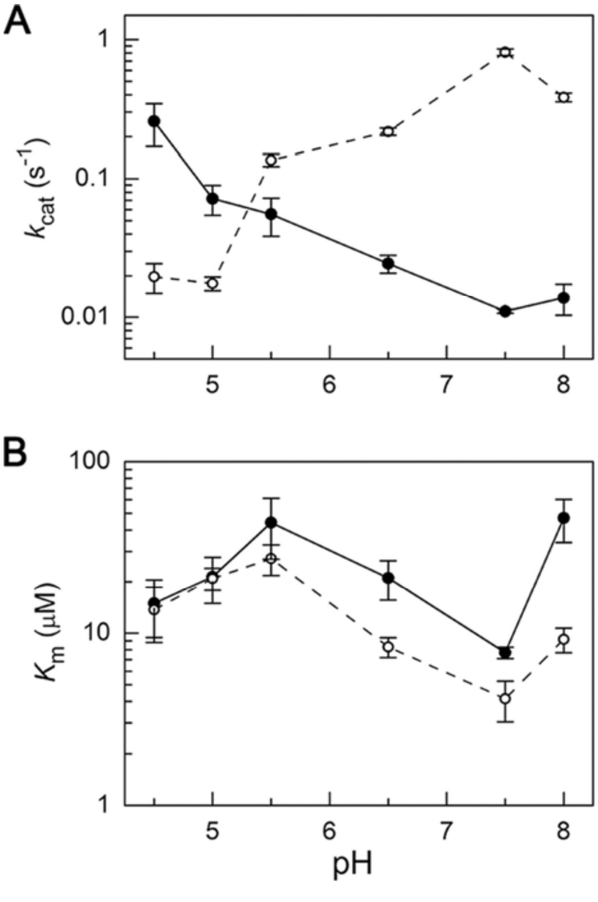

Figure 3.3 pH profile of Michaelis-Menten parameters of wild-type AMSDH (dashed line) and N169D mutant (solid line).

actually decreases with decreasing pH, opposite to what was observed with N169D, but their K_M profiles are similar. The increase in the catalytic rate of N169D with decreasing pH is consistent with the hypothesis that Asn169 acts to stabilize intermediates and transition states by donating a hydrogen for H-bonding interactions to the C6 oxygen of the substrate. At lower pH conditions, Asp169 becomes increasingly protonated, enhancing its ability to function as an H-bond donor, fulfilling the same role as Asn169 in the wild-type enzyme.

3.3.2 Crystal Structure of N169A and a Thioacyl Intermediate

To rule out aberrant structural changes as the cause for a lack of steady-state activity in N169A, the variant was crystallized, and its structure was determined by X-ray diffraction and refined to 1.99 Å resolution. The NAD^+-bound N169A variant structure is a homotetramer and agrees well with that of the binary complex structure of wtAMSDH (Figure 3.4A), with a root mean square deviation (RMSD) of 0.197 Å (PDB entry: 5KJ5).

Crystals of N169A were then soaked with the stable alternate substrate 2-HMS for 5 min to 20 h. Of all the datasets collected, those with shorter soaking times (less than 20 h) yielded diffraction maps with poor density for substrate or NAD^+, whereas the ones with the longest soaking times (20 h) show clear and continuous electron density for 2-HMS- and NAD^+-derived intermediate and product in the active site (Figure 3.4B).

The N169A intermediate structure from the 20-h in crystallo reaction was refined to 1.79 Å resolution. As compared with the NAD^+-bound N169A structure, Glu268 rotates more than 70° from its “passive” to its “active” conformation upon formation of the thioacyl intermediate to activate a water molecule for hydrolysis, and the nicotinamide head of NAD^+ moves 6 Å away from the active site as it has been reduced to NADH as seen in the crystal structure of wtAMSDH (5). Therefore, the crystal structure shows clear evidence of the in crystallo formation of a substrate-N169A adduct corresponding to a thioacyl intermediate (Figure 3.4B). However, under the same conditions, this intermediate was formed by wtAMSDH in 30–40 min. The lack of steady-state activity measured for this mutant may be accounted for by a combination of inefficient formation of the newly observed substrate-derived intermediate and an inability to prepare the thioacyl adduct for hydrolysis through the formation of a second tetrahedral intermediate.

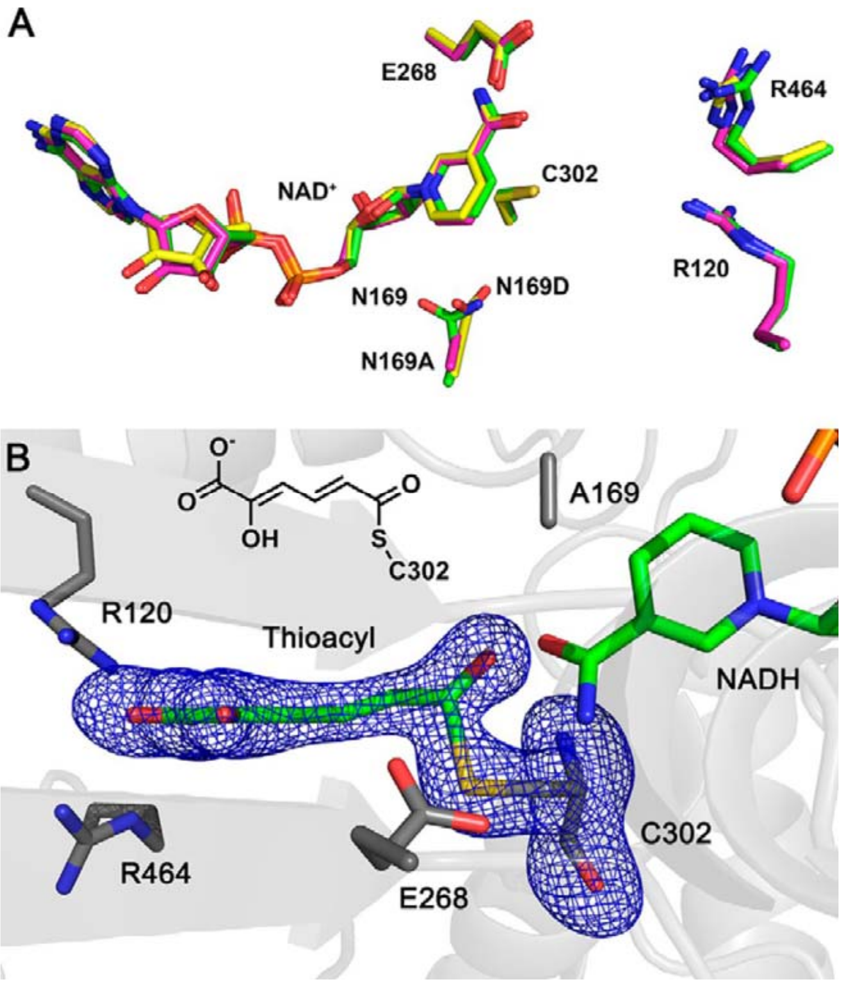

Figure 3.4 Superimposition of N169 variants with wtAMSDH and a thioacyl intermediate. N169A (magenta, 5KLN), N169D (yellow, 5KJ5), and wtAMSDH (green, 4I1W) in the binary complex form. (B) Electron density map of the thioacyl intermediate obtained from N169A-NAD$^+$ crystal reacted with 2-HMS for 20 h. Cys302, Glu268, Arg464, Arg120, Asn/Asp169 and NAD$^+$ are present as sticks. The omit maps for ligands and Cys302 are contoured to 3.0 σ and shown as a blue mesh.

3.3.3 Time-lapse in Crystallo Reaction of N169D

The NAD$^+$-bound N169D binary complex structure was determined and refined to 2.11 Å resolution. The mutant structure exhibits high similarity with the wtAMSDH binary complex with an RMSD of 0.173 Å (Figure 3.4A). Moreover, to ascertain whether there is any further information about the influence of the Asn-to-Asp alteration, the crystals of the N169D-NAD$^+$ mutant were mixed with 2-HMS for varying times. As a result, 11 crystal structures were solved with reaction times of 1 min to 23 h.

Among all structures solved, most of the structures showed incomplete or low occupancies of a specific reaction intermediate at the active site. However, three distinct reactive intermediates were captured at reaction times of 1, 5, and 30 min. These intermediates were reproducible, and their structures were refined to resolutions of 2.01, 2.17, and 2.10 Å, respectively (Table 3.2). The N169D ternary complex with 1-min reaction time (PDB entry: 5KLK) dataset exhibits the same tertiary and quaternary structural characteristics as compared with the wtAMSDH ternary complex structure. 2-HMS is H-bonded with Arg-120 and Arg-464 as its keto tautomer form, and the enol end is pointed to the opposite direction toward Cys-302 (Figure 3.5A). The N169D ternary complex with 5-min reaction time also has the same overall structural features. Interestingly, significant differences in the details of the active site of the N169D ternary complex with 5-min reaction time are found as compared with the wtAMSDH enzyme, where a thioacyl intermediate was observed (5).

Table 3.2 Crystallization data collection and refinement statistics

	NAD$^+$-N169D	2-HMS-NAD$^+$-N169D (1 min)	2-HMS-NAD$^+$-N169D (5 min)	2-HMS-NAD$^+$-N169D (30 min)	NAD$^+$-N169A	N169A-thioacyl intermediate (20 h)
PDB code	**5KJ5**	**5KLK**	**5KLL**	**5KLM**	**5KLN**	**5KLO**
Data collection						
Space group	$P2_12_12_1$	$P2_12_12_1$	$P2_12_12_1$	$P2_12_12_1$	$P2_12_12_1$	$P2_12_12_1$
Cell dimensions a, b, c (Å)	88.6, 142.4, 173.4	88.2, 142.9, 174.2	88.4, 143.1, 174.1	88.4, 142.0, 171.6	88.7, 141.0, 173.3	88.1, 141.7, 171.5
Resolution	31.5 - 2.11 (2.19 - 2.11)[a]	35.1 - 2.01 (2.08 - 2.01)	35.2 - 2.17 (2.25 - 2.17)	45.6 - 2.10 (2.18 - 2.10)	34.4 - 1.99 (2.06 - 1.99)	34.9 - 1.79 (1.85 - 1.79)
No. of observed reflections	125557 (12419)	145427 (14114)	115719 (11331)	124700 (12305)	148478 (14680)	193366 (17447)
Redundancy	14.2 (14.1)	12.0 (11.4)	14.3 (14.0)	7.9 (8.0)	12.1 (9.7)	11.7 (11.8)
Completeness (%)	99.8 (100.0)	98.7 (96.9)	99.6 (98.9)	99.8 (100.0)	99.8 (99.6)	95.3 (86.8)
I/sigma(I)	27.8 (2.9)	23.5 (2.0)	26.5 (3.5)	20.2 (1.8)	29.3 (2.9)	34.6 (2.7)
R_{merge} (%)[b]	11.6 (92.5)	11.6 (89.6)	13.1 (92.9)	11.7 (96.2)	10.1 (69.2)	7.6 (81.3)
Refinement[c]						
R_{work}	19.0	18.8	17.0	18.6	18.7	17.9
R_{free}	23.7	23.1	21.8	23.0	22.2	20.3
RMSD bond length (Å)[d]	0.008	0.007	0.008	0.007	0.008	0.007
RMSD bond angles (°)	1.10	1.12	1.07	1.10	1.14	1.11
Ramachandran statistics [e]						
Preferred (%)	97.2	97.1	97.1	97.2	97.2	97.7
Allowed (%)	2.8	2.8	2.7	2.6	2.7	2.1
Outliers (%)	0.2	0.1	0.3	0.2	0.2	0.2
Average B-factor (Å^2)						
Protein/atoms	44.6/14691	39.0/14705	36.1/14726	45.8/14685	37.6/14701	33.2/14679
NAD$^+$/atoms	47.6/176	42.9/176	N/A	51.4/176	34.0/176	39.5/176
Na$^+$/atoms	N/A	51.6/3	35.7/4	48.5/4	37.7/4	32.2/4
2-HMS or intermediates/ atoms	N/A	51.8/30	38.2/40	N/A	N/A	33.7/40
Solvent/atoms	48.3/843	44.0/1092	41.9/1179	51.3/864	46.2/1179	42.0/1475
All-atoms Clash score/percentile[e]	3.64/99	2.78/99	2.46/100	3.17/99	3.50/99	2.86/99
MolProbity score/percentile[e]	1.72/94	1.56/95	1.56/98	1.60/96	1.76/88	1.51/93

[a] Values in parentheses are for the highest resolution shell.

[b] $R_{\mathrm{merge}} = \Sigma_{\mathrm{hkl}}\Sigma_i |I_i(hkl) - \langle I(hkl)\rangle| / \Sigma_{\mathrm{hkl}}\Sigma_i I_i(hkl)$, in which the sum is over all the *i* measured reflections with equivalent miller indices *hkl*; $\langle I(hkl)\rangle$ is the averaged intensity of these *i* reflections, and the grand sum is over all measured reflections in the data set.

[c] All positive reflections were used in the refinement.

[d] According to Engh and Huber .

[e] Calculated by using MolProbity .

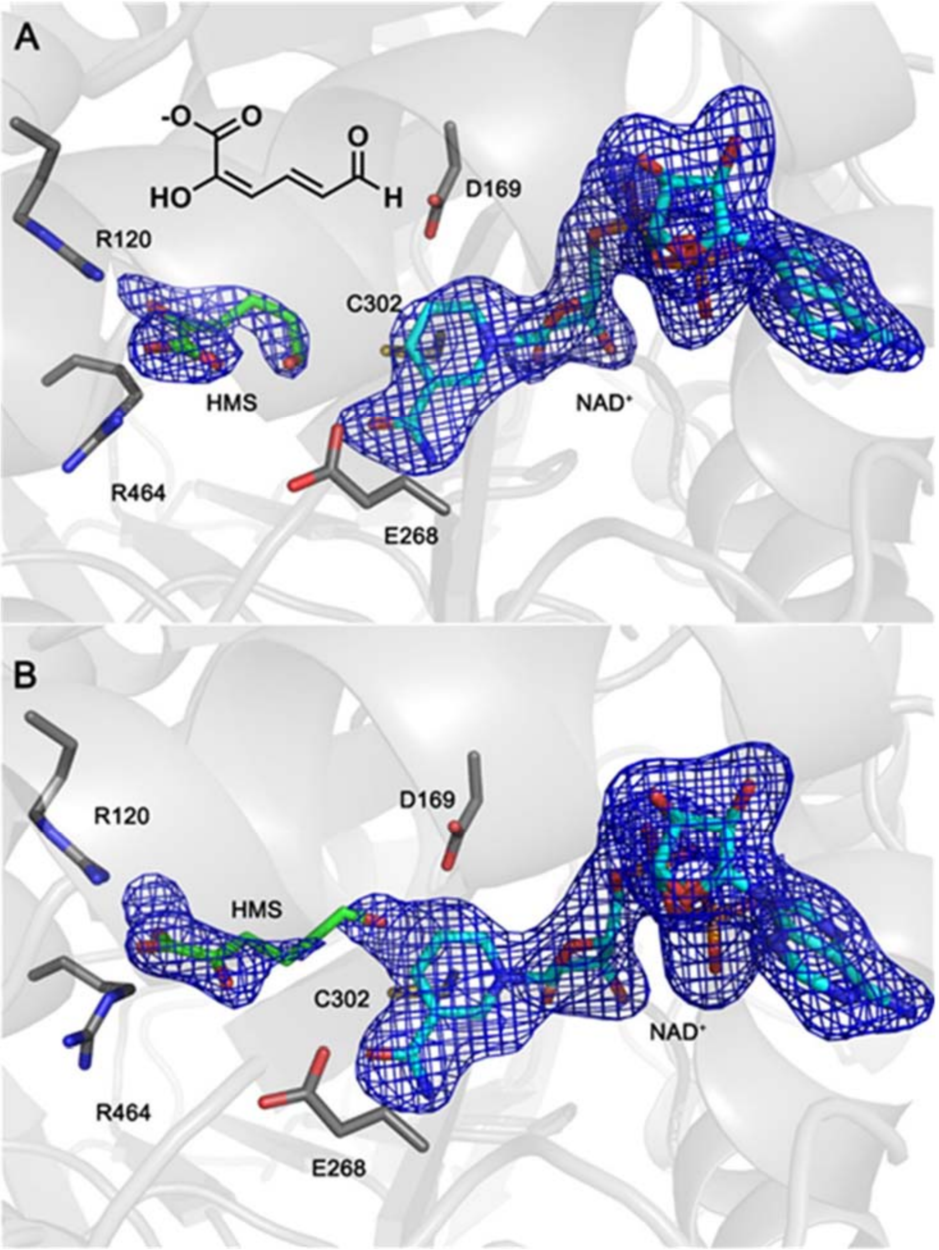

Figure 3.5 Intermediate crystal structures of N169D-NAD$^+$ binary complex reacted with 2-HMS. Soaking for 1 min (A, PDB entry: 5KLK) and for 30 min (B, PDB entry: 5KLM). Glu268 is present in the passive position as found in the ligand-free and binary complex structures, indicating that the dehydrogenation reaction has not occurred but isomerization reaction has taken place. The omit maps of 2-HMS and NAD$^+$ are contoured to 2.5 σ and shown as a blue mesh. The residues in the active site are shown as sticks.

As expected, 2-HMS is bound to the enzyme active site by two arginine residues in the active site of N169D in the same manner as seen in the wtAMSDH ternary complex structure (PDB entry: 4I2R). After soaking the co-crystalized NAD$^+$-N169D with 2-HMS for 5 min (PDB entry: 5KLL), 2-HMS adopts an extended conformation reminiscent of the previously captured thioacyl intermediate, but the electron density of the nicotinamide head of NAD$^+$ is not well defined. At longer soaking times (30 min, PDB entry: 5KLM), the electron density of the aldehyde portion of 2-HMS is not well defined, presumably due to increased conformational heterogeneity. The position of Glu268 and the nicotinamide head of NAD$^+$, however, are both well-defined and indicate that even after 30 min of soaking, hydride transfer from the substrate to NAD$^+$ has not yet occurred (Figure 3.5B).

3.3.4 Crystallographic Capture of a New Tautomerized Intermediate

In the 5-min N169D intermediate structure, Glu268 surprisingly remains in its passive state (i.e. pointing away from the substrate-binding pocket). In all previous intermediate structures (5) obtained with the same in crystallo reaction procedure from wtAMSDH, Glu268 is in an active position, rotated 73° toward the bound substrate from its resting passive position. The electron density of the nicotinamide moiety of NAD$^+$ is not well defined. Careful inspection of the electron density of 2-HMS in the N169D active site reveals that the carbon backbone of the substrate is distorted as compared with all previous structures (5). Specifically, 2-HMS shows significant out-of-plane rotation about its C3–C4–C5–C6 dihedral. Another key distinction between the 5-min N169D intermediate and previously solved structures is the interatomic distances around the aldehydic carbon of the substrate and nearby residues. The two values of interest are the distances between C6 of 2-HMS and the sulfur of Cys302 and between the oxo of 2-HMS and the terminal atom of Asn/Asp169, respectively.

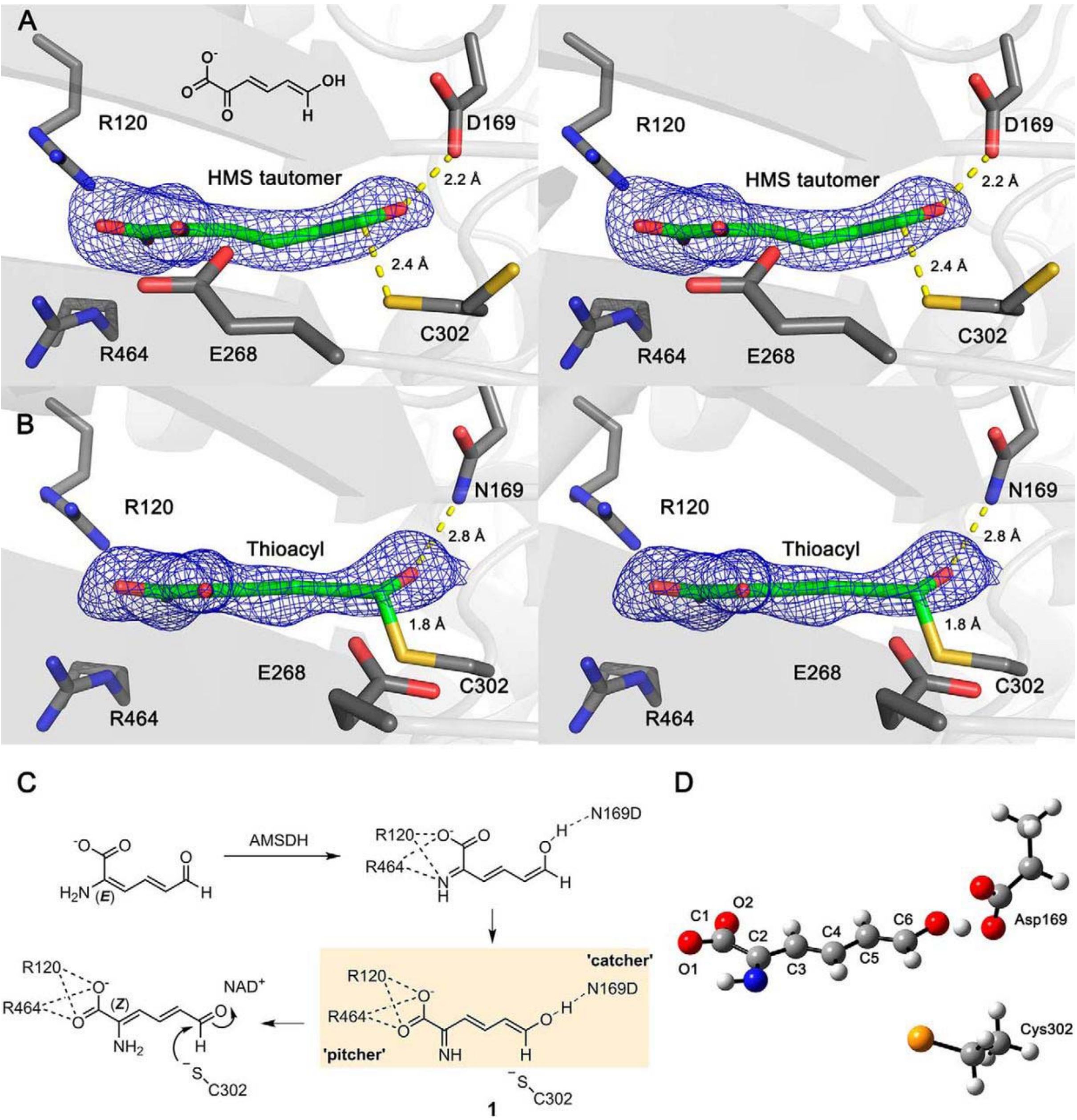

Figure 3.6 Crystallographic and computational evidence for an enol tautomer. A stereographic view of the omit map of a substrate-based intermediate in the co-crystalized crystals of N169D-NAD$^+$ soaked with 2-HMS for 5 min (A). The ligand density is fit with the enol tautomer of 2-HMS. This is shown side-by-side with the thioacyl intermediate trapped in the native enzyme (PDB entry: 4NPI) under identical conditions (B). The omit maps of intermediates in active site are contoured to 3.0 σ and show as a blue mesh. The active site residues interacting with the intermediate are included in the presentation. (C) The isomerization reaction in AMSDH N169D. (D) Optimized geometry of 2-AMS in its imine/enol tautomer with Cys302 and Asp169. C, H, O, N and S atoms are shown in grey, white, red, blue, and yellow, respectively.

In the N169D structure, the thiol moiety of Cys302 has two alternative conformations. In the first conformation, the thiol is pointed toward the nicotinamide ring of NAD$^+$, as seen previously in the wtAMSDH structure (PDB entry: 4I26) [22]. In the other confirmation, the thiol is in position for nucleophilic attack on the substrate, similar to the scenario found in the ternary complex structures of the wtAMSDH [22]. In wtAMSDH,the C6-sulfur distance between the substrate and Cys302 is 1.8 Å, indicating a formal covalent bond, whereas in the N169D variant, the shortest distance is 2.4 Å (**Error! Reference source not found.**A), at the shorter end of hydrogen-bonding range and too long to indicate a formal covalent carbon-sulfur bond. The other conformation of Cys302 is farther away from the substrate, 4.4 Å from C6 of the substrate. Thus, the substrate-derived intermediate is not covalently bound to the enzyme in this intermediate.

Additionally, the substrate oxo-Asp distance in the N169D mutant is 2.2 Å (**Error! Reference source not found.**A), whereas the substrate oxo-Asn distance in the wild-type thioacyl intermediate is 2.8 Å (**Error! Reference source not found.**B). The finding of what appears to be a very strong H-bond between the C6 oxygen of 2-HMS and the carboxylate moiety of Asp169 is unexpected, as the crystallization conditions (pH 7.9) should ensure that the side chain of Asp-169 is deprotonated, and an aldehydic oxygen is expected to carry a significant partial negative charge. With such a close observed distance, either Asp169 is protonated at pH 7.9, or 2-HMS can act as the donor in the formation of this hydrogen bond. The positions of NAD$^+$ and Glu268 in the structure of the 5-min reaction intermediate of N169D are also consistent with the structure of a later (30-min reaction time) structure (PDB entry: 5KLM) as shown in supplemental Figure 3.5, which has increased conformational heterogeneity for the bound substrate.

Taken together, the details of the N169D active site after reacting with 2-HMS for 5 min point to the capture of a keto/enol intermediate, which corresponds to an imine/enol intermediate, **1**, in the AMSDH mechanism (**Error! Reference source not found.**C). The findings of an extended substrate conformation in the active site with a C6-sulfur distance outside the covalent bond range, a glutamate in the passive position, an unreduced NAD$^+$, and a very short substrate oxo-Asp distance all suggest that N169D stabilizes an enol tautomer of the substrate that was not previously seen but was anticipated to facilitate isomerization prior to the dehydrogenation reaction.

3.3.5 Quantum Chemical Investigation of a Crystallographically Captured Intermediate

The crystal structure of the 2-HMS-derived intermediate structure of N169D is distinct from all previous structures of this enzyme or its mutants [22]. The straightforward explanation for the disparities between the N169D intermediate and the thiohemiacetal or thioacyl structures is that the introduction of a negative charge to the active site in the mutant protein leads to the preferential stabilization of the imine/enol tautomer. Such an intermediate is necessary for the isomerization of the substrate before the nucleophilic attack by Cys302. With such an isomerization reaction, the next dehydrogenase step is less sterically hindered.

Density functional theory calculations were carried out to assess the feasibility of this explanation. The starting models were generated from the 5-min 2-HMS-NAD$^+$-derived intermediate of N169D crystal structure (PDB entry: 5KLL) and optimized at the B3LYP/6-31G*+ level of theory. For calculations, the native substrate, 2-AMS, was used. The results are summarized in Table 3.3, where values are shown as the difference in free energy between the aldehyde tautomer as compared with the enol tautomer optimized under the same restraints (negative values indicate lower energy for the enol tautomer). Numbering convention and a representative optimization can be found in **Error! Reference source not found.**D.

Table 3.3 Geometry optimization of 2-AMS under various conditions: relative energy of the enol minus aldehyde tautomers

	ΔG (kcal mol^{-1})
2-AMS[a] only	-1.15
2-AMS[b], Asp169	-11.1
2-AMS[a,c], Asp169	-6.87
2-AMS[d], Asp169, Cys302	-5.81

[a]The C3-C4-C5-C6 dihedral is frozen;
[b]all heavy atoms except N are frozen;
[c]C1, C2, and all oxygens are frozen;
[d]C1, C2, O1, and O2 are frozen.

The first row of Table 3.3 shows the results of optimizing each of the tautomers with the C3–C4–C5–C6 dihedral angle fixed to what is observed in the crystal structure. Although the enol form is lower in energy, the difference between the two tautomers is small. The second row shows that inclusion of the carboxylate group of Asp169 drastically increases the difference in free energy between the aldehyde and the enol tautomers. Allowing more flexibility during the geometry optimization reduces the difference, as seen in the third row; however, the enol is still significantly lower in energy than the aldehyde. The inclusion of the side chain of Cys302 does not qualitatively change the results of optimization. Interestingly, if the optimization is performed with the carboxylate group of Asp169 protonated, as would be expected at lower pH values, the aldehyde tautomer optimizes to a structure with geometry nearly identical to the previously published thiohemiacetal intermediate trapped in the E268A mutant crystal (PDB entry: 4OU2). This observation suggests that when protonated, Asp169 can play the same role as Asn169 does in the wild-type enzyme.

3.4 Discussion

3.4.1 An Update to the Mechanism of AMSDH Action

In a previous report, insight was gained into the dehydrogenation mechanism of AMSDH by the capture of two important catalytic intermediates, thiohemiacetal **2** and thioacyl adducts **3** (5). The primary substrate and the catalytic intermediates are in distinct *E*/*Z* configurations at the C2–C3 position. Following our recent success, here, we have captured a new intermediate, which was not previously seen by reacting single crystals of the N169D mutant with a substrate analog. The new intermediate was trapped prior to the NAD^+-dependent oxidation reaction. A perusal of the new intermediate structure and computational analysis point to an isomerization intermediate in AMSDH before its expected dehydrogenase activity. A hidden isomerase-like catalytic mechanism is revealed for the dehydrogenase. Thus, an updated, and more complete, catalytic cycle of AMSDH is proposed (Figure 3.7). As compared with our first mechanistic model (5), the new catalytic mechanism removes the puzzle of the *E*-to-*Z* conformation difference previously observed in the catalysis and defines an unprecedented isomerization reaction mechanism mediated by a dehydrogenase.

The new tautomerization intermediate was captured from the N169D variant of AMSDH. The substitution of asparagine to aspartic acid at the 169 position provides enhanced stabilization of the enol intermediate as compared with the native enzyme, so that it accumulates in the mutant. It is likely that a similar intermediate also occurs in the native enzyme, but presumably it decays faster than it forms. At physiological pH, aspartic acid is typically deprotonated. The side chain of N169D is only able to donate an H-bond when protonated. While in the deprotonated state, the carboxylate moiety is restricted to receiving H-bonds. N169D should only be able to donate a hydrogen for the formation of an H-bond at lower pH values to stabilize intermediates.

With this understanding, the pH profile of the mutant was determined, and the results indicate a critical role of an H-bonding stabilization of the catalytic intermediates by Asn169. In contrast to aspartic acid, asparagine can both donate and receive hydrogen for forming H-bonding interactions and thus possesses a different pH profile.

3.4.2 The Catalytic Driving Force of Isomerization Reaction and the Role of Asn169

The results obtained in this work reveal a pitcher-and-catcher mechanism. At one end of the active site, two arginine residues (Arg120 and Arg464) function as the "pitcher," using

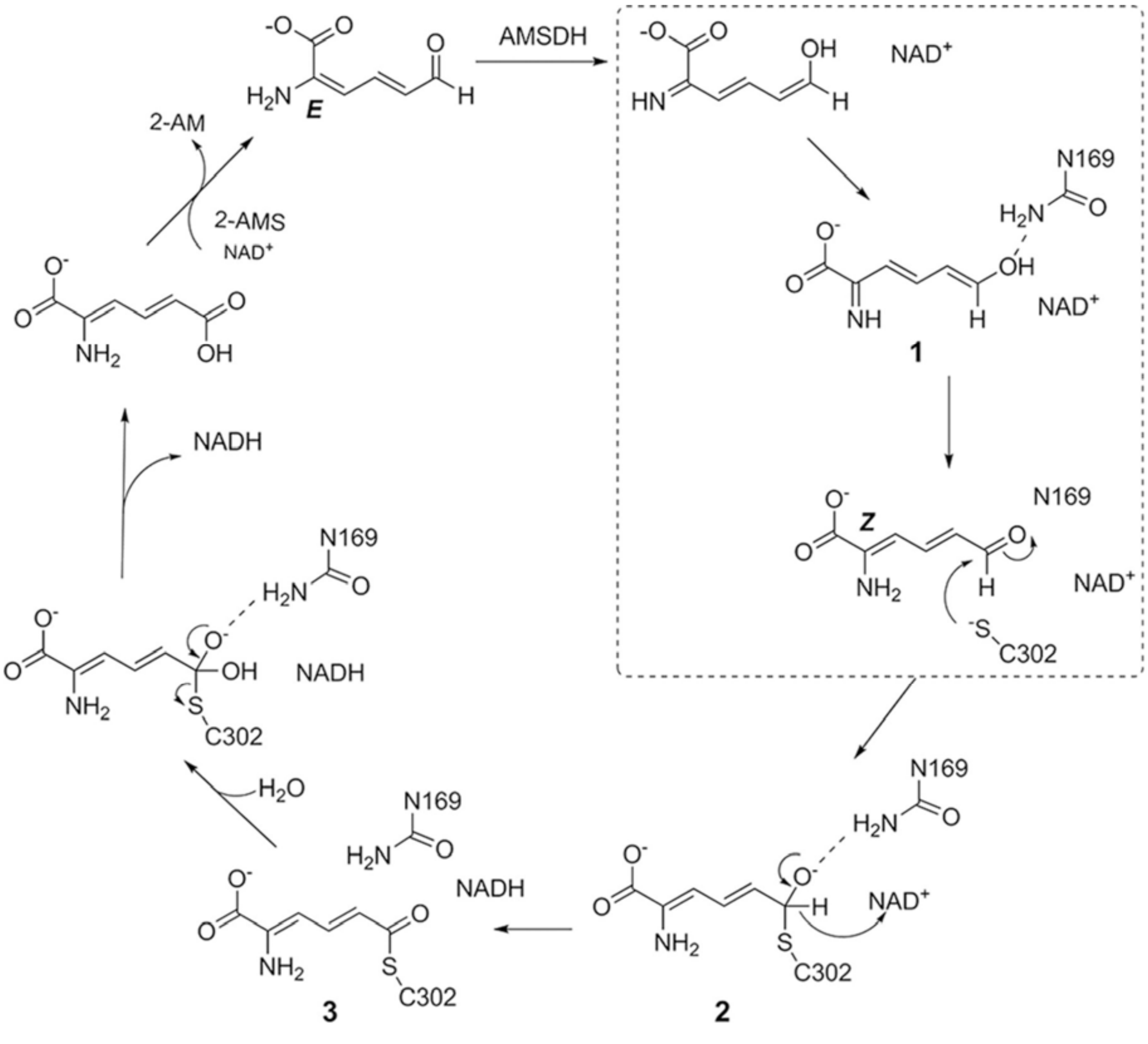

Figure 3.7 An updated catalytic mechanism of AMSDH. The isomerase reaction is highlighted in a dotted box

electrostatic forces to drive an isomerization (**Error! Reference source not found.**C). Because of the two arginine residues, the substrate binds in the 2-imine, 6-enol form. At the other end of the active site, Asn169 acts as the “catcher” by stabilizing the 2-enamine, 6-aldehyde form of the substrate, the necessary tautomer for dehydrogenation. In the N169D variant, however, the scenario is somewhat different. In wtAMSDH, the side chain of Asn169 can act as an H-bond donor with its amide moiety to stabilize the aldehydic oxygen of the substrate and subsequent reactive intermediates. By contrast, in the N169D variant, the deprotonated carboxylate group of the Asp169 can only accept H-bonds, giving an unexpected opportunity to capture an imine/enol tautomer during the *in crystallo* chemical reaction.

During the reaction catalyzed by AMSDH, the role of Asn169 is to stabilize partial negative charges of intermediates and transition states by acting as an H-bond donor with the C6 oxo group of the substrate-derived intermediates. It was a fortuitous discovery to capture a tautomer of the primary substrate during our quest to determine the precise role of Asn169. This finding allows for a deeper understanding of AMSDH (Figure 3.7), and the enzymatically mediated tautomerization mechanism is fully established.

3.4.3 The Necessity of the Isomerization Reaction

Upon recognizing that AMSDH performs an unexpected isomerization on its substrate, the question of why such an isomerization should take place naturally arises. There is a difference of ~4.2 kcal mol^{-1} in free energy between the 2-AMS 2-enamine, 6-aldehyde, 2*E* isomer and 2*Z* isomer (5). One reason for the presence of an intrinsic isomerase activity is perhaps to utilize this small but noticeable energy for the dehydrogenation reaction. Moreover, in the tertiary complex, the substrate in the active site was recognized by arginine residues in its original “compact” conformation (**Error! Reference source not found.**). After isomerization, the distance between C6 of the substrate and the sulfur of cysteine decreased from ~3.5 Å to ~2 Å, which also facilitates the nucleophilic attack from the cysteine in the subsequent step of the reaction. Thus, the isomerization reaction forces the substrate binding to the active site in a correct configuration for dehydrogenation.

Another consideration is that the enzyme following AMSDH in the kynurenine pathway is a deaminase that presumably works by adding water to the iminium ion of 2-AM, generating ammonia and 4-oxalocrotonate (Figure 3.8) [64]. The chemistry of deamination has been well studied and proceeds via backside nucleophilic attack of a water molecule or hydroxide ion on the electrophilic imine carbon. Such a reaction would be less sterically hindered on the observed product of AMSDH as compared with the expected product had no isomerization taken place.

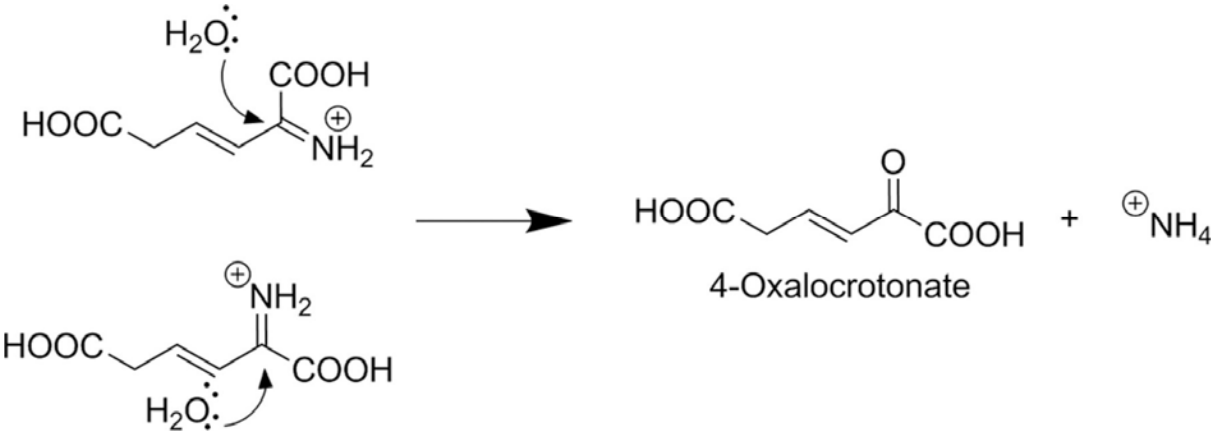

Figure 3.8 Backside attack on the immonium ion of 2-AM is less sterically hindered after isomerization. The expected chemical step for the enzyme downstream of AMSDH if there had been no isomerization, top left, and with isomerization, bottom left.

A broader look at the kynurenine pathway may provide further insight into both why an isomerization is needed at this point in the pathway as well as why AMSDH is best suited to perform such an activity. The metabolic intermediate two reactions upstream of 2-AMS is 3-hydroxyanthranilic acid (3-HAA) with a substituted benzene ring. The aromaticity of 3-HAA is broken by HAO as molecular oxygen is added across its C3–C4 bond. During the addition of oxygen, 3-HAA bidentately chelates the active-site iron ion of HAO with its hydroxyl and amino groups, ensuring that the resulting product, 2-amino-3-carboxymuconic semialdehyde (ACMS), will be formed with its two carboxylate groups trans to each other and its amine group cis to its 3-carboxyl group. This much of the stereochemistry has been previously verified [44]. A crystal structure of ACMSD bound with a competitive inhibitor also agreed with the two carboxylate groups of ACMS being trans to each other [20]. After decarboxylation by ACMSD, the kynurenine metabolite, 2-AMS, can rapidly, spontaneously decay to picolinic acid, presumably by an electrocyclization like its upstream metabolite, ACMS, which decays to quinolinic acid. The decay reaction to picolinic acid, a metabolic dead end, is relatively rapid with a half-life of 35 s at room temperature [22].

If one is to accept that an isomerization must be performed before the downstream deamination reaction, HAO, the first enzyme of the pathway available to perform the isomerization, is an untenable choice because it is directly chelated by its substrate and products across the very bond to isomerize. The next candidate, ACMSD, is more promising; however, if it were to catalyze the isomerization of the 2–3 bond of ACMS or 2-AMS, it would increase the rate of an already fast decay process [39] by putting 2-AMS in the correct conformation to form picolinic acid. AMSDH is then the logical choice to perform the isomerization, as it is the last enzyme for which the amine and aldehyde of the metabolite are in full conjugation to allow for facile tautomerization to an imine and enol form that can readily rotate about the C2–C3 bond. After oxidation to 2-aminomuconic acid, the barrier for tautomerization to the imine form to allow for isomerization is expected to be much larger. Hence, from both the metabolic pathway and the chemical logic standpoints, there is an intrinsic need for isomerization.

3.4.4 A Conserved Substrate Recognition Model in Kynurenine Pathway

In the kynurenine pathway, several intermediates are unstable. The in vitro decay rates of ACMS and 2-AMS are 0.015 and 1.2 min^{-1} at pH 7.4, respectively [39], which means that the enzymes responsible for them must compete with their non-enzymatic decay under differing metabolic states. Therefore, it is essential to recognize and stabilize those unstable intermediates by H-bonding within a short time during the enzymatic reactions. It was reported that two arginine residues from the adjoining units in ACMSD [19], the upstream neighbor of AMSDH in kynurenine pathway, are located in the binding pocket for H-bonding with the two carboxylate groups of ACMS and possible catalytic intermediates [19] [20]. In AMSDH, the substrate, 2-AMS, is even more unstable than ACMS, and thus it needs to be efficiently recognized and stabilized by the two arginine residues in AMSDH at one end and an asparagine residue at the other end to prevent spontaneous autocyclization of the substrate inside the enzyme.

3.4.5 Comparison with 4-Oxalocrotonate Tautomerase

Based on previously characterized dehydrogenases, there is no precedent for an aldehyde dehydrogenase to isomerize its bound substrate before performing its primary redox reaction. Interestingly, an enzyme in the tautomerase superfamily has been characterized in which 2-hydroxymuconate, the product of AMSDH with its alternate substrate, 2-HMS, is a reaction intermediate in the isomerization of 2-oxo-4-hexenedioate to 2-oxo-3-hexenedioate [65-66]. The enzyme, 4-oxalocrotonate tautomerase, has been well studied [65-71], and it binds its substrate with three arginine residues. This binding model is the same as that in the active site of the AMSDH ternary complex. The implication is that the two arginine residues, Arg120 and Arg464, in the active site of AMSDH facilitate a similar tautomerization.

3.5 Conclusion

An enzyme-mediated substrate tautomerization mechanism is found in the early stage of the dehydrogenase catalytic cycle of AMSDH. Our previous work suggested an *E*/*Z* isomerization of the substrate in the enzyme active site. However, the chemical mechanism of the isomerization was not studied [22]. The chemical mechanism of the hidden isomerization reaction was solved unexpectedly during our quest to delineate the precise role of Asn169. On the basis of the newly captured enol tautomer intermediate shown in our crystal structure and computational analysis, we propose an enzyme-mediated isomerization mechanism that proceeds through tautomerization catalyzed by the dehydrogenase as part of the AMSDH catalytic cycle (Figure 3.7). First, the 6-aldehyde form of the substrate, 2-AMS, is tautomerized to its 2-imine, 6-eneol form in the active site. Next, the substrate rotates about its C2–C3 bond to an extended conformation under the assistance of Asn169. Finally, the extended substrate is tautomerized back to the aldehyde form to allow for nucleophilic attack from the thiolate of Cys302 to carry out the natural dehydrogenation chemistry. As the electrostatic driving force identified for initiating tautomerization during AMSDH turnover is also found in other members of the aldehyde dehydrogenase superfamily, these findings may have broader implications for these and related enzymes.

3.6 Experimental Procedures

3.6.1 Site-directed Mutagenesis and Protein Preparation

The cloning and generation of expression plasmid of *Pseudomonas fluorescens* KU-7 AMSDH were described in a previous publication [22]. N169A, N169S, N169D, and N169Q single mutants were constructed by the PCR overlap extension mutagenesis method. The plasmid pET16b-AMSDH containing *amsdh* KU-7 was used as a template, and the forward primers were

5′-GTTATTTCTCCGTGGgcgCTGCCGTTGCTGTTG-3′for N169A, 5′-GTTATTTCTCCGTGGtctCTGCCGTTGCTGTTG-3′ for N169S, 5′-GTTATTTCTCCGTGGgatCTGCCGTTGCTGTTG-3′ for N169D, and 5′-GTTATTTCTCCGTGGcagCTGCCGTTGCTGTTG-3′ for N169Q.

Each mutant plasmid was verified by DNA sequencing and transformed to *Escherichia coli* BL21 (DE3). The isolation strategy of each mutant protein is the same as wtAMSDH [22].

3.6.2 Preparation of the Substrate 2-HMS and Kinetic Assay

The native substrate of AMSDH, 2-AMS, is too unstable for routine kinetic work [22]. As such, an alternate substrate by which the nitrogen atom of 2-AMS is substituted by oxygen, 2-hydroxymuconate semialdehyde, 2-HMS, was used to measure the dehydrogenase activity as described in our previous study [22]. 2-HMS was generated as described previously [45]. Briefly, 3-hydroxyanthranilic acid dioxygenase was used to catalyze the addition of molecular oxygen to 3-hydroxyanthranilic acid, generating ACMS [20, 38-39, 72]. As described previously, lowering the pH below 2 caused the chemical conversion of ACMS to 2-HMS [22]. The steady-state kinetics analyses were performed in a reaction mixture of 1 mM NAD^+ and 25 mM citrate buffer (pH 4.5–5.5) or HEPES buffer (pH 6.5–8.0). All assays were done at room temperature; the consumption of 2-HMS (λ_{max} at 375 nm, ϵ_{375} is 43,000 m^{-1} cm^{-1}) [22] was monitored with an Agilent 8453 diode-array spectrophotometer.

3.6.3 Crystallization, Data Collection, Processing, and Refinement

The N169A and N169D mutants were incubated with 10 eq of NAD^+ for 10 min and crystallized by the hanging-drop method and using a reservoir solution of 20–25% PEG 3350 and 0.2–0.3 m sodium phosphate dibasic monohydrate, pH 9.1. The cryoprotectant solution containing 13% PEG 3350 and ∼1 mM 2-HMS was employed to react with the NAD^+ co-crystalized mutant crystals. After incubation for 1 min to 20 h, the soaked crystals were flash-cooled in liquid nitrogen. X-ray diffraction datasets were collected at the SER-CAT beamline 22-ID of the Advanced Photon Source, Argonne National Laboratory, and were processed and scaled by HKL-2000 [73]. Using the wtAMSDH structure (PDB entry: 4I26) as the template, the structures of the mutants and catalytic intermediates were solved by molecular replacement and refined by employing the Phenix 1.10.1 [56] and Coot 0.8.3 [57]. PyMOL [58] was used in generating structural figures.

3.6.4 Quantum Chemical Calculations

Gaussian 03 Revision-E.01 was used to perform all calculations [60]. The crystal structure of N169D ternary complex (PDB entry: 5KLL) was used to build the starting models. Geometry optimizations and density functional theory calculations were done at the B3LYP/6-31G*+ levels.

4 REASSIGNMENT OF THE HUMAN ALDEHYDE DEHYDROGENASE ALDH8A1 (ALDH12) TO THE KYNURENINE PATHWAY IN TRYPTOPHAN CATABOLISM

This chapter is adapted from the published work authored by ID: Davis I, Yang Y, Wherritt D, and Liu A (2018) Reassignment of the human aldehyde dehydrogenase ALDH8A1 (ALDH12) to the kynurenine pathway in tryptophan catabolism. *Journal of Biological Chemistry*, 293(25), 9594 – 9603. DOI: 10.1074/jbc.RA118.003320

4.1 Abstract

The kynurenine pathway is the primary route for L-tryptophan degradation in mammals. Intermediates and side products of this pathway are involved in immune response and neurodegenerative diseases. This makes the study of enzymes, especially those from mammalian sources, of the kynurenine pathway worthwhile. Recent studies on a bacterial version of an enzyme of this pathway, 2-aminomuconate semialdehyde (2-AMS) dehydrogenase (AMSDH), have provided a detailed understanding of the catalytic mechanism and identified residues conserved for muconate semialdehyde recognition and activation. Findings from the bacterial enzyme have prompted the reconsideration of the function of a previously identified human aldehyde dehydrogenase, ALDH8A1 (or ALDH12), which was annotated as a retinal dehydrogenase based on its ability to preferentially oxidize 9-*cis*-retinal over *trans*-retinal. Here, we provide compelling bioinformatics and experimental evidence that human ALDH8A1 should be reassigned to the missing 2-AMS dehydrogenase of the kynurenine metabolic pathway. For the first time, the product of the semialdehyde oxidation by AMSDH is also revealed by NMR and high-resolution MS. We found that ALDH8A1 catalyzes the NAD$^+$-dependent oxidation of 2-AMS with a catalytic efficiency equivalent to that of AMSDH from the bacterium *Pseudomonas fluorescens*. Substitution of active-site residues required for substrate recognition,

binding, and isomerization in the bacterial enzyme resulted in human ALDH8A1 variants with 160-fold increased K_M or no detectable activity. In conclusion, this molecular study establishes an additional enzymatic step in an important human pathway for tryptophan catabolism.

4.2 Introduction

L-Tryptophan, an essential amino acid, has several metabolic fates in mammals: a building block for proteins, the precursor for serotonin and melatonin, and its complete catabolism through the kynurenine pathway (KP) to pyruvate via alanine, acetoacetate via glutaryl-CoA [74], NAD/NADH via quinolinic acid (QA or QUIN) [44], and several neurologically active compounds. Various kynurenine pathway metabolites are linked to the innate immune response and both neuroexcitatory and neurodepressive effects [11, 14, 61, 75]. Because of its potential medical significance, the KP has received increasing attention. The first and committing enzymes, tryptophan and indolamine dioxygenase, are active drug targets with inhibitors in clinical trials [75-77]. Recently, a downstream enzyme of the KP (Figure 4.1), 2-amino-3-carboxymuconate-6-semialdehyde decarboxylase (ACMSD), has received attention as a potential drug target [61]. Inhibition of ACMSD has been shown to slow down the reaction competing with QA formation and boost cellular NAD(H) levels [78].

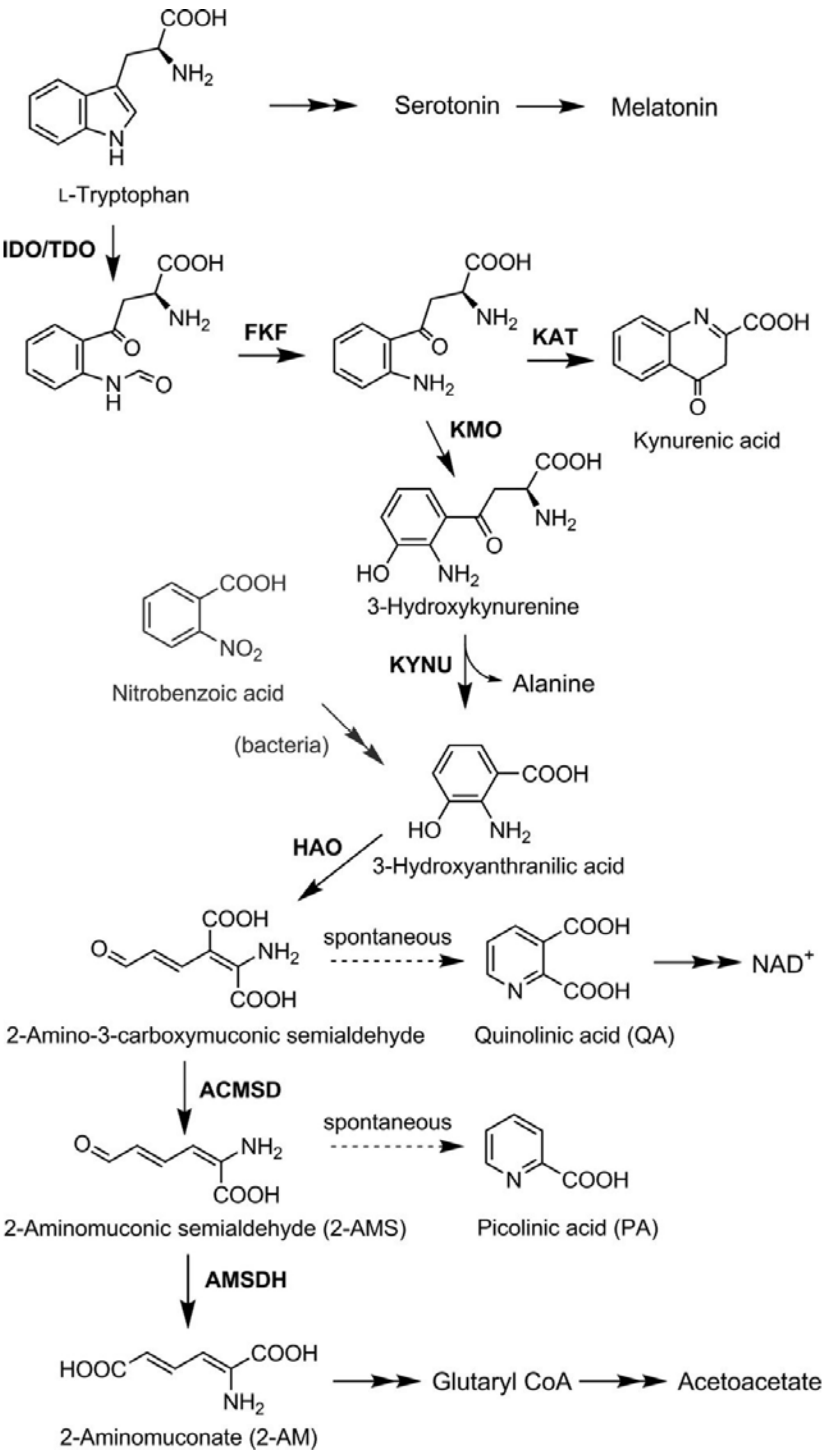

Figure 4.1 The kynurenine pathway. The enzymes identified in kynurenine pathway are: indoleamine 2,3-dioxygenase (IDO)/tryptophan 2,3-dioxygenase (TDO), N-formyl kynurenine formamidase (FKF), kynurenine 3-monooxygenase (KMO), kynurenine aminotransferase (KAT), kynureninase (KYNU), 3-hydroxyanthranilate-3,4-dioxygenase (HAO), 2-amino-3-carboxymuconate-6-semialdehyde decarboxylase (ACMSD), and the proposed enzyme 2-aminomuconate semialdehyde dehydrogenase (AMSDH).

To date, the KP pathway genes and their corresponding enzymes have not been identified beyond ACMSD [20, 79], although the metabolic pathway was published 53 years ago and has made its way into numerous biochemistry textbooks. One limiting factor for studying KP enzymes is that the identification of their mammalian genes has proved difficult. Initial characterization of the KP enzymes was performed from animal liver extracts [74]. Although these studies verified the activities and transformations of the KP, they were unable to provide much insight into the individual enzyme structures and mechanisms. Study of the KP enzymes stagnated until the discovery of an analogous KP in some bacteria [6, 80-84] and that 2-nitrobenzoate biodegradation shares many of the downstream proteins with the eukaryotic kynurenine pathway [46, 64, 85]. An additional difficulty for studying the KP enzymes, especially downstream proteins, is that several of the metabolic intermediates of the pathway are unstable and commercially unavailable. As shown in Figure 4.1, the substrates for ACMSD and its downstream neighbor, 2-aminomuconate semialdehyde dehydrogenase (AMSDH), are both unstable and spontaneously cyclize via a pericyclic reaction to their respective pyridine products, QA and picolinic acid (PA) [44].

Despite the difficulties mentioned above, much progress has been made in understanding the mechanisms of KP enzymes. Recently, AMSDH from *Pseudomonas fluorescens* (pfAMSDH) identified from the 2-nitrobenzoate biodegradation pathway has been studied at the molecular level. Crystal structures of the resting enzyme, NAD^+-bound complex, ternary complex, catalytic thioacyl and thiohemiacetal intermediates, and several mutants have been reported [22]. A hidden isomerase activity of AMSDH has also been uncovered [86]. Furthermore, the study of pfAMSDH revealed that, in addition to active-site residues that are broadly conserved across all aldehyde dehydrogenases, the hydroxymuconate semialdehyde dehydrogenase (HMSDH) family possesses two conserved arginine residues that are involved in substrate recognition and an isomerization activity [86].

In this work, we have identified a human enzyme annotated as a retinal dehydrogenase (ALDH8A1) that carries the hallmarks of an aminomuconate semialdehyde dehydrogenase. An overexpression system was constructed, and recombinant ALDH8A1 was tested for activity with two muconic semialdehyde substrates. The activity of selected active-site variants was also investigated, and the reaction products were verified with NMR and high-resolution MS. All evidence suggests that ALDH8A1 should be reconsidered as the aldehyde dehydrogenase of the kynurenine pathway of tryptophan catabolism.

4.3 Results and discussion

4.3.1 Identification of ALDH8A1 as a potential member of the kynurenine pathway

To continue studying the KP pathway at the molecular level, the next pressing step is to identify a mammalian AMSDH, especially the human version. We performed a BLAST search with pfAMSDH as the search sequence. The results revealed a human protein, ALDH8A1 (initially designated ALDH12), with 44% amino acid sequence identity to pfAMSDH. However, ALDH8A1 is currently annotated in the NCBI gene database as a retinal dehydrogenase. It was assigned as cis-retinal dehydrogenase based on its ability to oxidize 9-cis-retinal faster than all-trans-retinal, even though it was most active with benzaldehyde rather than the retinal substrates [87]. It was also noted in the original characterization that ALDH8A1 shares the closest nucleotide and protein sequence similarity with AMSDH, but it was not tested for such activity, presumably due to difficulty obtaining 2-aminomuconate semialdehyde (2-AMS). Here, we present evidence that ALDH8A1 may be more appropriately considered human AMSDH of the KP. AMSDH belongs to the HMSDH family. Our alignment of ALDH8A1 against AMSDH and several members of the HMSDH family showed not only high overall conservation but also that, in addition to residues required for aldehyde dehydrogenase activity (Asn155, Glu253, and Cys287), residues responsible for substrate recognition only in HMSDH enzymes are conserved in ALDH8A1, namely Arg109 and Arg451 (Figure 4.2, generated with ESPript [88]).

A homology structure model of ALDH8A1 was built using the iTASSER server [89]. An overlay of the homology model and pfAMSDH is shown in Figure 4.3A. The model shows full coverage of the human enzyme sequence, which overlays well with the bacterial enzyme with a root mean square deviation of 1.15 Å for 472 C-α carbons. In addition, all of the catalytically essential active-site residues from pfAMSDH (Arg109, Asn155, Glu253, Cys287, and Arg451 by ALDH8A1 numbering) are in the same location in the homology model as in the pfAMSDH structure (Figure 4.3B).

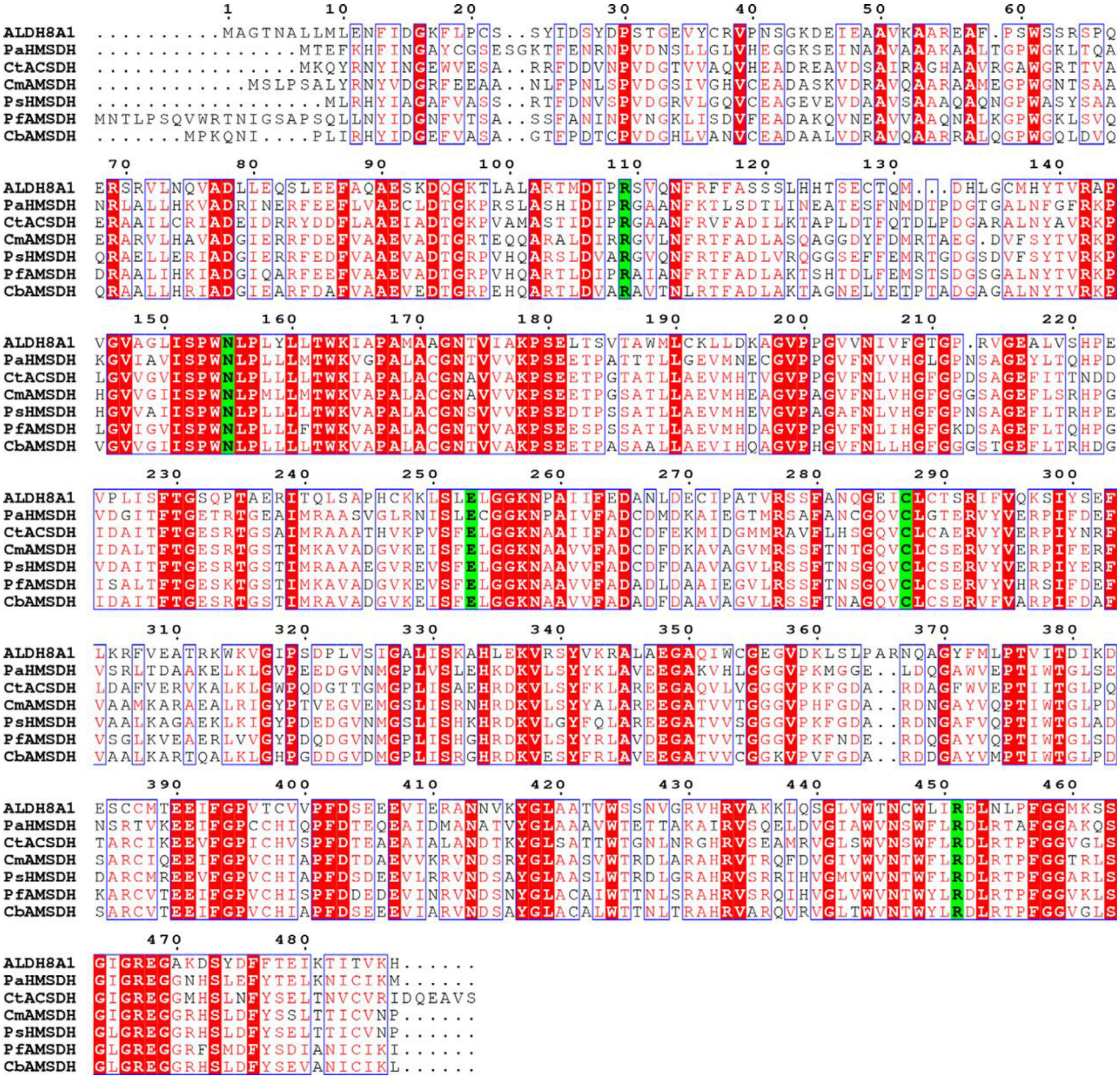

Figure 4.2 Sequence alignment of ALDH8A1 with HMSDH enzymes. Highly conserved residues are shown with red text and boxed in blue, strictly conserved residues are shown with a red background, and catalytic residues are shown with a green background. The enzymes chosen for alignment are as follows: ALDH8A1, GenBank: AAI13863; AMSDH from Pseudomonas fluorescens, GenBank: BAC65304; HMSDH from Paraglaciecola arctica, Accession No: WP_007618756; ACSDH from Comamonas testosterone, Accession No: YP_001967696; AMSDH from Cupriavidus metallidurans, GenBank: KWW33428; AMSDH from Cupriavidus basilensis, GenBank: AJG18463; HMSDH from Pseudomonas sp. M1, GenBank: ETM66811.

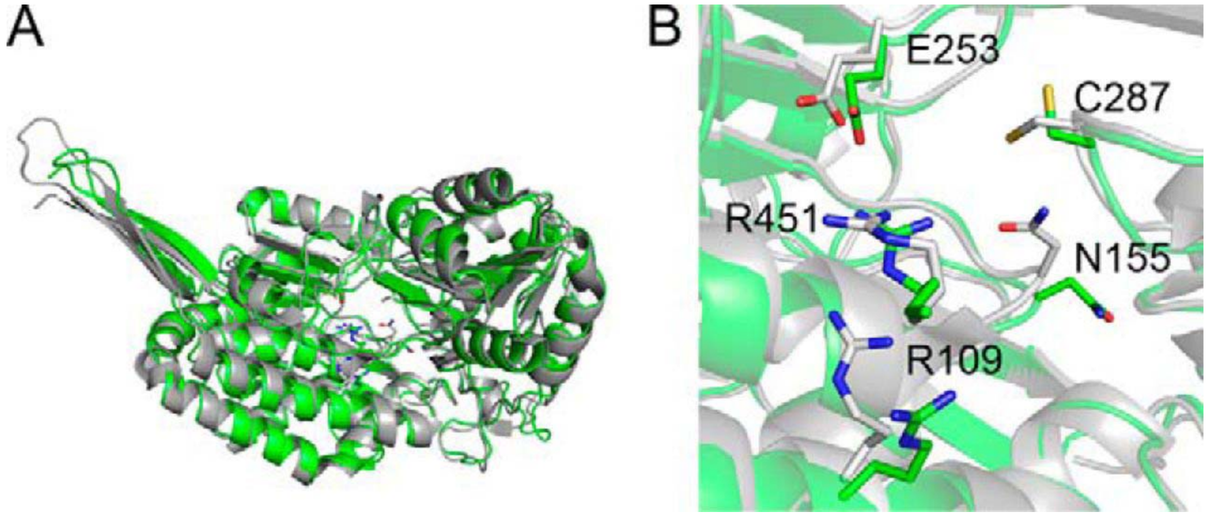

Figure 4.3 Homology model of ALDH8A1 and crystal structure of pfAMSDH. Overlay of a single polypeptide (A), and a zoom-in of the active site with catalytically relevant residues (B). ALDH8A1 is shown in green and pfAMSDH (PDB: 4I26) in grey.

4.3.2 ALDH8A1 can perform the NAD$^+$-dependent oxidation of 2-aminomuconic semialdehyde

The next question to arise was whether ALDH8A1 is able to catalyze the NAD$^+$-dependent oxidation of 2-AMS to 2-aminomuconate (2-AM). Pursuant to this end, an overexpression system was generated. The synthesized gene for human ALDH8A1 was ligated into pET-28a(+) vector with a cleavable N-terminal His$_6$ tag and transformed into *Escherichia coli* BL21(DE3) competent cells. The expressed protein was purified by nickel affinity chromatography (Figure 4.4A), and its ability to oxidize 2-AMS in a coupled-enzyme assay with ACMSD was tested. As shown in Figure 4.4B, ACMS has a broad absorbance band at 360 nm. Upon ACMSD-catalyzed decarboxylation to 2-AMS, the absorbance maximum red-shifted to 380 nm and then decayed as 2-AMS was nonenzymatically converted to PA. The inclusion of purified ALDH8A1 and 1 mM NAD$^+$ in an otherwise identical assay prevented the red shift, and instead, a broad absorbance band around 350 nm was observed that has been previously assigned as the oxidized product, 2-AM, and NADH (Figure 4.4C) according to the reaction scheme shown in Figure 4.4D. These results resemble those observed from pfAMSDH and show that ALDH8A1 is able to rapidly oxidize 2-AMS in solution. The presence of the expected product in the coupled-enzyme assay was also verified by NMR spectroscopy. As shown in Figure 4.5, the reaction mixture contained resonances consistent with 2-AM and expected cross-peaks in the ^{1}H-^{1}H COSY spectrum to show connectivity. Proton resonances were assigned based on similarity with 2-hydroxymuconic acid, which has been rigorously characterized [90].

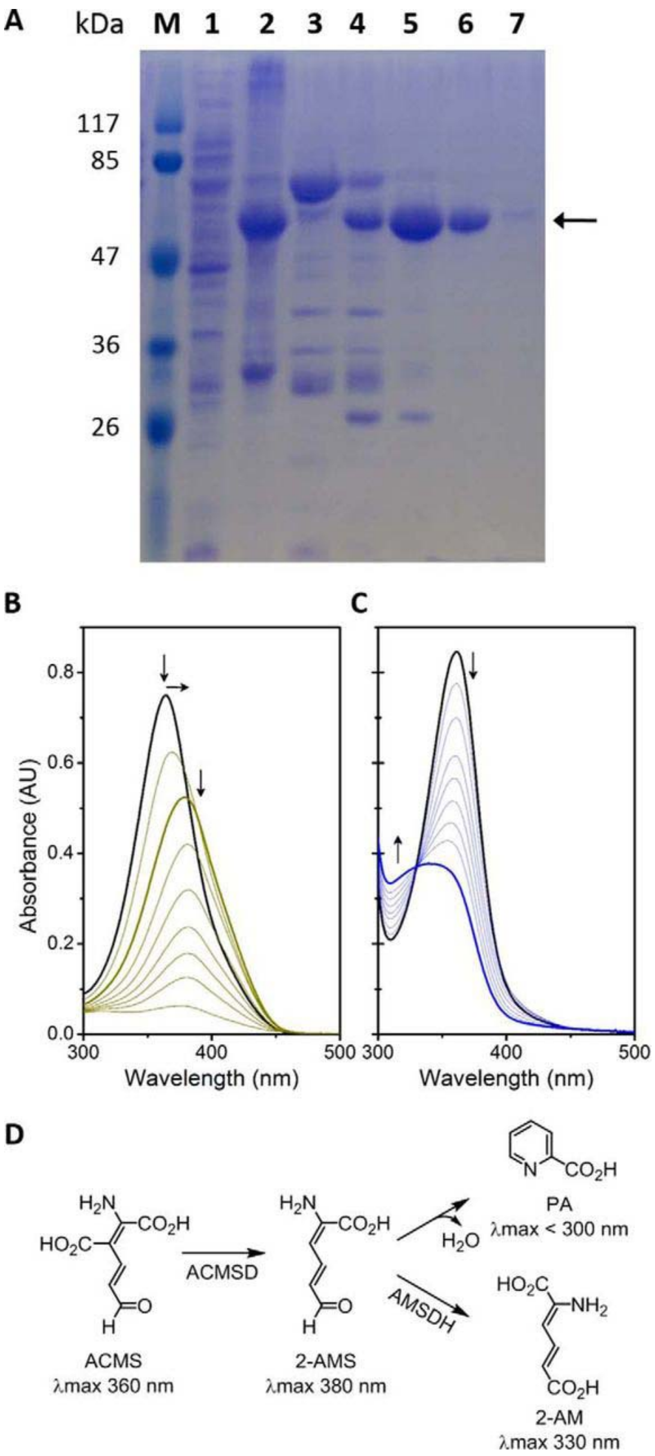

Figure 4.4 Purification and representative activity assay of ALDH8A1. (A) SDS-PAGE of a purification by Ni-NTA affinity chromatography. Lane 1 is clarified cell extract, 2 is cell pellet, 3 is flow-through, and 4-7 are fractions 1-4, respectively. Fractions 2 and 3 were collected for use. (B) Time course of ACMSD acting on ACMS to produce 2-AMS which decays to PA. (C) Coupled-enzyme assay with ACMSD and ALDH8A1 converting ACMS to 2-AM in the presence of NAD$^+$, and (D) Scheme showing the reactions in A and B as the top and bottom branches, respectively.

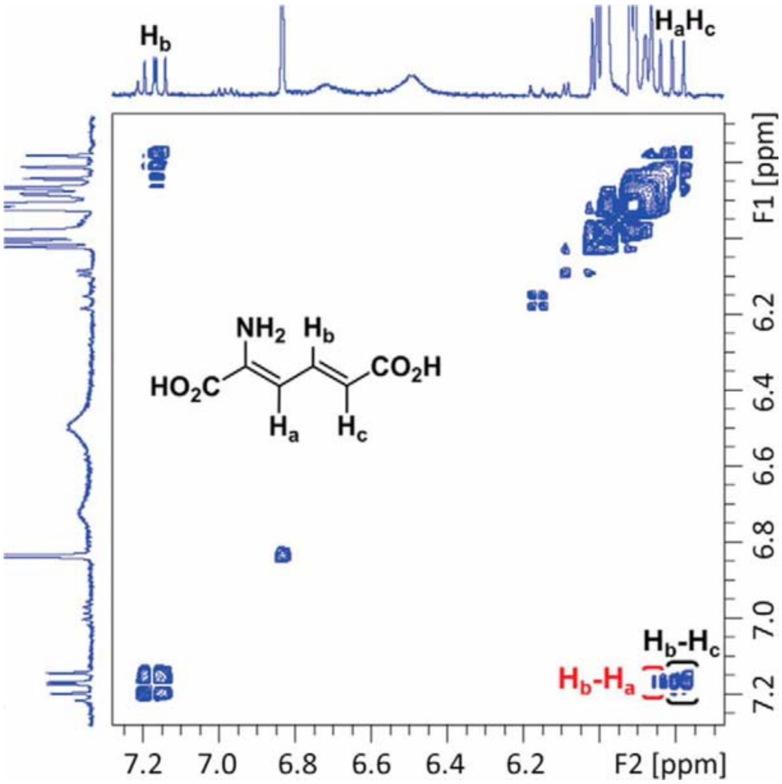

Figure 4.5 ^1H-^1H NMR COSY spectrum of a coupled-enzyme reaction mixture containing 2-AM. The highlighted cross-peaks show correlations of Hb with Ha and Hc. Details of the NMR experiment can be found in 4.5.4 NMR spectroscopy

4.3.3 Characterization of the reaction product of the ALDH8A1-catalyzed reaction

In initial studies of AMSDH, the identity of the product was inferred based on knowledge of the substrate structure and the catalytic cycle of the dehydrogenation reaction. The in crystallo characterization of the AMSDH reaction revealed that, in addition to oxidation of the aldehyde to its corresponding carboxylic acid, pfAMSDH also isomerizes the 2,3-double bond inside the active site prior to substrate oxidation [86]. In the process of trying to determine the conformation of the product of the reaction catalyzed by ALDH8A1, we noticed that the product, 2-AM (λ_{max} 330 nm), is unstable and is nonenzymatically bleached in a single kinetic phase with a half-life of 67 min (Figure 4.6A). High-resolution mass spectra were acquired of the 2-AM decay product after purification by HPLC. Mass spectra were collected in negative mode, and as shown in Figure 4.6B, the parent ion matches tautomerized hydroxymuconate, 2-oxo-3-hexenedioate, with 2.55-ppm mass accuracy. Furthermore, fragment ions from cleaving at either side of the keto group can be observed with nominal masses of 113 and 85 Da.

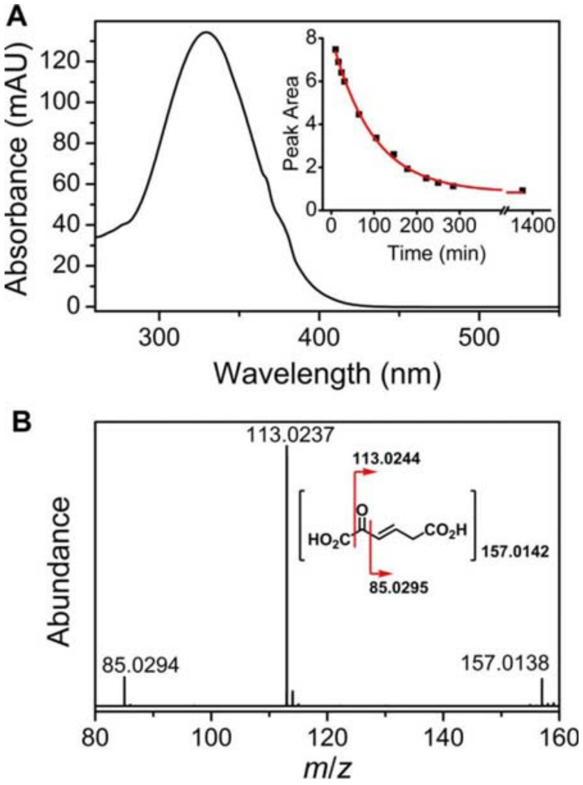

Figure 4.6 Analysis of the ALDH8A1 reaction product. (A) UV-visible spectrum of 2-AM and the time course of its nonenzymatic decay (inset). (B) MS-MS spectrum of the 2-AM decay product. mAU, milliabsorbance units. Details of the MS-MS experiment can be found in 4.5.5 Mass spectrometry

The downstream enzyme of AMSDH performs deamination on 2-AM to produce 2-hydroxymuconate, which is expected to tautomerize to its α,β-unsaturated ketone form, 2-oxo-3-hexenedioate, as shown in Figure 4.7. The deamination reaction is not known to be coupled to any other reaction, so it is expected to be thermodynamically preferred. As such, it may proceed nonenzymatically at a slower rate. To lend credence to the proposed nonenzymatic deamination followed by tautomerization, ACMSD–AMSDH coupled-enzyme assays were performed in H_2O and D_2O in separate experiments, and the reaction products were monitored by NMR

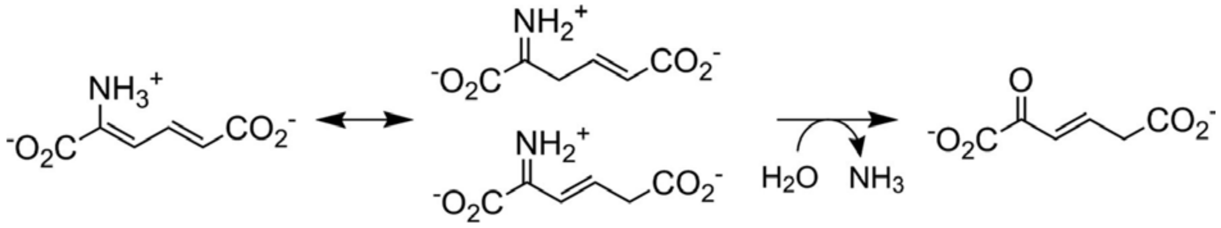

Figure 4.7 Proposed spontaneous decay mechanism for 2-aminomuconate.

spectroscopy (Figure 4.8). When performing the reaction in H_2O (Figure 4.8A), two doublets around 5.8 ppm and a doublet of doublets at 7.15 ppm can be observed to decay while a new doublet at 6.17 ppm and a doublet of triplets at 6.9 ppm arise. These new resonances are consistent with 2-oxohexenedioate observed in the study of 2-hydroxymuconate tautomerization [90]. Alternatively, upon enzymatic decarboxylation and oxidation performed in D_2O by ACMSD and AMSDH, respectively, the ^{1}H NMR spectrum shows two doublets at 7.1 and 5.8 ppm, corresponding to the protons on carbons 4 and 5 (H_b and H_c) of 2-AM, respectively (Figure 4.8B). The proton at the 3-position (H_a) is replaced with deuterium by running the ACMSD reaction in D_2O (Figure 4.9). The two doublets coalesce into a single resonance at 6.9 ppm over time. The decay of the resonance at 5.8 ppm indicates that the proton at the 5-position can eventually exchange with solvent, and the shift of the doublet at 7.1 to a singlet at 6.9 ppm implies that a chemical change takes place in addition to simple exchanging of protons for deuterons. The most likely candidate for such a chemical change is the replacement of the nitrogen at the 2-position with oxygen derived from water, i.e. deamination of 2-AM. Thus, the NMR spectra of the initial and final products of the ALDH8A1 reaction are consistent with 2-AM being the initially formed product, which then spontaneously deaminates and tautomerizes.

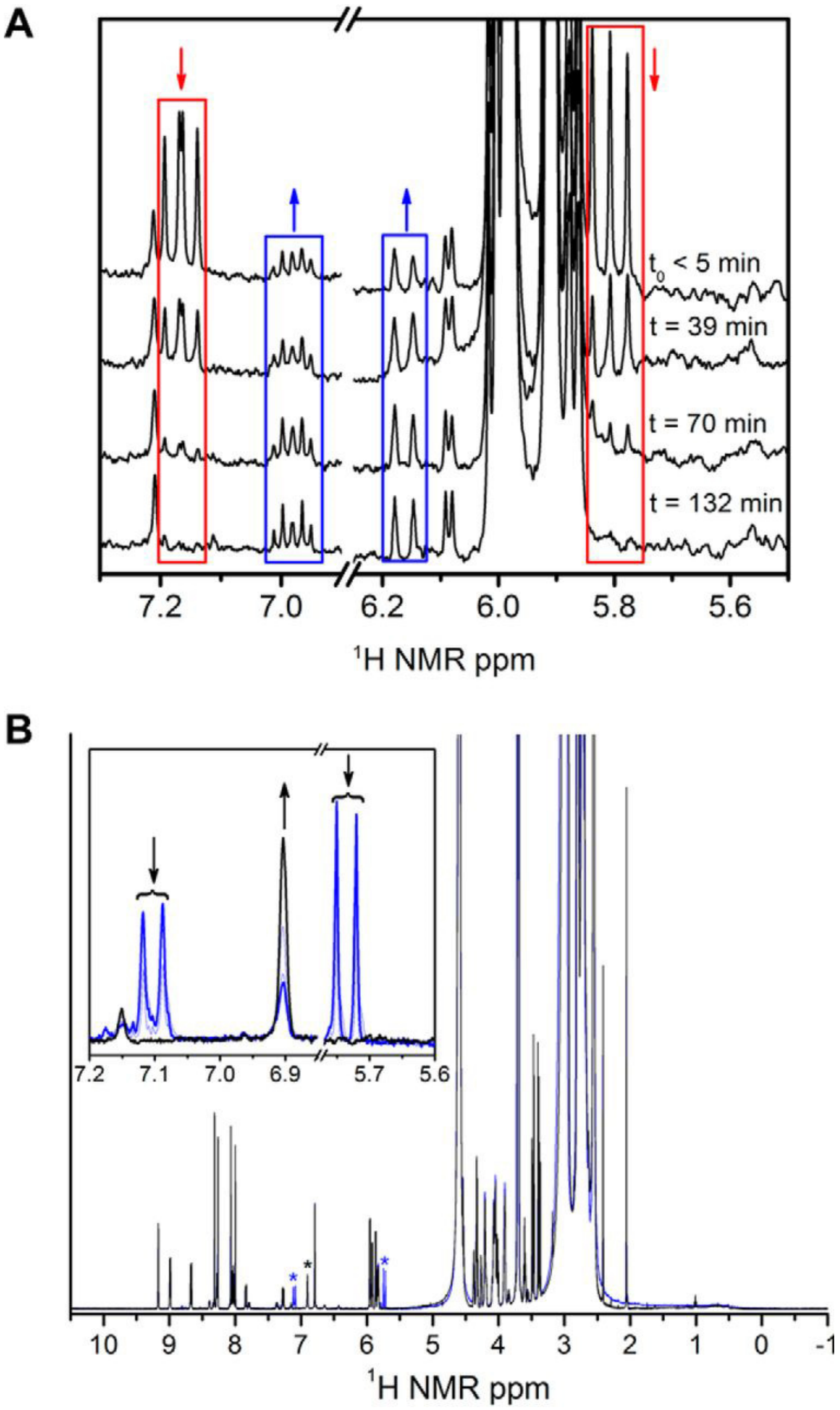

Figure 4.8 ^{1}H-NMR spectra monitoring the decay of 2-AM from a coupled-enzyme assay performed in H_2O (A) and D_2O (B).2-AM resonances are highlighted with red boxes, and the decay product, 2-oxo-hexenedioate, is highlighted with blue boxes. A zoomed-in view of the resonances corresponding to 2-AM and its decay product is shown in the inset in B. The initial and final spectra are shown as blue and black, respectively.

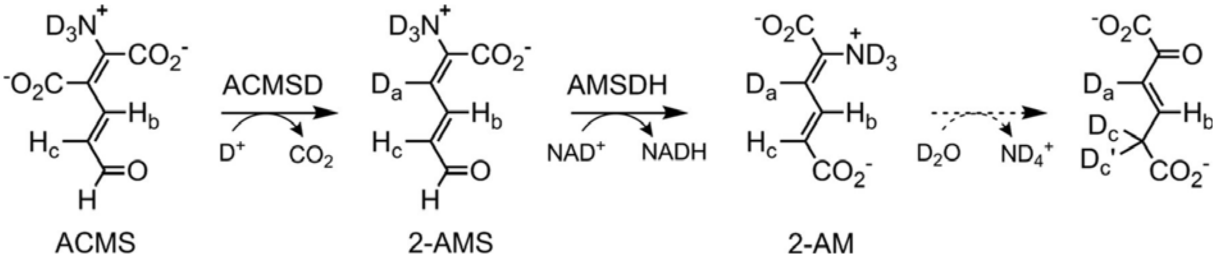

Figure 4.9 Coupled ACMSD-AMSDH assay performed in D_2O.

4.3.4 Determination of the kinetic parameters of ALDH8A1 and selected site-directed mutants

Although the coupled-enzyme assays presented above show that 2-AMS can serve as a substrate for ALDH8A1, such experiments are not amenable to extraction of enzymatic kinetic parameters. Instead, a substrate analog, 2-hydroxymuconate semialdehyde (2-HMS), in which the amino group of 2-AMS has been replaced with a hydroxyl group to prevent the nonenzymatic cyclization reaction, is used to determine kinetic parameters. The ^{1}H NMR spectrum of 2-HMS can be found in Figure 4.10 along with corresponding ^{1}D NOESY spectra, which show not only through-space interactions between protons but also in-phase resonances for the enol tautomer, which was previously implicated as an intermediate in the 2,3-bond isomerization reaction. The observation of resonances consistent with the enol form of 2-HMS in solution lends credence to the previously proposed tautomerization mechanism in pfAMSDH by showing that the enol form is energetically accessible. ALDH8A1 exhibits typical steady-state kinetics when acting on 2-HMS (Figure 4.11A). The data were fitted with the Michaelis–Menten equation to provide a k_{cat}, K_M, and k_{cat}/K_M of 0.42 s^{-1}, 590 nM, and 7.1×10^5 M^{-1} s^{-1}, respectively. A sub-micromolar K_M is at the lower end for the KP enzymes; however, such high commitment may be necessary to efficiently compete with the rapid decay of its substrate to PA.

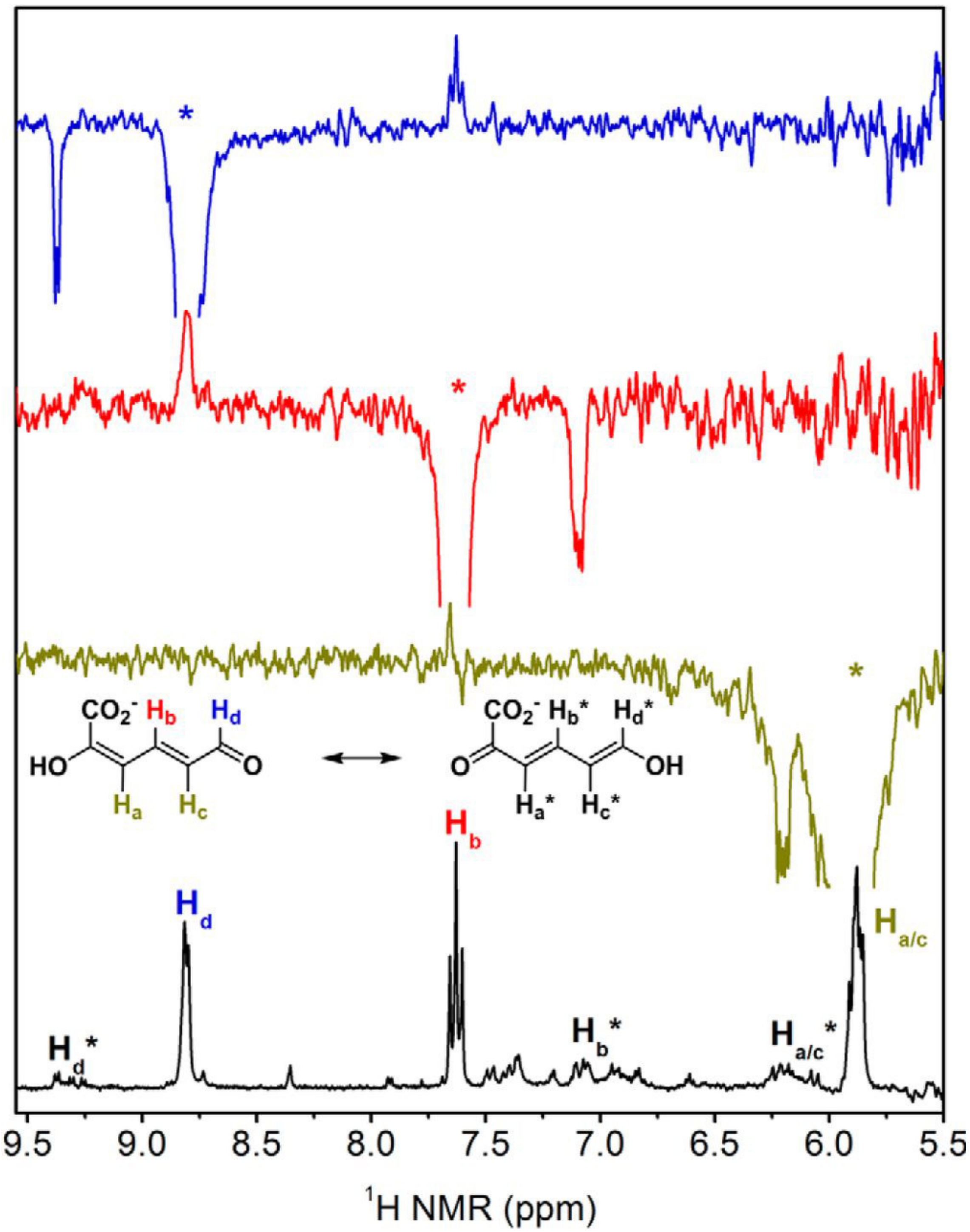

Figure 4.10 ^{1}H NMR spectrum of 2-HMS and 1D NOESY spectra show enol tautomer. NOESY spectra were acquired by irradiating at the resonance marked with an asterisk corresponding to the color-coded proton (Hd as blue, Hb as red, and Ha/c as mustard). Out-of-phase, positive resonances show through-space interactions between protons, and in-phase, negative resonances show the same proton in the enol tautomer as indicated by the isomerization shown. ^{1}H NMR spectrum of 2-HMS is shown at the bottom in black.

To further investigate the specificity of ALDH8A1 for α-substituted muconate semialdehydes, several active-site mutants were constructed. The two strictly conserved residues among the HMSDH family previously shown to be responsible for substrate recognition and binding, Arg109, and Arg451, were mutated to alanine, and their kinetic parameters for 2-HMS were determined. As summarized in Table 4.1, deletion of Arg109 by mutation to alanine generated a variant with a similar turnover number but approximately 160-fold increased K_M as compared with WT (Figure 4.11B). No detectable activity could be measured for the R451A variant. Additionally, the active-site asparagine (Asn155) responsible for stabilizing tetrahedral, oxyanion intermediates in general and involved in substrate isomerization in AMSDH was mutated to alanine, aspartic acid, and glutamine. The activity of the mutants was too low to determine kinetic parameters; however, specific activities for N155A, N155D, and N155Q were 7.4 ± 0.1, 20 ± 1, and 0.31 ± 0.03 nmol/mg/min, respectively. Of the same mutants in pfAMSDH, N169D also showed the highest activity (22). In other aldehyde dehydrogenases, mutation of the corresponding asparagine to alanine or aspartic acid reduced the activity by approximately 1,000-fold or below detectable limits (27, 28).

Table 4.1 Kinetic parameters of ALDH8A1 and variants for 2-HMS.

	k_{cat} (s^{-1})	K_M (μM)	k_{cat}/K_M (M^{-1} s^{-1})
ALDH8A1	0.42 ± 0.03	0.59 ± 0.10	7.1×10^5
R109A	1.06 ± 0.12	97 ± 13	1.1×10^4
R451A	ND[a]	ND	-
N169A/D/Q	< 0.02	ND	-

[a] Not determined

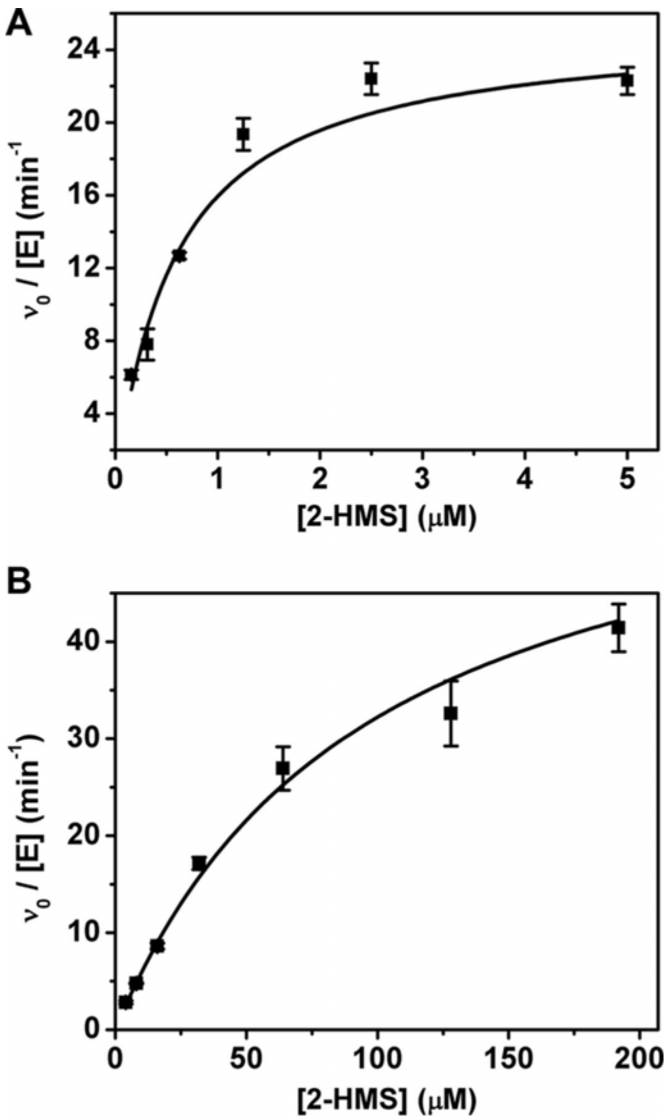

Figure 4.11 Determination of Michaelis–Menten parameters of ALDH8A1 and the R109A variant for 2-HMS. Reactions were monitored by the decrease in absorbance at 375 nm. ALDH8A1 and its R109A variant are shown in A and B, respectively. Error bars represent S.D.

4.4 Conclusion

The human enzyme ALDH8A1 (ALDH12) was shown to catalyze the NAD$^+$-dependent oxidation of 2-AMS with catalytic efficiency comparable with pfAMSDH. Mutation of the active-site residues, which were shown to be heavily involved with substrate recognition, binding, and isomerization in the bacterial enzyme, resulted in variants with 100-fold increased K_M or no detectable activity. As such, the ALDH8A1 enzyme, which was previously assigned as a *cis*-retinal dehydrogenase, should be reassigned as human AMSDH. It was also shown that the reaction product, 2-AM, can spontaneously deaminate in solution, ultimately forming 2-oxo-3-hexenedioate. This work thus establishes that the aldehyde dehydrogenase of the kynurenine pathway, first discovered 53 years ago from liver extracts [74], is ALDH8A1 (ALDH12). The kynurenine pathway of the tryptophan catabolic pathway in humans is therefore extended to AMSDH.

4.5 Experimental procedures

4.5.1 Cloning and site-directed mutagenesis

A DNA sequence that codes for human ALDH8A1 (accession number AF303134) was purchased from DNASU (Arizona State University) and ligated into pET28a(+) vector with NheI and HindIII restriction sites, creating an N-terminal His_6-tagged construct. The resultant plasmid was transformed into *E. coli* cell line BL21 (DE3), which was stored at −80 °C as a 20% (v/v) glycerol stock. Overexpression systems for R109A, R451A, N155A, N155Q, and N155D were constructed by PCR overlap extension using the WT as the starting template. The forward primers were 5′-CCATGGACATTCCCgcgTCTGTGCAGAA and 5′-CTGCTGGCTCATCgcgGAGCTGAACCTT for R109A and R451A, respectively, and 5′-GCTGGTCTGATCAGCCCCTGGgctTTGCCACTCTACTTGCTGACC, 5′-

GCTGGTCTGATCAGCCCCTGGcagTTGCCACTCTACTTGCTGACC, and 5′-GCTGGTCTGATCAGCCCCTGGgacTTGCCACTCTACTTGCTGACC for N155A, N155Q, and N155D, respectively.

4.5.2 Protein preparation

For all cultures, antibiotic selection under kanamycin was used. Cultures were started by streaking the appropriate glycerol stock onto an LB-agar plate, which was incubated overnight at 37 °C. A single colony was selected for further incubation in 15 ml of LB-Miller broth at 37 °C with 220 rpm shaking until an A_{600} of approximately 0.6 was achieved. Then 50 ml of LB-Miller broth was inoculated to an A_{600} of 0.0002 and incubated at 37 °C with 220 rpm shaking. Finally, once the 50-ml flask reached an A_{600} of approximately 0.6, it was used to inoculate 6 liters of LB-Miller broth in 12 two-liter baffled flasks to an A_{600} of 0.0002. The flasks were incubated at 37 °C with 220 rpm shaking. Upon reaching an A_{600} of 0.5, isopropyl β-D-1-thiogalactopyranoside was added to a final concentration of 800 μM to induce protein expression, the temperature was lowered to 16 °C, and the culture was incubated for an additional 12 h. Cells were harvested by centrifugation at 8,000 × g and resuspended in 50 mm KPi, 150 mm NaCl buffered to pH 8.0 with 0.1% (v/v) β-mercaptoethanol. Protein was released by cell disruption (LS-20, Microfluidics), and the cell debris was removed by centrifugation at 27,000 × g.

The protein of interest was purified by nickel affinity chromatography. Clarified, cell-free extract was applied to a nickel-nitrilotriacetic acid column and eluted with an imidazole gradient. The running and elution buffers were 50 mM KPi, 150 mM NaCl buffered to pH 8.0 with 5 mM 1,4-DTT with the elution buffer also containing 500 mM imidazole. The purified protein was then desalted to 25 mM HEPES buffer, pH 7.5, 5 mM 1,4-DTT, 1 mM NAD$^+$, 5% glycerol (w/v); concentrated to approximately 1 mM by 30-kDa centrifugal filters; flash frozen in liquid nitrogen; and stored at −80 °C until use. ACMSD used for coupled-enzyme assays was prepared as reported previously [19-20, 38-39, 72, 91].

4.5.3 *Kinetic assays*

The substrate analog 2-hydroxymuconic semialdehyde was prepared as reported previously [22]. Briefly, 3-hydroxyanthralinic acid was converted to 2-amino-3-carboxymuconic semialdehyde by purified 3-hydroxyanthranilic acid dioxygenase. 2-Amino-3-carboxymuconic semialdehyde was then nonenzymatically converted to 2-hydroxymuconic semialdehyde by lowering the pH below 2. After conversion, the solution was neutralized, and excess enzyme was removed by filtration.

The coupled-enzyme assays were initiated by addition of excess ACMSD (1 μM) to rapidly convert all ACMS to 2-AMS, which is in turn was converted to 2-aminomuconic acid by ALDH8A1. In the absence of ALDH8A1 and 1 mM NAD^+, the 2-AMS nonenzymatically decays to picolinic acid. Catalytic parameters were obtained using 2-HMS as the substrate. The decrease in absorbance as 2-HMS (λ_{max} at 375 nm, ε_{375} of 43,000 M^{-1} cm^{-1}) and NAD^+ are converted to 2-hydroxymuconic acid and NADH (ε_{375} of 1,900 M^{-1} cm^{-1}) was measured with an Agilent 8453 diode-array spectrometer. The reaction rate was calculated as the change in absorbance divided by the sum of the extinction coefficients of 2-HMS and NADH. Initial rates versus substrate concentration were fitted with the Michaelis–Menten equation.

$$v_0/[E]_T = \frac{k_{cat} \times [S]}{K_M + [S]}$$

Nonlinear least squares regression was performed with OriginPro 8.5.

4.5.4 NMR spectroscopy

All NMR spectra were recorded on a Bruker (Billerica, MA) Avance III HD 500-MHz spectrometer equipped with a CryoProdigy Probe at 300 K running TopSpin 3.5pl6. Spectra were recorded in D_2O or 90% H_2O, 10% D_2O and referenced to residual solvent (^{1}H, 4.70 ppm). One-dimensional ^{1}H spectra (pulse sequence, zg30) were recorded with 1-s relaxation delays, 65,536 data points, and multiplied with an exponential function for a line broadening of 0.3 Hz before Fourier transformation. Double quantum–filtered COSY (pulse sequence, cosygpmfppqf) spectra were acquired with spectral widths of 13.0 ppm with 2,048 × 128 data points and a relaxation delay of 2.0 s. 1D gradient-selected NOESY (pulse sequence, selnogp) spectra were recorded with a mixing time of 0.3 s and a 2-s relaxation delay and multiplied with an exponential function for a line broadening of 3 Hz before Fourier transformation. All NMR data were processed using MestReNova NMR version 11.0.3 software.

4.5.5 Mass spectrometry

The AMSDH reaction product, 2-aminomuconate, was isolated for mass spectrometric characterization by reverse-phase HPLC with an InertSustain C18 column (5-µm particle size, 4.6-mm inner diameter × 100 mm; GL Sciences Inc.) on a Dionex Ultimate 3000 HPLC equipped with a diode-array detector (Sunnyvale, CA). The crude reaction mixture was ultrafiltered (10-kDa cutoff) to remove protein, and separation was achieved using isocratic elution with 95% H_2O, 5% acetonitrile, and 0.5% formic acid. Mass spectra were collected on a maXis plus quadrupole-TOF mass spectrometer equipped with an electrospray ionization source (Bruker Daltonics). The instrument was operated in the negative ionization mode in the range $50 \leq m/z \leq 1{,}500$ and calibrated using ESI-L Low Concentration Tuning Mix (Agilent Technologies). Samples were introduced via syringe pump at a constant flow rate of 3 µL/min.

Relevant source parameters are summarized as follows: capillary voltage, 3500 V with a set end plate offset of −500 V; nebulizer gas pressure, 0.4 bar; dry gas flow rate, 4.0 L/min; source temperature, 200 °C. Mass spectra were averages of 1 min of scans collected at a rate of 1 scan per second. Collision-induced dissociation was achieved using a set collision energy of −20 eV. OtofControl software version 6.3 was used for data acquisition, and Compass Data Analysis software version 4.3 (Bruker Daltonics) was used to process all mass spectra. mMass software version 5.5.0 was used for all exact mass calculations [92].

5 PROBING BIS-FE(IV) MAUG: EXPERIMENTAL EVIDENCE FOR THE LONG-RANGE CHARGE-RESONANCE MODEL

This chapter is adapted from the published work coauthored by ID: Geng J, Davis I, and Liu A (2015) Probing Bis-Fe^{IV} MauG: Experimental Evidence for the Long-Range Charge-Resonance Model. *Angewandte Chemie International Edition*, 54(12), 3692 – 3696. DOI: 10.1002/anie.201410247

5.1 Abstract

The biosynthesis of tryptophan tryptophylquinone, a protein-derived cofactor, involves a long-range reaction mediated by a *bis*-Fe^{IV} intermediate of a diheme enzyme, MauG. Recently, a unique charge-resonance (CR) phenomenon was discovered in this intermediate, and a biological, long-distance CR model was proposed. This model suggests that the chemical nature of the *bis*-Fe^{IV} species is not as simple as it appears; rather, it is composed of a collection of resonance structures in a dynamic equilibrium. Here, we experimentally evaluated the proposed CR model by introducing small molecules to, and measuring the temperature dependence of, *bis*-Fe^{IV} MauG. Spectroscopic evidence was presented to demonstrate that the selected compounds increase the decay rate of the *bis*-Fe^{IV} species by disrupting the equilibrium of the resonance structures that constitutes the proposed CR model. The results support this new CR model and bring a fresh concept to the classical CR theory.

5.2 Introduction

Since its first documentation by Brocklehurst and Badgers in 1968, [93] charge-resonance (CR) phenomena have been actively researched by organic chemists [94]. In a typical CR event, one-electron oxidation of an aromatic compound generates a cation radical which spontaneously associates with its neutral parent molecule or another molecule of the cation radical to form noncovalent "sandwich-like" dimeric complexes. The former scenario stabilizes an odd number of spin/charge in a mixed-valence species, $(\Pi)_2^{\bullet+}$, and is classified as type I CR; the latter one stabilizes an even number of spin/charge in a dication diradical, $(\Pi^{\bullet+})_2$, and is classified as type II CR [95]. Notably, unique electronic absorption bands in the near-infrared (NIR) region arise from resonance stabilization of spin/charge in the CR complexes and are thereby termed as CR bands (**Error! Reference source not found.**) [96-99]. CR complexes represent the simplest intermolecular units that carry delocalized spin/charge. Investigation of these phenomena may provide the chemical basis for electron transfer (ET), conductivity, and ferromagnetism in many organic materials and metalloporphyrin complexes.

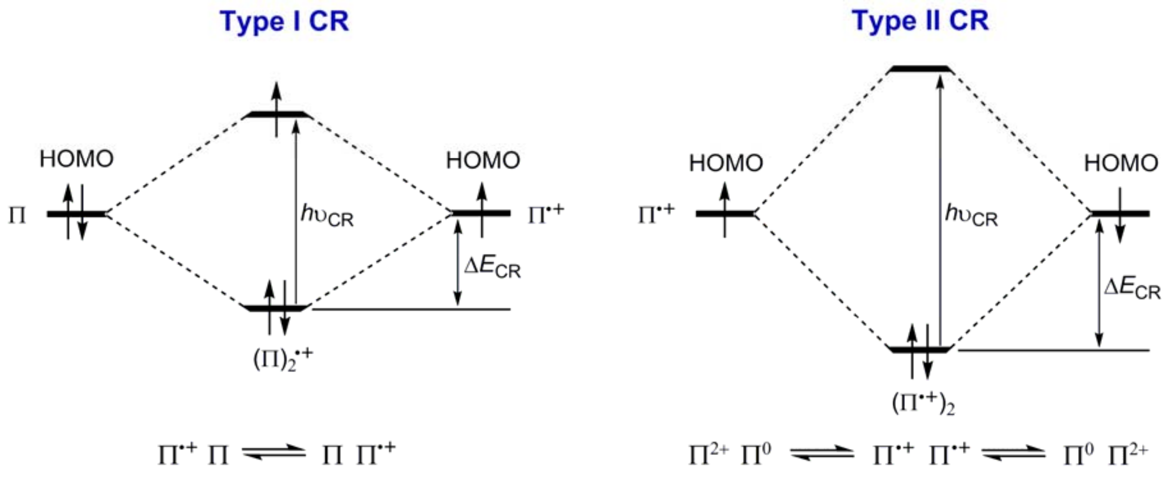

Figure 5.1 Qualitative MO diagrams for Charge Resonance. Type I CR in the mixed-valence cation radical $(\Pi)_2^{\bullet+}$ and Type II CR in the di-cation di-radical $(\Pi^{\bullet+})_2$. The origins of the CR stabilization energy (ΔE_{CR}) and the CR band ($h\nu_{CR}$) are illustrated.

Like many classical chemical models adopted by nature, the utilization of CR in biological systems to transiently stabilize spin/charge was first suggested in a pair of chlorophyll molecules, known as the "special pair", in bacterial photosynthetic reaction centers [100-101]. Recently, a second example was revealed from a diheme enzyme, MauG [95]. MauG is the terminal enzyme in the biogenesis pathway of a protein-derived cofactor, tryptophan tryptophylquinone (TTQ), [102] which is the catalytic center of methylamine dehydrogenase (MADH) [103]. MauG possesses two *c*-type hemes in distinct spin states: one is pentacoordinate, high-spin with an axial histidine ligand and the other is hexacoordinate, low-spin with an axial histidine-tyrosine ligand set (denoted as Heme_{5C} and Heme_{6C}, respectively, as shown in **Error! Reference source not found.**) [102, 104]. The substrate of MauG is a precursor protein of MADH, preMADH [105]. MauG performs three cycles of H_2O_2-dependent oxidation on two adjacent tryptophan residues of preMADH to produce TTQ (Figure 5.2a) [106]. Each two-electron oxidation cycle is suggested to be mediated by a unique *bis*-Fe^{IV} intermediate of MauG in which Heme_{5C} is in an oxyferryl state and Heme_{6C} is in a ferryl state with its two original axial ligands retained (Figure 5.2b) [107-108].

It is in the *bis*-Fe^{IV} intermediate that the CR phenomenon was proposed [95]. A broad electronic absorption band centered at 950 nm ($\varepsilon = ca.\ 7000\ \text{M}^{-1}\ \text{cm}^{-1}$) is present specifically in the *bis*-Fe^{IV} state of MauG (Figure 5.2c) [95]. It is noteworthy that the spectral properties of the NIR band are highly reminiscent of the reported CR spectroscopic signatures from metalloporphyrin complexes [99, 109]. The *bis*-Fe^{IV} species is electronically equivalent to two ferric hemes each coupled with a porphyrin cation radical, a scenario resembling the dication diradical complexes in type II CR. However, this case cannot be simply illustrated by the

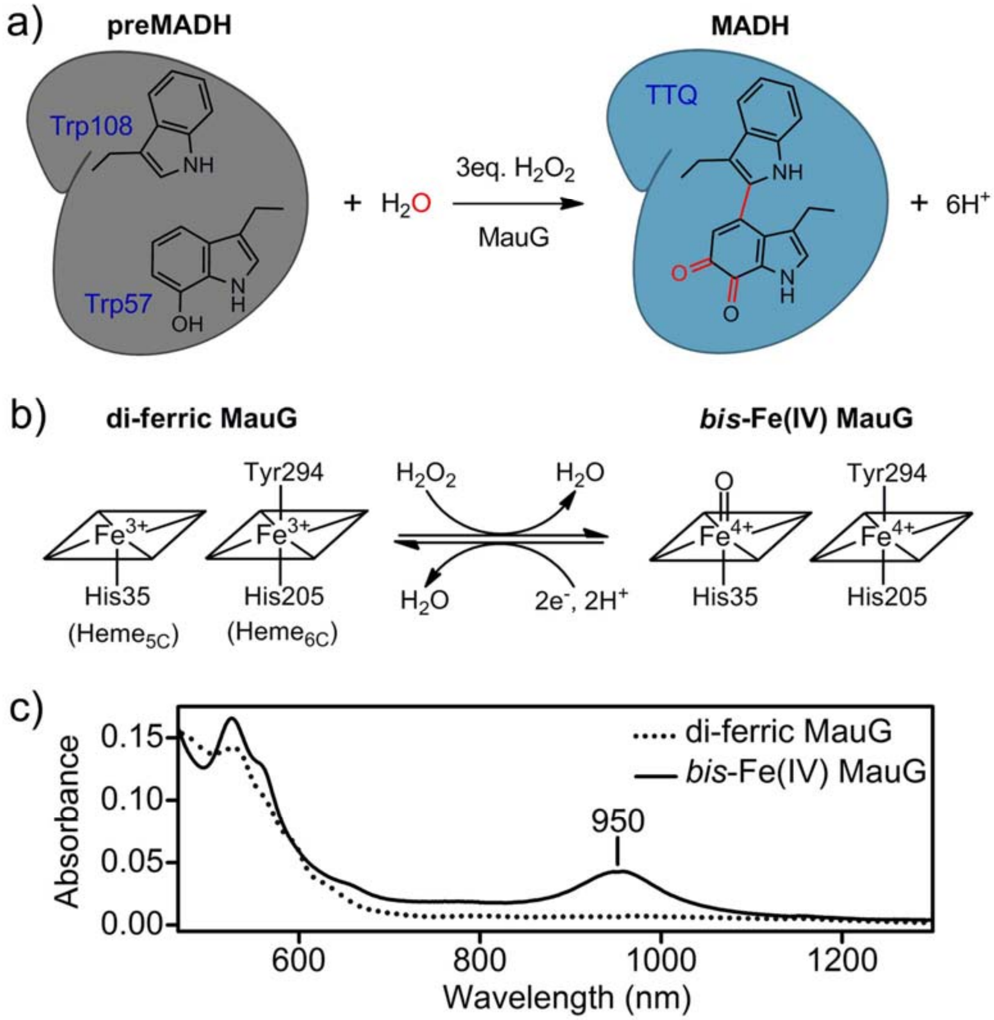

Figure 5.2 MauG-dependent TTQ biosynthesis and the *bis*-Fe^{IV} species of MauG. (a) Chemical reaction catalyzed by MauG. Posttranslational modifications on the two tryptophan residues of preMADH are shown in red. H_2O_2 serves as a co-substrate to provide oxidizing equivalents. (b) Chemical conversion between di-ferric and *bis*-Fe^{IV} MauG. (c) NIR electronic absorption band at 950 nm displayed by *bis*-Fe^{IV} MauG (5 μM). Ten equivalents of H_2O_2 was added to achieve a full conversion from di-ferric to *bis*-Fe^{IV} MauG.

classical CR models as the two porphyrin rings are about 14 Å apart (**Error! Reference source not found.**), a much wider separation than the interacting moieties in model CR complexes [110-111]. A significant conformational change that enables the diheme cofactor to fold into a “sandwich-like” dimer is unlikely to occur during the formation of the *bis*-Fe^{IV} species since the structure shown in **Error! Reference source not found.** was previously demonstrated to be in the catalytically active form by reactions in crystals [104]. Thus, a new class of CR, type III, was proposed, whereby resonance stabilization of spin/charge is facilitated by an additional π moiety, the Trp93 residue located between the hemes (Figure 5.3a) [95]. Electron/hole hopping through Trp93 was postulated to occur in the ET process between the hemes to enable CR stabilization. Ultrafast and reversible ET with Trp93 as the hopping site mimics the distribution of spin/charge as if this was in an extended conjugated system. Overall, the type III CR model represents a dynamic equilibrium of different electronically equivalent resonance structures as one electron from Trp93 cannot simultaneously fill two holes. This new CR model is supported by theoretical calculations, which predicted that in the *bis*-Fe^{IV} species electron/hole hopping through Trp93 makes possible a rate of inter-heme ET greater than 107 s^{-1}, in accordance with the reported ET rates from established model CR systems [95].

In this work, we aim to experimentally evaluate the proposed type III CR model and determine the chemical nature of *bis*-Fe^{IV} MauG, i.e., whether it is a single redox species or

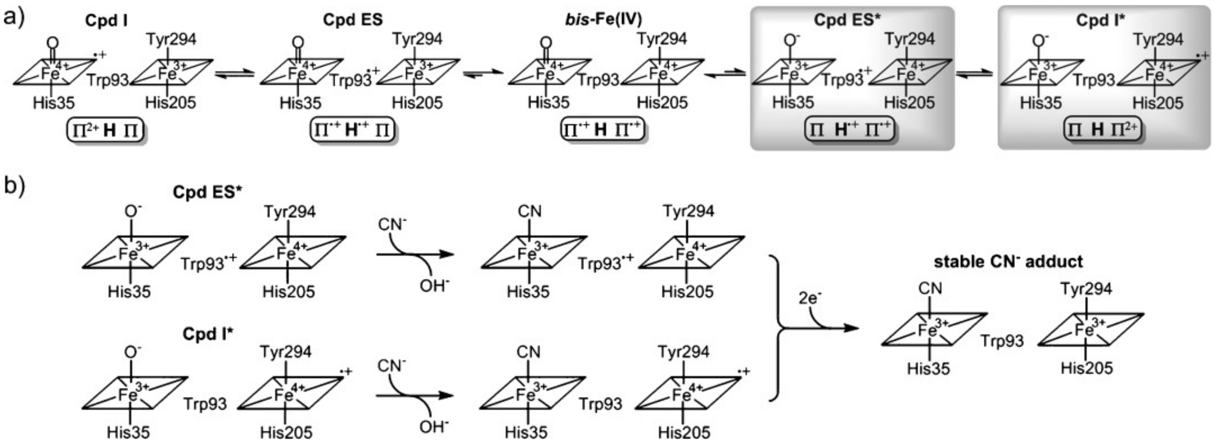

Figure 5.3 Type III CR in *bis*-Fe^{IV} MauG. a) Proposed resonance structures in the type III CR model. "H" represents a third aromatic moiety (i.e., the Trp93 residue in this case), which functions as a hopping relay to facilitate ET between the two primary aromatic moieties. The two resonance structures (Cpd ES* and Cpd I*) that can be potentially targeted by small-molecule ligands are highlighted with a grey background. b) Specific targeting of Cpd ES* and Cpd I* by CN^{-} to disrupt the type III CR in the *bis*-Fe^{IV} species.

composed of multiple resonance structures as predicted by the CR model. We introduced small-molecule ligands to disrupt the hypothesized equilibrium of high-valence species. The selected ligand molecules include cyanide (CN^{-}), imidazole (IM), and fluoride (F^{-}). They are all capable of binding to the heme iron when there is a coordinate vacancy, yet with different binding affinities. If *bis*-Fe^{IV} MauG is a single redox species, exogenous small-molecule ligands (CN^{-}, for instance) are not expected to cause a notable effect on its chemical properties because both hemes are coordinatively saturated and the axial ligands are either irreplaceable (Heme$_{5C}$) or inaccessible (Heme$_{6C}$) [104, 112]. However, if *bis*-Fe^{IV} MauG represents an equilibrium of resonance structures as proposed in Figure 5.3a, exogenous CN^{-} might be able to specifically target species like compound Cpd ES* and Cpd I* by outcompeting the relatively weakly associated axial ligand of Heme$_{5C}$ to generate the [Fe^{III}CN$^{-}\cdots$Trp93$^{\bullet+}\cdots$Fe^{IV}] and [Fe^{III}CN$^{-}\cdots$Trp93$\cdots$Fe$^{IV\,\bullet+}$] complexes, respectively (Figure 5.3b). Neither CN^{-} adduct is likely to be capable of maintaining the CR stabilization due to changes in heme redox properties, and it is anticipated that they will quickly decay to a stable, reduced state by releasing two oxidizing equivalents to the protein matrix or the solvent (Figure 5.3b). Previously, three methionine residues near Heme$_{5C}$ were identified to absorb the oxidizing equivalents from *bis*-Fe^{IV} in the absence of preMADH through ancillary ET pathways [113]. Despite the fact that Cpd ES* and Cpd I* are present only as minor species in the proposed CR model, [95] the dynamic exchange with other resonance structures allows the CN^{-}-induced disruption to gradually shift the equilibrium and break the electronic communication between the hemes. It will eventually destroy the CR stabilization, resulting in an accelerated decay of the *bis*-Fe^{IV} species to a di-ferric CN^{-} adduct (Figure 5.3b).

5.3 Results

In the absence of preMADH, *bis*-Fe^{IV} MauG does not misfire but instead exhibits extraordinary stability with a half-life of several minutes [114-115]. The NIR band at 950 nm can be used as a spectral signature to monitor the decay process of the *bis*-Fe^{IV} species [95]. Figure 5.4a shows that the introduction of CN^{-} to the *bis*-Fe^{IV} species led to an apparent increase in the decay rate of the NIR band, compared to a parallel experiment without CN^{-}. In the presence of 25 mM CN^{-}, the NIR spectral signature became completely diminished *ca*. 75 s after addition of CN^{-}, with a decay rate nearly one order of magnitude greater than that in the absence of CN^{-}. When different small-molecule ligands were examined, they exhibited different degrees of disruptive effects on the decay rate of the NIR band with CN^{-} presenting the most pronounced influence, followed by IM (Figure 5.4b). The F^{-} anion showed almost no observable effect. This trend correlates with the binding affinities of these small-molecule ligands to ferric heme centers; it is known that in many hemoproteins diatomic molecules like CN^{-} are the most tightly associated ligands, whereas small heterocyclic compounds like IM and halide anions are usually weaker ligands [116-117]. Figure 5.4c summarizes the decay rates of the NIR band in the absence and presence of these small-molecule ligands.

EPR spectroscopy was also used to characterize the aforementioned chemical events. As shown in the gray trace of Figure 5.5, there are three different heme species revealed from the EPR spectrum of di-ferric MauG, a high-spin species (Heme$_{5C}$), a major low-spin species (Heme$_{6C}$), and a minor low-spin species attributed as a freezing-induced artifact derived from the high-spin species [102, 118-119]. Exogenous CN^{-} was only able to coordinate to Heme$_{5C}$ and caused a spin transition to produce a new low-spin species with a very broad signal around g = 3.37, at the expense of the high-spin species (Figure 5.5, black trace). This low-spin signal is consistent with the formation of a hexacoordinate CN⁻ adduct of Heme5C, based on its similarity to the EPR signals of CN⁻ adducts reported from other hemoproteins [120]. In addition, the freezing-induced artifact was removed in the presence of CN⁻, confirming that it is derived from

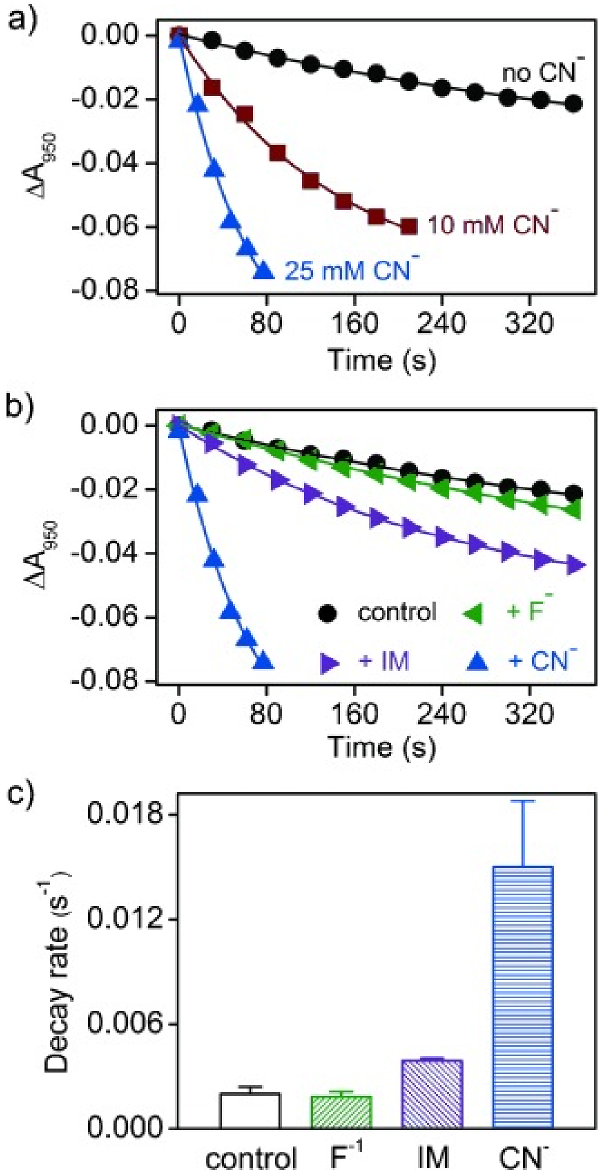

Figure 5.4 Disruption of *bis*-Fe^{IV} MauG by small-molecule ligands. a) Addition of CN⁻ accelerated the decay of the NIR band of *bis*-Fe^{IV} MauG. CN⁻ was added immediately after *bis*-Fe^{IV} formation. The solid lines are fits of the data to single-exponential decay. b) Effect of different small-molecule ligands on the decay of the NIR band. Each small-molecule ligand (25 mM) was added immediately after *bis*-Fe^{IV} formation. c) Decay rates of the NIR band in the absence and presence of small-molecule ligands.

the high-spin species of $Heme_{5C}$. Upon addition of H_2O_2 to di-ferric MauG, the high-spin and low-spin ferric signals are nearly absent, owing to the formation of the *bis*-Fe^{IV} species (Figure 5.5, blue trace) [114]. The introduction of CN^- to this system accelerated the decay of the newly generated *bis*-Fe^{IV} species as indicated by a more rapid return of the low-spin signal of $Heme_{6C}$, compared to a control sample without CN^- (Figure 5.5, red and green traces, respectively). It should be noted that $Heme_{6C}$ is buried in the protein matrix and inaccessible to exogenous small-molecule ligands [104, 112]. Thus, the accelerated decay of the ferryl species at the $Heme_{6C}$ site is likely due to disruptive events that remotely occurred at the $Heme_{5C}$ site and caused a loss of

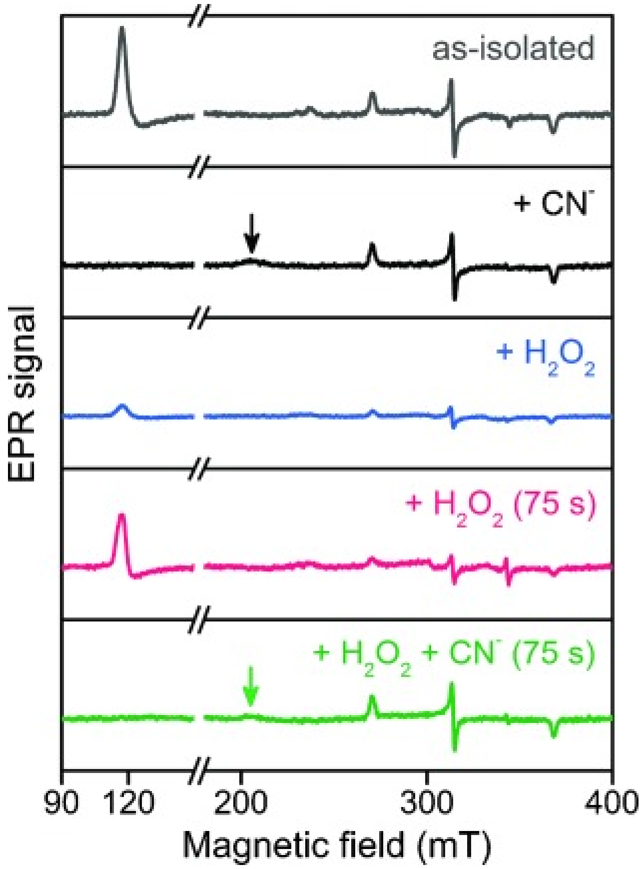

Figure 5.5 EPR spectra of MauG. Gray trace: as-isolated di-ferric MauG; black trace: MauG + 25 mM CN^-; blue trace: MauG + 1×H_2O_2; red trace: MauG + 1×H_2O_2 (frozen 75 s after reaction); green trace: MauG + 1×H_2O_2 + 25 mM CN^- (CN^- was added immediately after addition of H_2O_2 and the sample was frozen 75 s after addition of CN^-). The arrows indicate the CN^- adduct of $Heme_{5C}$ at g = 3.37.

the electronic communication between the two hemes. The sample freeze-quenched 75 s after addition of CN^- to *bis*-Fe^{IV} MauG displayed a spectrum that is almost identical to that of the sample containing the CN^- adduct of MauG (Figure 5.5, black and green traces, respectively). This observation suggests that almost all the newly generated *bis*-Fe^{IV} species was eliminated after the CN^- treatment for 75 s, consistent with the result obtained from monitoring the decay of the NIR band. It also indicates that the end product of this chemical processing is a di-ferric CN^- adduct of MauG, in accordance with our proposed scheme shown in Figure 5.3b.

Given the relatively high concentration of small-molecule ligands added to the system, it could be possible that direct reduction by these molecules or exchange of the ferryl oxo group with exogenous ligands occurred at the $Heme_{5C}$ site, thereby causing a more rapid decay of *bis*-Fe^{IV} MauG. Our further investigation on the Y294H mutant of MauG ruled out this possibility. Tyr294 is an axial ligand of $Heme_{6C}$ (**Error! Reference source not found.**). Mutation of this residue to histidine creates an axial *bis*-histidine ligand set at $Heme_{6C}$, which is not capable of stabilizing the ferryl oxidation state [121]. In the reaction between di-ferric Y294H MauG and H_2O_2, the two oxidizing equivalents from H_2O_2 are trapped at the $Heme_{5C}$ site in the form of a Cpd I-like species (Figure 5.6a), which presents a characteristic absorption band for Cpd I species at 655 nm but no NIR band at 950 nm (Figure 5.6b) [121-122]. The introduction of small-molecule ligands such as CN^- and IM to Y294H Cpd I had a minimal effect on its decay rate as revealed from the time-dependent spectral change at 655 nm (Figure 5.6c). Therefore, the observed accelerated decay of the *bis*-Fe^{IV} species from wild-type MauG in the presence of small-molecule ligands is unlikely due to direct reduction or ligand exchange on the oxyferryl species at the $Heme_{5C}$ site.

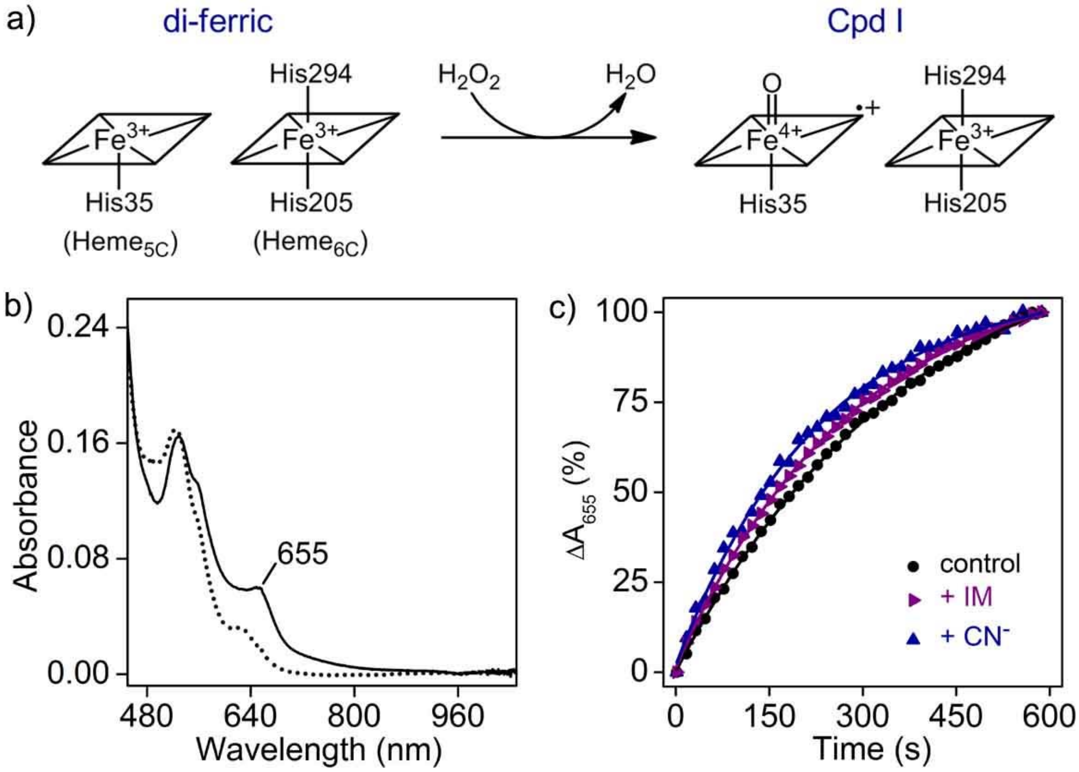

Figure 5.6 Cpd I-like species in Y294H MauG. (a) Chemical conversion from di-ferric to Cpd I Y294H MauG. (b) Optical absorption spectra of Y294H (5 µM) before (dotted trace) and after (solid trace) addition of H_2O_2. (c) Effect of small molecule ligands on the decay rate of Y294H Cpd I. Y294H Cpd I was generated by addition of a stoichiometric amount of H_2O_2 to di-ferric Y294H MauG (4.4 µM). Each small molecule ligand (25 mM) was added immediately after the formation of Y294H Cpd I. The solid lines are fits of the data to a single-exponential equation.

Furthermore, the effect of temperature on the spectral and kinetic properties of the NIR absorption feature was investigated over a temperature range of 2 to 30 °C. As reported from a previous study, MauG is not stable above the higher temperature [123], thereby limiting the temperature range. Within this interval, changes in temperature have no observable effect on the absorption maxima wavelength or the overall lineshape of the NIR band; however, the absorption intensity was seen to increase with decreasing temperature. Figure 5.7 shows that the decay rate of the NIR band increases as the temperature rises. Fitting of the experimental data by the Arrhenius equation yields an activation energy (E_a) of 18.6 kcal mol^{-1}. As mentioned

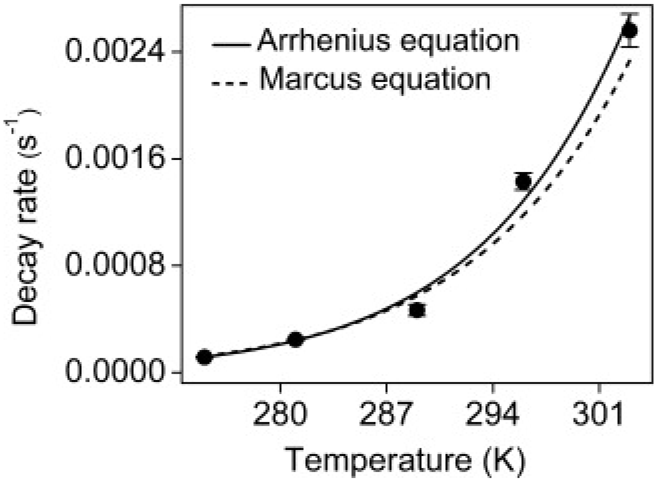

Figure 5.7 Temperature effect on the decay rate of the NIR band of *bis*-Fe^{IV} MauG.The *bis*-Fe^{IV} species was generated by addition of a stoichiometric amount of H_2O_2 to di-ferric MauG (15 µM). The data were fit to the Arrhenius equation (solid trace) to calculate the activation energy (E_a) and to the Marcus equation (dashed line) to calculate the reorganization energy (λ) of the ET reaction, respectively.

previously, the decay of the NIR band is associated with the decay of the *bis*-Fe^{IV} species through oxidation of the methionine residues near Heme$_{5C}$. The E_a value of the *bis*-Fe^{IV} self-decay reaction is comparable but slightly higher than those determined from H_2O_2-dependent oxidation reactions of methionine residues in other proteins or peptides [124-125]. The self-decay process of the *bis*-Fe^{IV} species can also be treated as an ET reaction from the methionine residues to the diheme cofactor. The experimental data was also analyzed using the classical ET theory [126] (see details in 5.5.4 Temperature-dependence studies.). Among the three methionine residues near Heme$_{5C}$, Met108 was identified as the first residue to be oxidized by *bis*-Fe^{IV} MauG [113]. The ET reaction was analyzed with Met108 as the electron donor and the diheme cofactor as the electron acceptor. Using the direct distance approach developed by Dutton and co-workers [127], a HARLEM [128] calculation on this ET reaction revealed an ET distance (r) of 7.31 Å and a decay constant (β) of 1.64 Å. Although the free energy change ($\Delta G°$) of this ET reaction is unknown, it can be estimated based on the redox potentials of the associated redox centers [129-130]. The reaction potential ($E°$) is anticipated to be within the range of 0 to 1 V, corresponding to a range of 0 to −23.1 kcal mol^{-1} for $\Delta G°$. In Figure 5.7, fitting of the experimental data by the Marcus equation with the input of these calculated parameters yields a range of the reorganization energy (λ) of 3.02 to 4.81 eV. This range is comparable but slightly larger than those calculated for other ET reactions from similar systems [123]. The increased values of E_a and λ for the *bis*-Fe^{IV} self-decay reaction highlight the role of CR in stabilizing the *bis*-Fe^{IV} species by elevating the energy barrier for self-oxidation reactions. This is achieved by expanding the single redox center to an extended conjugated system and thereby increasing the reorganization energy of the related ET reactions.

5.4 Conclusions

The *bis*-Fe^{IV} state of MauG is not a single redox species but rather an equilibrium of different electronically equivalent resonance structures. The data presented here provide supporting evidence for our proposed long-distance type III CR model, which brings a new concept to the well-documented CR phenomena.

5.5 Methods

5.5.1 Reagents.

Sodium cyanide (97%), imidazole (> 99%) and sodium fluoride (≥ 99%) were purchased from Sigma-Aldrich. H_2O_2 (30% v/v) was purchased from Fisher Scientific. The concentration of H_2O_2 was determined based on the molar absorptivity of 43.6 M^{-1} cm^{-1} at 240 nm.

5.5.2 Protein expression and purification.

Wild-type and Y294H MauG were expressed in *Paracoccus denitrificans* and purified as described previously [102, 121].

5.5.3 Spectroscopic characterizations.

All the spectroscopic experiments were performed in 50 mM potassium phosphate buffer, pH 7.5. The Vis-NIR spectra of MauG were recorded on an Agilent 8453 spectrometer, which has a photodiode-array detector with a detection range of 190–1100 nm. For wild-type MauG, the *bis*-Fe^{IV} species was generated by rapidly mixing di-ferric MauG (15 μM) with a stoichiometric amount of H_2O_2. The selected small molecule ligands were then introduced to the reaction system immediately after addition of H_2O_2. The time-dependent change of the NIR absorption band at 950 nm was monitored to evaluate the effect of these small molecule ligands on the decay rate of the *bis*-Fe^{IV} species. For Y294H MauG, a similar procedure was followed. The Compound I-like species of Y294H MauG was generated by rapidly mixing di-ferric Y294H (4.4 μM) with a stoichiometric amount of H_2O_2. The selected small molecule ligands were then introduced to the reaction system immediately after addition of H_2O_2. The time-dependent change of the absorption band at 655 nm was monitored. X-band EPR spectra were recorded in perpendicular mode on a Bruker ER200D spectrometer coupled with a 4116DM resonator at 100 kHz modulation frequency. The measurement temperature was maintained at 10 K using an ESR910 liquid helium cryostat and an ITC503 temperature controller from Oxford Instruments (Concord, MA). The heme concentration of each EPR sample was 200 μM.

5.5.4 Temperature-dependence studies.

The temperature-dependence studies of the spectral and kinetic properties of the NIR band were performed using an Agilent 8453 spectrometer with the cuvette holder coupled with a VWR MM7 temperature controller. The temperature range was from 2 to 30 °C. At each selected temperature, the Vis-NIR spectra of *bis*-Fe^{IV} MauG and its decay process were monitored over a period of time ranging from 10 min to 1 h. The *bis*-Fe^{IV} species was generated by rapidly mixing di-ferric MauG (15 μM) with a stoichiometric amount of H_2O_2. The temperature dependence of the decay rate of the NIR band was fit to the Arrhenius equation, where k is the decay rate, E_a is the activation energy, A is the pre-exponential factor, R is the gas constant, and T is the absolute temperature.

$$k = Ae^{-E_a/RT}$$

In this case, the self-decay process of *bis*-Fe^{IV} MauG is associated with oxidation of Met108, a residue in the distal pocket of $Heme_{5C}$ [113]. The temperature dependence of the decay rate of the NIR band was also analyzed using the classical electron transfer (ET) theory [123, 126] with Met108 as the electron donor and the *bis*-Fe^{IV} cofactor as the electron acceptor. First, a HARLEM [128] calculation was performed to determine the ET parameters (i.e., the ET distance (r) and the decay constant (β)), based on the crystal structure of MauG (PDB entry: 3L4M). The parameter β describes the efficiency of the intervening medium in mediating ET. The direct distance approach developed by Dutton and coworkers [127] was used to define the redox centers and the ET pathway. Specifically, the sulfur atom of Met108 was defined as the donor center, and the iron-porphyrin complex of $Heme_{5C}$ without the propionate groups was defined as the acceptor center. The temperature dependence of the decay rate of the NIR band was then fit to the Marcus equation, where k_{ET}, the ET rate from the donor to the acceptor, is treated as the decay rate of *bis*-Fe^{IV} MauG, $\Delta G°$ is the free energy change of the ET reaction, λ is the reorganization energy comprising inner-sphere and outer-sphere nuclear rearrangement, r_0 is the close contact distance (3 Å), k_0 is the characteristic frequency of nuclei (10^{13} s^{-1}, the maximal ET rate when the donor and acceptor are in van der Waals contact and $\lambda = \Delta G°$). To determine the relevant range of λ, the $\Delta G°$ value was allowed to change between 0 and -23.1 kcal/mol, which corresponds to a range from 0 to 1 V for the potential difference ($E°$) of the ET process.

$$k_{ET} = k_0 e^{-\beta(r-r_0)} e^{-(\Delta G^0+\lambda)^2/4\lambda RT}$$

6 RADICAL TRAPPING STUDY OF THE RELAXATION OF BIS-FE(IV) MAUG

This chapter is adapted from the published work authored by ID: Davis I, Koto T, and Liu A (2018) Radical Trapping Study of the Relaxation of *bis*-Fe(IV) MauG. *Reactive Oxygen Species*, 5(13), 46 – 55. DOI: 10.20455/ros.2018.801

6.1 Abstract

The di-heme enzyme, MauG, utilizes a high-valent, charge-resonance stabilized *bis*-Fe(IV) state to perform protein radical-based catalytic chemistry. Though the *bis*-Fe(IV) species is able to oxidize remote tryptophan residues on its substrate protein, it does not rapidly oxidize its own residues in the absence of substrate. The slow return of *bis*-Fe(IV) MauG to its resting di-ferric state occurs via up to two intermediates, one of which has been previously proposed by Ma et al. (*Biochem. J.* 2016; 473:1769) to be a methionine-based radical in a recent study. In this work, we pursue intermediates involved in the return of high-valent MauG to its resting state in the absence of the substrate by EPR spectroscopy and radical trapping. The *bis*-Fe(IV) MauG is shown by EPR, HPLC, UV-Vis, and high-resolution mass spectrometry to oxidize the trapping agent, 5,5-dimethyl-1-pyrroline N-oxide (DMPO) to a radical species directly. Nitrosobenzene was also employed as a trapping agent and was shown to form an adduct with high-valent MauG species. The effects of DMPO and nitrosobenzene on the kinetics of the return to di-ferric MauG were both investigated. This work eliminates the possibility that a MauG-based methionine radical species accumulates during the self-reduction of *bis*-Fe(IV) MauG.

6.2 Introduction

MauG is a di-heme enzyme responsible for oxidizing two tryptophan residues on its substrate protein (preMADH) to produce the tryptophan tryptophylquinone cofactor of methylamine dehydrogenase [102]. In order to perform the oxidation reactions, MauG itself must first be oxidized to a high-valent *bis*-Fe(IV) state by hydrogen peroxide (H_2O_2) [107]. The heme moieties of MauG are inequivalent with distinct coordination environments: one five-coordinate and one six-coordinate [104]. Only the five-coordinate heme is able to react with H_2O_2, but the two heme centers are able to efficiently share electrons [107, 112, 131]. The substrate protein is oxidized by *bis*-Fe(IV) MauG through electron-hole hopping, generating tryptophan radicals on preMADH over a long distance [106, 132].

Even though *bis*-Fe(IV) MauG is electronically equivalent to the highly-reactive compound I of cytochrome P450 enzymes (an oxoferryl porphyrin cation radical), *bis*-Fe(IV) MauG is stable for several minutes at neutral pH [95, 107-108, 133]. This unusual stability has been attributed to a type III charge-resonance phenomenon, by which the radical character of the high-valent species is shared over both hemes and with an intervening tryptophan residue [95, 133]. In the absence of its substrate, *bis*-Fe(IV) MauG will eventually return to its resting, di-ferric, state [134]. The return to the resting state is accompanied by oxidation of methionine residues on the surface of the protein adjacent to the buried five-coordinate heme center [113].

Recently, the mechanism by which *bis*-Fe(IV) MauG returns to the resting state has been studied kinetically [135]. It was shown through UV-Visible spectroscopy that MauG returns from its high-valent, *bis*-Fe(IV) state to its resting, di-ferric state via multiple intermediates: one at pH 7.4 and two at pH 9.0 [136]. As displayed in Figure 6.1, the first intermediate is proposed to be a protonated *bis*-Fe(IV) species, termed compound I-like. Intermediate I is only observed at basic pH values. The second intermediate, Intermediate II, is much longer lived and was proposed to be a single-electron reduced, mixed-valent species, termed compound II-like (i.e., an oxoferryl heme), with a one-electron oxidized methionine cation radical. A second electron transfer from methionine and proton from solvent to Intermediate II would then produce di-ferric

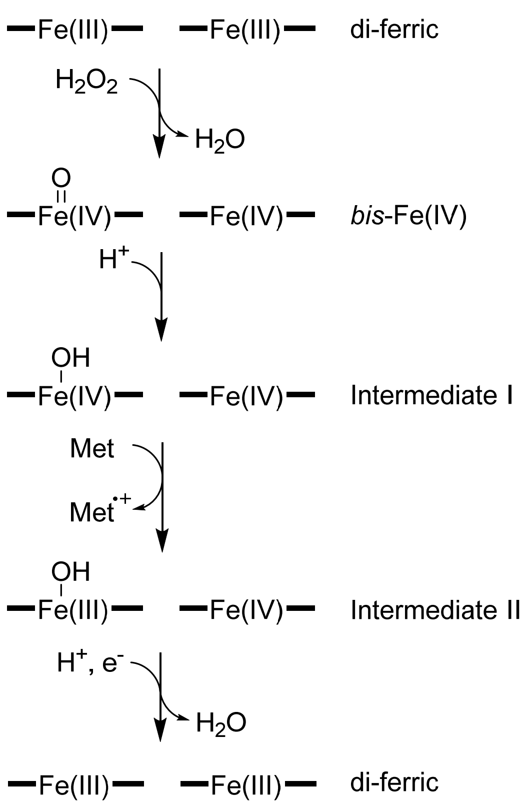

Figure 6.1 Various oxidation states of MauG.

MauG with an oxidized methionine residue. Protein-based radicals, particularly on tyrosine, tryptophan, and glycine residues, have been implicated in a large number of catalytic and electron transfer reactions in biology [137], including the long-range electron transfer reactions required for photosynthesis [138], respiration [139], and DNA synthesis [140] and repair [141]. Methionine oxidation by reactive oxygen species (ROS) and relevance to Alzheimer's disease has been proposed [142]. One electron chemical oxidation, irradiation, or photoreaction oxidation of free methionine amino acid or methionine residues in peptides has been studied computationally and experimentally [143-148]. Thus, it is highly significant to investigate the hypothesized methionine cation radical in MauG. In this work, we investigate the possibility of protein-based methionine radical involvement in the return of *bis*-Fe(IV) to di-ferric MauG.

6.3 Materials and Methods

6.3.1 Chemicals

5,5-Dimethyl-1-pyrroline N-oxide (DMPO) was purchased from Cayman Chemical (Ann Arbor, MI, USA). All other chemicals, including nitrosobenzene, were purchased from Sigma Aldrich (St. Louis, MO, USA) at the highest available grade.

6.3.2 Preparation of MauG

MauG was prepared as described previously [95, 102, 106-107, 112, 149]. Briefly, *P. denitrificans* cells carrying a plasmid for expression of MauG were grown in mineral salts medium at 30 ºC in 4 stages: 10 ml, 100 ml, 1 L, and 10 L. Tetracycline at 2 μg/mL was used for antibiotic selection. Cells were harvested by centrifugation, resuspended in phosphate buffer, and MauG was released from the periplasm by osmotic shock. Cell lysate was clarified by centrifugation, and the supernatant was collected. The His_6-tagged MauG was purified by nickel affinity chromatography, desalted to remove excess imidazole, and concentrated by ultrafiltration as described previously [95, 106, 149]. All reactions were carried out in 50 mM potassium phosphate buffered to pH 9.0 for optimized intermediate production.

6.3.3 UV-Visible Spectroscopy

The kinetics of the decay of *bis*-Fe(IV) MauG was measured with an Agilent 8453 spectrophotometer (Santa Clara, CA, USA). MauG and H_2O_2 were mixed to a final concentration of 5 μM each, and the return to the ground state was monitored in the absence and presence of DMPO (500 μM) from a fresh stock solution prepared under dark. As a precaution, the stock solution was subjected to multiple vacuum-argon cycles to remove potential trace amount of nitric oxide ($NO^•$) from decayed spin trap but otherwise used without further purification.

6.3.4 Electron Paramagnetic Resonance (EPR) Spectroscopy

Room-temperature, continuous-wave EPR spectra were collected in a quartz flat cell with a Bruker (Billerica, MA, USA) E560 spectrometer and Superhigh-Q (SHQE)-W resonator at 9.74 GHz, 100 kHz modulation frequency, 0.1 or 0.3 mT modulation amplitude, and 31.7 mW microwave power. Time courses were measured with 20 s per scan over a 10 mT sweep width at the $g = 2$ region.

6.3.5 High-Performance Liquid Chromatography (HPLC) and High-Resolution Mass Spectrometry

Chromatographic separation was performed with a Dionex UltiMate 3000 HPLC equipped with a diode array detector (Sunnyvale, CA, USA). The reaction mixture from the spin-trapping EPR experiment was applied to a C18 column and separation was achieved with a linear gradient of 100% solvent A (94.9% H_2O, 5% acetonitrile, and 0.1% trifluoroacetic acid) to 85% solvent A, 15% solvent B (94.9% acetonitrile, 5% H_2O, and 0.1% trifluoroacetic acid) over 7.5 min at 1.2 mL/min. Fractions were collected, and mass spectra were obtained on a maXis plus quadrupole-time of flight mass spectrometer equipped with an electrospray ionization source (Bruker Daltonics) operated in the positive ionization mode. Samples were introduced via syringe pump at a constant flow rate of 3 μL/min. Source parameters are summarized as follows: capillary voltage, 3500 V; nebulizer gas pressure, 0.4 bar; dry gas flow rate, 4.0 L/min; source temperature, 200 °C. Mass spectra were averages of one minute of scans collected at a rate of 1 scan per second in the range $50 \leq m/z \leq 1500$. Compass Data Analysis software version 4.3 (Bruker Daltonics) was used to process all mass spectra.

6.4 Results

6.4.1 EPR Measurement of the Relaxation of bis-Fe(IV) MauG

It was previously reported that at pH 9.0, the return to the resting state from *bis*-Fe(IV) requires more than 25 min and proceeds via two intermediates, the latter of which was proposed to be a methionine radical which maximizes at ~5 min after the formation of the high-valent species [136]. In order to investigate whether or not the auto-reduction of *bis*-Fe(IV) MauG involves a long-lived protein radical intermediate, the high-valent state of MauG (50 μM) was prepared by mixing with an equimolar amount of H_2O_2. The solution containing the *bis*-Fe(IV) MauG was then transferred to a quartz flat-cell, and the EPR spectrum at the $g = 2$ region was repeatedly scanned 30 times over 10 mins with 83 s having elapsed from the mixing of MauG with H_2O_2 and the beginning of the first scan. All scans are indistinguishable and contain only noise (data not shown). Since Intermediate I is expected to maximize at ca. 100 s and Intermediate II at 300 s, the absence of an EPR signal during the return of MauG from its high-valent to its resting state suggests that a stable protein radical is not involved.

6.4.2 Radical Trapping with DMPO

While the experiment described in 6.4.1 above does not support the presence of a long-lived radical species during the conversion of *bis*-Fe(IV) MauG to the di-ferric state in the absence of substrate, it does not exclude the possibility of a transient, reactive radical being formed in the process. To test the possibility of a transient radical species being formed during the relaxation of *bis*-Fe(IV) MauG, the high-valent species of MauG (150 μM) was prepared by mixing with an equimolar amount of H_2O_2 and then mixed with DMPO (1.5 mM) before repeated EPR measurements with a dead time of 85 s between addition of the oxidant and the start of the first scan. Inclusion of DMPO during the relaxation process produces a 7-line EPR

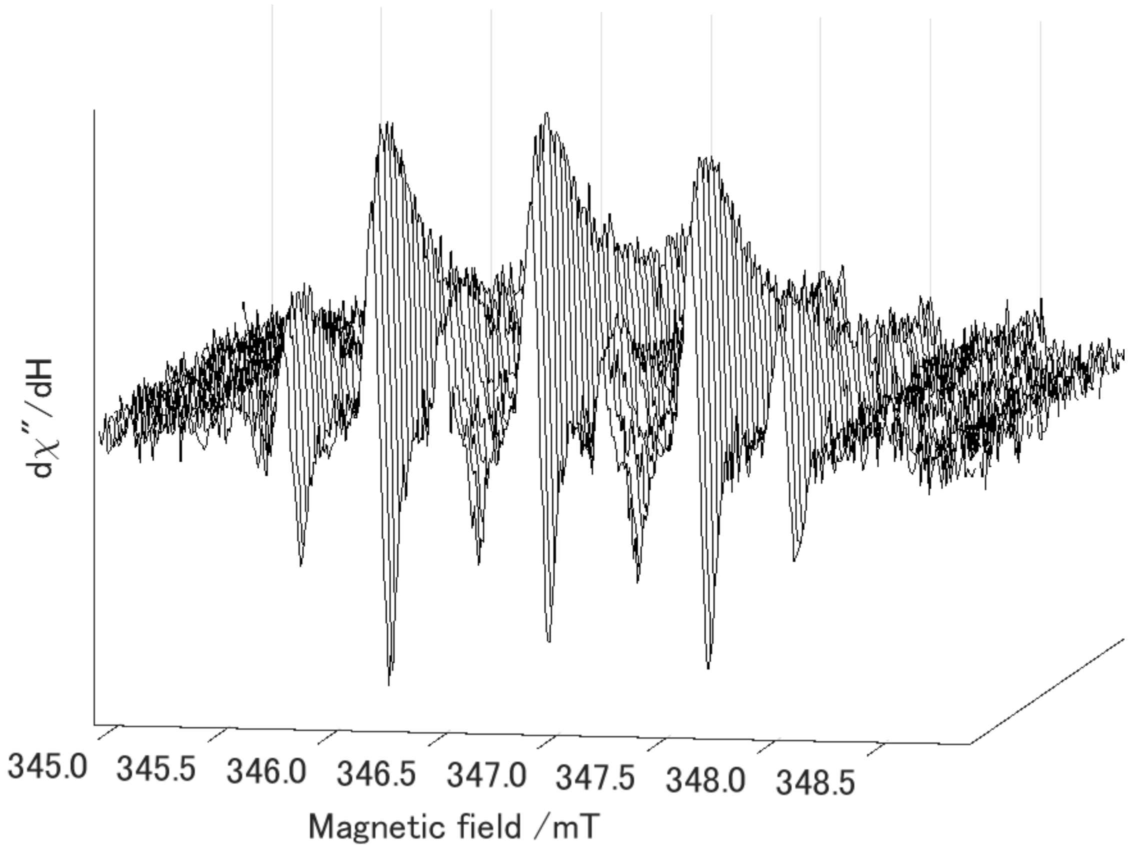

Figure 6.2 Time-resolved EPR spectra of *bis*-Fe(IV) MauG with DMPO. MauG (150 μM) was mixed with an equimolar concentration of H_2O_2 before adding DMPO (1.5 mM) and transferring the reaction mixture to a quartz flat cell. The first scan began 85 s after initial mixing, and a subsequent scan was recorded every ca. 23 s. The spectra were recorded at room temperature, 9.74 GHz, 31.7 mW microwave power, 100 kHz modulation frequency, 0.1 mT modulation amplitude, 10 mT sweep width, 20 s sweep time.

signal (Figure 6.2) which maximizes at ca. 160 s after mixing and then slowly decays. At the experimental pH of 9.0, MauG returns to the resting state via two intermediates. The appearance and decay of the transient EPR signal follows closely the first, Compound I-like, intermediate identified by UV-Vis spectroscopy [136]. To eliminate the second, Compound II-like, intermediate as the source of the EPR signal, a parallel experiment was performed in which the DMPO was added 300 s after the formation of *bis*-Fe(IV) MauG, at which point Intermediate I should be nearly gone and Intermediate II should be maximized. Samples made in this way show only a trace NO signal which is also seen in control samples of DMPO alone (Figure 6.3A, top).

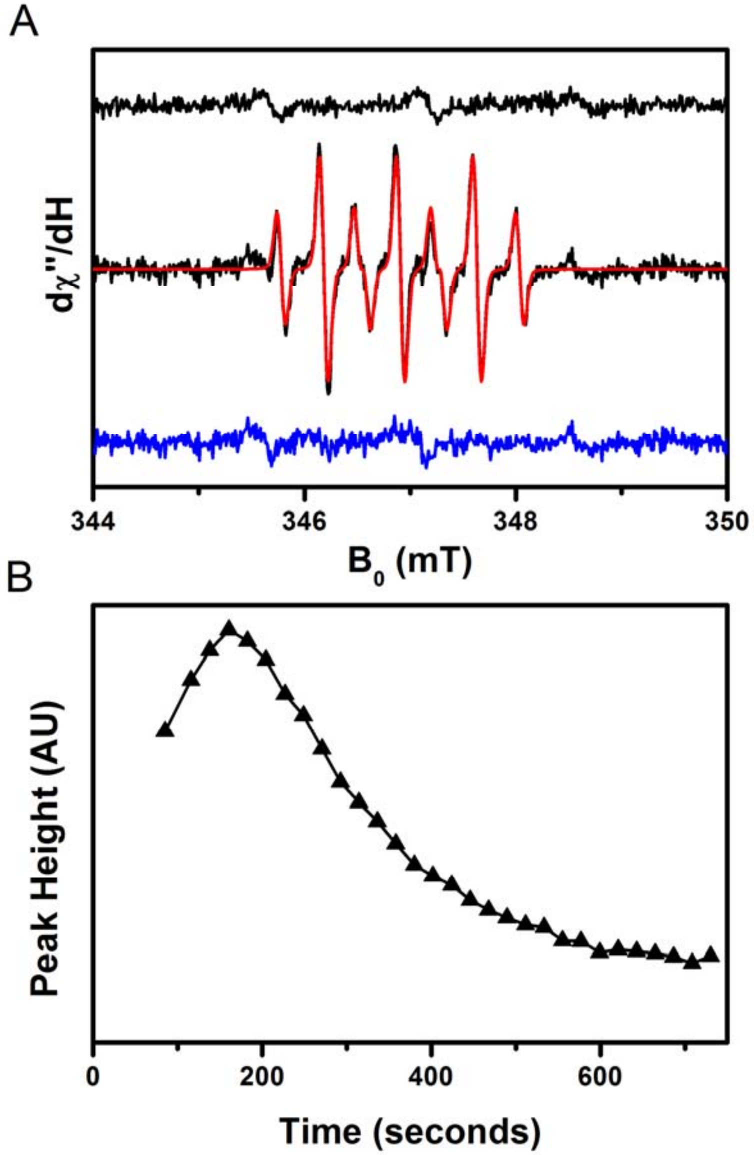

Figure 6.3 Identification of a transient radical species.(A) EPR spectrum of DMPO alone (top), the transient radical (middle, black), spectral simulation (middle, red), and residual from fitting, bottom, blue; (B) Peak-to-trough height for the radical species over time. Spectrometer conditions are the same as in Figure 6.2.

6.4.3 Identification of the Transient Radical

The radical species observed can be simulated with a single component centered at g = 2.0068 with hyper-fine interactions from one nitrogen nucleus, A_N = 20.0 MHz, and 2 equivalent protons, A_H = 11.0 MHz (Figure 6.3A, middle) with a residual (Figure 6.3A, bottom) which is indistinguishable from the control, DMPO only (Figure 6.3A, top). The signals grow in and maximize at ~160 s, as seen in Figure 6.3B. These observations are inconsistent with a radical trapped by DMPO and are instead indicative of a radical of an oxidized DMPO product termed 5,5-dimethyl-2-oxo-pyrroline-1-oxyl (DMPOX) [150-153]. The presence of a DMPOX radical is further confirmed by performing chromatographic separation of the reaction mixture (Figure 6.4A) and analyzing the major fractions by high-resolution mass spectrometry. The second largest peak of the chromatogram has an absorbance maximum at 266 nm (Figure 6.4B) and shows one major ion by mass spectrometry which corresponds to a protonated DMPOX, 1-hydroxy-5,5-dimethylpyrrolidin-2-one (DMPOXH) within 3.07 ppm mass accuracy (Figure 6.4C).

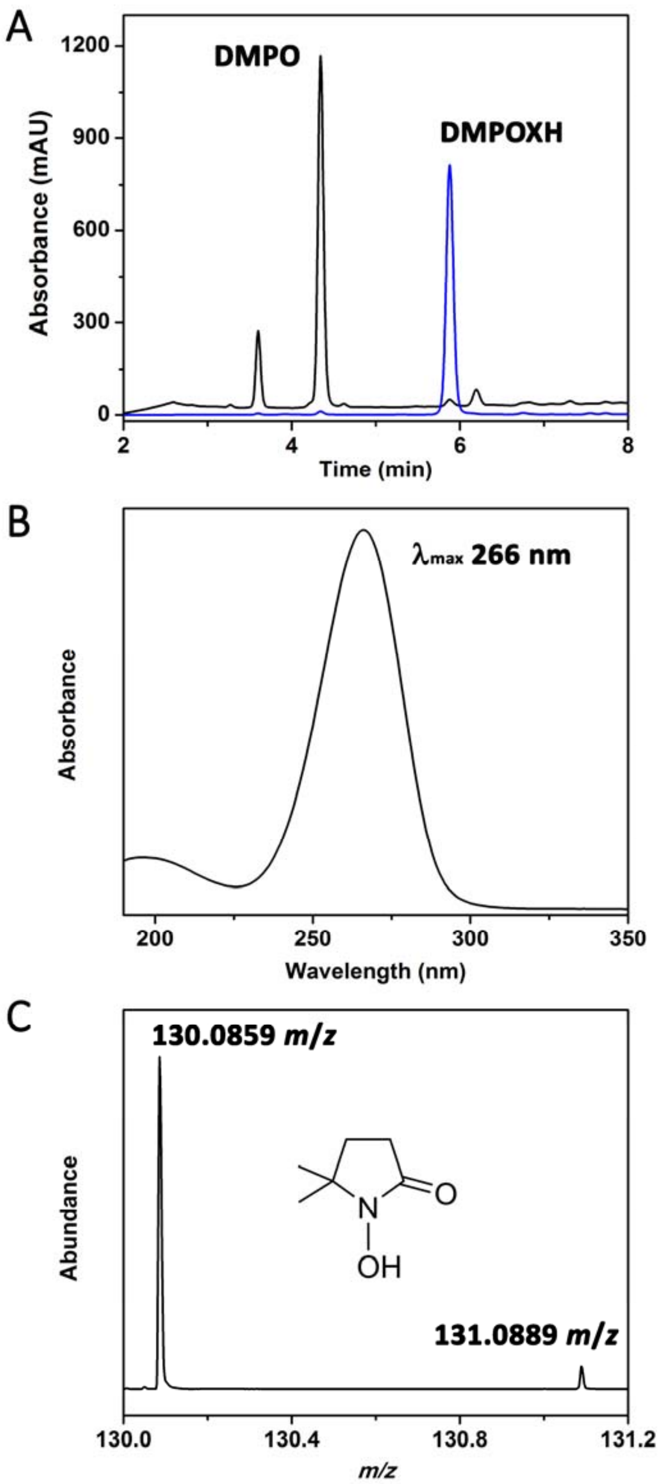

Figure 6.4 Characterization of the transient radical species.(A) HPLC chromatogram of the reaction mixture at 227 nm, black, and 266 nm, blue; (B) UV-Vis spectrum of the DMPOXH extracted from the chromatogram in A; (C) high-resolution mass spectrum of the peak corresponding to DMPOXH collected in positive ion mode.

6.4.4 Radical Trapping with Nitrosobenzene

Since the nitrone-based radical trap, DMPO, acts as a substrate for MauG, generating a DMPOX radical, we employed other spin traps in our attempts to trap the proposed methionine radical. Figure 6.5 shows the EPR results with nitrosobenzene (NB) as an alternative spin trap. As can be seen in Figure 6.5, top two traces, respectively, di-ferric MauG and di-ferric MauG mixed with NB show no major resonances at room temperature. However, if NB is added after the formation of *bis*-Fe(IV), a new asymmetric radical species can be observed (Figure 6.5, 3rd trace). The spectrum can be simulated (blue) with a somewhat rhombic *g*-tensor, 2.00798, 2.00650, 2.00349, and a very anisotropic hyperfine coupling to one nitrogen atom, A_N 0.35, 22.2, 75.2 MHz, and 0.887 mT Gaussian line broadening. To determine whether the radical is localized on the protein or in solution, the sample was filtered with a 10 kDa cut-off centrifugal filter (MauG MW is 42 kDa) to separate the flow-through (Figure 6.5, 4th trace) and retained protein (Figure 6.5, 5th trace); the measurement was initiated 50 min after initial radical formation. Virtually no signal can be seen in the filtrate, and the retained protein shows approximately one-quarter of the initial intensity after re-dilution to the starting volume, though there is slightly less splitting in the low-field g-component. Thus, we conclude that the EPR signal is a protein-based radical. An additional experiment was performed in which NB was added 300 s after formation of *bis*-Fe(IV) MauG to assess the ability of Intermediate II to form an adduct (Figure 6.5, bottom trace). The delayed addition of NB leads to accumulation of less than 10% compared to direct addition, indicating that *bis*-Fe(IV) and Intermediate I are the most likely candidates for trapping with NB.

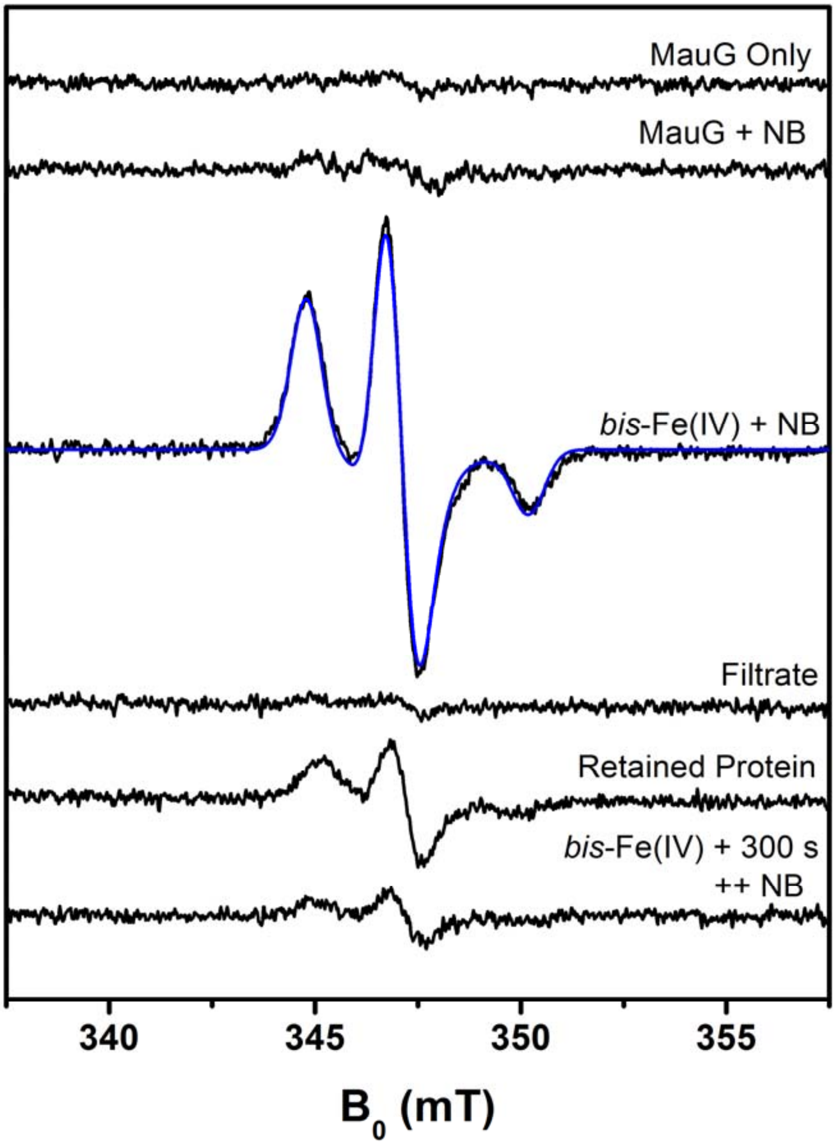

Figure 6.5 EPR of Radical Trapping with MauG and Nitrosobenzene. From top to bottom, rt EPR spectra of MauG (50 µM), MauG mixed with NB (1 mM), a radical trapped by nitrosobenzene after mixing with *bis*-Fe(IV) MauG (black) and simulated spectrum (blue). The sample was then filtered by a 10 kDa spin filter. The next spectrum is the flow-through, followed by the filtered protein. The final spectrum contained *bis*-Fe(IV) aged for 300 s before addition of NB. Spectra were recorded at room temperature, 9.74 GHz, 31.7 mW microwave power, 100 kHz modulation frequency, 0.3 mT modulation amplitude, 30 mT sweep width, 80 s sweep time, average of 4 scans.

6.4.5 Effect of Spin Traps on the Kinetics of the Return to Resting State

The decay of *bis*-Fe(IV) MauG was observed by UV-Visible spectroscopy alone and in the presence of nitrosobenzene and DMPO (Figure 6.6 black, blue, and red, respectively). With MauG alone, the decay of the charge resonance band requires two summed exponential functions with rate constants of 0.83 ± 0.17 and 0.2 ± 0.04 min^{-1}, respectively. Addition of either spin trap immediately after the formation of *bis*-Fe(IV) resulted in a much faster return to the ground state. Additionally, while the data which includes spin traps show significant residuals from fitting with a single exponential, fits with a double exponential equation do not converge and all parameters show complete dependency. The estimated rates with the inclusion of nitrosobenzene and DMPO are 0.94 ± 0.20 and 2.8 ± 0.5 min^{-1}, respectively. These results are consistent with high-valence forms of MauG being able to readily react with nitrosobenzene and DMPO.

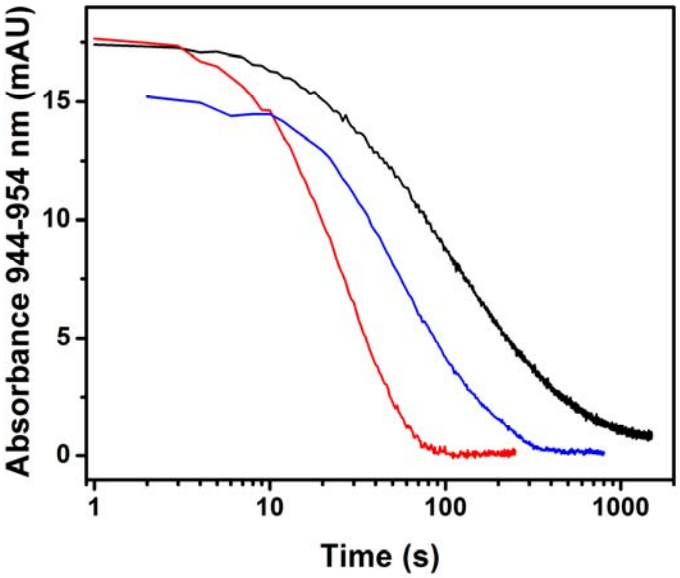

Figure 6.6 Kinetics of the Decay of the Charge Resonance Band of MauG. Representative time courses of the disappearance of the charge resonance band of *bis*-Fe(IV) disappearing as MauG returns to the resting, di-ferric state, black; the effect of nitrosobenzene, blue; and the effect of DMPO on the return to the resting state, red. Absorbance was averaged over 944 – 954 nm to improve signal-to-noise ratio.

6.5 Discussion

Methionine residues are known to play a role in proteins as a sacrificial reductant to protect other, functionally important, residues from oxidative damage [154]. This appears to be the case in MauG, as it has three methionine residues on its surface which be-come oxidized as MauG redox cycles without the presence of its substrate [113]. The observation of two intermediates in the auto-reduction of *bis*-Fe(IV) MauG by UV-Vis spectroscopy makes MauG a promising candidate for the characterization or capture of a methionine radical in a protein. Previously characterized methionine radicals were generated photochemically with free amino acids, leaving an open question as to how a protein environment might affect a methionine radical [148, 155]. We sought to characterize or capture any possible radical species formed during the return of *bis*-Fe(IV) MauG to the resting state. Following the return to the di-ferric state by EPR spectroscopy did not produce any signals which could be attributed to a protein-based radical. We then attempted to trap any potential transient radical species with DMPO and NB. With DMPO, rather than trapping a protein-based radical, we observed that either *bis*-Fe(IV) MauG or Intermediate I is able to directly oxidize the spin trap to a DMPOX radical. We then attempted to trap a radical from Intermediate II by adding the trapping agent 300 s into the decay process, when Intermediate I should be nearly fully converted to Intermediate II. Delaying the addition of DMPO is able to remove the oxidation issue; however, no trapped radical species were observed. Furthermore, the rates of return from the *bis*-Fe(IV) to di-ferric state, as monitored by UV-Visible spectroscopy, were increased over 3-fold by the addition of DMPO. The radical observed during the relaxation of *bis*-Fe(IV) MauG in the presence of DMPO does not agree with any published DMPO trapped radicals [153]. Rather, the radical arises from direct oxidation of DMPO to a so-called DMPOX species. The first published spectrum of the DMPOX radical arose in the attempt to trap a radical in the reaction of hematin with cumene hydroperoxide [151]. The assignment was made by comparison with a previously synthesized and characterized compound whose hyperfine coupling constants were reported in various solvents excluding any aqueous solutions [150]. Several similar compounds give rise to EPR signals with comparable coupling patterns and constants [156]. The rigorous assignment of the structure of the DMPOX radical was made later by direct synthesis and oxidation of DMPOX and measuring its EPR spectrum in various water/methanol mixtures [152]. It is also possible to produce the DMPOX radical from DMPO and singlet oxygen [157]. Even though DMPO is unable to trap any radicals within this system, NB is capable of rapidly forming an adduct with *bis*-Fe(IV) MauG or Intermediate I. The trapped radical is dissimilar to most radicals trapped with NB as it displays *g*-anisotropy at room temperature and only shows hyperfine coupling to a single nitrogen atom with extreme anisotropy, indicating that the *g*- and *A*-tensors may not coincide. A very similar species has been observed at liquid-nitrogen temperatures in an inorganic system [158], however their room temperature measurements are more similar to typical NB-trapped radicals with several coupled protons. Another study with a similarly-shaped radical signal at room temperature claimed to have used 2-methyl-2-nitrosopropane to trap a tyrosyl radical on cytochrome *c* [159]. The rapidness of the reaction between *bis*-Fe(IV) and NB indicates that the adduct is formed with *bis*-Fe(IV) or Intermediate I, both of which still carry two oxidizing equivalents. The absence of significant trapping at the later time suggests that NB is able to trap a radical on the tryptophan 199 of MauG which is responsible for passing oxidizing equivalents to its substrate protein.

6.6 Conclusion

In summary, though the reactive species of MauG returns to its resting state with two distinct intermediates, neither contains a long-lived protein radical. Furthermore, no radical adduct was able to be trapped by incubation of DMPO with *bis*-Fe(IV) MauG at various time points. Instead, the first intermediate is able to oxidize DMPO to produce a DMPOX radical while returning to its resting, diferric state. Conversely, NB is able to trap a radical with *bis*-Fe(IV) or Intermediate I MauG to form a long-lived radical with unusual spectral characteristics.

7 HIGH-FREQUENCY/HIGH-FIELD ELECTRON PARAMAGNETIC RESONANCE AND THEORHETICAL STUDIES OF TRYPTOPHAN-BASED RADICALS

This chapter is adapted from the published work co-first authored by ID: Davis I, Koto T, Terrell JR, Kozhanov A, Krzystek J, and Liu A (2018) High-Frequency/High-Field Electron Paramagnetic Resonance and Theoretical Studies of Tryptophan-Based Radicals. *Journal of Physical Chemistry A*, 122(12), 3170 – 3176. DOI: 10.1021/acs.jpca.7b12434

7.1 Abstract

Tryptophan-based free radicals have been implicated in a myriad of catalytic and electron transfer reactions in biology. However, very few of them have been trapped so that biophysical characterizations can be performed in a high-precision context. In this work, tryptophan derivative-based radicals were studied by high-frequency/high-field electron paramagnetic resonance (HFEPR) and quantum chemical calculations. Radicals were generated at liquid nitrogen temperature with a photocatalyst, sacrificial oxidant, and violet laser. The precise g-anisotropies of L- and D-tryptophan, 5-hydroxytryptophan, 5-methoxytryptophan, 5-fluorotryptophan, and 7-hydroxytryptophan were measured directly by HFEPR. Quantum chemical calculations were conducted to predict both neutral and cationic radical spectra for comparison with the experimental data. The results indicate that under the experimental conditions, all radicals formed were cationic. Spin densities of the radicals were also calculated. The various line patterns and g-anisotropies observed by HFEPR can be understood in terms of spin-density populations and the positioning of oxygen atom substitution on the tryptophan ring. The results are considered in the light of the tryptophan and 7-hydroxytryptophan diradical found in the biosynthesis of the tryptophan tryptophylquinone cofactor of methylamine dehydrogenase.

7.2 Introduction

The essential amino acid tryptophan is used both as a building block for proteins and as a precursor of various bioactive compounds. In mammals, tryptophan not utilized for protein synthesis is catabolized by two major pathways: kynurenine and serotonin biosynthesis. In the brain, tryptophan is transformed to serotonin and then melatonin, two molecules involved in mood and sleep, respectively [160-161]. In other tissues, mostly liver, the kynurenine pathway is capable of transforming tryptophan to alanine and acetoacetate via glutaryl–coenzyme A for energy production. The kynurenine pathway also produces several neuroactive side products, one of which is the precursor for nicotinamide adenine dinucleotide biosynthesis [11, 80, 162-163].

As a protein building block, tryptophan is used for structural roles [164] and electron transport [138, 165] and is occasionally modified to serve as a cofactor for various enzymes [103, 166]. Tryptophan also plays important redox roles in biology. Tryptophan-based free radicals have been found in cytochrome *c* peroxidase [167], *Bulkholderia pseudomallei* catalase-peroxidase [168], lignin peroxidase [169], versatile peroxidase [170], and mutagenic or modified forms of azurin and ribonucleotide reductase [171-174]. One notable example of tryptophan being used as radical intermediates for synthesis of an enzyme cofactor is in methylamine dehydrogenase (MADH). The active site of MADH contains a tryptophan tryptophylquinone (TTQ) cofactor consisting of two cross-linked tryptophan residues, one of which has been hydroxylated at the 6 and 7 positions and oxidized to the corresponding quinone [103]. The TTQ cofactor is generated from a precursor protein, preMADH, which contains no cross-link and only one hydroxylation at the 7-position, as shown in Figure 7.1, by the diheme enzyme MauG [102]. MauG is able to redox cycle between its resting di-ferric and a high-valent *bis*-Fe(IV) species, which carries two oxidizing equivalents [107]. The *bis*-Fe(IV) state of MauG has been shown to be able to oxidize preMADH, generating two distinct radicals reported as a tryptophan and a 7-hydroxytryptophan radical that undergo spontaneous radical recombination and deprotonation to form the cross-link necessary for TTQ formation [106]. The two radicals observed in preMADH upon oxidation by *bis*-Fe(IV) MauG display g-anisotropy intermediate between other measured tryptophan and tyrosine radicals [139].

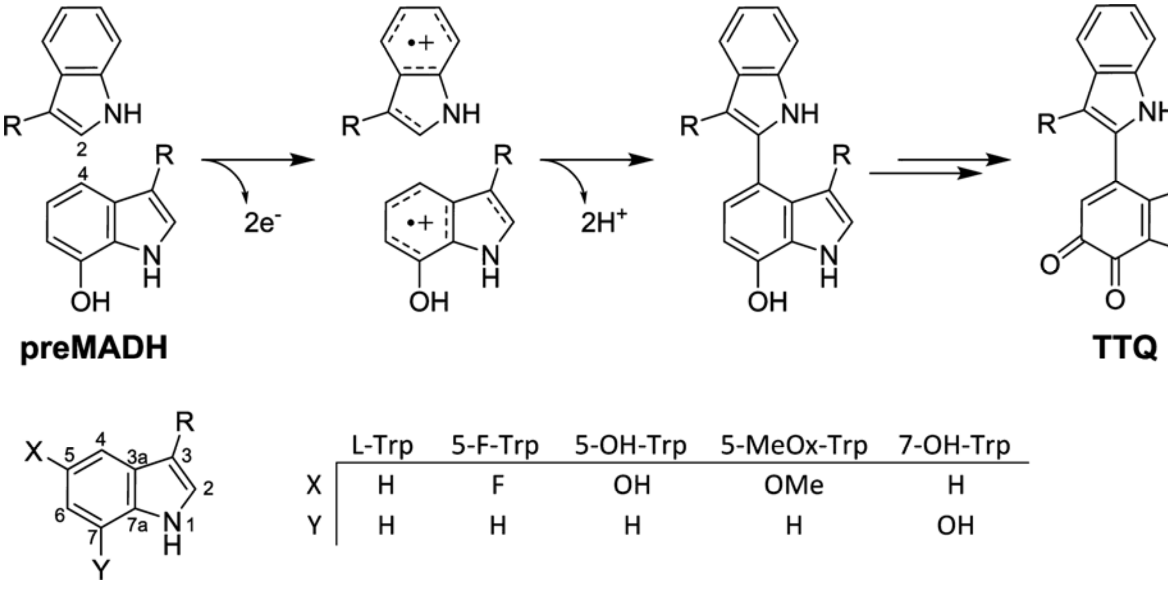

	L-Trp	5-F-Trp	5-OH-Trp	5-MeOx-Trp	7-OH-Trp
X	H	F	OH	OMe	H
Y	H	H	H	H	OH

Figure 7.1 Crosslink Formation in preMADH during TTQ Biosynthesis and Compounds under Investigation in This Study

In the initial EPR characterization of the intermediate formed upon reaction of preMADH with *bis*-Fe(IV) MauG, stoichiometry and spin quantitation indicated that two radicals were formed on preMADH concomitant with the reduction of MauG to its resting di-ferric state. EPR spectra of the preMADH-based intermediate measured at X-band (9 GHz) were unable to determine whether the signals arose from multiple similar species or multiple equivalents of a single species. Therefore, high-frequency/high-field (HFEPR) studies with a 15 T magnet were pursued [106]. Measurements of the preMADH-based radical at 416 GHz revealed two sets of overlapping signals with differing g-anisotropies. On the basis of the *g*-anisotropies Δg ($g_z - g_x$), overall reaction, and crystal structure of preMADH and MADH, the two radical species were assigned to the tryptophan and 7-hydroxytryptophan (7-OH-Trp) which are cross-linked during TTQ biosynthesis, with the latter assigned to the signal with larger *g*-value anisotropy.(22)

If the two radicals observed in the preMADH-based intermediate are indeed the residues involved in forming the cross-linked TTQ cofactor, the close proximity of these two residues (ca. 3 Å from edge to edge) raises an immediate question as to why no through-space coupling interactions are observed in the EPR spectra. Two radical species at such a distance would be expected to interact with each other. In the case of weak exchange, an exchange-coupling interaction would be expected to produce a much broader signal. But line broadening was not observed from the preMADH diradical EPR spectrum. Strong interactions such as antiferromagnetic coupling would lead to an EPR silent species, whereas ferromagnetic coupling would produce an integer spin system with resonances appearing in different locations due to zero-field splitting contributions [175].

One potential explanation for the lack of coupling may be that the close proximity of two cation radicals enforced by the protein scaffold in preMADH may perturb the spin density distributions of the radicals or cause electrostatic repulsion. An additional complication to interpreting the previous findings is that no other 7-OH-Trp radical has been previously characterized by EPR spectroscopy, so it is impossible to know what features observed in the diradical intermediate are intrinsic to the 7-OH-Trp and how those features may be perturbed in the context of a diradical species. The closest example is a UV–vis absorbance study of the 7-hydroxyindole radical [176]. Therefore, there is a need to analyze HFEPR spectra of isolated tryptophan and 7-OH-Trp to provide insight into the contributions made by the close proximity of two cation radicals and the protein scaffold on the radical spectra.

In this work, we adapted a recently developed rhenium/ruthenium-based photocatalyst to generate organic radicals [177]. This novel method has been successfully used in the transient kinetics study of tyrosyl radicals in solution. Here, we extended this approach to spectroscopically characterize tryptophan radicals in solid state at cryogenic temperatures. The resulting tryptophan and various tryptophan derivative-based radicals are amenable to characterization by HFEPR. The results are interpreted with quantum chemical calculations to clarify the effects of substituents on the *g*-anisotropy of tryptophan-based radicals.

7.3 Materials and Methods

7.3.1 Chemicals

All chemicals, including the Ru(III) complex, were purchased from Sigma-Aldrich in their highest available purity and were used without further purification with the exception of 7-hydroxytryptophan which was purchased from Ryan Scientific Inc.

7.3.2 Synthesis of Photocatalyst

Tricarbonyl(1,10-phenanthroline)(4-hydroxymethylpyridyl)rhenium(I) hexafluorophosphate, $[Re(phen)(CO)_3(PyCH_2OH)]PF_6$, was prepared by a literature method [177]. Briefly, $[Re(phen)(CO)_3(NCMe)]PF_6$ was dissolved in tetrahydrofuran with $PyCH_2OH$, and the mixture was heated under reflux for 18 h. The product was purified to analytically pure form by recrystallization after exchanging solvent to a minimal amount of DCM and slow addition of diethyl ether.

7.3.3 EPR Spectroscopy

Compounds under study were dissolved in 40% phosphoric acid with the rhenium photocatalyst and ruthenium sacrificial oxidant before being frozen in liquid nitrogen at 1, 1.5, and 5 mM, respectively. Frozen samples were irradiated at 77 K for 30 min with a 405 nm, 120 mW laser. Radical formation was verified by X-band (9 GHz) EPR spectroscopy, and the experimental conditions were optimized on the basis of the X-band EPR results. HFEPR samples were generated in sample cups of ca. 150 μL volume. HFEPR spectra were recorded at the EMR Facility at the National High Magnetic Field Laboratory in Tallahassee, FL. The 15-T magnet-based spectrometer has been described previously [178]. All spectra were acquired at 4.5 K, 406.4 GHz, and 0.3 mT modulation amplitude with the presence of an atomic hydrogen standard to calibrate the magnetic field [179]. A series of experiments was also performed on a 25 T resistive “Keck” magnet in the DC Facility at ~700 GHz [180]. HFEPR simulations of the experimental spectra were performed using the EPR simulation program DOUBLET [181].

7.3.4 Quantum Chemical Calculations

All calculations were implemented with the ORCA quantum chemistry program package (version 3.0.3) [182]. Full geometry optimizations were performed using the B3LYP hybrid functional with RIJCOSX approximation [183-184] in combination with the def2-TZVP(-f) basis set for all atoms with tight SCF convergence criteria for both cation and neutral radical forms of tryptophan and four substituted tryptophan derivatives: 7-hydroxytryptophan (7-OH-Trp), 5-hydroxytryptophan (5-OH-Trp), 5-methoxytryptophan (5-MeOx-Trp), and 5-fluorotryptophan (5-F-Trp). The basis sets used for geometry optimization were also used for *g*-tensor and spin population calculations. The calculations included consideration of solvent effects assuming the presence of a dielectric continuum with the conductor-like screening model (COSMO) [185] and the dielectric constant of water [186].

7.4 Results and Discussion

7.4.1 Solid-State, Photocatalytic Radical Generation

Tryptophan free radicals are short-lived, with an estimated $t_{1/2}$ of less than 1 ms in solution. To circumvent this issue, we adapted a recently developed photocatalyst method by Nocera et al., which has been used by others to generate tyrosyl radicals in solution for transient absorption spectroscopy [177], and optimized it for HFEPR studies. As illustrated in Figure 7.2, the radical species were generated with the use of a rhenium photocatalyst and ruthenium sacrificial oxidant. All compounds, L-Trp, D-Trp, 5-F-Trp, 5-MeOx-Trp, 5-OH-Trp, and 7-OH-Trp, were dissolved in 40% phosphoric acid, respectively, with photocatalyst and sacrificial

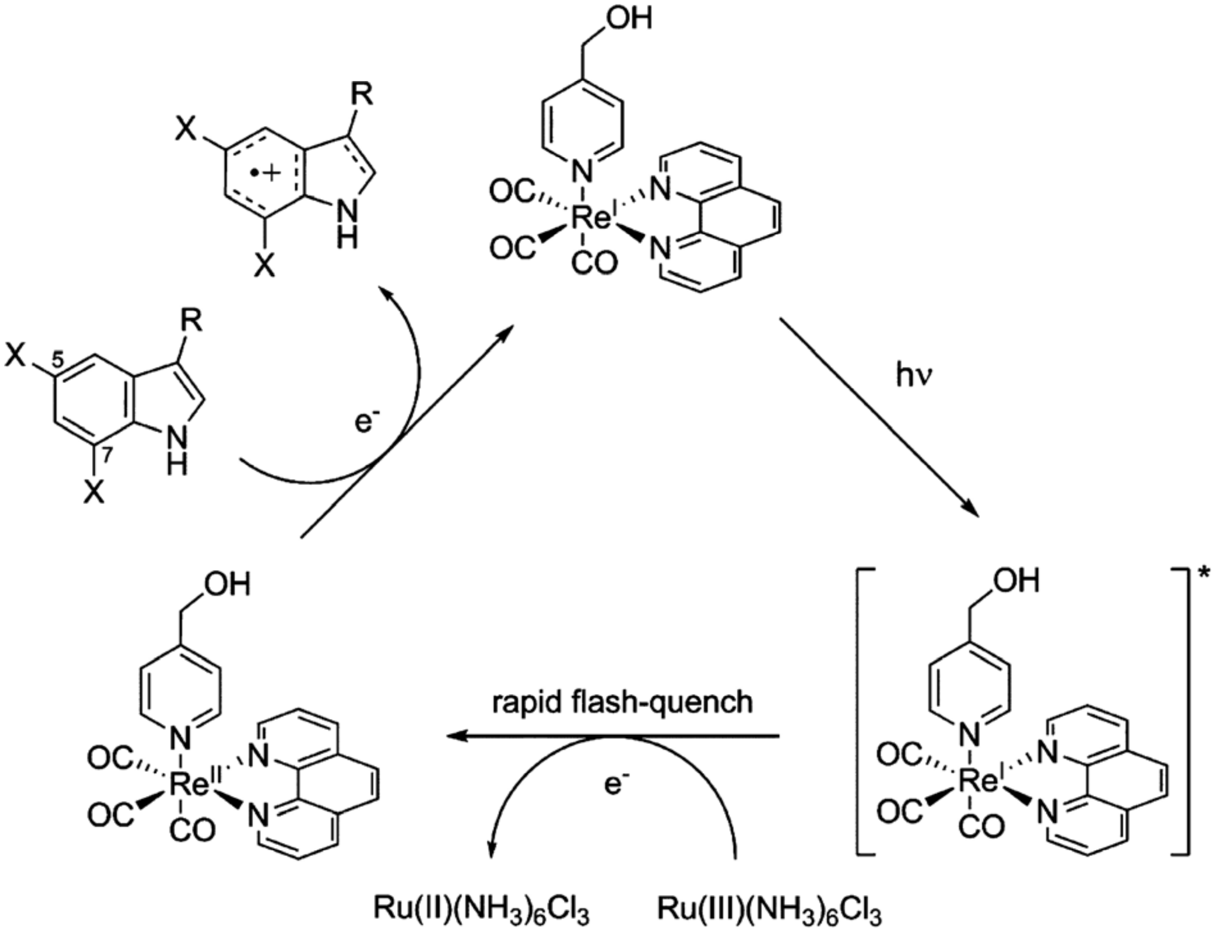

Figure 7.2 Photocatalytic method for generating tryptophan-based radicals

oxidant so that the frozen solutions would form a transparent glass, allowing facile photoexcitation of the rhenium catalyst at cryogenic temperatures. Solubility issues arose with other common glass-forming solvents [187]. The oxidation of tryptophan and several of its analogues, including 7-OH-Trp, were initiated by photoexcitation of the rhenium complex. The excited-state rhenium complex is then oxidized by the sacrificial ruthenium oxidant. The oxidized Re(II) species can in turn oxidize tryptophan or one of its analogues to its respective radical, presumably cation, species. Because the radical is formed at cryogenic temperatures, it is not rapidly quenched. Also, the photocatalytic method allows for the use of nonionizing violet light, which prevents the formation of solvated electrons or multiple undesirable radical species that might otherwise interfere with species of interest.

7.4.2 HFEPR Characterization

The radical forms of L-Trp, D-Trp, 5-F-Trp, 5-MeOx-Trp, 5-OH-Trp, and 7-OH-Trp were successfully generated by the photocatalytic method and subsequently analyzed by HFEPR spectroscopy after optimization of the experimental conditions. Exclusion of any of the elements, photocatalyst, sacrificial oxidant, indole derivative, or laser light gave rise to samples with no radical signals. Aside from D- and L-tryptophan, all other compounds studied were racemic mixtures. The presence of concentrated phosphoric acid, catalyst, or sacrificial oxidant resulted in significant absorption of the transmitted sub-THz wave power, which in turn limited the signal-to-noise ratio of the spectra. However, with sufficient averaging, the spectra were fully interpretable. Experiments at higher frequency/field (~700 GHz/25 T, respectively) were, however, unsuccessful. Due to increased power losses through the solvent at elevated sub-THz frequencies, the resulting spectra were not amenable to analysis due to very low S/N ratio, even with averaging.

Figure 7.3 shows the HFEPR spectra of tryptophan radicals generated by the photocatalytic method. Three distinct spectral patterns can be recognized for the experimental HFEPR spectra: axial with *g*-parallel larger than *g*-perpendicular for Trp and 5-F-Trp; axial with *g*-parallel smaller than *g*-perpendicular for 7-OH-Trp; and rhombic for 5-OH-Trp and 5-MeOx-Trp. Experimentally determined *g*-values and Δg are summarized in Table 7.1, and the full spectrum of each radical including the magnetic field standard [179] and simulation can be found in Figure 7.4–Figure 7.9. X-band EPR spectra of L-Trp, 5-OH-Trp, 5-MeOx-Trp, and 7-OH-Trp can be found in Figure 7.10–Figure 7.13. Spectra of L- and D-tryptophan both produce axial EPR spectra with slightly different principal *g*-values; however, they have very similar *g*-anisotropies (Δg, $g_{\mathrm{max}} - g_{\mathrm{min}}$) of 102×10^{-5} and 100×10^{-5}, respectively. Even at the magnetic fields used for this study (15 T), all the principal *g*-values of tryptophan cannot be fully resolved, and the radicals produce axial spectra with g_{min} and g_{mid} largely overlapping. Replacing hydrogen in the 5-position with a highly electronegative fluorine, 5-F-Trp, did not perturb the line shape; however, it did lead to a slight increase in the Δg to 110×10^{-5}.

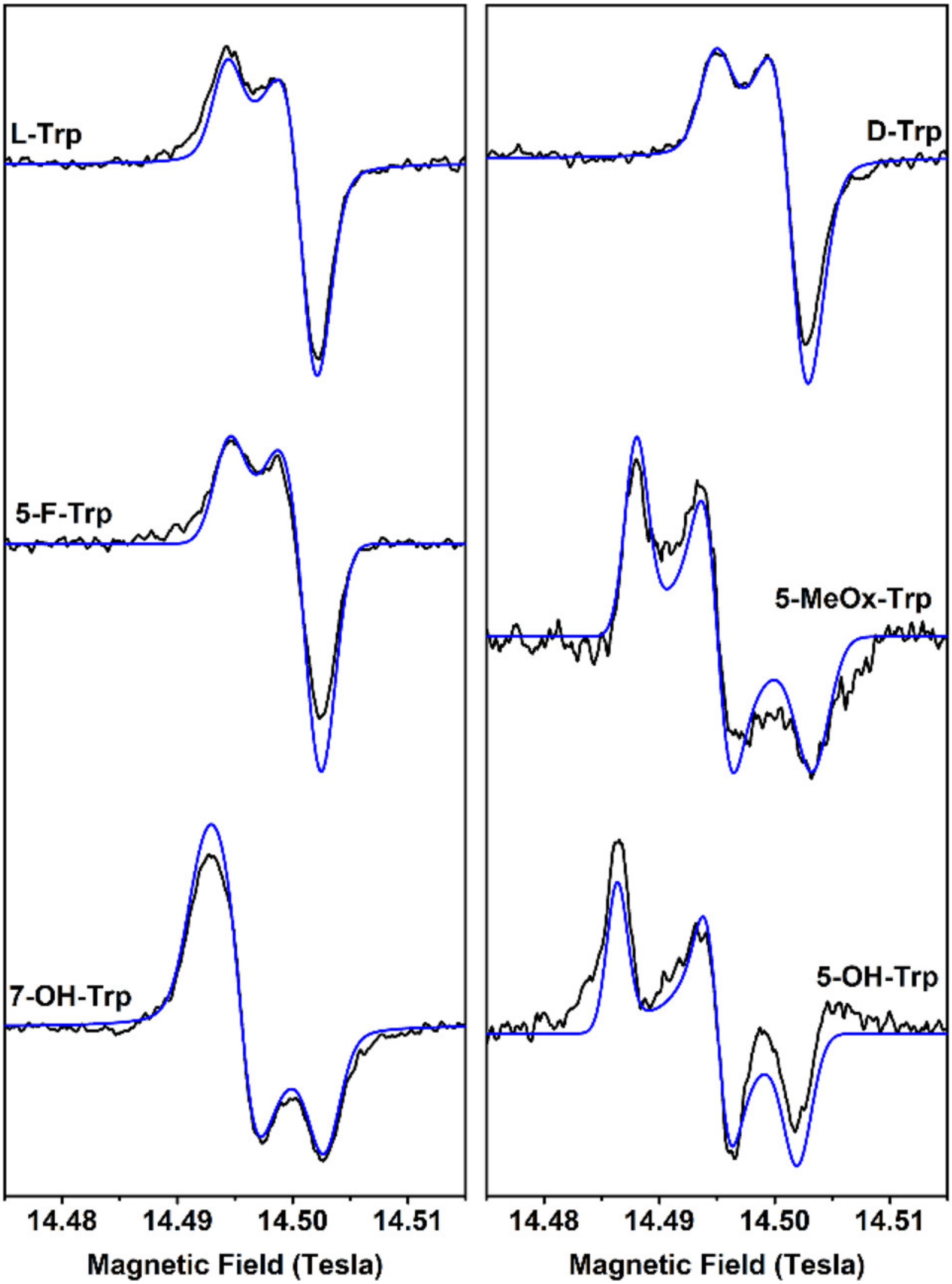

Figure 7.3 HFEPR spectra of tryptophan-based radicals. Spectra were measured with 406.4 GHz, 0.3 mT modulation amplitude, at 4.5 K (black trace) and corresponding simulated spectra (blue trace). Simulation parameters can be found in Table 7.1.

Table 7.1 Experimentally determined and calculated g-values for tryptophan derivatives

		g_{min}	g_{mid}	g_{max}	Span[a]	Span / L-Trp	Skew[b]
L-Trp	exp.	2.00227	2.00240	2.00329	102	-	0.873
	cation	2.00226	2.00255	2.00325	99	-	0.698
	neutral	2.00225	2.00288	2.00366	140	-	0.551
7-OH-Trp	exp.	2.00213	2.00313	2.00358	145	1.422	0.310
	cation	2.00225	2.00318	2.00360	135	1.361	0.312
	neutral	2.00225	2.00303	2.00407	183	1.300	0.574
5-OH-Trp	exp.	2.00223	2.00319	2.00439	216	2.118	0.556
	cation	2.00224	2.00321	2.00427	203	2.043	0.521
	neutral	2.00224	2.00322	2.00416	192	1.368	0.488
5-MeOx-Trp	exp.	2.00205	2.00319	2.00416	211	2.069	0.460
	cation	2.00223	2.00335	2.00442	219	2.213	0.491
	neutral	2.00225	2.00313	2.00451	226	1.608	0.608
5-F-Trp	exp.	2.00217	2.00244	2.00327	110	1.078	0.755
	cation	2.00227	2.00256	2.00322	95	0.959	0.695
	neutral	2.00227	2.00290	2.00375	148	1.052	0.575

[a] Span is Δg, the difference between g_{min} and g_{max} x 10^5.

[b] Skew is $(g_{max} - g_{mid}) / (g_{max} - g_{min})$

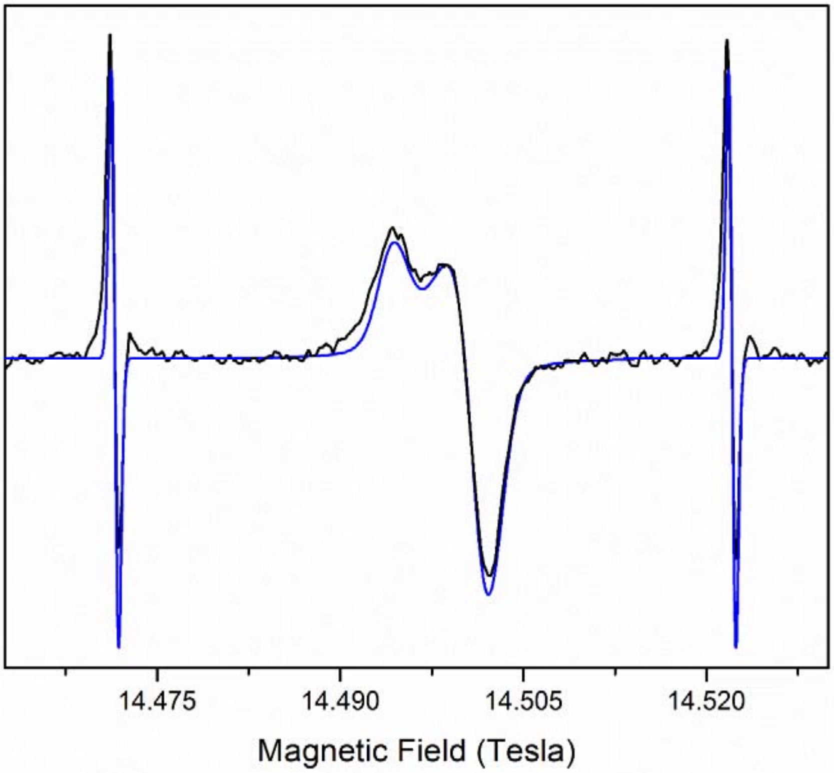

Figure 7.4 Full HFEPR spectrum of L-tryptophan radical and field standard. The spectrum is an average of 16 scans collected with 406.4 GHz, 0.3 mT modulation amplitude, at 4.5 K (black trace) and corresponding simulated spectrum (blue trace).

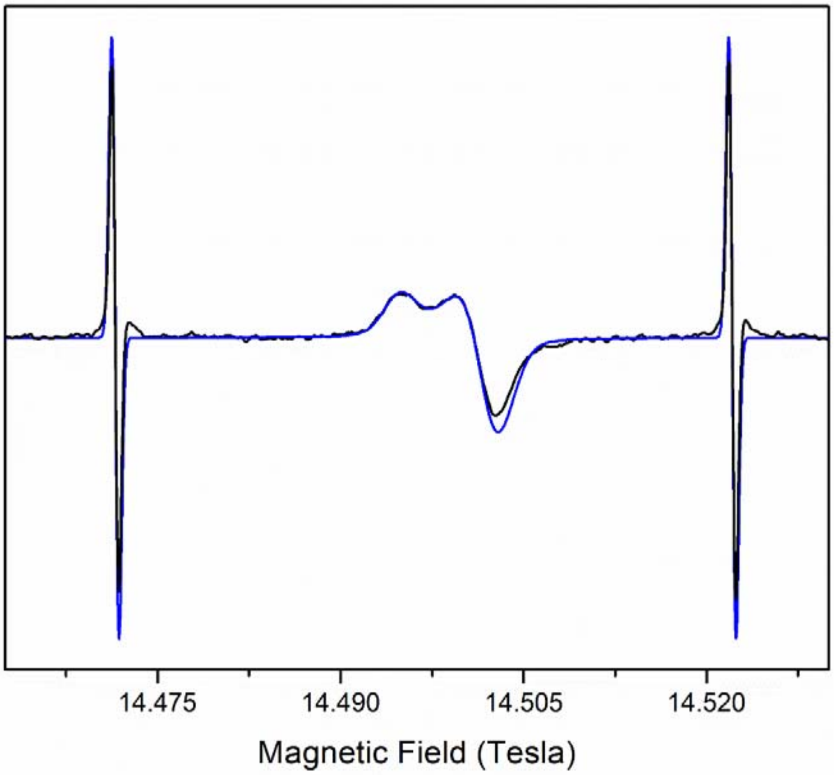

Figure 7.5 Full HFEPR spectrum of D-tryptophan radical and field standard. The spectrum is an average of 10 scans collected with 406.4 GHz, 0.3 mT modulation amplitude, at 4.5 K (black trace) and corresponding simulated spectrum (blue trace).

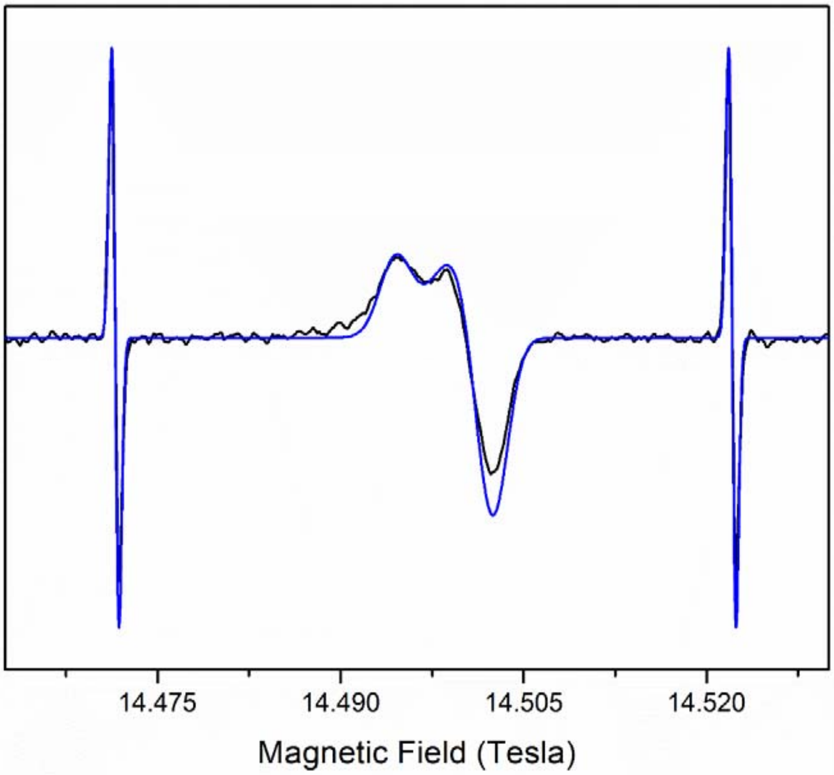

Figure 7.6 Full HFEPR spectrum of 5-fluorotryptophan radical and field standard. The spectrum is an average of 20 scans collected with 406.4 GHz, 0.3 mT modulation amplitude, at 4.5 K (black trace) and corresponding simulated spectrum (blue trace).

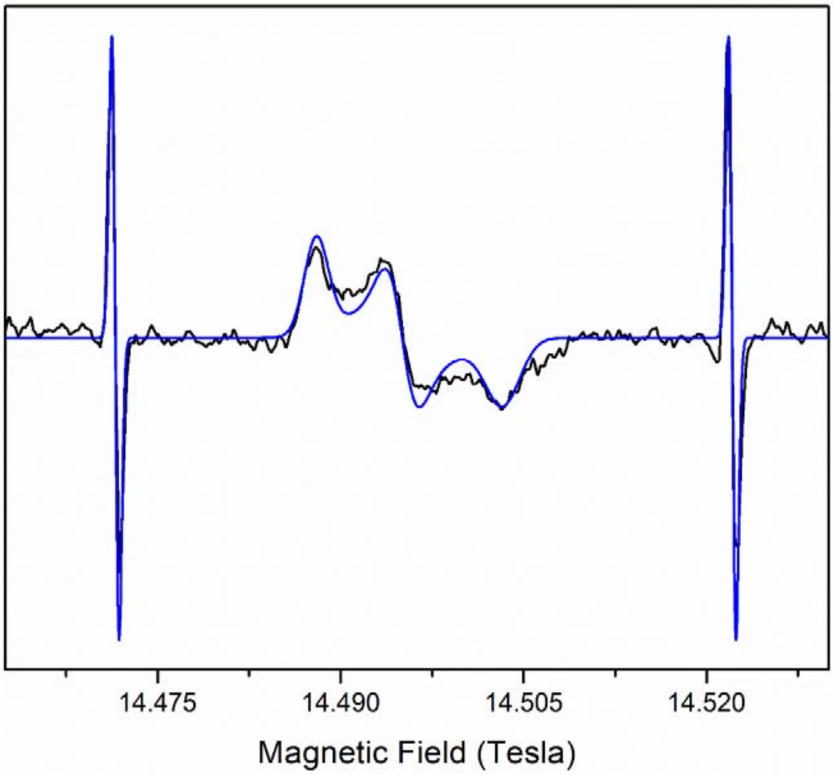

Figure 7.7 Full HFEPR spectrum of 5-methoxytryptophan radical and field standard. The spectrum is an average of 30 scans collected with 406.4 GHz, 0.3 mT modulation amplitude, at 4.5 K (black trace) and corresponding simulated spectrum (blue trace).

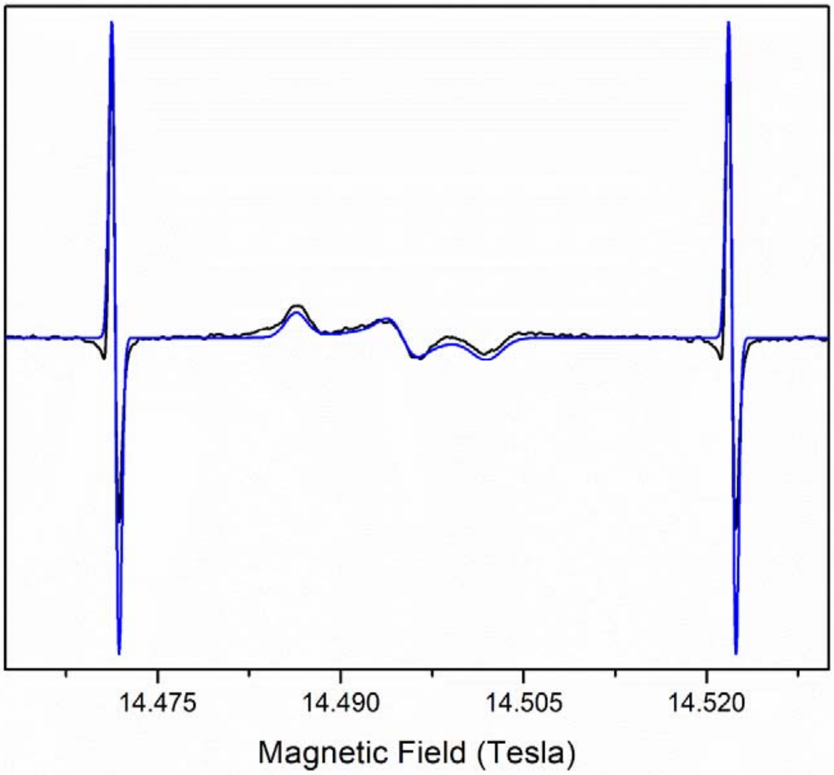

Figure 7.8 Full HFEPR spectrum of 5-hydroxytryptophan radical and field standard. The spectrum is an average of 25 scans collected with 406.4 GHz, 0.3 mT modulation amplitude, at 4.5 K (black trace) and corresponding simulated spectrum (blue trace).

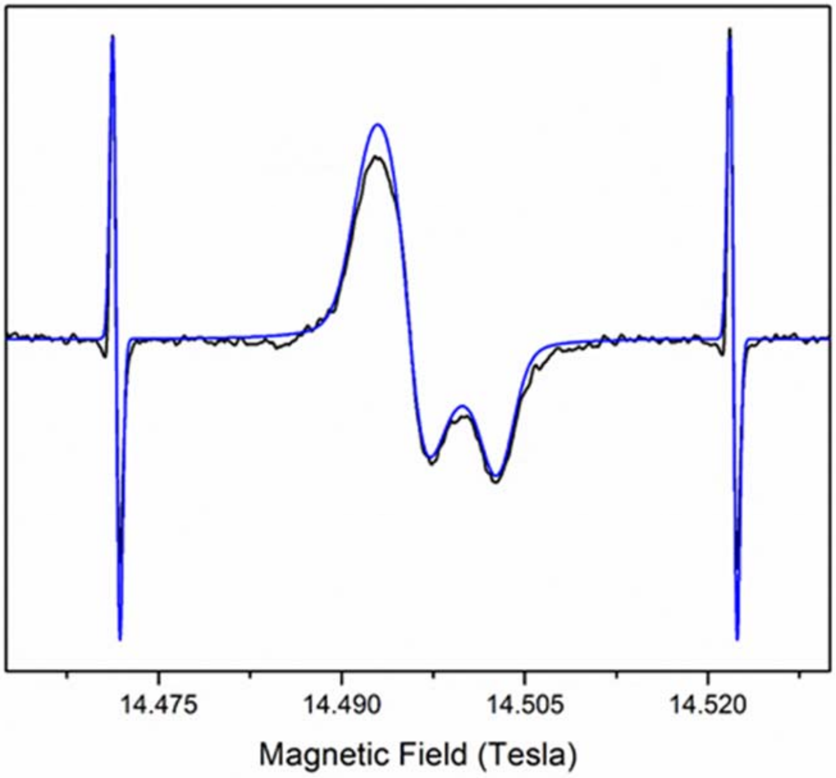

Figure 7.9 Full HFEPR spectrum of 7-hydroxytryptophan radical and field standard. The spectrum is an average of 16 scans collected with 406.4 GHz, 0.3 mT modulation amplitude, at 4.5 K (black trace) and corresponding simulated spectrum (blue trace).

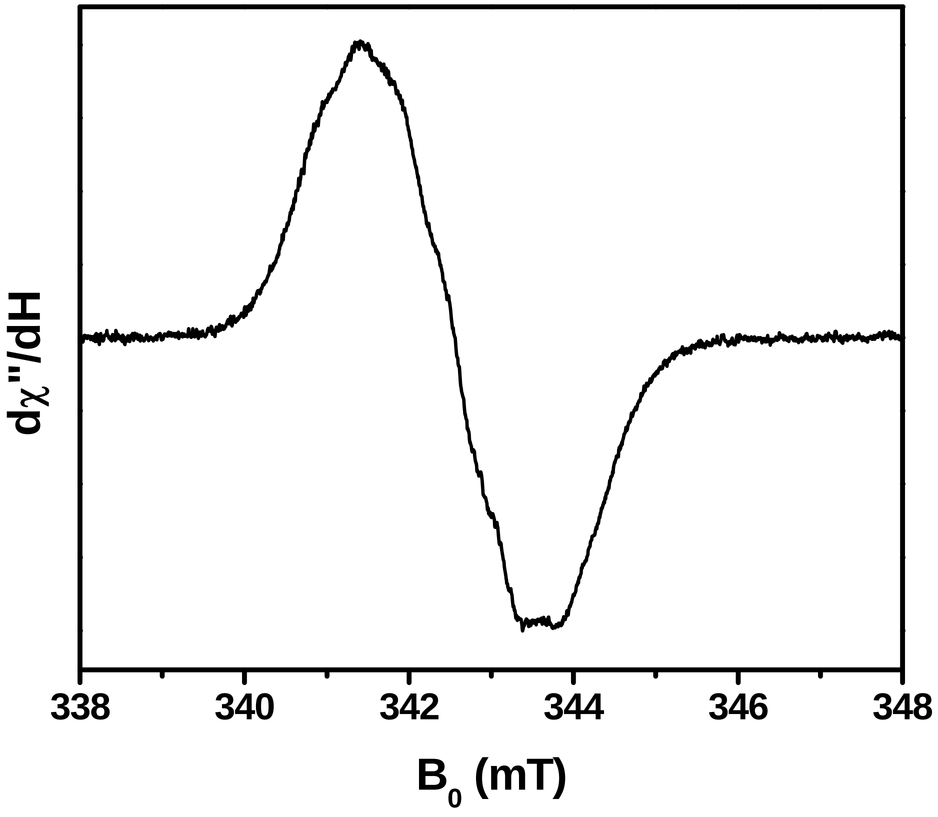

Figure 7.10 X-band EPR spectrum of L-tryptophan radical. Instrument parameters: 9.6 GHz, 100 kHz modulation frequency, 0.01 mT modulation amplitude, 77 K.

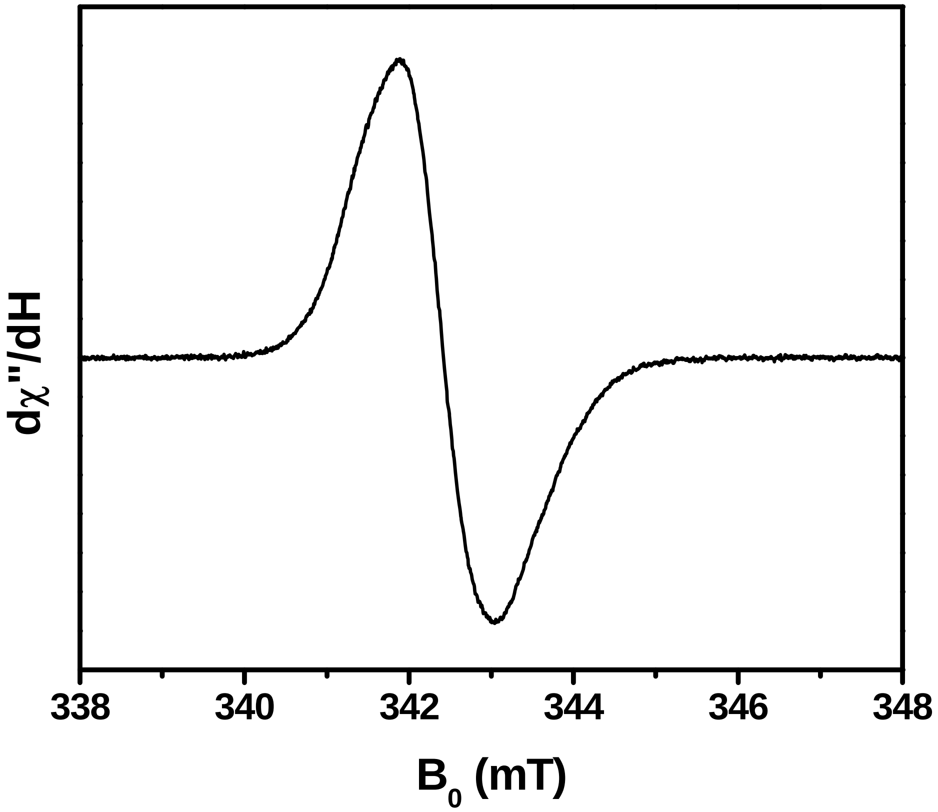

Figure 7.11 X-band EPR spectrum of 5-hydroxytryptophan radical. Instrument parameters: 9.6 GHz, 100 kHz modulation frequency, 0.01 mT modulation amplitude, 77 K.

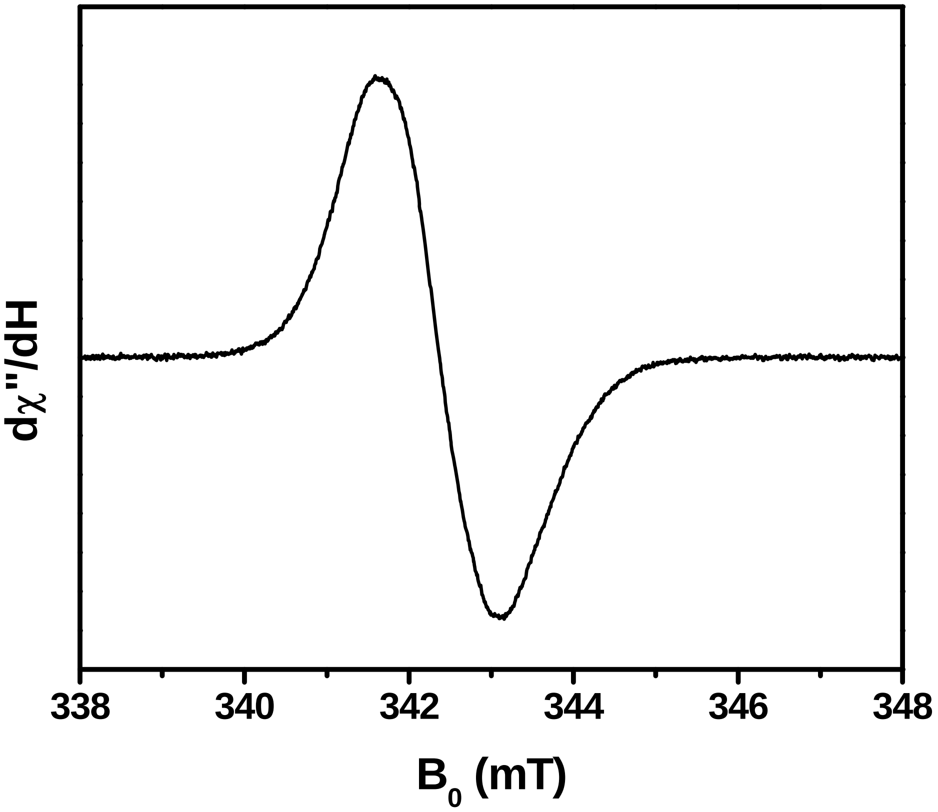

Figure 7.12 X-band EPR spectrum of 5-methoxytryptophan radical. Instrument parameters: 9.6 GHz, 100 kHz modulation frequency, 0.01 mT modulation amplitude, 77 K.

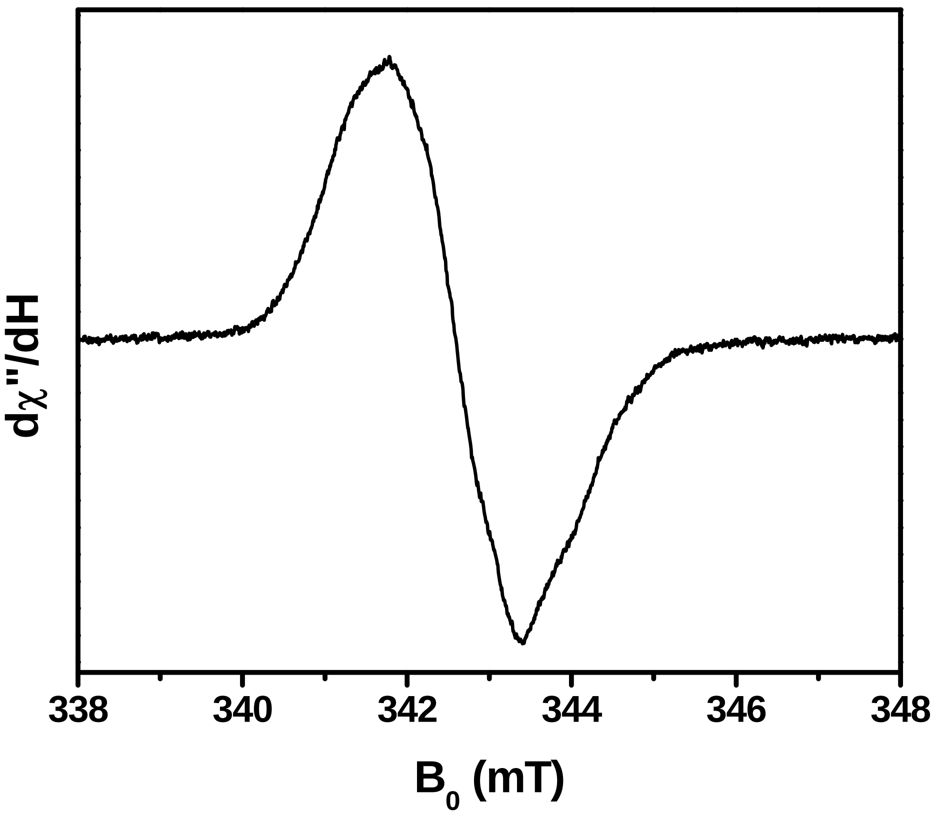

Figure 7.13 X-band EPR spectrum of 7-hydroxytryptophan radical. Instrument parameters: 9.6 GHz, 100 kHz modulation frequency, 0.01 mT modulation amplitude, 77 K.

Substitution at the 5-position with a methoxy or hydroxyl group, 5-MeOx-Trp and 5-OH-Trp, respectively, however, gave rise to rhombic signals with completely resolved *g*-values and a doubling of the Δ*g* to 211 × 10^{-5} and 216 × 10^{-5}, respectively. Similarly to the unsubstituted tryptophan, substitution with a hydroxyl group at the 7-position, 7-OH-Trp, gives rise to an axial signal; however, in this case, the g_{mid} and g_{max} could not be resolved, opposite to what was seen with the unsubstituted tryptophan. The 7-OH-Trp radical also showed an increased Δ*g*, intermediate between unsubstituted tryptophan and 5-OH-Trp at 145 × 10^{-5}. The *g*-anisotropy has been previously found to be a sensitive indicator for differentiating tyrosyl and tryptophanyl radicals [106, 173, 188]. The OH substitution on the phenyl ring of tryptophan is anticipated to increase the Δ*g* value. Comparing 7-OH-Trp and L-Trp radicals, the ratio of the Δ*g* for the photogenerated species is 1.422, slightly larger than the 1.352 obtained from HFEPR spectra of enzymatically oxidized preMADH.(22)

7.4.3 Quantum Chemical Calculations

Density functional theory calculations were performed to interpret the origin of the above experimental findings theoretically in terms of spin populations and *g*-tensors for both cation and neutral radical forms of the compounds measured. Cationic radical structures are derived from

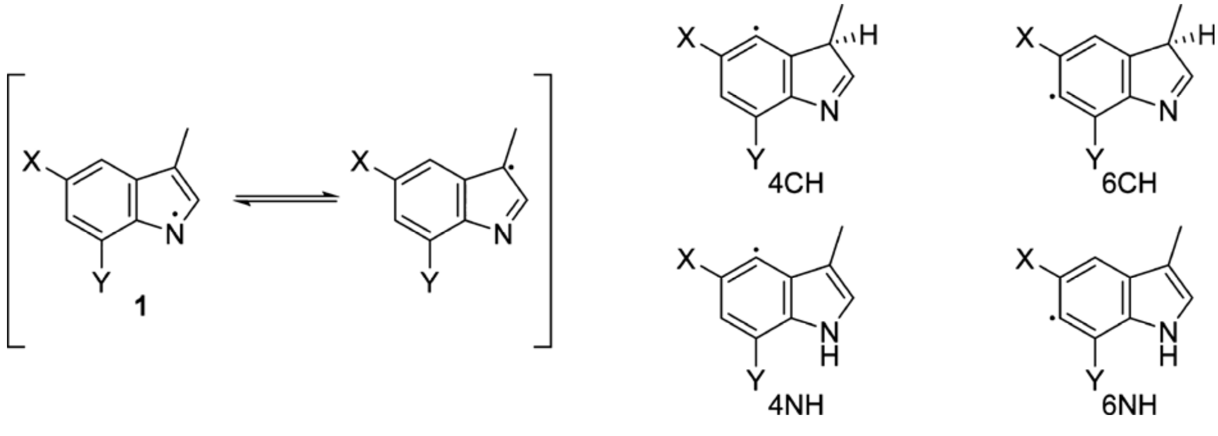

Figure 7.14 Potential neutral radical structures resulting from π-radical delocalization over the indole ring.

their parent indole derivative less one electron; however, there is some ambiguity as to what chemical structure may be most appropriate for a neutral radical species. Geometry optimization and energy calculation indicate that only structures in which the indole nitrogen is deprotonated should be used for further consideration, as other possible neutral radicals are significantly higher in energy, as shown in Figure 7.14 and Table 7.2.

Table 7.2 Calculated energies (kcal mol^{-1}) of different forms of neutral indole radicals as compared to **1**.

	X	Y	4CH	4NH	6CH	6NH
Unsubs.	H	H	36.8310	20.4730	37.4073	21.2050
7-OH	H	OH	39.9200	23.4033	40.8399	24.1682
5-OH	OH	H	37.5223	23.1598	38.9827	23.6731
5-MeOx	OMe	H	38.8657	24.3535	38.1734	23.2923
5-F	F	H	37.9905	22.1130	39.2172	22.6526

The calculated *g*-values and associated anisotropies for both cation and neutral radicals are summarized in Table 7.1. Comparing the predicted Δ*g* of the cation and neutral radical forms, at 406.4 GHz, L-Trp, 5-F-Trp, and 7-OH-Trp cation radicals are all expected to give rise to spectra with axial splitting, whereas neutral radicals should show fully resolved, rhombic patterns. Therefore, because the experimentally observed spectra are not fully resolved, they are expected to arise from their respective cationic radicals. For both 5-OH-Trp and 5-MeOx-Trp, the calculated Δ*g* for the cationic forms are closer to the experimental data than the neutral forms; however, the difference is less significant than that of the other tryptophan-based compounds. As such, *g*-anisotropy alone is insufficient to determine the protonation state of 5-OH-Trp and 5-MeOx-Trp radicals. A summary of tryptophan-based radicals characterized by HFEPR and our predicted neutral radicals can be found in Figure 7.15.

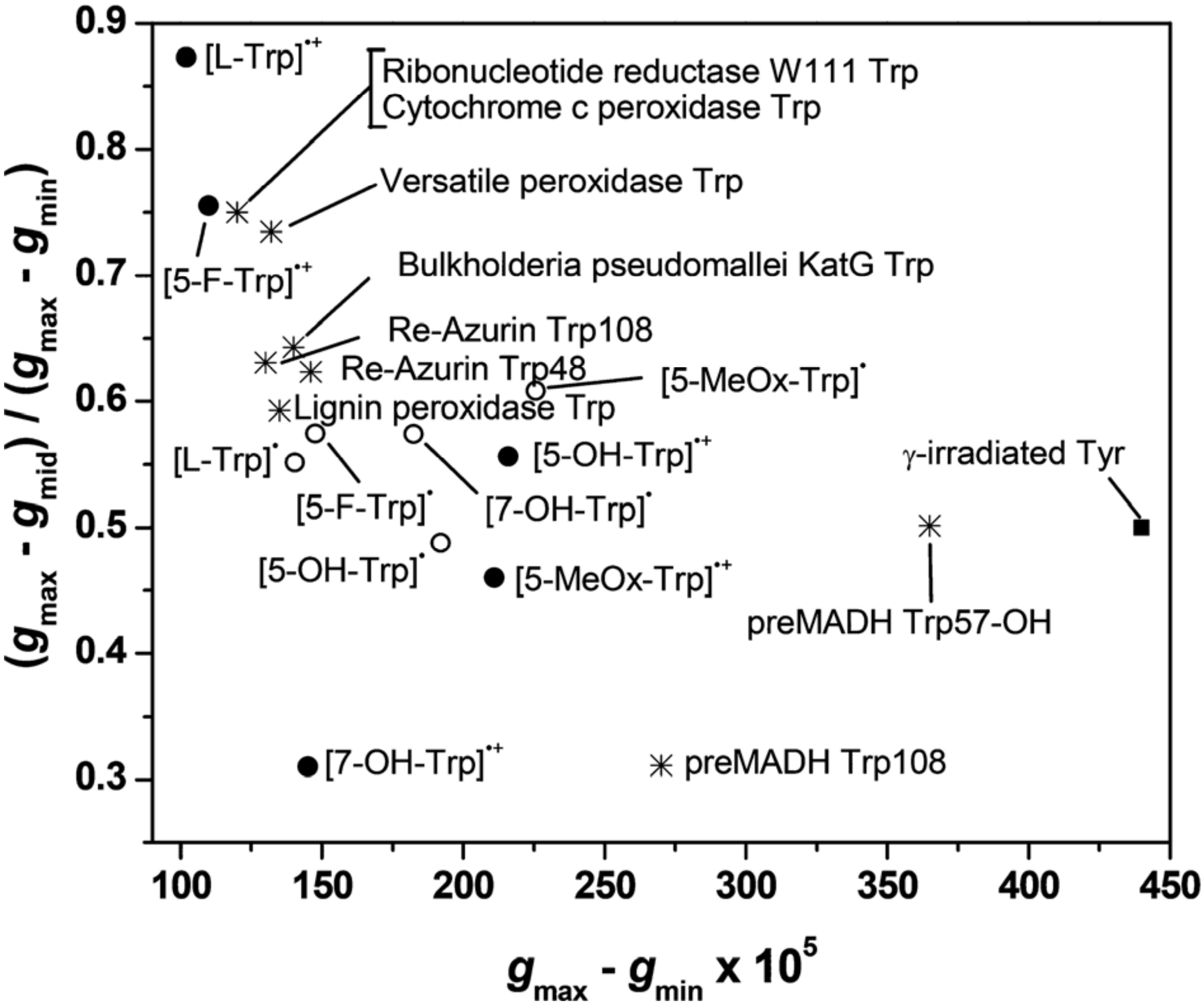

Figure 7.15 Plot of *g*-value anisotropy versus rhombicity of various tryptophan radical species.Tryptophan-based radicals measured in protein are represented by stars, cation radicals measured in this work are closed circles, and neutral radicals (as calculated in this study) are open circles. The *y*-axis shows rhombicity, where 1.0 and 0.0 are completely axial, and the *x*-axis shows *g*-value anisotropy, with 0 representing a purely isotropic signal.

To gain insight into the origin of Δg, spin populations were considered for each of the potential radical species. Mulliken spin populations are schematically shown by the size of circles in Figure 7.16A and summarized in Table 7.3. Spin density distributions have also been previously measured for L-Trp and related compounds in solution by rapid mixing with Ce(IV) as an oxidant, and those distributions are in qualitative agreement with our cationic L-Trp radical [189]. L-Trp and 5-F-Trp have similar spin distributions with the largest spin population on C3 in both cation and neutral radical forms. One significant difference between neutral and cationic L-Trp radicals is that only the cationic species show radical spin density on C2, the position of the cross-link in TTQ. Similarly, 7-OH-Trp shows significant spin density on its TTQ cross-linked carbon, C4, which is diminished upon deprotonation (Figure 7.16B). Of the compounds studied, only 5-OH-Trp and 5-MeOx-Trp show any spin density at the C5 position and the corresponding substituted oxygen, leading to their rhombic spectra.

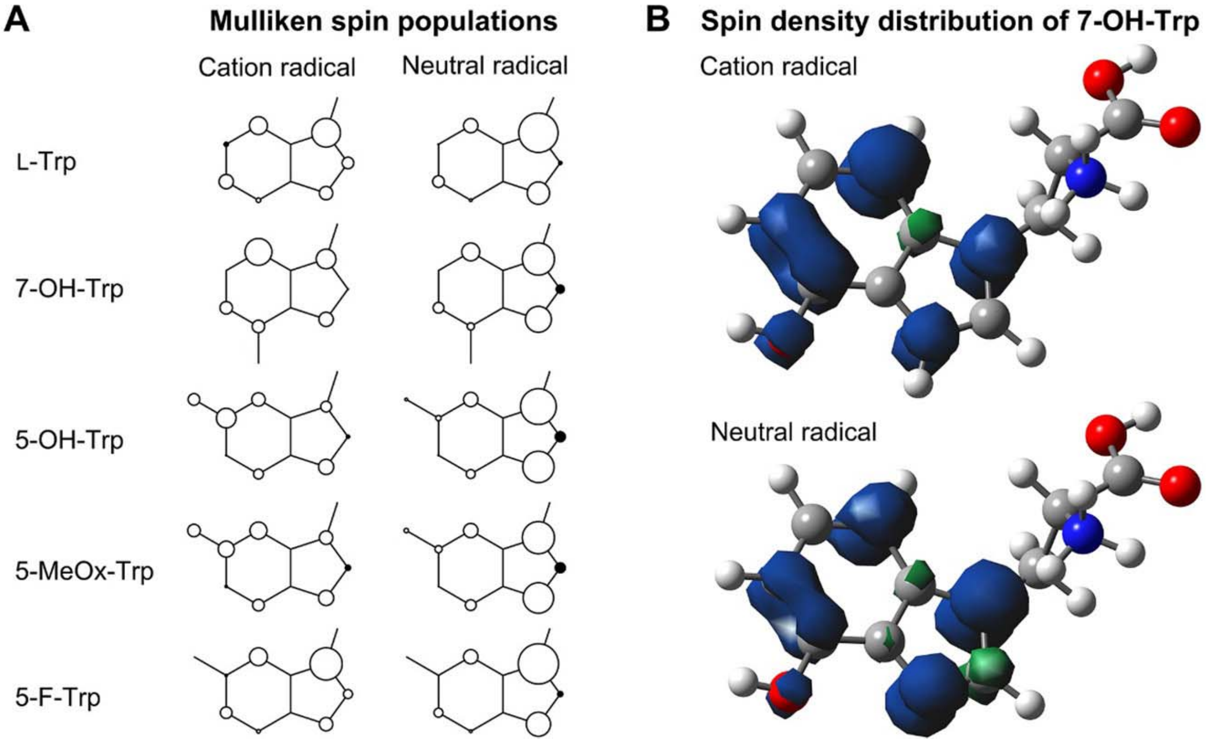

Figure 7.16 Spin density distributions of tryptophan-based radicals. (A) Mulliken spin populations (p-orbital π-component) for the radical forms of tryptophan derivatives. The open and solid circles symbolize positive and negative spin densities, respectively. The size of the circles represents the magnitude of the density. (B) Three-dimensional representation of the spin density distribution of cationic and neutral 7-OH-Trp radicals.

Table 7.3 Mulliken spin populations (pπ/p-component) for tryptophan-based radicals.

Cation Radicals

	Unsubs.		7-OH		5-OH		5-MeOx		5-F	
1N	0.12	0.13	0.16	0.18	0.15	0.18	0.16	0.19	0.14	0.16
2C	0.12	0.11	-0.03	-0.06	-0.03	-0.05	-0.06	-0.08	0.09	0.08
3C	0.31	0.40	0.21	0.27	0.10	0.11	0.12	0.15	0.36	0.45
4C	0.22	0.27	0.32	0.40	0.15	0.17	0.19	0.23	0.22	0.28
5C	-0.07	-0.11	-0.02	-0.05	0.23	0.26	0.18	0.20	-0.05	-0.08
6C	0.18	0.22	0.15	0.17	-0.02	-0.04	-0.03	-0.06	0.14	0.18
7C	0.05	0.05	0.15	0.17	0.10	0.11	0.12	0.15	0.04	0.04
O/F	-	-	0.09	0.09	0.14	0.14	0.15	0.16	0.00	0.00
Neutral Radicals										
1N	0.25	0.26	0.29	0.31	0.36	0.38	0.34	0.37	0.27	0.29
2C	-0.05	-0.10	-0.10	-0.15	-0.12	-0.17	-0.12	-0.17	-0.08	-0.13
3C	0.45	0.57	0.35	0.44	0.33	0.40	0.32	0.40	0.46	0.59
4C	0.17	0.22	0.21	0.27	0.15	0.17	0.16	0.19	0.17	0.21
5C	-0.04	-0.07	0.01	-0.01	0.12	0.13	0.11	0.12	-0.02	-0.04
6C	0.14	0.17	0.12	0.14	-0.05	-0.07	-0.05	-0.07	0.10	0.13
7C	0.03	0.02	0.10	0.10	0.14	0.18	0.15	0.19	0.03	0.03
O/F	-	-	0.04	0.04	0.05	0.05	0.06	0.07	0.00	0.00

7.5 Conclusion

We have shown for the first time, through the novel use of a photocatalyst system that can generate organic radicals at cryogenic temperatures in a frozen glass without the need for ionizing radiation, HFEPR spectra of L-Trp and 7-OH-Trp cationic radicals in free solution. Producing radicals in this way prevents generation of confounding signals from solvated electrons or other unwanted free radicals. Cationic radical spectra were collected for species relevant to the formation of TTQ in MADH, and the experimental *g*-anisotropies were interpreted in terms of spin populations. The experimental HFEPR spectral patterns are sensitive to the location of oxygen substitution. The cationic radicals have low pK_a values and thus would be expected to decay to neutral radicals spontaneously. The neutral radical forms are predicted to give rhombic spectra, mainly due to delocalization on N1 and C3 positions, even in the absence of oxygen substitution. As related to TTQ biosynthesis, the C2 of an L-Trp residue, and the C4 of a 7-OH-Trp residue form a new covalent bond. This study shows that the radical recombination that forms the TTQ cross-link may be more likely when the respective Trp-based radicals are in their protonated states because the carbon atoms of L-Trp and 7-OH-Trp that form the cross-link have more radical character in their respective protonated states. This finding provides new physical insight about the unusual 7-OH-Trp radical and opens a new possibility for the cross-linking reaction, as it was previously thought that the cation radicals initially generated by MauG would have to spontaneously deprotonate before cross-link formation [106].

REFERENCES

1. Peters, J. C., Tryptophan Nutrition and Metabolism: An Overview. In *Kynurenine and Serotonin Pathways.*, Schwarcz, R., Young, S.N., Brown, R.R., Ed. Springer: Boston, MA, 1991; Vol. 294.
2. Hayaishi, O., (1993) My life with tryptophan - Never a dull moment. *Protein Sci. 2*, 472-475.
3. Lapin, I. P.; Oxenkrug, G. F., (1969) Intensification of the central serotoninergcic processes as a possible determinant of the thymoleptic effect. *The Lancet 293* (7586), 132-136.
4. Raison, C. L.; Dantzer, R.; Kelley, K. W.; Lawson, M. A.; Woolwine, B. J.; Vogt, G.; Spivey, J. R.; Saito, K.; Miller, A. H., (2010) CSF concentrations of brain tryptophan and kynurenines during immune stimulation with IFN-α: relationship to CNS immune responses and depression. *Mol. Psychiatry 15* (4), 393-403.
5. Raison, C. L.; Miller, A. H., (2013) Do cytokines really sing the blues? *Cerebrum 2013*, 10-10.
6. Colabroy, K. L.; Begley, T. P., (2005) Tryptophan catabolism: Identification and characterization of a new degradative pathway. *J. Bacteriol. 187*, 7866-7869.
7. Geng, J.; Liu, A., (2014) Heme-dependent dioxygenases in tryptophan oxidation. *Arch. Biochem. Biophys. 544*, 18-26. [PMID: 24295960]
8. Mándi, Y.; Vecséi, L., (2012) The kynurenine system and immunoregulation. *J. Neural. Transm. 119* (2), 197-209.

9. Schwarcz, R.; Bruno, J. P.; Muchowski, P. J.; Wu, H.-Q., (2012) Kynurenines in the mammalian brain: when physiology meets pathology. *Nature Reviews Neuroscience 13* (7), 465-477.

10. Fetzner, S., (2012) Ring-cleaving dioxygenases with a cupin fold. *Appl. Environ. Microbiol. 78* (Copyright (C) 2012 American Chemical Society (ACS). All Rights Reserved.), 2505-2514.

11. Stone, T. W.; Darlington, L. G., (2002) Endogenous kynurenines as targets for drug discovery and development. *Nat. Rev. Drug Discov. 1* (8), 609-20.

12. Stone, T. W.; Stoy, N.; Darlington, L. G., (2013) An expanding range of targets for kynurenine metabolites of tryptophan. *Trends Pharmacol. Sci. 34* (2), 136-143.

13. Miller, A. H., (2013) Conceptual Confluence: The Kynurenine Pathway as a Common Target for Ketamine and the Convergence of the Inflammation and Glutamate Hypotheses of Depression. *Neuropsychopharmacology 38* (9), 1607-1608.

14. Schwarcz, R., (2004) The kynurenine pathway of tryptophan degradation as a drug target. *Curr. Opin. Pharmacol. 4* (1), 12-17.

15. Stone, T. W.; Mackay, G. M.; Forrest, C. M.; Clark, C. J.; Darlington, L. G., (2003) Tryptophan metabolites and brain disorders. *Clinical Chemistry and Laboratory Medicine 41* (7), 852-9.

16. Irwin, M. R.; Miller, A. H., (2007) Depressive disorders and immunity: 20 years of progress and discovery. *Brain, Behav., Immun. 21* (4), 374-383.

17. Beal, M. F.; Matson, W. R.; Swartz, K. J.; Gamache, P. H.; Bird, E. D., (1990) Kynurenine Pathway Measurements in Huntington's Disease Striatum: Evidence for Reduced Formation of Kynurenic Acid. *Journal of neurochemistry. 55* (4), 1327-1339.

18. La Cruz, V. P.-D.; Carrillo-Mora, P.; Santamaría, A., (2012) Quinolinic Acid, an Endogenous Molecule Combining Excitotoxicity, Oxidative Stress and Other Toxic Mechanisms. *International Journal of Tryptophan Research 5*, IJTR.S8158.

19. Huo, L.; Davis, I.; Chen, L.; Liu, A., (2013) The power of two: arginine 51 and arginine 239* from a neighboring subunit are essential for catalysis in α-amino-β-carboxymuconate-ε-semialdehyde decarboxylase. *J. Biol. Chem. 288* (43), 30862-30871. [PMCID: PMC3829401].

20. Huo, L.; Liu, F.; Iwaki, H.; Li, T.; Hasegawa, Y.; Liu, A., (2015) Human α-amino-β-carboxymuconate-ε-semialdehyde decarboxylase (ACMSD): A structural and mechanistic unveiling. *Proteins 83* (1), 178-187.

21. Grant, R. S.; Coggan, S. E.; Smythe, G. A., (2009) The Physiological Action of Picolinic Acid in the Human Brain. *International Journal of Tryptophan Research 2*, IJTR.S2469.

22. Huo, L.; Davis, I.; Liu, F.; Andi, B.; Esaki, S.; Iwaki, H.; Hasegawa, Y.; Orville, A. M.; Liu, A., (2015) Crystallographic and spectroscopic snapshots reveal a dehydrogenase in action. *Nat. Commun. 6*, 5935.

23. Zhang, Y.; Colabroy, K. L.; Begley, T. P.; Ealick, S. E., (2005) Structural studies on 3-hydroxyanthranilate-3,4-dioxygenase: The catalytic mechanism of a complex oxidation involved in NAD biosynthesis. *Biochemistry 44* (Copyright (C) 2012 American Chemical Society (ACS). All Rights Reserved.), 7632-7643.

24. Crunkhorn, S., (2014) Genentech dives deeper into the next wave of cancer immunotherapies. *Nature Reviews Drug Discovery 13* (12), 879-879.

25. Keszthelyi, D.; Troost, F. J.; Masclee, A. A. M., (2009) Understanding the role of tryptophan and serotonin metabolism in gastrointestinal function. *Neurogastroenterology & Motility 21* (12), 1239-1249.

26. Myint, A.-M.; Kim, Y. K.; Verkerk, R.; Scharpé, S.; Steinbusch, H.; Leonard, B., (2007) Kynurenine pathway in major depression: Evidence of impaired neuroprotection. *Journal of Affective Disorders 98* (1), 143-151.

27. Ogawa, T.; Matson, W. R.; Beal, M. F.; Myers, R. H.; Bird, E. D.; Milbury, P.; Saso, S., (1992) Kynurenine pathway abnormalities in Parkinson's disease. *Neurology 42* (9), 1702.

28. Guillemin G.J., W. K. R., Smith D.G., Smythe G.A., Croitoru-Lamoury J., Brew B.J., *Quinolinic acid in the pathogenesis of alzheimer's disease*. Springer: Boston, MA, 2003; Vol. 527.

29. Guidetti P., S. R., *3-Hydroxykynurenine and Quinolinate: Pathogenic Synergism in Early Grade Huntington's Disease?* Springer: Boston, MA, 2003; Vol. 527.

30. Kerr, S. J.; Armati, P. J.; Guillemin, G. J.; Brew, B. J., (1998) Chronic exposure of human neurons to quinolinic acid results in neuronal changes consistent with AIDS dementia complex. *AIDS 12* (4).

31. Heyes, M. P.; Brew, B. J.; Martin, A.; Price, R. W.; Salazar, A. M.; Sidtis, J. J.; Yergey, J. A.; Mouradian, M. M.; Sadler, A. E.; Keilp, J.; Rubinow, D.; Markey, S. P., (1991) Quinolinic acid in cerebrospinal fluid and serum in HIV-1 Infection: Relationship to clinical and neurological status. *Ann. Neurol. 29* (2), 202-209.

32. Heyes, M. P.; Saito, K.; Lackner, A.; Wiley, C. A.; Achim, C. L.; Markey, S. P., (1998) Sources of the neurotoxin quinolinic acid in the brain of HIV-1-infected patients and

retrovirus-infected macaques. *FASEB J. 12* (Copyright (C) 2012 American Chemical Society (ACS). All Rights Reserved.), 881-896.

33. Perozich, J.; Nicholas, H.; Wang, B.-C.; Lindahl, R.; Hempel, J., (1999) Relationships within the aldehyde dehydrogenase extended family. *Protein Sci. 8* (1), 137-146.

34. Unden, G.; Bongaerts, J., (1997) Alternative respiratory pathways of Escherichia coli: energetics and transcriptional regulation in response to electron acceptors. *Biochimica et Biophysica Acta (BBA) - Bioenergetics 1320* (3), 217-234.

35. Nicholls, D. G., (2002) Mitochondrial function and dysfunction in the cell: its relevance to aging and aging-related disease. *The International Journal of Biochemistry & Cell Biology 34* (11), 1372-1381.

36. Hempel, J.; Nicholas, H.; Lindahl, R., (1993) Aldehyde dehydrogenases: Widespread structural and functional diversity within a shared framework. *Protein Sci. 2* (11), 1890-1900.

37. Hasegawa, Y.; Muraki, T.; Tokuyama, T.; Iwaki, H.; Tatsuno, M.; Lau, P. C. K., (2000) A novel degradative pathway of 2-nitrobenzoate via 3-hydroxyanthranilate in Pseudomonas fluorescens strain KU-7. *FEMS Microbiol. Lett. 190* (2), 185-190.

38. Li, T.; Walker, A. L.; Iwaki, H.; Hasegawa, Y.; Liu, A., (2005) Kinetic and spectroscopic characterization of ACMSD from *Pseudomonas fluorescens* reveals a pentacoordinate mononuclear metallocofactor. *J. Am. Chem. Soc. 127* (35), 12282-12290. [PMID: 16131206].

39. Li, T.; Ma, J.; Hosler, J. P.; Davidson, V. L.; Liu, A., (2007) Detection of transient intermediates in the metal-dependent non-oxidative decarboxylation catalyzed by α-

amino-β-carboxymuconate-ε-semialdehyde decarboxylase. *J. Am. Chem. Soc. 129* (30), 9278-9279. [PMID: 17625866].

40. Perez-Miller, S. J.; Hurley, T. D., (2003) Coenzyme Isomerization Is Integral to Catalysis in Aldehyde Dehydrogenase. *Biochemistry 42* (23), 7100-7109.

41. Muñoz-Clares, R. A.; González-Segura, L.; Díaz-Sánchez, Á. G., (2011) Crystallographic evidence for active-site dynamics in the hydrolytic aldehyde dehydrogenases. Implications for the deacylation step of the catalyzed reaction. *Chem. Biol. Interact. 191* (1), 137-146.

42. Geoghegan, K. F.; Dixon, H. B. F.; Rosner, P. J.; Hoth, L. R.; Lanzetti, A. J.; Borzilleri, K. A.; Marr, E. S.; Pezzullo, L. H.; Martin, L. B.; LeMotte, P. K.; McColl, A. S.; Kamath, A. V.; Stroh, J. G., (1999) Spontaneous α-N-6-Phosphogluconoylation of a "His Tag" inEscherichia coli:The Cause of Extra Mass of 258 or 178 Da in Fusion Proteins. *Anal. Biochem. 267* (1), 169-184.

43. Blanco, J.; Moore, R. A.; Viola, R. E., (2003) Capture of an intermediate in the catalytic cycle of L-aspartate-β-semialdehyde dehydrogenase. *Proceedings of the National Academy of Sciences 100* (22), 12613.

44. Colabroy, K. L.; Begley, T. P., (2005) The pyridine ring of NAD is formed by a nonenzymatic pericyclic reaction. *J. Am. Chem. Soc. 127* (3), 840-841.

45. Ichiyama, A.; Nakamura, S.; Kawai, H.; Honjo, T.; Nishizuka, Y.; Hayaishi, O.; Senoh, S., (1965) Studies on the Metabolism of the Benzene Ring of Tryptophan in Mammalian Tissues: II. ENZYMIC FORMATION OF α-AMINOMUCONIC ACID FROM 3-HYDROXYANTHRANILIC ACID. *J. Biol. Chem. 240* (2), 740-749.

46. He, Z.; Davis, J. K.; Spain, J. C., (1998) Purification, characterization, and sequence analysis of 2-aminomuconic 6-semialdehyde dehydrogenase from *Pseudomonas pseudoalcaligenes* JS45. *J. Bacteriol. 180* (17), 4591-5.

47. Abriola, D. P.; Fields, R.; Stein, S.; MacKerell, A. D.; Pietruszko, R., (1987) Active site of human liver aldehyde dehydrogenase. *Biochemistry 26* (18), 5679-5684.

48. Kitson, T. M.; Hill, J. P.; Midwinter, G. G., (1991) Identification of a catalytically essential nucleophilic residue in sheep liver cytoplasmic aldehyde dehydrogenase. *Biochem. J 275* (1), 207-210.

49. Farres, J.; Wang, T. T. Y.; Cunningham, S. J.; Weiner, H., (1995) Investigation of the Active Site Cysteine Residue of Rat Liver Mitochondrial Aldehyde Dehydrogenase by Site-Directed Mutagenesis. *Biochemistry 34* (8), 2592-2598.

50. Steinmetz, C. G.; Xie, P.; Weiner, H.; Hurley, T. D., (1997) Structure of mitochondrial aldehyde dehydrogenase: the genetic component of ethanol aversion. *Structure 5* (5), 701-711.

51. Moore, S. A.; Baker, H. M.; Blythe, T. J.; Kitson, K. E.; Kitson, T. M.; Baker, E. N., (1998) Sheep liver cytosolic aldehyde dehydrogenase: the structure reveals the basis for the retinal specificity of class 1 aldehyde dehydrogenases. *Structure 6* (12), 1541-1551.

52. D'Ambrosio, K.; Pailot, A.; Talfournier, F.; Didierjean, C.; Benedetti, E.; Aubry, A.; Branlant, G.; Corbier, C., (2006) The First Crystal Structure of a Thioacylenzyme Intermediate in the ALDH Family: New Coenzyme Conformation and Relevance to Catalysis. *Biochemistry 45* (9), 2978-2986.

53. Park, J.; Rhee, S., (2013) Structural Basis for a Cofactor-dependent Oxidation Protection and Catalysis of Cyanobacterial Succinic Semialdehyde Dehydrogenase. *J. Biol. Chem. 288* (22), 15760-15770.

54. Park, J.; Rhee, S., (2013) Structural basis for a cofactor-dependent oxidation protection and catalysis of cyanobacterial succinic semialdehyde dehydrogenase. *J. Biol. Chem. 288* (22), 15760-70.

55. Wang, X.; Weiner, H., (1995) Involvement of Glutamate 268 in the Active Site of Human Liver Mitochondrial (Class 2) Aldehyde Dehydrogenase As Probed by Site-Directed Mutagenesis. *Biochemistry 34* (1), 237-243.

56. Adams, P. D.; Afonine, P. V.; Bunkoczi, G.; Chen, V. B.; Davis, I. W.; Echols, N.; Headd, J. J.; Hung, L.-W.; Kapral, G. J.; Grosse-Kunstleve, R. W.; McCoy, A. J.; Moriarty, N. W.; Oeffner, R.; Read, R. J.; Richardson, D. C.; Richardson, J. S.; Terwilliger, T. C.; Zwart, P. H., (2010) PHENIX: a comprehensive Python-based system for macromolecular structure solution. *Acta Crystallographica Section D 66* (2), 213-221.

57. Emsley, P.; Cowtan, K., (2004) Coot: model-building tools for molecular graphics. *Acta Crystallographica Section D 60* (12 Part 1), 2126-2132.

58. W.L., D. *The PyMOL Molecular Graphics System*, 1.7.0.0; Schrödinger, LLC: New York, 2014.

59. Orville, A. M.; Buono, R.; Cowan, M.; Heroux, A.; Shea-McCarthy, G.; Schneider, D. K.; Skinner, J. M.; Skinner, M. J.; Stoner-Ma, D.; Sweet, R. M., (2011) Correlated single-crystal electronic absorption spectroscopy and X-ray crystallography at NSLS beamline X26-C. *Journal of Synchrotron Radiation 18* (3), 358-366.

60. M.J., F. *Gaussian 03, Revision E.01*, Gaussian, Inc.: 2004.

61. Davis, I.; Liu, A., (2015) What is the tryptophan kynurenine pathway and why is it important to neurotherapeutics? *Expert Rev. Neurother. 15* (7), 719-721.

62. Dazzi, C.; Candiano, G.; Massazza, S.; Ponzetto, A.; Varesio, L., (2001) New high-performance liquid chromatographic method for the detection of picolinic acid in biological fluids. *Journal of Chromatography B: Biomedical Sciences and Applications 751* (1), 61-68.

63. Cobessi, D.; Tête-Favier, F.; Marchal, S.; Branlant, G.; Aubry, A., (2000) Structural and biochemical investigations of the catalytic mechanism of an NADP-dependent aldehyde dehydrogenase from Streptococcus mutans. *J. Mol. Biol. 300* (1), 141-52.

64. Muraki, T.; Taki, M.; Hasegawa, Y.; Iwaki, H.; Lau, P. C. K., (2003) Prokaryotic homologs of the eukaryotic 3-hydroxyanthranilate 3,4-dioxygenase and 2-amino-3-carboxymuconate-6-semialdehyde decarboxylase in the 2-nitrobenzoate degradation pathway of *Pseudomonas fluorescens* strain KU-7. *App. Environm. Microbiol. 69* (Copyright (C) 2012 American Chemical Society (ACS). All Rights Reserved.), 1564-1572.

65. Chen, L. H.; Kenyon, G. L.; Curtin, F.; Harayama, S.; Bembenek, M. E.; Hajipour, G.; Whitman, C. P., (1992) 4-Oxalocrotonate tautomerase, an enzyme composed of 62 amino acid residues per monomer. *J. Biol. Chem. 267* (25), 17716-17721.

66. Metanis, N.; Brik, A.; Dawson, P. E.; Keinan, E., (2004) Electrostatic Interactions Dominate the Catalytic Contribution of Arg39 in 4-Oxalocrotonate Tautomerase. *J. Am. Chem. Soc. 126* (40), 12726-12727.

67. Taylor, A. B.; Czerwinski, R. M.; Johnson, W. H.; Whitman, C. P.; Hackert, M. L., (1998) Crystal Structure of 4-Oxalocrotonate Tautomerase Inactivated by 2-Oxo-3-

pentynoate at 2.4 Å Resolution: Analysis and Implications for the Mechanism of Inactivation and Catalysis. *Biochemistry 37* (42), 14692-14700.

68. Burks, E. A.; Yan, W.; Johnson, W. H.; Li, W.; Schroeder, G. K.; Min, C.; Gerratana, B.; Zhang, Y.; Whitman, C. P., (2011) Kinetic, Crystallographic, and Mechanistic Characterization of TomN: Elucidation of a Function for a 4-Oxalocrotonate Tautomerase Homologue in the Tomaymycin Biosynthetic Pathway. *Biochemistry 50* (35), 7600-7611.

69. Terrell, C. R.; Burks, E. A.; Whitman, C. P.; Hoffman, D. W., (2013) Structural and kinetic characterization of two 4-oxalocrotonate tautomerases in Methylibium petroleiphilum strain PM1. *Arch. Biochem. Biophys. 537* (1), 113-124.

70. Huddleston, J. P.; Burks, E. A.; Whitman, C. P., (2014) Identification and characterization of new family members in the tautomerase superfamily: Analysis and implications. *Arch. Biochem. Biophys. 564*, 189-196.

71. Burks, E. A.; Fleming, C. D.; Mesecar, A. D.; Whitman, C. P.; Pegan, S. D., (2010) Kinetic and Structural Characterization of a Heterohexamer 4-Oxalocrotonate Tautomerase from Chloroflexus aurantiacus J-10-fl: Implications for Functional and Structural Diversity in the Tautomerase Superfamily. *Biochemistry 49* (24), 5016-5027.

72. Li, T.; Iwaki, H.; Fu, R.; Hasegawa, Y.; Zhang, H.; Liu, A., (2006) α-Amino-β-carboxymuconic-ε-semialdehyde decarboxylase (ACMSD) is a new member of the amidohydrolase superfamily. *Biochemistry 45* (21), 6628-6634. [PMID: 16716073].

73. Otwinowski, Z.; Minor, W., [20] Processing of X-ray diffraction data collected in oscillation mode. In *Methods Enzymol.*, Academic Press: 1997; Vol. 276, pp 307-326.

74. Nishizuka, Y.; Ichiyama, A.; Gholson, R. K.; Hayaishi, O., (1965) Studies on the metabolism of the benzene ring of tryptophan in mammalian tissues. I. Enzymatic formation of glutaric acid from 3-hydroxyanthranilic acid. *J. Biol. Chem. 240*, 733-739.

75. Cervenka, I.; Agudelo, L. Z.; Ruas, J. L., (2017) Kynurenines: Tryptophan's metabolites in exercise, inflammation, and mental health. *Science 357* (6349, eaaf9794), 1-8.

76. Ananieva, E., (2015) Targeting amino acid metabolism in cancer growth and anti-tumor immune response. *World journal of biological chemistry 6* (4), 281-289.

77. Pilotte, L.; Larrieu, P.; Stroobant, V.; Colau, D.; Dolusic, E.; Frederick, R.; De Plaen, E.; Uyttenhove, C.; Wouters, J.; Masereel, B.; Van den Eynde, B. J., (2012) Reversal of tumoral immune resistance by inhibition of tryptophan 2,3-dioxygenase. *Proc. Natl. Acad. Sci. U. S. A. 109* (7), 2497-502.

78. Pellicciari, R.; Liscio, P.; Giacchè, N.; De Franco, F.; Carotti, A.; Robertson, J.; Cialabrini, L.; Katsyuba, E.; Raffaelli, N.; Auwerx, J., (2018) α-Amino-β-carboxymuconate-ε-semialdehyde Decarboxylase (ACMSD) inhibitors as novel modulators of *de novo* nicotinamide adenine dinucleotide (NAD^+) biosynthesis. *J. Med. Chem. 61* (3), 745-759.

79. Fukuoka, S.; Ishiguro, K.; Yanagihara, K.; Tanabe, A.; Egashira, Y.; Sanada, H.; Shibata, K., (2002) Identification and expression of a cDNA encoding human alpha-amino-beta-carboxymuconate-epsilon-semialdehyde decarboxylase (ACMSD). A key enzyme for the tryptophan-niacine pathway and "quinolinate hypothesis". *J. Biol. Chem. 277* (38), 35162-35167.

80. Kurnasov, O.; Goral, V.; Colabroy, K.; Gerdes, S.; Anantha, S.; Osterman, A.; Begley, T. P., (2003) NAD biosynthesis: identification of the tryptophan to quinolinate pathway in bacteria. *Chem. Biol. 10* (12), 1195-204.

81. Lima, W. C.; Varani, A. M.; Menck, C. F. M., (2009) NAD biosynthesis evolution in bacteria: Lateral gene transfer of kynurenine pathway in xanthomonadales and flavobacteriales. *Mol. Biol. Evol. 26*, 399-406.

82. Phillips, R. S., (2014) Structure and mechanism of kynureninase. *Arch. Biochem. Biophys. 544*, 69-74.

83. Wogulis, M.; Chew, E. R.; Donohoue, P. D.; Wilson, D. K., (2008) Identification of formyl kynurenine formamidase and kynurenine aminotransferase from *Saccharomyces cerevisiae* using crystallographic, bioinformatic and biochemical evidence. *Biochemistry 47* (6), 1608-1621.

84. Phillips, R. S.; Anderson, A. D.; Gentry, H. G.; Guner, O. F.; Bowen, J. P., (2017) Substrate and inhibitor specificity of kynurenine monooxygenase from *Cytophaga hutchinsonii*. *Bioorg. Med. Chem. Lett. 27* (8), 1705-1708.

85. Nishino, S. F.; Spain, J. C., (1993) Degradation of nitrobenzene by a *Pseudomonas pseudoalcaligenes*. *Appl. Environ. Microbiol. 59* (8), 2520-2525.

86. Yang, Y.; Davis, I.; Ha, U.; Wang, Y.; Shin, I.; Liu, A., (2016) A pitcher-and-catcher mechanism drives endogenous substrate isomerization by a dehydrogenase in kynurenine metabolism. *J. Biol. Chem. 291* (51), 26252-26261.

87. Lin, M.; Napoli, J. L., (2000) cDNA cloning and expression of a human aldehyde dehydrogenase (ALDH) active with 9-cis-retinal and identification of a rat ortholog, ALDH12. *J. Biol. Chem. 275* (51), 40106-12.

88. Gouet, P.; Robert, X.; Courcelle, E., (2003) ESPript/ENDscript: extracting and rendering sequence and 3D information from atomic structures of proteins. *Nucleic Acids Res. 31* (13), 3320-3323.

89. Yang, J.; Yan, R.; Roy, A.; Xu, D.; Poisson, J.; Zhang, Y., (2015) The I-TASSER Suite: protein structure and function prediction. *Nat. Methods 12* (1), 7-8.

90. Whitman, C. P.; Aird, B. A.; Gillespie, W. R.; Stolowich, N. J., (1991) Chemical and enzymic ketonization of 2-hydroxymuconate, a conjugated enol. *J. Am. Chem. Soc. 113* (8), 3154-3162.

91. Huo, L.; Fielding, A. J.; Chen, Y.; Li, T.; Iwaki, H.; Hosler, J. P.; Chen, L.; Hasegawa, Y.; Que, L.; Liu, A., (2012) Evidence for a dual role of an active site histidine in α-amino-β-carboxymuconate-ε-semialdehyde Decarboxylase. *Biochemistry 51* (29), 5811-5821. [PMCID: PMC3419591].

92. Strohalm, M.; Hassman, M.; Kosata, B.; Kodicek, M., (2008) mMass data miner: an open source alternative for mass spectrometric data analysis. *Rapid Commun. Mass Spectrom. 22* (6), 905-908.

93. Badger, B.; Brocklehurst, B., (1968) Formation of dimer cations of aromatic hydrocarbons. *Nature 219*, 263.

94. Heckmann, A.; Lambert, C., (2012) Organic mixed-valence compounds: A playground for electrons and holes. *Angew. Chem. Int. Ed. 51* (2), 326-392.

95. Geng, J.; Dornevil, K.; Davidson, V. L.; Liu, A., (2013) Tryptophan-mediated charge-resonance stabilization in the *bis*-Fe(IV) redox state of MauG. *Proc. Natl. Acad. Sci. USA 110* (24), 9639-9644.

96. Kochi, J. K.; Rathore, R.; Magueres, P. L., (2000) Stable dimeric aromatic cation-radicals. Structural and spectral characterization of through-space charge delocalization. *J. Org. Chem. 65* (21), 6826-36.

97. Takai, A.; Gros, C. P.; Barbe, J. M.; Guilard, R.; Fukuzumi, S., (2009) Enhanced electron-transfer properties of cofacial porphyrin dimers through π-π interactions. *Chem. Eur. J. 15* (13), 3110-3122.

98. Bloch-Mechkour, A.; Bally, T.; Marcinek, A., (2011) Dimer radical cations of indole and indole-3-carbinol: Localized and delocalized radical cations of diindolylmethane. *J. Phys. Chem. A 115* (26), 7700-7708.

99. Brancato-Buentello, K. E.; Kang, S. J.; Scheidt, W. R., (1997) Metalloporphyrin mixed-valence π cation radicals: Solution stability and properties. *J. Am. Chem. Soc. 119* (12), 2839-2846.

100. Breton, J.; Nabedryk, E.; Parson, W. W., (1992) A new infrared electronic transition of the oxidized primary electron donor in bacterial reaction centers - a way to assess resonance interactions between the bacteriochlorophylls. *Biochemistry 31* (33), 7503-7510.

101. Kanchanawong, P.; Dahlbom, M. G.; Treynor, T. P.; Reimers, J. R.; Hush, N. S.; Boxer, S. G., (2006) Charge delocalization in the special-pair radical cation of mutant reaction centers of *Rhodobacter sphaeroides* from Stark spectra and nonadiabatic spectral simulations. *J. Phys. Chem. B 110* (37), 18688-18702.

102. Wang, Y.; Graichen, M. E.; Liu, A.; Pearson, A. R.; Wilmot, C. M.; Davidson, V. L., (2003) MauG, a novel diheme protein required for tryptophan tryptophylquinone biogenesis. *Biochemistry 42* (24), 7318-7325.

103. McIntire, W. S.; Wemmer, D. E.; Chistoserdov, A.; Lidstrom, M. E., (1991) A new cofactor in a prokaryotic enzyme: tryptophan tryptophylquinone as the redox prosthetic group in methylamine dehydrogenase. *Science 252* (5007), 817-24.

104. Jensen, L. M. R.; Sanishvili, R.; Davidson, V. L.; Wilmot, C. M., (2010) *In crystallo* posttranslational modification within a MauG/pre-methylamine dehydrogenase complex. *Science 327* (5971), 1392-1394.

105. Pearson, A. R.; De la Mora-Rey, T.; Graichen, M. E.; Wang, Y.; Jones, L. H.; Marimanikkupam, S.; Agger, S. A.; Grimsrud, P. A.; Davidson, V. L.; Wilmot, C. M., (2004) Further Insights into Quinone Cofactor Biogenesis: Probing the Role of mauG in Methylamine Dehydrogenase Tryptophan Tryptophylquinone Formation. *Biochemistry 43* (18), 5494-5502.

106. Yukl, E. T.; Liu, F.; Krzystek, J.; Shin, S.; Jensen, L. M. R.; Davidson, V. L.; Wilmot, C. M.; Liu, A., (2013) Diradical intermediate within the context of tryptophan tryptophylquinone biosynthesis. *Proc. Natl. Acad. Sci. U.S.A. 110* (12), 4569-4573.

107. Li, X.; Fu, R.; Lee, S.; Krebs, C.; Davidson, V. L.; Liu, A., (2008) A catalytic di-heme *bis*-Fe(IV) intermediate, alternative to an Fe(IV)=O porphyrin radical. *Proc. Natl. Acad. Sci. U.S.A. 105* (25), 8597-8600.

108. Geng, J.; Davis, I.; Liu, F.; Liu, A., (2014) Bis-Fe(IV): nature’s sniper for long-range oxidation. *J Biol Inorg Chem 19* (7), 1057-1067.

109. Fuhrhop, J. H.; Wasser, P.; Riesner, D.; Mauzerall, D., (1972) Dimerization and π bonding of a zinc porphyrin cation radical. Thermodynamics and fast reaction kinetics. *J. Am. Chem. Soc. 94* (23), 7996-8001.

110. Lindeman, S. V.; Rosokha, S. V.; Sun, D.; Kochi, J. K., (2002) X-ray structure analysis and the intervalent electron transfer in organic mixed-valence crystals with bridged aromatic cation radicals. *J. Am. Chem. Soc. 124* (5), 843-855.

111. Song, H.; Orosz, R. D.; Reed, C. A.; Scheidt, W. R., (1990) Dimerization of metalloporphyrin π cation radicals. Characterization of two novel dimers: $[Zn(OEP^{\bullet})(OH_2)]_2(ClO_4)_2$ and $[Ni(OEP)]_2(ClO_4)_2$. *Inorg. Chem. 29*, 4274-4282.

112. Fu, R.; Liu, F.; Davidson, V. L.; Liu, A., (2009) Heme iron nitrosyl complex of MauG reveals an efficient redox equilibrium between hemes with only one heme exclusively binding exogenous ligands. *Biochemistry 48* (49), 11603-11605.

113. Yukl, E. T.; Williamson, H. R.; Higgins, L.; Davidson, V. L.; Wilmot, C. M., (2013) Oxidative damage in MauG: implications for the control of high-valent iron species and radical propagation pathways. *Biochemistry 52* (52), 9447-9455.

114. Li, X. H.; Fu, R.; Lee, S. Y.; Krebs, C.; Davidson, V. L.; Liu, A., (2008) A catalytic di-heme *bis*-Fe(IV) intermediate, alternative to an Fe(IV)=O porphyrin radical. *Proc. Natl. Acad Sci. U. S. A. 105* (25), 8597-8600.

115. Lee, S.; Shin, S.; Li, X.; Davidson, V. L., (2009) Kinetic mechanism for the initial steps in MauG-dependent tryptophan tryptophylquinone biosynthesis. *Biochemistry 48* (11), 2442-2447.

116. Viola, F.; Aime, S.; Coletta, M.; Desideri, A.; Fasano, M.; Paoletti, S.; Tarricone, C.; Ascenzi, P., (1996) Azide, cyanide, fluoride, imidazole and pyridine binding to ferric and ferrous native horse heart cytochrome c and to its carboxymethylated derivative: a comparative study. *J. Inorg. Biochem. 62* (3), 213-22.

117. Winkler, W. C.; Gonzalez, G.; Wittenberg, J. B.; Hille, R.; Dakappagari, N.; Jacob, A.; Gonzalez, L. A.; Gilles-Gonzalez, M. A., (1996) Nonsteric factors dominate binding of nitric oxide, azide, imidazole, cyanide, and fluoride to the rhizobial heme-based oxygen sensor FixL. *Chem. Biol. 3* (10), 841-50.

118. Chen, Y.; Naik, S. G.; Krzystek, J.; Shin, S.; Nelson, W. H.; Xue, S.; Yang, J. J.; Davidson, V. L.; Liu, A., (2012) Role of calcium in metalloenzymes: Effects of calcium removal on the axial ligation geometry and magnetic properties of the catalytic diheme center in MauG. *Biochemistry 51* (8), 1586-1597.

119. Feng, M.; Jensen, L. M. R.; Yukl, E. T.; Wei, X.; Liu, A.; Wilmot, C. M.; Davidson, V. L., (2012) Proline 107 is a major determinant in maintaining the structure of the distal pocket and reactivity of the high-spin heme of MauG. *Biochemistry 51* (8), 1598-1606.

120. Van Doorslaer, S.; Tilleman, L.; Verrept, B.; Desmet, F.; Maurelli, S.; Trandafir, F.; Moens, L.; Dewilde, S., (2012) Marked Difference in the Electronic Structure of Cyanide-Ligated Ferric Protoglobins and Myoglobin Due to Heme Ruffling. *Inorg. Chem. 51* (16), 8834-8841.

121. Abu Tarboush, N.; Jensen, L. M. R.; Feng, M.; Tachikawa, H.; Wilmot, C. M.; Davidson, V. L., (2010) Functional importance of tyrosine 294 and the catalytic selectivity for the bis-Fe(IV) state of MauG revealed by replacement of this axial heme ligand with histidine. *Biochemistry 49* (45), 9783-9791.

122. Abu Tarboush, N.; Shin, S.; Geng, J.; Liu, A.; Davidson, V. L., (2012) Effects of the loss of the axial tyrosine ligand of the low-spin heme of MauG on its physical properties and reactivity. *FEBS Lett.*, in press.

123. Choi, M.; Shin, S.; Davidson, V. L., (2012) Characterization of Electron Tunneling and Hole Hopping Reactions between Different Forms of MauG and Methylamine Dehydrogenase within a Natural Protein Complex. *Biochemistry 51* (35), 6942-6949.

124. Pan, B.; Abel, J.; Ricci, M. S.; Brems, D. N.; Wang, D. I. C.; Trout, B. L., (2006) Comparative Oxidation Studies of Methionine Residues Reflect a Structural Effect on Chemical Kinetics in rhG-CSF. *Biochemistry 45* (51), 15430-15443.

125. Thirumangalathu, R.; Krishnan, S.; Bondarenko, P.; Speed-Ricci, M.; Randolph, T. W.; Carpenter, J. F.; Brems, D. N., (2007) Oxidation of Methionine Residues in Recombinant Human Interleukin-1 Receptor Antagonist: Implications of Conformational Stability on Protein Oxidation Kinetics. *Biochemistry 46* (21), 6213-6224.

126. Marcus, R. A.; Sutin, N., (1985) Electron transfers in chemistry and biology. *Biochimica et Biophysica Acta (BBA) - Reviews on Bioenergetics 811* (3), 265-322.

127. Page, C. C.; Moser, C. C.; Chen, X.; Dutton, P. L., (1999) Natural engineering principles of electron tunnelling in biological oxidation–reduction. *Nature 402* (6757), 47-52.

128. V., K. I. *HARLEM—Molecular Modeling Package*, 2000.

129. Bergès, J.; de Oliveira, P.; Fourré, I.; Houée-Levin, C., (2012) The One-Electron Reduction Potential of Methionine-Containing Peptides Depends on the Sequence. *The Journal of Physical Chemistry B 116* (31), 9352-9362.

130. Battistuzzi, G.; Bellei, M.; Bortolotti, C. A.; Sola, M., (2010) Redox properties of heme peroxidases. *Arch. Biochem. Biophys. 500* (1), 21-36.

131. Li, X.; Feng, M.; Wang, Y.; Tachikawa, H.; Davidson, V. L., (2006) Evidence for redox cooperativity between *c*-type hemes of MauG which is likely coupled to oxygen

activation during tryptophan tryptophylquinone biosynthesis. *Biochemistry 45* (3), 821-828.

132. Abu Tarboush, N.; Jensen, L. M.; Yukl, E. T.; Geng, J.; Liu, A.; Wilmot, C. M.; Davidson, V. L., (2011) Mutagenesis of tryptophan199 suggests that hopping is required for MauG-dependent tryptophan tryptophylquinone biosynthesis. *Proc. Natl. Acad. Sci. USA 108* (41), 16956-61.

133. Geng, J.; Davis, I.; Liu, A., (2015) Probing *bis*-Fe(IV) MauG: Experimental evidence for the long-range charge-resonance model. *Angew Chem Intl Ed 54* (12), 3692-3696.

134. Shin, S.; Lee, S.; Davidson, V. L., (2009) Suicide inactivation of MauG during reaction with O_2 or H_2O_2 in the absence of its natural protein substrate. *Biochemistry 48* (42), 10106-10112.

135. Ma, Z.; Williamson, H. R.; Davidson, V. L., (2015) Roles of multiple-proton transfer pathways and proton-coupled electron transfer in the reactivity of the *bis*-Fe(IV) state of MauG. *Proc. Natl. Acad. Sci. USA 112* (35), 10896-10901.

136. Ma, Z.; Williamson, Heather R.; Davidson, Victor L., (2016) Mechanism of protein oxidative damage that is coupled to long-range electron transfer to high-valent haems. *Biochem. J. 473* (12), 1769.

137. Stubbe, J.; van der Donk, W. A., (1998) Protein radicals in enzyme catalysis. *Chem. Rev. 98* (2), 705-762.

138. Nelson, N.; Yocum, C. F., (2006) Structure and function of photosystems I and II. *Annu. Rev. Plant Biol. 57*, 521-565.

139. Svistunenko, D. A.; Wilson, M. T.; Cooper, C. E., (2004) Tryptophan or tyrosine? On the nature of the amino acid radical formed following hydrogen peroxide treatment of cytochrome *c* oxidase. *Biochim. Biophys. Acta, Bioenerg. 1655*, 372-380.

140. Stubbe, J.; Nocera, D. G.; Yee, C. S.; Chang, M. C., (2003) Radical initiation in the class I ribonucleotide reductase: long-range proton-coupled electron transfer? *Chem Rev 103* (6), 2167-201.

141. Aubert, C.; Vos, M. H.; Mathis, P.; Eker, A. P. M.; Brettel, K., (2000) Intraprotein radical transfer during photoactivation of DNA photolyase. *Nature 405* (6786), 586-590.

142. Schoeneich, C., (2005) Methionine oxidation by reactive oxygen species: reaction mechanisms and relevance to Alzheimer's disease. *Biochim. Biophys. Acta 1703* (2), 111-119.

143. Pogocki, D.; Burlinska, G.; Wasowicz, T.; Sadlo, J.; Bobrowski, K., (1994) Radical induced oxidation of sulfur-containing amino acids. An ESR study. *Mol Phys Rep 6*, 224-9.

144. Goez, M.; Rozwadowski, J., (1998) Reversible pair substitution in CIDNP: The radical cation of methionine. *J Phys Chem A 102* (41), 7945-7953.

145. Pogocki, D.; Serdiuk, K.; Schoeneich, C., (2003) Computational characterization of sulfur-oxygen three-electron-bonded radicals in methionine and methionine-containing peptides: Important intermediates in one-electron oxidation processes. *J Phys Chem A 107* (36), 7032-7042.

146. Zhao, J.; Ng, C. M. D.; Chu, I. K.; Siu, K. W. M.; Hopkinson, A. C., (2009) Methionine, α-methylmethionine and S-methylcysteine radical cations: generations and dissociations in the gas phase. *Phys Chem Chem Phys 11* (35), 7629-7639.

147. Fourre, I.; Berges, J.; Houee-Levin, C., (2010) Structural and topological studies of methionine radical cations in dipeptides: electron sharing in two-center three-electron bonds. *J Phys Chem A 114* (27), 7359-7368.

148. Yashiro, H.; White, R. C.; Yurkovskaya, A. V.; Forbes, M. D. E., (2005) Methionine radical cation: structural studies as a function of pH using X- and Q-band time-resolved electron paramagnetic resonance spectroscopy. *J Phys Chem A 109* (26), 5855-5864.

149. Geng, J.; Huo, L.; Liu, A., (2017) Heterolytic O-O bond cleavage: Functional role of Glu113 during *bis*-Fe(IV) formation in MauG. *J Inorg Biochem 167*, 60-67.

150. Aurich, H. G.; Trosken, J., (1971) Losungsmittelabhangigkeit der ESR-spektren von alkyl-acyl-nitroxiden. *Liebigs Ann Chen 745*, 159-163.

151. Floyd, R. A.; Soong, L. M., (1977) Spin trapping in biological systems. Oxidation of the spin trap 5,5-dimethyl-1-pyrroline-1-oxide by a hydroperoxide-hematin system. *Biochem. Biophys. Res. Commun. 74* (1), 79-84.

152. Rosen, G. M.; Rauckman, E. J., (1980) Spin trapping of the primary radical involved in the activation of the carcinogen *N*-hydroxy-2-acetylaminofluorene by cumene hydroperoxide-hematin. *Mol. Pharmacol. 17* (2), 233-8.

153. Buettner, G. R., (1987) Spin trapping: ESR parameters of spin adducts. *Free Radic Biol Med 3* (4), 259-303.

154. Stadtman, E. R.; Levine, R. L., (2003) Free radical-mediated oxidation of free amino acids and amino acid residues in proteins. *Amino Acids 25* (3), 207-218.

155. Makino, K., (1979) Studies on spin-trapped radicals in .gamma.-irradiated aqueous solutions of DL-methionine by high performance liquid chromatography and ESR spectroscopy. *J Phys Chem 83* (19), 2520-2523.

156. Mackor, A.; Wajer, T. A. J. W.; de Boer, T. J., (1968) C-nitroso compounds—VI. *Tetrahedron 24* (4), 1623-1631.

157. Bilski, P.; Reszka, K.; Bilska, M.; Chignell, C. F., (1996) Oxidation of the spin trap 5,5-dimethyl-1-pyrroline *N*-oxide by singlet oxygen in aqueous solution. *J. Am. Chem. Soc. 118* (6), 1330-1338.

158. Neidlinger, A.; Kienz, T.; Heinze, K., (2015) Spin trapping of carbon-centered ferrocenyl radicals with nitrosobenzene. *Organometallics 34* (21), 5310-5320.

159. Qian, S. Y.; Chen, Y. R.; Deterding, L. J.; Fann, Y. C.; Chignell, C. F.; Tomer, K. B.; Mason, R. P., (2002) Identification of protein-derived tyrosyl radical in the reaction of cytochrome c and hydrogen peroxide: characterization by ESR spin-trapping, HPLC and MS. *Biochem. J. 363* (Pt 2), 281-288.

160. Popova, N. K., (2006) From genes to agressive behavior: the role of serotonergic system. *Bioessays 28*, 495-503.

161. Vanecek, J., (1998) Cellular mechanisms of melatonin action. *Physiol. Rev. 78* (3), 687-721.

162. Stone, T. W.; Mackay, G. M.; Forrest, C. M.; Clark, C. J.; Darlington, L. G., (2003) Tryptophan metabolites and brain disorders. *Clinical Chemistry and Laboratory Medicine 41* (7), 852-859.

163. Gholson, R. K.; Rao, D. R.; Henderson, L. M.; Hill, R. J.; Koeppe, R. E., (1957) The metabolism of DL-tryptophan-7α-C^{14} by the rat. *J. Biol. Chem. 230*, 197-184.

164. Uttamkumar, S.; Pal, D.; Chakrabarti, P., (2000) Environment of tryptophan side chains in proteins. *Proteins: Struct., Funct., Bioinf. 38*, 288-300.

165. Byrdin, M.; Eker, A. P. M.; Vos, M. H.; Brettel, K., (2003) Dissection of the triple tryptophan electron transfer chain in *Escherichia coli* DNA photolyase: Trp382 is the primary donor in photoactivation. *Proc. Natl. Acad. Sci. U. S. A. 100* (15), 8676-8681.

166. Datta, S.; Mori, Y.; Takagi, K.; Kawaguchi, K.; Chen, Z.-W.; Okajima, T.; Kuroda, S. i.; Ikeda, T.; Kano, K.; Tanizawa, K.; Mathews, F. S., (2001) Structure of a quinohemoprotein amine dehydrogenase with an uncommon redox cofactor and highly unusual crosslinking. *Proc. Natl. Acad. Sci. USA 98* (25), 14268-14273.

167. Ivancich, A.; Dorlet, P.; Goodin, D. B.; Un, S., (2001) Multifrequency high-field EPR study of the tryptophanyl and tyrosyl radical intermediates in wild-type and the W191G mutant of cytochrome c peroxidase. *J. Am. Chem. Soc. 123* (21), 5050-8.

168. Colin, J.; Wiseman, B.; Switala, J.; Loewen, P. C.; Ivancich, A., (2009) Distinct role of specific tryptophans in facilitating electron transfer or as [Fe(IV)=O Trp(*)] intermediates in the peroxidase reaction of *Bulkholderia pseudomallei* catalase-peroxidase: a multifrequency EPR spectroscopy investigation. *J. Am. Chem. Soc. 131* (24), 8557-63.

169. Smith, A. T.; Doyle, W. A.; Dorlet, P.; Ivancich, A., (2009) Spectroscopic evidence for an engineered, catalytically active Trp radical that creates the unique reactivity of lignin peroxidase. *Proc. Natl. Acad. Sci. U. S. A. 106* (38), 16084-16089.

170. Pogni, R.; Baratto, M. C.; Teutloff, C.; Giansanti, S.; Ruiz-Duenas, F. J.; Choinowski, T.; Piontek, K.; Martinez, A. T.; Lendzian, F.; Basosi, R., (2006) A tryptophan neutral radical in the oxidized state of versatile peroxidase from *Pleurotus eryngii*: a combined multifrequency EPR and density functional theory study. *J. Biol. Chem. 281* (14), 9517-9526.

171. Stoll, S.; Shafaat, H. S.; Krzystek, J.; Ozarowski, A.; Tauber, M. J.; Kim, J. E.; Britt, R. D., (2011) Hydrogen bonding of tryptophan radicals revealed by EPR at 700 GHz. *J. Am. Chem. Soc. 133* (45), 18098-18101.

172. Potsch, S.; Lendzian, F.; Ingemarson, R.; Hornberg, A.; Thelander, L.; Lubitz, W.; Lassmann, G.; Graslund, A., (1999) The iron-oxygen reconstitution reaction in protein R2-Tyr-177 mutants of mouse ribonucleotide reductase. EPR and electron nuclear double resonance studies on a new transient tryptophan radical. *J. Biol. Chem. 274* (25), 17696-704.

173. Bleifuss, G.; Kolberg, M.; Potsch, S.; Hofbauer, W.; Bittl, R.; Lubitz, W.; Graslund, A.; Lassmann, G.; Lendzian, F., (2001) Tryptophan and tyrosine radicals in ribonucleotide reductase: a comparative high-field EPR study at 94 GHz. *Biochemistry 40* (50), 15362-8.

174. Olshansky, L.; Greene, B. L.; Finkbeiner, C.; Stubbe, J.; Nocera, D. G., (2016) Photochemical generation of a tryptophan radical within the subunit interface of ribonucleotide reductase. *Biochemistry 55* (23), 3234-40.

175. Abe, M., (2013) Diradicals. *Chem. Rev. 113* (9), 7011-7088.

176. Al-Kazwini, A. T.; O'Neill, P.; Adams, G. E.; Cundall, R. B.; Junino, A.; Maignan, J., (1992) Characterisation of the intermediates produced upon one-electron oxidation of 4-, 5-, 6- and 7-hydroxyindoles by the azide radical. *J. Chem. Soc., Perkin Trans. 2* (4), 657-661.

177. Pizano, A. A.; Lutterman, D. A.; Holder, P. G.; Teets, T. S.; Stubbe, J.; Nocera, D. G., (2012) Photo-ribonucleotide reductase β2 by selective cysteine labeling with a radical phototrigger. *Proc. Natl. Acad. Sci. U. S. A. 109* (1), 39-43.

178. Hassan, A. K.; Pardi, L. A.; Krzystek, J.; Sienkiewicz, A.; Goy, P.; Rohrer, M.; Brunel, L.-C., (2000) Ultrawide band multifrequency high-field EMR technique: A methodology for increasing spectroscopic information. *J. Magn. Reson. 142*, 300-312.

179. Stoll, S.; Ozarowski, A.; Britt, R. D.; Angerhofer, A., (2010) Atomic hydrogen as high-precision field standard for high-field EPR. *J. Magn. Reson. 207*, 158-163.

180. Zvyagin, S. A.; Krzystek, J.; van Loosdrecht, P. H. M.; Dhalenne, G.; Revcolevschi, A., (2004) High-field ESR study of the dimerized-incommensurate phase transition in the spin-Peierls compound $CuGeO_3$. *Physica B Condens. Matter 346-347* (Supplement C), 1-5.

181. Ozarowski, A.; Lee, H. M.; Balch, A. L., (2003) Crystal environments probed by EPR spectroscopy. Variations in the EPR spectra of Co(II)(octaethylporphyrin) doped in crystalline diamagnetic hosts and a reassessment of the electronic structure of four-coordinate cobalt(II). *J. Am. Chem. Soc. 125* (41), 12606-14.

182. Neese, F., (2012) The ORCA program system. *Comput. Mol. Sci. 2*, 73-78.

183. Neese, F.; Wennmohs, F.; Hansen, A.; Becker, U., (2009) Efficient, approximate and parallel Hartree–Fock and hybrid DFT calculations. A 'chain-of-spheres' algorithm for the Hartree–Fock exchange. *Chem. Phys. 356* (1), 98-109.

184. Petrenko, T.; Kossmann, S.; Neese, F., (2011) Efficient time-dependent density functional theory approximations for hybrid density functionals: analytical gradients and parallelization. *J. Chem. Phys. 134* (5), 054116 (1-14).

185. Klamt, A.; Schuurmann, G., (1993) COSMO: a new approach to dielectric screening in solvents with explicit expressions for the screening energy and its gradient. *J. Chem. Soc., Perkin Trans. 2* (5), 799-805.

186. Sinnecker, S.; Rajendran, A.; Klamt, A., (2006) Calculation of solvent shifts on electronic g-tensors with the conductor-like screening model (COSMO) and its self-consistent generalizatoin to real solvents (COSMO-RS). *J. Phys. Chem. A 110*, 2235-2245.

187. Drago, R. S., *Physical Methods in Chemistry*. 2nd ed.; W. B. Saunders Co.: Philadelphia, 1992.

188. Liu, A.; Barra, A.-L.; Rubin, H.; Lu, G.; Gräslund, A., (2000) Heterogeneity of the Local Electrostatic Environment of the Tyrosyl Radical in Mycobacterium tuberculosis Ribonucleotide Reductase Observed by High-Field Electron Paramagnetic Resonance. *J. Am. Chem. Soc. 122* (9), 1974-1978.

189. Connor, H. D.; Sturgeon, B. E.; Mottley, C.; Sipe, H. J.; Mason, R. P., (2008) L-tryptophan radical cation electron spin resonance studies: connecting solution-derived hyperfine coupling constants with protein spectral interpretations. *J. Am. Chem. Soc. 130* (20), 6381-6387.

LIST OF PUBLICATIONS

1. Wang X, Davis I, Liu A, and Shamsi SA (2013) Development of a CZE-ESI-MS assay with a sulfonated capillary for profiling picolinic acid and quinolinic acid formation in multienzyme system. *Electrophoresis 34*(12), 1828-1835 (DOI: doi.org/10.1002/elps.201200679).

2. Wang X, Davis I, Liu A, Miller A, and Shamsi SA (2013) Improved separation and detection of picolinic acid and quinolinic acid by capillary electrophoresis-mass spectrometry: Application to the analysis of human cerebrospinal fluid. *J. Chromatogr. A. 1316*(5), 147-153 (DOI: doi.org/10.1016/j.chroma.2013.09.085).

3. Huo L, Davis I, Chen L, and Liu A (2013) The Power of two: Arginine 51 and arginine 239* from a neighboring subunit are essential for catalysis in α-amino-β-carboxymuconate-ε-semialdehyde decarboxylase. *J. Biol. Chem., 288*(43), 30862-30871 (DOI: 10.1074/jbc.M113.496869).

4. Geng J, Davis I, Liu F, and Liu A (2014) Bis-Fe(IV): Nature's sniper for long-range oxidation. *J. Biol. Inorg. Chem., 19*(7), 1057-1067 (DOI: 10.1007/s00775-014-1123-8).

5. Huo L*, Davis I*, Liu F, Andi B, Esaki S, Hiroaki I, Li T, Hasegawa Y, Orville AM, and Liu A (2015) Crystallographic and spectroscopic snapshots reveal a dehydrogenase in action. *Nat. Commun.* 6:5935 (DOI: 10.1038/ncomms6935).

6. Geng J, Davis I, and Liu A (2015) Probing bis-Fe(IV) MauG: Experimental evidence for the long-range charge-resonance model. *Angew. Chem. Int. Ed., 54*, 3692-3696 (DOI: 10.1002/ange.201410247 & 10.1002/anie.201410247).

7. Liu F, Geng J, Gumpper RH, Barman A, Davis I, Ozarowski A, Hamelberg D, and Liu A (2015) An iron reservoir to the catalytic metal: The rubredoxin iron in an extradiol dioxygenase. *J. Biol. Chem., 290*(25), 15621-15634 (DOI: 10.1074/jbc.M115.650259).

8. Davis I and Liu A (2015) What is the tryptophan kynurenine pathway and why is it important to neurotherapeutics? *Expert Review of Neurotherapeutics, 15*(7), 719-721 (DOI: 10.1586/14737175.2015.1049999).

9. Yang Y*, Davis I*, Ha U, Wang Y, Shin I, and Liu A (2016) A pitcher-and-catcher mechanism drives endogenous substrate isomerization by a dehydrogenase in kynurenine metabolism. *J. Biol. Chem., 291*(51), 26252-26261 (DOI: 10.1074/jbc.M116.759712).

10. Dornevil K, Davis I, Fielding AJ, Terrell JR, Ma L, and Liu A (2017) Cross-linking of dicyclotyrosine by the cytochrome P450 enzyme CYP121 from Mycobacterium tuberculosis proceeds through a catalytic shunt pathway. *J. Biol. Chem., 292*(33), 13645-13657 (DOI: 10.1074/jbc.M117.794099).

11. Njuma OJ, Davis I, Ndontsa EN, Krewall JR, Liu A, and Goodwin DC (2017) Mutual synergy between catalase and peroxidase activities of the bifunctional enzyme KatG is

facilitated by electron-hole hopping within the enzyme. *J. Biol. Chem., 292*(45), 18408-18421 (DOI: 10.1074/jbc.M117.791202).

12. Fielding AJ, Dornevil K, Ma L, Davis I, and Liu A (2017) Probing ligand exchange in the P450 enzyme CYP121 from Mycobacterium tuberculosis: Dynamic equilibrium of the distal heme ligand as a function of pH and temperature. *J. Am. Chem. Soc., 139*(48), 17484-17499 (DOI: 10.1021/jacs.7b08911).

13. Thompson CV, Davis I, DeGayner JA, Arman HD, Tonzetich ZJ (2017) Iron Pincer Complexes Incorporating Bipyridine: A Strategy for Stabilization of Reactive Species. *Organometallics, 36*(24), 4928-4935 (doi.org/10.1021/acs.organomet.7b00772).

14. Davis I, Koto T, and Liu A (2018) Radical trapping study of the relaxation of bis-Fe(IV) MauG. *Reactive Oxygen Species, 5*(13), 46-55 (DOI: 10.20455/ros.2018.801).

15. Davis I*, Koto T*, Terrell JR, Kozhanov A, Krzystek J, and Liu A (2018) High-frequency/high-field EPR and theoretical studies of tryptophan-based radicals. *J. Phys. Chem. A, 122*(12), 3170-3176 (DOI: 10.1021/acs.jpca.7b12434).

16. Davis I, Yang Y, Wherritt D, and Liu A (2018) Reassignment of the human aldehyde dehydrogenase ALDH8A1 (ALDH12) to the kynurenine pathway in tryptophan catabolism. *J. Biol. Chem., 293*(25), 9594-9603 (DOI: 10.1074/jbc.RA118.003320).

17. Krishnan VM, Davis I, Baker TM, Curran DJ, Arman H, Neidig ML, Liu A, and Tonzetich ZJ (2018) Backbone dehydrogenation in pyrrole-based pincer ligands *Inorg. Chem., 57*(15), 9544-9553 (DOI: 10.1021/acs.inorgchem.8b01643).

18. Li J, Griffith WP, Davis I, Shin I, Wang J, Li F, Wang Y, Wherritt D, and Liu A (2018) Cleavage of a carbon–fluorine bond by an engineered cysteine dioxygenase. *Nat. Chem. Biol., 14*(9), 853-860 (DOI: 10.1038/s41589-018-0085-5).

19. Li J, Koto, T, Davis I, and Liu A (2019) Probing the Cys-Tyr cofactor biogenesis in cysteine dioxygenase by the genetic incorporation of fluorotyrosine. *Biochemistry, 58*(17), 2218-2227 (DOI: 10.1021/acs.biochem.9b00006).

20. Wang Y, Davis I, Shin I, Wherritt DJ, Griffith WP, Dornevil K, Colabroy KL, and Liu A (2019) Biocatalytic carbon-hydrogen and carbon-fluorine bond cleavage through hydroxylation promoted by a histidyl-ligated heme enzyme. *ACS Catal., 9*(6), 4764-4776 (DOI: 10.1021/acscatal.9b00231).

21. Yang Y, Davis I, Matsui T, Rubalcava I, and Liu A (2019) Quaternary structure of α-amino-β-carboxymuconate-ε-semialdehyde decarboxylase (ACMSD) controls its activity. *J. Biol. Chem., 294*(30), 11609-11621 (DOI: 10.1074/jbc.RA119.009035).

22. Nguyen RC, Yang Y, Wang Y, Davis I, and Liu A (2020) Substrate-assisted hydroxylation and *O*-demethylation in the peroxidase-like cytochrome P450 enzyme CYP121. *ACS Catalysis, 10*(2), 1628-1639 (DOI: 10.1021/acscatal.9b04596).

23. Wang Y, Davis I, Yang Y, Chen Y, Naik SG, Griffith WP, and Liu A (2020) Characterization of the non-heme iron center of cysteamine dioxygenase and its interaction with substrates. *J. Biol. Chem., 295*(33), 11789-11802 (DOI: 10.1074/jbc.RA120.013915).

24. Wang Y, Liu KF, Yang Y, Davis I, and Liu A (2020) Observing 3-hydroxyanthranilate-3,4-dioxygenase in action through a crystalline lens. *Proc. Natl. Acad. Sci. U. S. A. 2020, 117*(33) 19720-19730 (DOI: 10.1073/pnas.2005327117).

25. Li J, Davis I, Griffith WP, and Liu A (2020) Formation of monofluorinated radical cofactor in galactose oxidase through copper-mediated C−F bond scission. *J. Am. Chem. Soc., 142*(44), 18753-18757 (DOI: 10.1021/jacs.0c08992).

26. Yang Y, Borel T, de Azambuja F, Johnson D, Sorrentino JP, Udokwu C, Davis I, Liu A, and Altman RA (2021) Diflunisal derivatives as modulators of ACMS decarboxylase targeting the tryptophan-kynurenine pathway. *J. Med. Chem., 64*(1), 797–811 (DOI: 10.1021/acs.jmedchem.0c01762).

27. Traore ES, Li J, Chiura T, Geng J, Sachla A, Yoshimoto F, Eichenbaum Z, Davis I, Max P*, and Liu A (2021) Heme binding to HupZ with a C-terminal tag from Group A Streptococcus. *Molecules, 26*(3), 549 (DOI: 10.3390/molecules26030549).

28. Shin I, Davis I, Nieves-Merced K, Wang Y, McHardy S, and Liu A (2021) A novel catalytic heme cofactor in SfmD with a single thioether bond and a bis-His ligand set revealed by de novo crystal structural and spectroscopic study. *Chem. Sci., 12*(11), 3984-3998 (DOI: 10.1039/D0SC06369J).

29. Wang Y, Davis I, Shin I, Xu H, and Liu A (2021) Molecular rationale for partitioning between C-H and C-F bond activation in heme-dependent tyrosine hydroxylase. *J. Am. Chem. Soc., 143*(12), 4680-4693 (DOI: 10.1021/jacs.1c00175).